MARS VOLCANIC EVOLUTION: SPECTROSCOPIC ANALYSIS OF IGNEOUS COMPOSITIONS

BY
JOHN ROMA SKOK
B.S., CORNELL UNIVERSITY, 2007
M.S., BROWN UNIVERSITY, 2009

A DISSERTATION SUBMITTED IN PARTIAL FULFILLMENT OF THE REQUIREMENTS FOR THE DEGREE OF DOCTOR OF PHILOSOPHY IN THE DEPARTMENT OF GEOLOGICAL SCIENCES AT BROWN UNIVERSITY

PROVIDENCE, RHODE ISLAND
MAY 2013

This dissertation by John Roma Skok is accepted in its present form by the Department of Geological Sciences as satisfying the dissertation requirement for the degree of Doctor of Philosophy.

Date	John F. Mustard, Ph.D., Advisor

Recommended to the Graduate Council

Date	James W. Head III, Ph.D., Reader
Date	Malcolm Rutherford, Ph.D., Reader
Date	Amy Barr, Ph.D. Reader
Date	Steven W. Ruff, Ph.D., Reader

Approved by the Graduate Council

Date	Peter M. Weber Dean of the Graduate School

John Roma (J.R.) Skok
Date of birth: October 14, 1985
Place of birth: Johnson City, NY, USA

Education

May 2012	PhD, Geological Sciences Brown University, Providence, RI
May 2009	ScM, Geological Sciences Brown University, Providence, RI
May 2007	BS, Geological Sciences Cornell University, Ithaca, NY
May 2003	Owego Free Academy, Owego, NY

Additional Traning:
NSF Antarctic Field Season, McMurdo Dry Valleys, Fall 2010
NASA Planetary Volcanology Field Workshop, Hawaii, July 2010
NASA Planetary Science Summer School, JPL, Neptune Flagship Mission, July 2009
NASA Spaceward Bound MRDS Crew 53, Utah, December 2006

Professional Experience:

Compact Reconnaissance Imaging Spectrometer for Mars (CRISM) Science Team Collaborator, 9/2007-present

Graduate Research Fellow, *Brown University*, 9/2007-present

Mars Exploration Rovers (MER) PANCAM Undergraduate Researcher, 10/2003-5/2007

New York Space Grant Internship NASA Marshall, Huntsville, Al 6/2007-8/2007
Advisor: Dr. Doug Rickman, Lunar Soil Simulant Development

New York Space Grant Internship NASA Marshall, Huntsville, Al 6/2006-8/2006
Advisor: Dr. Jessica Gaskin, Development of a miniature Environmental- Election Scanning Microscope

Kopernik Observatory Science Instructor, Vestal, NY, 10/1999-8/2004

Peer Reviewed Publications:

Skok, J.R., J.F. Mustard, L.L Tornabene, C. Pan, D. Rogers, S.L. Murchie (In Submission) A Spectroscopic Analysis of Martian Crater Central Peaks: Formation of the Ancient Crust. *J. Geophys. Res.* CRISM Special Issue.

Skok, J.R. J. F. Mustard, B. L. Ehlmann, R.E. Milliken, S. L. Murchie, (2010) Silica deposits in the Nili Patera caldera on the Syrtis Major volcanic on Mars. *Nat. Geo*., 3, 838- 841, DOI:10.1038/NGEO990

Skok, J. R., J. F. Mustard, S. L. Murchie, M. B. Wyatt, and B. L. Ehlmann (2010), Spectrally distinct ejecta in Syrtis Major, Mars: Evidence for environmental change at the Hesperian-Amazonian boundary, *J. Geophys. Res.*, 115, E00D14, doi:10.1029/2009JE003338.

CONFERENCE PUBLICATIONS AND PRESENTATIONS

Skok, J.R. et al. Martian Hot Springs? Silica deposits in the Nili Patera Caldera. *(Invited talk)* P31G-03. AGU 2011

Skok, J.R. et al. Composition of the Primary Crust of Mars: Observations of Deeply Excavated Crater Central Peaks. P11A-1583. AGU 2011

Parente, M., **Skok, J.R.** and I. Baarstad. Simulating a Mars mission for the identification of samples of high mineralogical interest using a portable imaging spectrometer. P33D-1784. 2011 AGU

Skok, J.R. et al. Volcanically Driven Hydrothermal Systems in Post-Noachian Mars: Hotspots of Habitability on a Changing Planet. Exploring Mars Habitability 2011

Skok, J.R. et al. Spectroscopic and Morphological Analysis of Alga Crater's Central Peak: Implications for Mars Primary Crust Formation. 42st LPSC 2011

Tornabene, L.L. et al. and **J.R. Skok**. High-resolution morphologic and spectral characteristics of Crater-exposed Bedrock on Mars: Insights into the petrogenesis, stratigraphy and geologic history of the Martian crust. AGU 2010

Ehlmann, B.L. et al. and **J.R. Skok**. Impact Craters as Probes of the Ancient Martian Southern Highlands: Insights on Aqueous Alteration (Invited) AGU 2011

Skok, J.R. et al. Crystalline Igneous Crust of Mars: New Insights from the Southern Highlands. 41st LPSC 2010

Tornabene, L.L., et al and **Skok, J.R.**, A Crater-exposed Bedrock Database for Mars with Applications for Determining the Composition and Structure of the Upper Crust, 41st LPSC 2010

Murchie, S.L. et al. and J.R. Skok. New results from the MRO/CRISM investigation. 38th CSOPAR 2010

Skok, J.R. et al. Silica Deposits in the Nili Patera Volcanic Caldera, Syrtis Major, Mars AGU 2009

Skok, J.R. et al. Identification of Primary Noachian Crustal Blocks on Mars with CRISM Observations. 40th LPSC 2009

Skok, J.R. et al. CRISM-OMEGA Observations of Compositionally Distinct Crater Ejecta in the Syrtis Major Region of Mars. AGU 2008

Skok, J.R. et al. Compositionally Distinct Ejecta Blankets in Syrtis Major: Implications for Environmental Change. 39th LPSC 2008

Rask, J.C. et al and **Skok, J**. The Spaceward Bound Field Training Curriculum for Moon and Mars Analog Environments. LEAG Workshop on Enabling Exploration: The Lunar Outpost and Beyond. 2007

Rask, J.C., et al. and **Skok, J**. The Spaceward Bound Field Training Curriculum for Moon and Mars Analog Environments. 38th LPSC 2007

Bell, J.F., III et al. and **Skok, J.R.**, High Spatial Resolution Visible Wavelength Orbital Multipectral Imaging of Mars from the Mars Odyssey THEMIS-VIS Instrument. 37th LPSC 2006

Acknowledgments

These acknowledgements, like my entire life, must begin with my Mom. She gave me unconditional love, and taught me to follow my dreams. She said it was her job to give me 'roots and wings' and for her, I fly every chance I get. I cannot thank her enough for painting those glow-in-the-dark stars on my ceiling when I was four years old, making the heavens my first and last thought of every day. I am grateful for her encouraging me to volunteer at the Kopernik Observatory and providing three years of midnight rides. None of this would be possible without her support. To my Dad, I am grateful that he did his job when needed and never tried to stand in my way. My Grandma tried to give me a spiritual side, which I found, to her chagrin, on Mars and the other unearthly parts of this world. To Jet, no boy has had a better friend than you and I wish I had just one ounce of your focus and dedication.

Owego Free Academy helped sow the seeds of my ambition and gave me opportunities and character traits that have lead me here. Authentic Science Research Class with Mr. Russell led me to study Mars scientifically for the first time and I have yet to stop. My time on the school's baseball team with Mr. Aubel and Mr. Francisco taught me that hard work and persistence can achieve goals when talent, or a lack thereof, cannot. This lesson, more than any other, helped me persevere through graduate school. My time at Kopernik Observatory fueled my obsessions and set my path.

From Cornell University, I must thank my geology professors, Bryan Isacks and Matt Pritchard plus the others who helped me switch from a suffering physicist to a satisfied geologist. Jim Bell gave me a job working with the Mars Rovers, the single

proudest achievement of my undergraduate years. Working in that Mars lab began friendships that have lasted and grown with time. Eldar, Tim, Jonathon, Chase, Dimity, Briony, Ryan, Melissa, and James all set a bright example. I am thankful to know them all.

During the summers after my junior and senior years, I was lucky enough to work at NASA's Marshall Space Flight Center in Huntsville, AL. Jessica Gaskin was my mentor during the first summer as we designed a mini-SEM. Her patience, while I got used to a real lab, was greatly appreciated, even after I broke the lab's SEM vacuum chamber with shearing enthusiasm. My second summer with Doug Rickman gave me my first taste of the Moon and insight into the strange mind of an economic geologist. My deepest thanks to the Cavers and Caves of Alabama, that changed my life forever.

I am thankful to all of the Brown University professors who have engaged, challenged and supported me on this path. In particular, I would like to thank Mike Wyatt who sent me to Antarctica, Carle Pieters for forcing me to sharpen my ideas, Jim Head for painting the big picture and being an extraordinary host during memorable dinners with the astronauts, Steve Parman for forcing me to consider the Earth and Alberto Saal's raw enthusiasm. My fellow students have provided guidance and reassurance in tough times. I felt welcomed to the Mustard group by Leah Roach and Bethany Ehlmann, whose example would have been impossible to emulate but did set the bar high for success. Many other students welcomed me to Brown including Peter Isaacson, Rachel Klima, Sam Schon, Caleb Fassett, Joe Levy, Teresa Garcia and Laura Kerber. I am grateful to David Abt and his invitation to join the Hold On, Alaska softball team, a source of good times and great friends. Over the years the new crops of students came

and each brought their own character to the group. The additions to the Mustard group were a constant source of support and commissary. Janette Wilson, Rebecca Greenberger, Tim Goudge, Marc Mayes and Steph Spera will keep the group strong for years to come. Former postdoc Mario always brought a burst of energy and shared a memorable time roaming around Spain to Rio Tinto. I want to thank Jay, David, Mark and Sylvain for not murdering me in an Antarctic tent, I will do my best to repay that favor. A particular thanks must go to Leah Cheek. As a common compatriot in the afterhours mission room world, she became a trusted friend and confidant. Her perspective was always appreciated and she made the hard times seem conquerable. I am and will always be in her debt.

A special bond exists with those who began their journey with me and who were bonded in scavenger hunts, colloquium duties and were my guide posts as milestones and deadline came and went. Good luck to you incoming class of 2007 (man, that seems long ago), Angela Stickle, Debra Hurwitz, Brendan Hermalyn, Li Gao and Heather Ford.

Thanks to all the other students who shared a simile or occasional field trip; Nick, Jenny, Colin, Steph, Mary and the others too important to name. Beyond the Geology Department, Mathew Riolo was a good friend and an ever ready tennis partner and helped me get out of the Geo world once in a while. Thank you to the White Mountains and the many weekends you reminded me of the beauty of his word and refreshed my drive for geology. I may have complained about them often, but the hills of New England do offer something special.

A few friends stood out in seeing me through the dark times and celebrating the bright. Lucy Ooi was for several years my vital ally despite her Cornell-based rivalry

driven dislike for Brown. Yun Wang showed me that the PhD was achievable and was vital source of support during my later years.

My fullest thanks to Jack Mustard who gave me opportunities I could only dream of. He supported my ideas when I had no faith in them and taught me to see the value in the work I do. I tried hard to live up to the example he set and the expectations I felt he had for me. I will strive to make him proud.

Finally I thank you, the reader. For finding and opening my thesis and reading at least up to here. It is to you I dedicate my words. Keep reading and you will see the results of five years of human life. Keep reading and make those all worthwhile.

Preface

The earliest spacecraft images of Mars uncovered a barren world of ancient impacts craters and towering volcanoes. Decades of research and a string of increasingly capable spacecraft has since revealed a dynamic planet with a complex geologic record. But it is still these craters and volcanoes that dominate the surface and the history of Mars. This thesis explores several stages in the evolution of Martian volcanism (often with the help of impact craters) to understand how the planet formed and has since evolved.

Motivated by the goal to understand the formation of the ancient crust of Mars, we use the high resolution capabilities of the CRISM instrument to investigate the deep crust excavated in impact crater central peaks. Chapter one details the first step in this process. Here we describe the spectroscopic methods and geologic units of two well preserved and exposed crater central peaks, Alga and Ostrov craters. This work is the first record of using the full modified Gaussian modal (MGM) to determine mafic cation compositions in CRISM data and gives an in depth look at the morphology and mafic composition of Martian central peak structures. Detailed analysis, discussion and HiRISE DEM of Alga was contributed by Livio Tornabene. Thermal analysis of Alga and Ostrov with THEMIS data was contributed by Con Pan and Deanne Rogers.

The problem introduced in Chapter One is expanded in Chapter Two to look at 23 central peaks around Mars to investigate the global nature of the deeply excavated crust. We find that many of the observations made in Chapter One are found globally and we use this to create a model of the ancient crustal formation that is consistent with isotopic, geophysical and our compositional observations.

Chapter Three developed out of more practical motivations and only tangentially addressed an important part in the evolution of Martian volcanism. It was based on the single most important question facing the Mars community in this decade: where to send the flagship Mars Science Laboratory spacecraft. Chapter Three is the result of the work to understand the Northeast Syrtis region and propose location as a landing site for MSL. The most detailed of several projects to constrain this area was the analysis of a Hesperian fluvial system that straddles the boundary between the Syrtis Major volcanics and the Noachian plains of Nili Fossae and Isidis Basin. The details of the fluvial system infer how the Syrtis Major volcanics interacted with ancient climate to result in the observed features. The interplay of water and volcanoes on Mars is an on-going concern and Chapter Three investigates a small piece of this puzzle.

Chapter Four continues the look at the interplay of volcanics and water by investigating the final stage in a particular volcano's evolution. Again focusing on Syrtis Major, previous studies have found a late-stage light-toned volcanic flow in the volcano's Nili Patera caldera that thermal infrared analysis determined to have a dacitic composition. On basaltic Mars, evidence of evolved magmas are exceedingly rare and this site proved to be an ideal location to study the properties of a long lived, evolved volcanic system. CRISM observations of this caldera show silica deposits determined to be the results of a volcanically driven hydrothermal system that has remained remarkably well preserved and spectrally exposed. Chapter Four uses spectroscopic, morphological and application of terrestrial system analogs to determine the nature, extent and history of the hydrothermal system and explores the implications in terms of volcanism systems and habitability.

Chapter Five is a synthesis that brings together the arc of this project and ties together the chapters to tell the larger story of Martian volcanic evolution. It focuses on some of the big issues brought up by this work and some of the questions that grew from it and still need to be resolved. It then offers some possible directions for future work and ideas to continue advancing this work and the understanding of the Martian igneous evolution.

Table of Contents

Chapter 1:

Spectroscopic Analysis of Martian Crater Central Peaks: 1. A Window into the Ancient Crust.

J.R. Skok[1], J.F. Mustard[1], L.L Tornabene[2], C.Pan[3], S.L. Murchie[4], D. Rogers[3]

1. Department of Geological Sciences, Brown University

2. Department of Earth Sciences, University of Western Ontario

3. Department of Geosciences, Stony Brook University

4. Johns Hopkins University/Applied Physics Laboratory

Abstract

The ancient crust of Mars is well preserved but poorly exposed on the single plate planet. The surface has seen 4.5 Ga of modification by volcanism, alteration and impacts, all obscuring the ancient crustal material. However, large impacts have the potential to excavate intact megablocks and brecciated samples of this ancient, unmodified crust in central peak structures. The morphology and mineralogy of two well-exposed central peaks in the 19-km diameter Alga Crater and the 70-km diameter Ostrov crater were examined in detail as an initial look into the excavated Martian crust. High-resolution observations of the central peak units are quantitatively analyzed with the modified Gaussian model (MGM) to determine mineral cation composition. Analysis shows that the central peaks of these two craters are comprised of adjacent bedrock units that include dunites with intermediate to fayalitic compositions, low-calcium pyroxenites and materials interpreted to be impact melts. The observation of mineralogically segregated units with high-Fe content suggests a crustal formation process that promotes compositional segregation and a high degree of crystal fractionation.

Introduction

Observations from the Mars Reconnaissance Orbiter (MRO) spacecraft are providing a more detailed look at the Martian geologic record than ever before. These datasets allow observations at previously unattainable resolutions. One area of research that particularly benefits from the increased resolution is the study of impact crater central peaks. Central peaks act as a window into the crust of Mars but are typically only a few kilometers in scale. These high-resolution datasets allow the detailed morphologic

and spectroscopic analysis of exposed lithologies. Understanding the excavated crust of Mars is critical, because the absence of plate tectonics could have preserved the earliest crust. This early crust is not preserved on the Earth [Wilde at al., 2001] and is fundamentally different from the ancient lunar highlands that formed from plagioclase floatation [Wood et al., 1970]. Mars offers an opportunity to understand how early planetary crusts form and evolve on terrestrial planets.

Current understanding of the initial formation of Mars is derived from laboratory analysis of Martian meteorites [eg. Mittlefehldt, 1994; Nyquist et al., 2001; McSween et al., 2002] and the development of geophysical models [Elkins-Tanton et al., 2005]. Meteoritic studies have constrained the start of solar system formation at 4.567 Gyr with Martian accretion and core formation following quickly within 12.4±4 Myr thereafter [Debaille et al., 2007]. The melts that lead to the current Mars meteorite collection require at least four unique mantle source regions with age of formations ranging from 4,535±7 Myr to 4,457 Myr [Debaille et al., 2007]. This puts geochemical constraints on the duration of mantle formation, which would have had to last for at least 100 Myr [Debaille et al. 2007]. These dates are complimented by geophysical modeling to understand how the Martian mantle would form and with what minerals. While several models have attempted to explain this process based on slightly different assumptions and starting values [Bertka and Fei, 1997; Borg and Draper, 2003], we focus on the work by Elkins-Tanton et al. [2005], which specifically predicts the mineral compositions that would result from mantle and crust formation. This model also predicts the mineral cation composition as a function of depth. Beginning with a 2000 km deep magma ocean, high-Mg olivine and pyroxene crystallize first and settle from the magma ocean into a

cumulate pile. As this crystallization continues the magma ocean becomes shallower and more Fe-rich, resulting in a density inversion where the dense Fe-rich minerals are above the less-dense Mg-rich minerals. This would be corrected by a large scale overturn process that would raise the Mg-rich minerals toward the surface and sink the denser Fe-rich minerals in mantle scale diapirs [Whitehead and Luther, 1975]. The rising Mg-rich minerals will experience large scale decompressional melting [Ahren and Turcotte, 1979], creating magma that would erupt and form the majority of the ancient Martian crust. Four and a half billion years of impacts, alteration and volcanism would then melt, brecciate, and bury this ancient crust, creating the modern surface. Younger craters have the potential to excavate samples of this buried ancient crust in central peak structures allowing direct observations of its composition and morphology.

We focus this study on the central peaks of Alga and Ostrov craters (Figure 1). Alga crater, a 19 km crater within the 86 km diameter crater, Chekalin crater, offers some of the strongest mafic visible and near infrared (VNIR) spectral absorption features observed on Mars. We apply the modified Gaussian model (MGM, described below) to the remote observations of distinct mineralogic units within the central peak of Alga to demonstrate that compositional determinations can be made with Compact Reconnaissance Imaging Spectrometer for Mars (CRISM) [Murchie et al., 2007] data. While Alga represents one of the best case scenarios for compositional determination, we also apply the same techniques to the nearby central peak in Ostrov crater (Figure 1) to compare the results and gain further understanding of crustal composition. Demonstrating that CRISM observations allow the use of laboratory derived analytical methods to determine composition will open up much more of the planet to high-resolution spectral

analysis and the detailed examination of the spatially small ancient crustal exposures [Chapter 2].

Methods

This project aims to understand the nature of the deep, ancient crust of Mars by examining the composition and morphology of crustal exposures. On Mars, crustal exposures occur in three major types of environments; outflow channels [Loizeau et al., 2010], tectonic rifting such as in Valles Marineris [Flahaut et al., 2011], and impact craters [Melosh, 1989]. Of these, impact craters are the most globally pervasive. The deepest excavated material is exposed in the central peak structures [Melosh, 1989]. The vertical relief of central peaks is the key to preserving the strong spectral signatures by allowing surface refreshing and preventing crater fill from obscuring the observations. Since we require compositional analysis capable of distinguishing multiple lithologies within these peaks, we will use spectral data from the CRISM instrument to identify, map and analyze the central peak units for two prominent impact craters. Multispectral, 100m/pixel resolution data from the Thermal Emission Imaging System (THEMIS) instrument [Christensen et al., 2004] are also used to interpret the peak mineralogy. Morphology of both central peaks was analyzed with High Resolution Imaging Science Experiment (HiRISE) [McEwen et al., 2007], 25 cm/pixel imagery. Stereo HiRISE observations of the Alga central peak were processed into a digital elevation model that allowed determination of precise topography and aids in identifying unit relationships [McEwen et al., 2007].

CRISM. The primary dataset used in this study were observations from the CRISM VNIR hyperspectral imaging instrument [Murchie et al., 2007]. CRISM acquires full resolution targeted (FRT) images at 18 meter per pixel spatial resolution and 544 spectral bands ranging from 0.32 – 4.0 μm. CRISM observations were corrected for instrumental artifacts and were converted into I/F [Murchie et al., 2007]. A simple multiplicative correction was used to remove the atmospheric contribution to the spectra. This was determined using a volcano scan method developed and tested on ISM [Bibring et al., 1989] and Observatoire pour l'Mineralogie, l'Eau, les Glaces, et l'Activite (OMEGA) [Mustard et al., 2005]. A detailed description of the volcano scan method is in McGuire et al., [2009]. The CRISM data are collected on a short wavelength S-detector (VNIR: 362-1053 nm) and a long wavelength L-detector (IR: 1002 -3920 nm). Full wavelength modeling requires detector coordination. Ratioed spectra were calculated for each detector independently, then joined by removing the overlapping spectral data (1000 nm – 1053 nm) from the S-detector data and including an additive scaling factor on the S-detector data to match the value of the minimum wavelength of the L-detector [Murchie et al., 2007]. The absolute value of the ratioed value is dependent on the relative albedo of the region of interest and denominator area and does not affect modeling as long as the values are consistent between detectors. Mafic mineral deposits are identified with mafic parameter maps that highlight spatial regions with characteristic spectral absorptions [Pelkey et al., 2007; Salvatore et al 2010]. The parameter equations used to identify olivine, low-Calcium pyroxene (LCP) and high-Calcium pyroxene (HCP), respectively, are given below:

OLINDEX2:

$$\left(\left(\frac{RC1054-R1054}{RC1054}\right)*0.1\right)+\left(\left(\frac{RC1211-R1211}{RC1211}*0.1\right)+\left(\left(\frac{RC1329-R1329}{RC1329}\right)*0.4\right)+\left(\left(\frac{RC1474-R1474}{RC1474}*0.4\right)\right)\right) \quad (1)$$

LCPINDEX:

$$\left(\frac{R1330-R1050}{R1330+R1050}\right)*\left(\frac{R1330-R1815}{R1330+R1815}\right) \quad (2)$$

HCPINDEX:

$$\left(\frac{\mathrm{R1470-R1050}}{\mathrm{R1470+R1050}}\right)*\left(\frac{\mathrm{R1470-R2067}}{\mathrm{R1470+R2067}}\right) \quad (3)$$

Where R#### is the reflectance value at ####nm and RC#### denotes the value of a point at a wavelength of #### nm along a modeled line that follows the average slope of the spectrum. Average spectra were collected from regions of interest in the mineral deposits and were ratioed to a spectrally bland region in the same column of pixels, typically in the crater floor fill. Region of interest center locations and pixel number are listed and shown in the Appendix 1 and 2.

MGM Method. The modified Gaussian method (MGM) [Sunshine et al., 1990] was used to estimate the cation compositions of the minerals olivine and pyroxene (Figure 2). The MGM deconvolves overlapping absorptions of mafic mineral spectra into their fundamental absorption components. Individual absorption components are modeled as modified Gaussian distributions that mathematically describe the specific shape of electronic transition absorptions and are parameterized by a band center, band width, and band strength. The MGM models a spectrum's absorption features with Gaussian distributions and relates them to known absorption features. Gaussians are defined as:

$$g(x) = s * \exp\left(-\frac{(x-\mu)^2}{2\sigma}\right) \quad (4)$$

where *s* is band strength, σ is the band width, and μ is the band center. The MGM superimposes several Gaussians onto a continuum to model the spectrum with known absorption features at fixed wavelengths due to specific electronics transitions, discussed further below. MGM computations are carried out in energy and natural log reflectance space and thus overlapping absorptions are additive and can be modeled using linear inverse theory [Sunshine et al., 1990]. The inversion method applied in Sunshine et al. [1990] is the stochastic inversion of Tarantola and Valette [1982] that allows for the inclusion of a priori information as constraints on the solutions. Sunshine and Pieters [1993] showed that the constraints helped to stabilize the inversion process and prevent physically unrealistic solutions. The inversion is an iterative process and all absorption band parameters and the continuum are free to move until the residual errors between the log of the actual spectrum and the log of the modeled spectrum are less that 10^{-5} between consecutive model runs [Sunshine et al., 1990].

Initial MGM development was performed on laboratory measurements of pyroxenes [Sunshine and Pieters, 1990; Sunshine et al., 1993] with later development using laboratory measurements with a range of olivine compositions [Sunshine et al., 1998]. MGM has since been used on laboratory measurements of lunar olivine [Isaacson et al., 2010], remotely sensed lunar olivine from the M^3 instrument [Isaacson et al., 2011], laboratory and remotely sensed Martian pyroxenes [Kanner et al., 2007], remote terrestrial observations [Combe et al., 2006] and Martian mafic mixtures from OMEGA observations [Clenet, 2011]. This investigation is the first full treatment of CRISM data

using the MGM for compositional determination. Initial selection of Gaussian absorption properties (band center, band width, and band strength) was determined based on knowledge of the spectral properties of mafic minerals (Table 1) [Burns, 1993; Sunshine et al., 1993; Sunshine and Pieters, 1998], and the model was then allowed to automatically modify these values to produce the best fit to the observed spectrum. In cases where the automatic fitting routine failed to provide a satisfactory fit, attempts were made to refine the fit by first fitting a continuum before allowing freedom of the individual band absorptions.

Olivine Analysis. Olivine ($(Mg, Fe)_2SiO_4$) is a magnesium-iron silicate with a nesosilicate structure. It is spectrally identified in the near-infrared by a broad absorption centered near 1 μm that is the superposition of three overlapping absorptions caused by electronic transitions in Fe^{2+} ions located in distorted octahedral crystal lattice sites [Burns, 1970; 1974; 1993]. The exact band center of each of these absorptions is related to the relative proportion of Fe and Mg in the M1 and M2 sites with increasing Mg causing shorter wavelength absorptions and increasing Fe longer causing wavelength absorptions [Burns 1970; King and Ridley 1987; Sunshine and Pieters, 1998]. To avoid spectral effects outside the diagnostic 1 μm band, we only model from 0.8 μm to 1.8 μm but visually check that there are no 2 μm spectral features related to pyroxene. Three bands are used to model this absorption (Table 1) with the resulting fitted band centers determining the composition [Sunshine and Pieters 1998; Isaacson et al, 2010]. To determine the composition of a given spectrum, the three band centers are fit to a laboratory derived compositional trend line to fit for least error using the following relationship [Isaacson et al., 2010].

$$A = \left[\frac{1112.3}{1.2179^2} + \frac{2373}{2.2^2} + \frac{1335.9}{1.0309^2}\right] \quad (5)$$

$$B = \left(\frac{1}{1.2179^2} + \frac{1}{2.2^2} + \frac{1}{1.0309^2}\right) \quad (6)$$

$$Fo = B^{-1} * \left[A - \left(\frac{M1-1}{1.2179} + \frac{M2}{2.2} + \frac{M1-2}{1.0309}\right)\right] \quad (7)$$

Where A and B are constants that constrain the slope of the experimentally determined compositional relationship that relates the composition of the olivine to the band center for each of the three olivine absorptions. M1-2, M2, and M1-2 represent the band centers (in nm) for the three olivine absorptions. Fo is the cation composition ratio of Mg wt.% /(Mg wt.% + Fe wt.%) ranging from 0 (100% Fe) to 100 (100% Mg).

The formula can be modified to be fit to any two band inputs if needed. When modeling CRISM data we found that limiting analysis to the L detector data produces most reliable results because of the L+S detector alignment. The natural properties of the long wavelength M1-2 feature gives it the most wavelength variability per change in composition, meaning that small changes in bandcenters will have the least effect on the modeled composition making it the most stable feature band to fit. For these reasons, we include the modeled fits both using all three olivine bands and alternatively only using the M2 and M1-2 bands.

Pyroxene Analysis. Pyroxene ((Ca, Mg, Fe)Si_2O_6) is spectrally identified by absorptions at 1 and 2 μm with the band center slightly dependent on the Mg-Fe cation content and strongly dependent on the Ca content [Adams 1974; Cloutis et al., 1986; Cloutis et al., 1991; Klima et al., 2007] and a weak 1.2 μm absorption. The pyroxene absorptions are caused by crystal field transitions of iron in octahedral coordination with the 1- and 2-μm absorptions due to the composition of the M2 crystallographic site. This

causes distortion in the crystal structure based on the size of the cation. The 1.2 μm absorption is due to molecular distortion in the M1 crystallographic site [Burns, 1993]. Pyroxene Ca content can be determined by modeling each absorption as a combination of endmember low-calcium and high-calcium pyroxenes. Kanner et al. [2007] has shown that the ratio of modeled endmember absorption strengths is proportional to the relative composition of each endmember. Since pyroxene composition is spectrally distinguished by the Ca content, we refer to high-Ca (HCP) and low-Ca (LCP) compositions. This spectral determination does not distinguish structural variants of orthropyroxene (OPX) and clinopyroxene (CPX). However, in practice LCP strongly coincides with OPX while HCP coincides with CPX. Pyroxene is modeled in two ways. The first is with 5 absorptions (Table 1); the LCP and HCP endmembers of both the 1 and 2 μm absorptions and an absorption at 1.2 μm are used to provide a reliable fit but not used to determine composition. Ca content is determined by taking the ratio of the modeled LCP endmember band strength and dividing by the combination of the LCP and HCP strength, LCP/(LCP+HCP) determining the normalized band strength ratio (NBSR) [Kanner et al., 2007]. This is done for both the 1 and 2 μm absorptions. A value of 1.0 indicates there is only LCP while a value of 0.0 indicates only HCP, with intermediate values proportional to the relative Ca content. The second way pyroxene is modeled is with a single 1 and 2 μm absorption to calculate the overall band centers for classification against terrestrial pyroxenes.

MGM Continuum Testing. The results derived from the MGM are influenced by the assumptions that go into the modeling. To build on the strong legacy of laboratory work, we adopted many of the previously used assumptions, particularly

concerning initial band position, widths and strengths which are derived from the mineral structure and spectral properties of examined minerals (Table 1) [Burns, 1993; Sunshine et al. 1993, Sunshine and Pieters, 1998]. We have, however, reconsidered the traditional laboratory treatment of the spectral continuum [Sunshine et al., 1990; 1993, Hiroi et al., 2001] in order to account for the different viewing conditions that characterize spacecraft observations. The initial MGM was tested and verified using a linear, horizontal continuum in wavelength space that was found to produce accurate results with clean samples and controlled observations [Sunshine et al., 1990; 1993]. Later work with laboratory spectra of Martian meteorites and remote observations from the OMEGA instrument around Mars used a continuum curved in wavelength space continuum (defined with a two term polynomial equation) to best fit the spectral character of the observations [Kanner et al., 2007]. In this study these continuum shapes, along with one that is linear and angled were tested both for their ability to reproduce accurate compositional results and create results that are compositionally consistent among the observations (Figure 3). These three types of continua (horizontal, sloped and curved in wavelength space) were applied to four examples of olivine laboratory spectra and two pyroxenes of varying composition. The olivine test showed that both the curved and angled continuum produced modeled compositions closest to the values determined from chemical analysis, with the curved method producing the most consistent results (Table 2). The pyroxene modeling showed that both the curved and horizontal continua produced reasonable compositional results but with the curved continuum again providing the most accurate results. Based on these tests and the legacy of Kanner et al., [2007], we use a continuum curved in wavelength space throughout the rest of the study.

Allowing the continuum to curve to fit the spectra should better compensate for the effects of surficial oxides at short wavelengths, the region where the curved continuum will have the most significant effect.

Ratio Testing. Reliable mafic mineral absorption modeling requires spectra that are free from spectral artifacts. In the laboratory, this is done by measuring only the desired mineral separates. However, Martian spectra, even examples with strong mineral absorptions, contain signatures of surface and atmospheric dust and systematic instrument errors that must be removed before modeling. The ratio technique divides the spectrum of interest by a spectrum taken from a spectrally bland area in the same detector column. This removes the spectral features common to both regions and leaves only the spectra unique to the region of interest.

In order to use the MGM technique on remote ratioed data, we first must show that it works on ratioed laboratory data. This was tested by calculating a series of spectral mixtures with the Hapke mixing equations (Figure 4) [Hapke, 1981]. In this test, we mix a laboratory olivine spectrum with a spectrally bland laboratory spectrum of palagonite. Palagonite was chosen because it is spectrally similar to observations of wide spread Martian dust [Guinness et al. 1987]. Mixtures range from 100% to 10% olivine with steps at every 10%. As expected, the mixed spectra produce MGM modeled results and olivine compositions much different than the initial sample (100% olivine) (Table 3A). However once the ratio is applied by dividing the mixture by the palagonite the relative band centers calculated for all spectra with at least 20% olivine are within 10% of the original olivine's composition (Table 3B). This supports the use of the ratio technique to remove the spectral effects of mixed materials in real observations.

Error Consideration. MGM was developed and tested by analyzing laboratory spectral measurements of well characterized samples. However, errors from initial conditions lead to an error of ±5 Fo# for olivine [Isaacson and Pieters, 2010]. Additional errors are derived when applying the MGM to remote sensing data with lower signal-to-noise and additional spectral components. Extensive analysis has determined errors for applying MGM to remote sensing data sets. Isaacson and Pieters [2010] determined a composite error for the MGM of olivine with the M^3 dataset to be ±20 relative Fo# units. Applying the MGM to pyroxenes with laboratory and OMEGA data determined that the calcium content can be constrained to ±10% [Kanner et al., 2007].

THEMIS TIR. We use the multispectral thermal infrared observations from the THEMIS instrument [Christensen et al., 2004] to provide an independent check on the composition. THEMIS operates both a TIR multispectral mode with nine bands between from 6.8 to 14.9 μm with 100-m per pixel resolution and a visible mode with five bands and 18-m per pixel resolution. Hyperspectral observations from the TES instrument were examined for both the Alga and Ostrov central peaks. Alga's central peak did not have high quality data coverage. A few TES spectra were available for Ostrov's central peak; however these were determined to have artifacts invalidating mineral determinations.

THEMIS daytime multispectral images with warm (>265 K) surface temperatures were selected for detailed analysis of the two central peaks. The images were calibrated and atmospherically corrected using the methods described by Bandfield et al. [2004]. Spectrally distinct units within each scene were determined by examining CRISM mafic parameters and THEMIS decorrelation stretch (DCS) [Gillespie et al., 1986] images. To quantitatively map the spectral unit distributions, spectra were extracted from distinct

units identified in the DCS images and averaged. These spectra were then used to model the scene emissivity with a linear least-squares minimization routine. For both Alga and Ostrov, the most olivine-rich spectral units could be modeled as a combination of another unit in the scene plus a laboratory spectrum of olivine. Because of this, the olivine-rich spectral unit does not represent a true end-member and the olivine-rich unit spectrum was replaced with a pure olivine spectrum for mapping the spectral unit distributions [Rogers and Bandfield, 2009]. Root-mean-square (RMS) error images calculated from the least-squares minimization were examined to ensure that all surfaces were relatively well-modeled by the spectral library.

Results

Alga Crater. Alga crater is 19 km wide and is located just east of the center of the 85 km diameter degraded Chekalin crater. The Alga crater rim shows layered light-toned olivine-bearing outcrops, best exposed to the southeast. The western and northern crater wall and terraces show scattered exposures of olivine- and pyroxene-bearing outcrops. The central peak of Alga is ~200 m high and exposes a complex relationship among local mafic units. The terrain was divided into four units based on morphologic and spectroscopic analysis of the central peak (Figure 5): a distinct light-toned olivine-bearing unit, a pyroxene-bearing bedrock unit, a light-toned pyroxene unit found on the floor of the crater and a fine-grained deposit with a varying clast content that are interpreted to be an impact melt unit on the flanks of the central peak (Figure 6). Representative regions of each unit were analyzed with the methods described above to determine the cation composition and lithology.

Alga Crater Olivine Unit. The olivine-bearing unit correlates with partially to well-exposed relatively light-toned massive outcrops and relatively dark deposits bearing abundant light-toned clasts, which drape and appear to flow off the bedrock of the central uplift on the northern slopes. The olivine-rich outcrops are located primarily on the northern and western slopes of the central peak with a few small megablocks observed on the eastern side. This unit typically features a sharp boundary with the adjacent units that are easily observed by the relative albedo contrast, but the unit is also characterized by a dense network of dark fractures and mantles of dark-toned materials, interpreted to be impact melts generated by the Alga-forming event. Spectrally the ratioed olivine exhibits the characteristic olivine absorptions and no other detectable spectral features (Figure 7) in the VNIR range. Regions of interest were selected from ten locations within the unit for MGM analysis (Appendix 1.1, 1.2). MGM modeling and composition determination yields modeled result range of $Fo_{9\text{-}43}$ with a mean of Fo_{18} (Table 4A).

Alga Crater Pyroxene-Bearing Bedrock Unit. The pyroxene-bearing bedrock unit comprises the remaining bulk of the central peak bedrock units, dominating the peak's southern portion. The expression of this spectral unit is similar to that of the olivine unit (both light-toned massive and highly fractured bedrock in addition to clast-rich flows), but they are not as nearly well-exposed and appear to possess more draped deposits of clastic impact melts superimposed on them. Fractures within this unit display a variety of textures ranging from rounded and semi-angular on west side of the peak to tabular fractures on certain parts of the eastern slope of the peak (Figure 8). Spectral analysis of eight regions of interest (Appendix 1.2, 2.2) all confirm low-calcium pyroxene with similar band centers. A slightly longer 2 μm band for the observed 1 μm band position

indicates that this unit is relatively Fe-rich [Adams, 1974; Cloutis and Gaffey, 1991]. NBSR values of each of the pyroxene absorption feature show reassuring agreement between the 1 and 2 μm absorptions (Table 4B), supporting the absence of olivine spectral effects, which typically expresses itself as a modification of the 1 μm absorption features. The elevated NBSR values (2 μm: 0.59-0.61) support a LCP enrichment of this pyroxene unit.

Alga Crater Light-Toned Pyroxene Unit. The second pyroxene-bearing unit is located on the crater floor in two distinct occurrences just south and east of the central peak. This unit is lighter than the pyroxene-bearing bedrock and is significantly brecciated with a wide range of clast sizes. The lighter-tone of the bedrock makes this unit easy to detect and distinguish from the darker background material of the crater floor. MGM spectral analysis of 7 regions (Appendix 1.3, 2.3) show well-formed pyroxene spectral features with band centers similar to the pyroxene bedrock unit, again consistent with a relatively high-Fe, low calcium pyroxene. However this unit displays less VNIR spectral contrast, creating more error in the spectral modeling (Figure 9). The lower spectral contrast may be caused by several contributing factors, the most likely being smaller grain sizes or the intimate mixing of a spectrally neutral but high albedo material. Both of these options would lead to the albedo contrast and observed spectral properties, but the rocky appearance of the outcrop would support the mixing hypothesis with a material similar to the glassy melt unit described below.

Three of the regions of interest (ROI: 1, 2, 5) display a noticeable secondary absorption feature centered at 2.2 μm superimposed on the pyroxene absorption. This absorption (Figure 10) is similar in width and position to a metal-OH feature, particularly

Si-OH [Anderson and Wickersheim, 1964]. These spectral features may indicate that this unit is a mixture of pyroxene and a silica-rich impact melt or potentially a product of an impact induced hydrothermal activity. The presence of these features in only a few of the examined regions may be due to a heterogeneous molecular hydration throughout this unit.

Alga Crater Impact Melt. The final unit that figures prominently in the central peak is a fine-grained deposit that displays weak pyroxene spectra features makes up a large part of the western portion of the central peak (Figure 11). This unit is characterized by potential flow textures going down slope and contains meter-sized clasts of the pyroxene-bearing bedrock at low elevations. The melt is located on the central peak apex and fills the peak's northern, southern and eastern couloirs. The high elevation regions of this unit near the peak summit appear clast free at HiRISE's 25 cm/pixel resolution. Near the base of the peak the melt contains meter sized clasts of the pyroxene-bearing material. All examined regions of the melt unit on the central peak show detectable pyroxene spectral signatures (Appendix 1.4, 2.4). The pyroxene band centers are similar to the other pyroxene units but much weaker band depths (Figure 12).

Pyroxene Unit Comparison. The Pyroxene Bedrock, Light-Toned Pyroxene, and Impact Melt units all display clear pyroxene spectral absorptions with similar band centers but have a significant difference in band depth (Figure 12). The Pyroxene Bedrock has a low calcium signature with a well-developed 1.2 μm shoulder caused by Fe^{2+} in the M1 site [Klima et al., 2008]. Strong spectral absorptions make this unit the best developed pyroxene member in the scene. Conversely, the impact melt unit has a weak pyroxene band depth and is thought to be comprised of an intimate mixture of

spectrally neutral glass with clasts of the pyroxene units providing the relatively weak spectral absorptions. The remaining Light-Toned Pyroxene unit has an intermediate band depth but similar band positions as the Pyroxene Bedrock signifying similar composition but with the possible addition of a brightening spectrally neutral component. Under this model, the three pyroxene units are accessing the same lithologic material but are including varying degrees of spectrally neutral materials. The Impact Melt unit would have a quenched glass component to the matrix that would provide the spectral modification, while the modifying material in the Light-Toned Unit is less clear. Impact glass produced in this impact is a possibility as is melt from the preexisting Chekalin crater or other nearby crater basins. Alternative materials such as plagioclase and quartz could also provide the desired spectral effect but are difficult to constrain with current observations.

Ostrov Crater. The nearby Ostrov crater provides another well exposed central peak to apply the MGM compositional analysis. Ostrov is a 65 km diameter crater located 150 km to the southwest of Alga. Ostrov has had significantly more erosional modification and deposition than Alga, with a deeply dissected rim and multiple fans filling the crater resulting in the emplacement of sediments throughout the most of the crater depression. The central peak structure stands above these deposits and display strong mafic absorption features (Figure 13). While Ostrov displays several important similarities with Alga, it is simplified with only clearly discernible units, an olivine-bearing and a pyroxene-bearing unit and a third spectrally bland region that may be analogous to the glassy melt unit. Much like we see in Alga, these units are strongly dominated by the single mineral with little evidence of spectral mafic mixing.

Ostrov Crater Olivine Unit. The olivine-bearing unit in Ostrov (Figure 13) is characterized by the inclusion of many small light-toned outcrops with the olivine dominated region but otherwise is morphologically similar to the pyroxene-bearing unit. The unit has a very sharp boundary with the pyroxene-bearing units and shows no spectral signature of a pyroxene component, again indicating minimal pyroxene**.** A spectral feature near 0.9 μm affects the fit of the M1 absorption in each of the ratioed spectra, requiring the use of the M2 and M1-2 bands for determining the cation composition. The MGM analysis of four regions of interest within the olivine unit result in slightly elevated Fo# compared to the Alga olivine unit (Appendix 1.5, 2.5). The measured olivine spectra had atypical response in the S-detector data. This response is unsuitable for full MGM modeling due to distortion of the M1-1 spectral band. The long wavelength shoulder of the olivine spectra is well formed and suitable for modeling making the calculation of the Fo# that was done with only the M2 and M1-2 absorptions more reliable for this unit. The high-quality of the near-infrared data and well-developed olivine absorption in this region makes the modeled fit reliable even with the two bands. The longest wavelength M1-2 absorption is the best constrained by the spectra and least dependent on small band center shifts. This unit displays values ranging Fo_{44}-Fo_{56} with a mean of Fo_{50}.

Ostrov Crater Pyroxene Unit. The Ostrov crater pyroxene unit spatially dominates the central peak structure. Nine regions of interest have been selected for MGM processing based the extent of pyroxene exposure (Appendix 1.6, 2.6). The resulting band center determination is consistent with a very low Ca, moderate Fe pyroxene (Figure 14). NBSR values of these pyroxenes show close agreement between

the 1 and 2 μm values, supporting a relatively pure pyroxene composition. NBSR values fall in the rage from 0.6-0.8, indicating enrichment in LCP. Compared to the Alga pyroxene these are even more enriched in LCP and have slightly less Fe content (Table 4B).

THEMIS Analysis of Central Peaks. Analysis of THEMIS observations of Alga's central peak identifies three main spectral units (Figure 15). The first type is dominated by olivine, but is not a spectral match to pure olivine. The THEMIS spectrum is consistent with olivine plus one or more components; a good spectral match can be achieved with a 60:40 mixture of olivine and a palagonite-like high-silica poorly crystalline phase. It can also be well modeled as a mixture of olivine plus the surrounding central peak surface. The second spectral type maps to the majority of central peak and is spectrally consistent with TES Surface Type 1 [Bandfield et al., 2000], within the THEMIS spectral range, though the spectral bands of THEMIS limit the determination of a precise mineralogy. The third type is spectrally similar to an intermediate between Surface Type 1 and Surface Type 2 [Bandfield et al., 2000] and maps to the crater floor and rim. Surface Type 1 is considered to be basaltic in nature. Surface Type 2 is consistent with altered basalt [Wyatt et al., 2002] or some elevated silica content and may represent the mixture of the central peak mafics with a glassy impact melt component.

THEMIS analysis of Ostrov central peak (Figure 15) can distinguish three spectral units. The first maps to the CRISM olivine-bearing units and is dominated by olivine, but is not a spectral match to pure olivine, similar to the Alga olivine unit. The second type maps to the pyroxene-bearing units and is spectrally consistent with high

concentrations of LCP; however the coarse resolution prohibits precise and unique mineralogic assignments. The third type has low emissivity in shorter wavelengths (~8.5-9.5 μm) and higher emissivity in longer wavelengths (11-12 μm), consistent with a low abundance of mafic minerals.

Discussion

While the central peaks expose deeply buried material, the history of that material is dependent on the complex history of the local area. Alga crater would expose ejecta from Argyre basin to the south and is within the outer rings of Ladon and Chekalin craters. This history would have resulted in intense brecciation of the crust, burial of impact products (e.g. melts), and potentially basin related volcanism [Schultz and Glicken 1979]. This history makes reconstructing the ancient crust from modern exposures a difficult task. However, detailed observations can still characterize the composition and first order properties of the ancient crustal materials.

Rock Type Determination. VNIR spectroscopy of mafic minerals is sensitive to cation composition of the dominate mineralogy but may not detect minerals without a distinct near-infrared signature or sufficient abundance. Rock compositional results must then include assumptions about the target materials and an understanding of the VNIR and TIR spectroscopic ranges. One notable limitation with the VNIR spectral range is that the plagioclase absorption feature can only be observed if it contains trace amounts of Fe^{2+} and is present in extremely high abundances (>~85%) [Bell and Mao, 1973; Cheek et al., 2011; Crown and Pieters, 1985]. The strong mafic signatures of the units reported here overwhelm any potential signature from plagioclase, limiting our ability to

reliably report on its presence, abundance and composition with the VNIR observations. The application of THEMIS IR observations can help constrain the silicate compositions though they have spatial and spectral resolution limits. Near-infrared observations are well suited for the detection of Fe-bearing olivine and pyroxene minerals**.** The compositional determination of the Alga olivine-bearing lithology focuses on the complete absence of a 2 µm pyroxene absorption indicating pyroxene content less than ~5-10% and THEMIS observations show spectra consistent with an olivine endmember with an additional spectral component. These observations indicate that this unit has a composition in the range of a dunite (>90% olivine) (also spectrally consistent with troctolite as suggested by the THEMIS observations) composition with a fayalite composition ranging from Fo_{45-7} (Table 4A).

The pyroxene-bearing lithologies are interpreted using similar reasoning. The 1 µm region can be fully modeled with the expected pyroxene absorptions without requiring an olivine component at slightly longer wavelengths. VNIR observations indicate nearly pure pyroxene with olivine content less than 5%, suggesting a pyroxenite lithology (although spectral analysis cannot rule out a borderline noritic composition). This is consistent with but not uniquely confirmed by the THEMIS observations. The band centers of the observed pyroxenes are both in the low range on the pyroxene continuum indicating low-Ca content but the relativity long-wavelength band center of the 1 µm absorption, while still in the LCP range, suggests a Fe-enrichment. While there is some spread to the observations they are generally consistent with an enrichment of low-calcium and relatively high-Fe cation content. These results would signify an average composition in the range of a Fe-rich pigeonite. However, large scale spatial

mixing would have difficulty discriminating between pure pigeonite and an intimate mixture of endmember minerals such as an augite-ferrosilite mixture.

The light-toned pyroxene unit also shows no evidence of mixture with other minerals and is similar in cation composition to the pyroxene-bearing bedrock with weaker band depth. We suggest that this is most easily explained as a mixture with the pyroxene-bearing bedrock and a spectrally featureless material, most likely an impact melt unit. This would have the effect of attenuating the absorption feature band depth but keeping the band centers fixed as observed [Tompkins and Pieters, 2010]. Current observations are unable to determine the pyroxene proportion of the unit.

The melt unit is dominated by a spectrally bland glass unit with a small proportion of pyroxene causing weak absorptions. The position of the fine grained melt unit in the overall unit stratigraphy is still uncertain, but we suggest two possible scenarios. The first is that the impact melt formed from the pyroxene bedrock unit during the formation of Alga crater and it covered a portion of the central peak, entraining clasts of pyroxene-bearing material. This scenario is supported by the presence of possible flow like features (seen in Figures 6 and 11) that could represent the remnants from the early flow and solidification process. However, Alga crater is relatively old with a population of superimposed craters and weathered ejecta. Over time erosion may be expected to wear away a surficial veneer of impact melt. The second scenario is that the melt was produced in a previous basin scale impact event (e.g. Ladon or Argyre basin formation) and was emplaced as part of deep crustal stratigraphy. The impact that formed Alga would have then excavated the impact melt along with the adjacent crustal rocks to form the observed

peak. The relatively weak nature of the melt would cause preferential erosion and the observed recession of this unit.

The central peak of Ostrov crater has only two discernible units and unlike Alga, these are only easily distinguished with spectral mapping. The units are an olivine-bearing unit seen in three locations and a pyroxene-bearing unit comprising the rest of the central peak (Figure 13). Similar to the Alga units, we observe no mafic mixing in the VNIR or TIR, again indicating that the units are dominated by a single mafic mineral and are determined to be dunite and orthopyroxenite dominated respectively. The olivine-bearing unit has significantly higher Fo# than the Alga olivine units. While it is difficult to draw conclusions about the exposed crust from two examples, we note compositional diversity and relatively high Fe contents compared to most of the reported values from other Martian olivine samples, typically ranging from Fo_{30-80} [Koeppen and Hamilton, 2008; McSween et al., 2006]. The Ostrov pyroxene-bearing unit is compositionally similar to the Alga pyroxene unit characterized by high-Fe, low-Ca pyroxene.

These two crater central peaks offer a look into the composition of the deep crust of Mars. While not representative of the whole crust, we begin to see some important trends. The first is that in both examples we observe cumulate outcrops, dunites and pyroxenites, with no evidence of mixtures of these minerals. This may indicate that the ancient crust was largely formed in large, slow cooling magma bodies similar to terrestrial large mafic intrusions [Cawthorn, 1996] rather than a series of quick cooling lava flows. The second is that the olivine displays a range of compositions from intermediate to fayalitic , with a significant Fe-enrichment compared to other measured Martian olivine. Finally, the observed pyroxenes seem to be dominated by a high-Fe,

low-Ca calcium composition. This is consistent with the high Fe values seen in the olivine-bearing units and with the LCP pyroxenes seen in Noachian terrains throughout Mars [Mustard et al., 2007].

The observations that the ancient Martian crustal material has been mineralogically segregated with a range of Fe-rich compositions indicate that it had a petrographic history fundamentally different than the basalts that cover most of the surface [Rogers and Christensen, 2007; Poulet et al., 2009]. This ancient crust would have had to experience crystal segregation into the observed dunites and orthopyroxenites. These layers would have to be thick enough to become brecciated clasts several hundreds to thousands of meters across and must occur close enough in proximity that a single central peak can excavate both units. Only a few known methods exist for segregating minerals on large scales. These include dunite channels in harzburgite as seen in ophiolites [Kelemen et al., 1995], olivine deposition from komatite surface volcanic flows [Walter, 1998], or melt fractionation of basin induced impact melts [Warren et al., 1996]. The analysis of additional central peaks from across Mars would have the potential to better constrain the composition and character of the early crust and support one of these formation hypotheses [Chapter 2]

Conclusions

Alga and Ostrov craters have well exposed, mafic central peaks ideally suited for spectroscopic analysis of deeply exposed crustal materials. Combined VNIR and TIR observations show that the central peaks are formed primarily from olivine and pyroxene-dominated units. MGM analysis of Alga olivine gives fayalitic values with a Fo#:$_{18\pm11}$.

Ostrov's olivine unit has more intermediate values that average $Fo_{50\pm 6}$ (Table 4A). The main pyroxene units for both central peaks are spectrally similar and dominated by a high-Fe, low calcium pyroxene with the Ostrov pyroxenes having a slightly higher proportion of LCP.

The spectral analysis of the mafic units indicate that there are relatively little mafic mixing, so that the olivine-bearing units are likely a dunite to troctolite lithology, while the pyroxene–bearing unit are pyroxenites dominated by minerals with a low-Ca pigeonite composition. The relative purity of these units supports a high degree of crystal segregation during formation. These examples are most consistent with a crustal formation process that would have allowed slow cooling and cumulate settling to form the ancient crust.

Acknowledgements

We are very grateful for the fine work of the NASA MRO project team and the fine job by the CRISM Science Operations Center (SOC). This work was supported by NASA through a subcontract with the Applied Physics Lab at the Johns Hopkins University.

References:

Adams, J.B., (1974), Visible and near-infrared diffuse reflectance: Spectra of pyroxenes as applied to remote sensing of solid objects in the Solar System. *J. Geophys. Res.*, 79, 4829-4836.

Agee, C.B. and D. Walker (1993), Olivine flotation in mantle melt. *Earth Planet. Lett.*, 114. 315-324.

Ahren, J.L. and E.R. Turcotte (1979), Magma micration beneath an ocean ridge. *Earth Planet. Sci. Lett*., 45, 115-122.

Anderson, J. H., Jr., and K. A. Wickersheim (1964), Near infrared characterization of water and hydroxyl groups on silica surfaces, *Surf. Sci.*, **2**, 252– 260, doi:10.1016/0039-6028(64)90064-0.

Bandfield et al., (2000), A Global view of Martian Surface Compositions from MGS-TES. *Science,* 287, 1626, DOI: 10.1126/science.287.5458.1626.

Bandfield, J. L., D. Rogers, M. D. Smith, and P. R. Christensen (2004), Atmospheric correction and surface spectral unit mapping using Thermal Emission Imaging System data, *J. Geophys. Res.,* 109, E10008, doi:10.1029/2004JE002289.

Bell, P.M. and H.K. Mao (1973) Optical and chemical analysis of iron in Luna 20 plagioclase. *Geo. Cos. Acta.*, 37, 4, 755-759.

Bertka, C.M. and Y. Fei (1997), Mineralogy of the Martian interior up to core-mantle boundary pressures. *J. Geophys. Res.*, 102, B3 5251-5264.

Bibring et al., (1989), Results from the ISM experiment. *Nature*, 341, 591-593, doi:10.1038/341591a0.

Borg, L.E and D.S. Draper (2003), A petrogenetic model for the origin and compositional variation of the martian basaltic meteorites. *Met. & Planet. Sci*. 38, 1713-1731.

Bowen, N.L. (1928), The Evolution of Igneous Rocks. Princeton University Press, Princeton, N.J.

Bowen, N.L. (1932), The system FeO-SiO2. *Amer. J. Sci.*, 5th Ser., 24, 188-213.

Burns, R.G., (1970), Crystal field spectra and evidence of cation ordering in olivine minerals, *Am. Mineral*., 55, 1608-1632.

Burns, R.G., (1974), The polarized spectra of iron in silicates: Olivine a discussion of neglected contributions from Fe2+ ions in M(1) sites, *Am. Mineral*., 59, 625-629.

Burns, R. G. (1993), Mineralogical Applications of Crystal Field Theory, 2nd ed., 551 pp., Cambridge University Press, Cambridge.

Cawthorn, R.G. (ed.) (1996) Layered Intrusions. Elsevier, Amsterdam, Netherlands.

Cheek et al., (2011), Spectral Characteristics of Plagioclase with variable iron content: Applications to remote sensing of the lunar crust. LPSC 2011. Houston, TX.

Christensen et al., (2004), The Thermal Emission Imaging System (THEMIS) for the Mars 2001 Odyssey Mission. *Space Sci. Rev.*, 110, 85-130.

Clenet et al., (2011), A new systematic approach using the Modified Gaussian Model: Insight for the characterization of chemical composition of olivines, pyroxenes and olivine–pyroxene mixtures. *Icarus*, 213, 404–422.

Clenet, H. (2011), Télédétection hyperspectrale : minéralogie et pétrologie, Application au volcan Syrtis Major (Mars) et à l'ophiolite d'Oman. PhD Thesis, Doctorat De L'Universite De Toulouse.

Cloutis, E. A., M. J. Galley, T. L. Jackowski, and R. L. Reed (1986), Calibrations of phase abundance, composition, and particle size distributions for olivine-orthopyroxene mixtures from reflectance spectra, *J. Geophys. Res.*, 91, pp. 11,641-11,653.

Cloutis, E.A., Gaffey, M.J. (1991), Pyroxene spectroscopy revisited: Spectral composition corrwlations and relationship to geothermometry. *J. Geophys. Res.*, 96, 22809-22826.

Combe, J.-P., P. Launeau, P. Pinet, D. Despan, E. Harris, G. Ceuleneer, and C. Sotin (2006), Mapping of an ophiolite complex by high-resolution visible-infrared spectrometry, *Geochem. Geophys. Geosyst*., 7, Q08001, doi:10.1029/2005GC001214.

Crown, D.A. and C.M. Pieters (1985) Spectral Properties of Plagioclase and Pyroxene Mixtures. 16th LPSC, Houston, TX.

Debaille, V., Brandon, A.D., Yin, Q.Z., and B. Jacobsen, (2007), Coupled ^{142}Nd-^{143}Nd evidence for a protracted magma ocean in Mars. *Nature,* 450, 525-528, doi:10.1038/nature06317.

Debaille, V., Brandon, A.D., O'Neill, C.O., Yin, Q.-Z., and B. Jacobsen (2009), Early martian mantle overturn inferred from isotopic composition of nakhlite meteorites. *Nature Geosci.*, 2, 548-552.

Elkins-Tanton, L. T., Hess, P.C., and E. M Parmentier (2005), Possible formation of ancient crust on Mars through magma ocean processes. *J. Geophys. Res*., 110, E12S01, doi:10.1029/2005JE002480.

Flahaut et al. (2011), Dikes of distinct composition intruded into Noachian-aged crust exposed in the walls of Valles Marineris. *Geophys. Res. Lett*. 38. L15202, doi:10.1029/2011GL048109.

Gaffey, S. J., (1986), Spectral reflectance of carbonate minerals in the visible and near-infrared (0.35-2.55 microns): Calcite, aragonite, and dolomite, *Am. Mineral*., 71, 151-162.

Gillespie, A. R., Kahle, A. B., and Walker, R. E., 1986, Color Enhancement of Highly Correlated Images. I. Decorrelation and HSI Contrast Stretches.: Remote Sensing of Environment, v. 20, p. 209-235.

Guinness et al., (1987), On The Spectral Reflectance Properties of Materials Exposed at the Viking Landing Sites. *J. Geophys. Res.*, 92,B4,E575-E587.

Hapke, B., (1981), Bidirectional reflectance spectroscopy, 1., Theory, *J. Geophys. Res.*, 86, 3039-3054.

Hiroi, T. and S. Sasaki (2001), Importance of space weathering simulation products in compositional modeling of asteroids: 349 Dembowska and 449 Aeternitas as examples. *Met. Planet. Sci.*, 36, 1587-1596.

Irvine, T.N. et al., (1998), Included blocks (and blocks within blocks) in the Skaergaard intrusion: Geologic relations and the origins of rhythmic modally graded layers. *GAS Bulletin*, 110, 11, 1398-1447.

Isaacson, P.J. and C.M. Pieters (2010), Deconvolution of lunar olivine reflectance spectra: Implications for remote compositional assessment. *Icarus*, 210, 1, 8-13.

Isaacson, P. J., et al., (2011), Remote compositional analysis of lunar olivine-rich lithologies with Moon Mineralogy Mapper (M3) spectra, *J. Geophys. Res.*, 116, E00G11, doi:10.1029/2010JE003731.

Kanner, L. C., J. F. Mustard, A. Gendrin (2007), Assessing the limits of the Modified Gaussian Model for remote spectroscopic studies of pyroxenes on Mars. *Icarus* 187 442-456, doi:10.1016/j.icarus.2006.10.025 14.

Kelemen et al., (1995), Extraction of mid-ocean-ridge basalt from the upwelling mantle by focused flow of melt in dunite channels. *Nature*. 375, 747-753.

King, T.V.V., Ridley, W.I., (1987), Relation of the spectroscopic reflectance of olivine to

mineral chemistry and some remote sensing implications. *J. Geophys. Res*., 92, 11457–11469.

Klima, R.L., Pieers, C.M., and M.D. Dyar (2007), Spectroscopy of synthetic Mg-Fe pyroxenes I: Spin-allowed and spin-forbidden crystal field bands in the visible and near-infrared. *Met. Planet. Sci*., 42, 235-253.

Klima, R.L., Pieters, C.M, and M.D.Dyar (2008), Characterization of the 1.2 µm M ! pyroxene band : Extracting cooling history from near-IR spectra of pyroxenes and pyroxene-dominated rocks. *Met. & Planet. Sci*., 43, 1591-1604.

Koeppen, W. C., and V. E. Hamilton (2008), Global distribution, composition, and abundance of olivine on the surface of Mars from thermal infrared data. *J. Geohpys. Res.*, 113, E05001.

Loizeau et al., (2010) Stratigraphy in the Mawrth Vallis region through OMEGA HRSC color imagery and DTM. *Icarus*, 205, 396-418.

Malin, M. C., et al. (2007), Context Camera Investigation on board the Mars Reconnaissance Orbiter, *J. Geophys. Res.*, 112, E05S04, doi:10.1029/2006JE002808.

McEwen et al. (2007), Mars Reconnaissance Orbiter's High Resolution Imaging Science Experiment (HiRISE). *J. Geophys. Res.,* **112**, E05S02, doi:10.1029/2005JE002605.

McGuire, et al., (2009), An improvement to the volcano-scan algorithm for atmospheric correction of CRISM and OMEGA spectral data. *Planet. Space Sci.*, 57, 809-815.

McSween, H. Y. (2002), The rocks of Mars, from far and near. *Met. Planet. Sci*., 37, 7-25.

McSween, H. Y., et al., (2006), Characterization and petrologic interpretation of olivine-rich basalts at Gusev Crater, Mars, *J. Geophys. Res.,* 111, E02S10, doi:10.1029/2005JE002477.

Melosh (1989), *Impact cratering: A geologic process.* Oxford University Press.

Murchie, S., et al., (2007), Compact Reconnaissance Imaging Spectrometer for Mars (CRISM) on Mars Reconnaissance Orbiter (MRO). *J. Geophys. Res*., 112, E05S03, doi:10.1029/2006JE002682.

Mustard et al., (2005), Olivine and Pyroxene Diversity in the Crust of Mars. *Science*, 307, 1594 doi: 10.1126/science.1109098.

Mustard et al., (2007), Mineralogy of the Nili Fossae region with OMEGA/Mars Express data: 1. Ancient impact melt in the Isidis Basin and implications for the transition from the Noachian to Hesperian. *J. Geophys. Res.*, 112, E08S03, doi:10.1029/2006JE002834.

Pelkey, S. M., et al., (2007), CRISM multispectral summary products: Parameterizing mineral diversity on Mars from reflectance, *J. Geophys. Res.*, 112, E08S14, doi:10.1029/2006JE002831.

Poulet, F., J.-P. Bibring, Y. Langevin, J. F. Mustard, N. Mangold, M. Vincendon, B. Gondet, P. Pinet, J.-M. Bardintzeff, and B. Platevoet (2009), Quantitative compositional analysis of Martian mafic regions using MEx/OMEGA reflectance data: 1. Methodology, uncertainties and examples of application, *Icarus,* 201, 69–83.

Rogers, A.D., Christensen, P.R., and J.L. Bandfield (2005), Compositional heterogeneity of the ancient Martian crust: Analysis of Ares Vallis bedrock with THEMIS and TES data. *J. Geophys. Res*., 110, E05010.

Rogers, A. D., and P. R. Christensen (2007), Surface mineralogy of Martian low-albedo regions from MGS-TES data:Implications for upper crustal evolution and surface alteration, *J. Geophys. Res*., 112, E01003, doi:10.1029/2006JE002727.

Rogers, A.D. and J.L. Bandfield (2009), Mineralogical characterization of Mars Science Laboratory candidate landing sites from THEMIS and TES. *Icarus*, 203, 437-453.

Salvatore, M. R., J. F. Mustard, M. B. Wyatt, and S. L. Murchie (2010), Definitive evidence of Hesperian basalt in Acidalia and Chryse planitiae, *J. Geophys. Res.*, 115, E07005, doi:10.1029/2009JE003519.

Schultz, P.H. and H. Glicken (1979), Impact Crater and Basin Control of Igneous Processes on Mars. *J. Geophys. Res*., 84, B14.

Skok, J. R., J. F. Mustard, S. L. Murchie, M. B. Wyatt, and B. L. Ehlmann (2010), Spectrally distinct ejecta in Syrtis Major, Mars: Evidence for environmental change at the Hesperian-Amazonian boundary, *J. Geophys. Res.*, 115, E00D14, doi:10.1029/2009JE003338.

Sparks, R.S.J. and H.E. Huppert (1984), Density changes during the fractional crystallization of basaltic magmas: fluid dynamic implications. *Contrib Mineral Petrol*, 85, 300-309.

Sunshine, J.M., Pieters, C.M., and S.F. Pratt (1990), Deconvolution of mineral absorption bands: An improved approach. *J. Geophys. Res*., 95, 6955-6966.

Sunshine, J.M. and C.M. Pieters (1993), Estimating modal abundances from modified from spectra of natural and laboratory pyroxene mixtures using the modified Gaussian model. *J. Geophys. Res*., 98, 9075-9087.

Sunshine, J.M. and C.M. Pieters (1998), Determining the composition of olivine from reflectance spectroscopy. *J. Geophys. Res*., 103, 13675-13688.

Tarantola, A., and B. Valette, (1982), Generalized non-linear inverse problems solved using the least squared criterion. *Rev. Geophys.,* 20 , 219-232.

Tompkins, S. and C.M. Pieters (2010) Spectral characteristics of lunar impact melts amd inferred mineralogy. *Met & Planet. Sci., 45,* 7, 1152-1169.

Tornabene et al., (2010), A crater-exposed bedrock database for Mars with applications for determining the composition and structure of the upper crust. 41st LPSC, Houston, TX.

Walter, M.J. (1998), Meeting of Garnet Peridotite and the Origin of Komatiite and Depleted Lithosphere. *J. Petrology*, 39, 1, 29-60.

Warren, P. H., Claeys, P., and Cedillo-Pardo, E., (1996), Mega-impact melt petrology (Chicxulub, Sudbury, and the Moon): Effects of scale and other factors on potential for fractional crystallization and development of cumulates, *in* Ryder,

G., Fastovsky, D., and Gartner, S., eds., The Cretaceous-Tertiary Event and Other Catastrophes in Earth History: Boulder, Colorado, Geological Society of America Special Paper 307.

Wilde et al., (2001), Evidence from detrital zircons for the existence of continental crust and oceans on the Earth 4.4 Gyr ago. *Nature*, 409, 175-178.

Whitehead, J.A. and D.S. Luther, (1975), Dynamics of Laboratory Diapir and Plume Models. J. Geophys. Res. 80, 5, 705-717.

Wood, J.A., Dickey, J.S., Marvin, U.B., Powell, B.N., (1970), Lunar anorthosites and a geophysical model of the Moon. *Proc. Apollo 11 Lunar Sci. Conf*. 1, 965–988, 16.

Wyatt, M.B. and H.Y. McSween (2002), Spectral evidence for weathered basalt as an alternative to andesite in the northern lowlands of Mars. *Nature*, 417, 263-266.

Tables

Table 1: List of initial MGM modeled absorption properties. (Band strength in natural log reflectance).

Absorption Feature	Band center (μm)	Band width (μm)	Band depth
Olivine M1	0.9	0.228	-0.08
Olivine M2	1.08	0.176	-0.08
Olivine M1-2	1.28	0.424	-0.08
Pyroxene 1 μm	1	0.288	-0.08
Pyroxene 2 μm	2	0.424	-0.08
Pyroxene 1 μm LCP	0.9	0.228	-0.08
Pyroxene 1 μm HCP	1.08	0.228	-0.08
Pyroxene 1.2 μm	1.28	0.176	-0.08
Pyroxene 2 μm LCP	1.9	0.424	-0.08
Pyroxene 2 μm HCP	2.3	0.424	-0.08

Table 2A: Comparison of MGM results of laboratory spectra to measured composition. (All spectra from RELAB database: Ol1: OL-JMS-001, Ol2: OL-JMS-002, Ol3:OL-JMS-003, Ol4:OL-JMS-004, Pyroxene: 23: c1xp23, 24: c1xp24)

Curved	M1_1	M2	M1-2	Spectral Composition	Lab Measured Chemistry	Difference
Ol1	842	1033	1208	91	86	5
Ol2	850	1032	1208	87	90	3
Ol3	854	1034	1223	77	91	14
Ol4	844	1033	1209	89	91	2
					Mean Difference:	6
Linear Angled	M1_1	M2	M1-2	Spectral Composition	Lab Measured Chemistry	Difference
Ol1	835	1033	1207	94	86	8
Ol2	830	1029	1204	99	90	9
Ol3	830	1029	1221	90	91	1
Ol4	834	1031	1207	95	91	4
					Mean Difference:	6
Linear Straight	M1_1	M2	M1-2	Spectral Composition	Lab Measured Chemistry	Difference
Ol1	834	1034	1205	95	86	10
Ol2	829	1029	1201	101	90	11
Ol3	830	1029	1216	92	91	1
Ol4	833	1032	1203	97	91	7
					Mean Difference:	7

Table 2B: Comparison of MGM results of laboratory spectra to measured composition.

Curved	1 µm LCP Bandcenter	1 µm LCP Banddepth	1 µm HCP Bandcenter	1 µm HCP Banddepth	1 µm NBSR	2 µm LCP Bandcenter	2 µm LCP Banddepth	2 µm HCP Bandcenter	2 µm HCP Banddepth	2 µm NBSR	LCP Fraction
23	911	-1.10	1057	-0.03	0.98	1840	-0.84	2405	-0.26	0.76	60
24	946	-0.20	1002	-0.59	0.25	1914	-0.27	2326	-0.35	0.43	40

Linear Angled	1 µm LCP Bandcenter	1 µm LCP Banddepth	1 µm HCP Bandcenter	1 µm HCP Banddepth	1 µm NBSR	2 µm LCP Bandcenter	2 µm LCP Banddepth	2 µm HCP Bandcenter	2 µm HCP Banddepth	2 µm NBSR	LCP Fraction
23	981	-2.32	1023	2.04	8.29	1831	-0.80	2405	-0.40	0.67	60
24	637	-0.57	991	-0.87	0.40	1926	-2.49	2329	-0.32	0.89	40

Linear Stright	1 µm LCP Bandcenter	1 µm LCP Banddepth	1 µm HCP Bandcenter	1 µm HCP Banddepth	1 µm NBSR	2 µm LCP Bandcenter	2 µm LCP Banddepth	2 µm HCP Bandcenter	2 µm HCP Banddepth	2 µm NBSR	LCP Fraction
23	967	-1.50	1022	-0.72	0.67	1840	-0.72	2332	-0.12	0.86	60
24	640	-0.83	986	-0.82	0.50	1935	-0.36	2351	-0.26	0.59	40

Table 3A: Results of MGM modeling of Hapke mixture of olivine-palagonite as a function of olivine percent. Olivine spectrum is Relab: Ol-JMS-001 if measured Fo_{85}. We see that MGM modeling of pure olivine is within 6 Fo units from actual with modeled result becoming degraded with additional palagonite as expected.

Olivine-Palagonite Mixture

Percent Ol	M1-1	M2	M1-2	Modeled Composition	Comp Fitting Error
0	844	905	1460	-13	61733
10	798	981	1424	8	38988
20	963	1050	1362	-51	3062
30	961	1056	1327	-32	1879
40	943	1053	1291	-4	1569
50	924	1050	1264	19	1248
60	911	1048	1241	38	1363
70	896	1046	1220	56	1335
80	881	1043	1210	69	979
90	867	1041	1209	77	440
100	851	1038	1220	79	31

Table 3B: Results of Mixtures in 3A divided by Palagonite.

Percent Ol	M1-1	M2	M1-2	Modeled Composition	Comp Fitting Error
0	900	1080	1280	14	68
10	892	1065	1239	43	452
20	847	1047	1188	95	535
30	825	1039	1177	112	254
40	816	1034	1171	121	180
50	818	1034	1171	120	166
60	822	1034	1174	117	159
70	830	1035	1184	108	105
80	834	1035	1198	99	13
90	830	1031	1204	98	28
100	851	1038	1220	79	31

Table 4A: Results of olivine MGM results. Column description: 1) ROI # (Appendix 1) 2) M1-1 band center 3) M2 band center 4) M1-2 band center 5) Calculated composition from 3 band fit (Fo#). 6) Least squares error to fit. 7) Calculated composition for fit to M2 and M1-2 (Fo#) 8) Absolute difference between two calculated compositions.

Alga Olivine Unit	M1-1	M2	M1-2	3-Band Comp (Fo#)	Comp Fitting Error	2-Band Comp (Fo#)	Comp Difference
1	877	1046	1257	45	160	46	1
2	899	1072	1282	16	3	15	1
3	889	1063	1290	18	270	11	7
4	901	1069	1298	7	172	2	5
5	902	1069	1293	9	87	6	3
6	897	1067	1289	14	91	10	3
7	902	1067	1285	14	43	14	0
8	900	1079	1281	14	44	13	1
9	896	1064	1276	22	26	23	1

Ostrov Olivine Unit	M1-1	M2	M1-2	3-Band Comp (Fo#)	Comp Fitting Error	2-Band Comp (Fo#)	Comp Difference
1	843	1035	1264	59	1408	44	15
2	836	1035	1254	68	1172	53	15
3	838	1031	1251	70	1123	56	13
4	837	1034	1263	63	1653	45	18

Table 4B: Results of MGM analysis of pyroxene composition.

Alga Pyroxene Bedrock	1 µm LCP Bandcenter	1 µm LCP Banddepth	1 µm HCP Bandcenter	1 µm HCP Banddepth	1 µm NBSR	2 µm LCP Bandcenter	2 µm LCP Banddepth	2 µm HCP Bandcenter	2 µm HCP Banddepth	2 µm NBSR	1 µm Bandcenter	2 µm Bandcenter
1	889	-0.11	1075	-0.05	0.67	1760	-0.12	2145	-0.08	0.59	933	1893
2	886	-0.12	1064	-0.07	0.63	1746	-0.14	2138	-0.10	0.59	938	1884
3	893	-0.09	1075	-0.05	0.66	1757	-0.10	2152	-0.07	0.59	941	1892
4	890	-0.11	1075	-0.06	0.64	1751	-0.13	2133	-0.09	0.59	941	1886
5	889	-0.10	1078	-0.04	0.72	1773	-0.12	2135	-0.08	0.60	922	1896
6	896	-0.08	1068	-0.06	0.59	1759	-0.14	2131	-0.09	0.60	957	1890
7	892	-0.10	1080	-0.04	0.71	1769	-0.12	2132	-0.08	0.61	927	1891
8	893	-0.08	1065	-0.03	0.74	1782	-0.10	2148	-0.07	0.59	916	1909
9	894	-0.11	1082	-0.06	0.63	1743	-0.13	2129	-0.08	0.61	950	1867

Alga Light-toned Pyroxene	1 µm LCP Bandcenter	1 µm LCP Banddepth	1 µm HCP Bandcenter	1 µm HCP Banddepth	1 µm NBSR	2 µm LCP Bandcenter	2 µm LCP Banddepth	2 µm HCP Bandcenter	2 µm HCP Banddepth	2 µm NBSR	1 µm Bandcenter	2 µm Bandcenter
1	911	-0.09	1060	-0.04	0.69	1833	-0.07	2196	-0.04	0.64	937	1936
2	910	-0.07	1055	-0.04	0.64	1799	-0.07	2190	-0.04	0.62	948	1921
3	932	-0.05	1068	-0.01	0.79	1852	-0.05	2229	-0.03	0.62	944	1963
4	917	-0.06	1067	-0.04	0.63	1805	-0.06	2195	-0.04	0.61	948	1933
5	919	-0.06	1066	-0.03	0.64	1794	-0.05	2188	-0.03	0.62	953	1917
6	909	-0.05	1059	-0.04	0.56	1778	-0.05	2186	-0.03	0.63	965	1899
7	929	-0.03	1067	-0.02	0.67	1828	-0.04	2220	-0.02	0.65	954	1924

Ostrov Pyroxene	1 µm LCP Bandcenter	1 µm LCP Banddepth	1 µm HCP Bandcenter	1 µm HCP Banddepth	1 µm NBSR	2 µm LCP Bandcenter	2 µm LCP Banddepth	2 µm HCP Bandcenter	2 µm HCP Banddepth	2 µm NBSR	1 µm Bandcenter	2 µm Bandcenter
1	901	-0.23	1099	-0.06	0.79	1801	-0.21	2142	-0.11	0.65	918	1892
2	899	-0.16	1086	-0.05	0.76	1850	-0.17	2199	-0.08	0.68	898	1912
3	902	-0.15	1110	-0.05	0.74	1912	-0.26	2528	-0.16	0.62	827	1892
4	903	-0.16	1103	-0.04	0.80	1839	-0.17	2183	-0.07	0.70	911	1904
5	896	-0.20	1083	-0.05	0.80	1841	-0.16	2162	-0.07	0.71	916	1911
6	898	-0.20	1078	-0.07	0.74	1775	-0.19	2168	-0.11	0.63	919	1877
7	901	-0.10	1151	-0.04	0.71	1936	-0.22	2517	-0.18	0.56	916	2141
8	891	-0.22	1078	-0.03	0.86	1834	-0.16	2142	-0.05	0.77	902	1887
9	920	-0.15	1077	-0.02	0.88	1894	-0.12	2299	0.00	1.00	981	1979
10	900	-0.15	1141	-0.02	0.89	1908	-0.25	2563	-0.21	0.54	805	1875

Figure Captions

Figures 1. Context Map A) Alga and Ostrov craters are located just east of the Margaritifer-Uzboi fluvial system, south of Ladon and east of Holden Crater. (MOLA DEM) B) Alga is a 18 km crater just off center of the 86 km Chekalin Crater. (CTX: P18_007929_1555_XI_24S026W) C) Ostrov is a modified 65 km crater (CTX: P17_007639_1514_XN_28S027W)

Figure 2. MGM Example. A) MGM run on laboratory Olivine with Fo # 96 (Relab sample: c3po53). Left top) RMS error between the observed spectra and modeled fit. Left Middle) Three olivine absorptions with fitted positions, widths, and strengths. Initial positions, depths and widths are listed in Table 1**.** Left Bottom) Olivine spectra (cross hatched points) with fit (black line) and curved continuum (thin black line). B) MGM run on laboratory Pyroxene (Relab Sample: c1xp23). Right top) RMS error between the observed spectra and modeled fit. Right middle) Five absorptions with fitted positions, widths, and strengths. Right Bottom) Pyroxene spectra (cross hatched points) with fit (black line) and curved continuum (thin black line).

Figure 3. Continuum Verification. MGM fits with i) curved, ii) angled and iii) straight continuum for both olivine (A) and pyroxene (B). Curved continuum proved to be the most accurate and was used for the rest of this study. Results listed in Table 2A and 2B.

Figure 4. Ratioed Results A) Hapke mixing of Olivine and a Martian dust analog palagonite spectra. The Olivine spectrum (C3PO53) was acquired from the RELAB spectral library with a measured Fo# of 96.9. MGM results are shown in Table 3A B) Mixed spectra ratioed to palagonite denominator to recover original absorption features. MGM results are shown in Table 3B C) Olivine-Palagonite Hapke mixture modeled band centers plotted against composition. D) Mixture divided by Palagonite modeled band centers plotted against composition.

Figure 5. Map of Alga crater central peak units. A) Olivine-bearing unit, B) Pyroxene-bearing unit, C) Light-toned pyroxene, D) Possible melt unit. CRISM FRT00006415 mafic parameters on HiRISE PSP_007573_1555. R:Olindex2, G:LCPindex, B:HCPindex.

Figure 6. Oblique view of Alga Crater from HiRISE draped on HiRISE DEM (5x vertical exaggeration). A) View from south showing main peak structure dominated by Pyroxene-bearing bedrock. Light-toned Pyroxene unit seen to south and east of main peak. B) View of peak from west. Light toned units to left and bottom are Olivine-bearing. The potential melt unit is on the peak flank following the central couloir. C) View from east showing tabular nature of Pyroxene-bearing bedrock unit.

Figure 7. Alga Olivine Results. Olivine deposits shown in dotted lines in A, B, C. regions correspond to Regions of interest shown in appendix 1.1. D) Truncated spectra used in

MGM modeling. E) MGM modeled olivine band center fits, results in table 4A. F) Full spectral range of Alga crater olivine from Regions of interests in Appendix 1.1, 2.1.

Figure 8. Alga Pyroxene Results A) Southwest portion of Alga central peak containing most of the Pyroxene Bedrock Unit. B) Ratioed Alga pyroxene spectra used in MGM analysis. C) Alga crater Pyroxene Bedrock 1-, 2 µm band centers plotted against terrestrial pyroxene band centers [Adams, 1974, Cloutis, 1991]. From bottom left to upper right, pyroxene composition goes from Mg-rich to Fe-rich to Ca-rich. Alga pyroxene plot as low-Ca, moderate-Fe. D) Pyroxene NBSR demonstrating a consistent LCP enrichment. Values listed in Table 4B.

Figure 9. Alga Light-toned Pyroxene Results A) HiRISE view of southern Light-toned Pyroxene Unit. B) HiRISE view of eastern Light-toned Pyroxene Unit. C) Ratioed Alga Light-toned Pyroxene spectra used in MGM analysis. D) Alga crater Light-toned Pyroxene 1-, 2 µm band centers plotted against terrestrial pyroxene band centers [Adams, 1974, Cloutis, 1991]. From bottom left to upper right, pyroxene composition goes from Mg-rich to Fe-rich to Ca-rich. Alga Light-toned pyroxene plot as low-Ca, moderate to high Fe. E) Pyroxene NBSR demonstrating a consistent LCP enrichment. Values listed in Table 4B.

Figure 10. Selected Light-toned Pyroxene Spectra (ROI: 1 , 2, 5 Appendix 1.3, 2.3). Spectra highlight the 2.2 µm feature consistent with Si-OH feature, potentially the result of hydration of a silica rich impact melt or an impact induced hydrothermal system.

Figure 11. Impact Melt A) HiRISE view of northern section of Alga central peak with impact melt unit centered in dotted line.. B) Ratioed Alga impact melt spectra (ROI: Appendix 1.4, 2.4)

Figure 12. Pyroxene comparison. Here we plot representative spectral from the pyroxene bedrock, light-toned pyroxene, and impact melt units. We see that the band centers are similar but a strong difference in absorption strength. We suggest that all three units are sampling the same composition units but are distinguished by differing quantities of a post-impact spectrally modifying component such as an impact glass.

Figure 13. Ostrov crater. A) Ostrov crater with CRISM parameter overlain on HiRISE and CTX. (R:Ol2index, G:LCPindex, B:HCPindex). CRISM:FRT00017D02, HiRISE: PSP_017357_1530, CTX: P17_007639_1514_XN_28S027W. B) HiRISE of northern olivine deposit. C) HiRISE of eastern olivine ridge. Shows olivine-bearing light-toned clasts. D) Ratioed olivine spectra used in analysis (Appendix 1.5, 2.5). Degraded S detector data (700 nm-1000 nm) caused bad band fitting results (E). Composition is determined with M2 and M1-2 expressed in L detector (1000 nm- 1800 nm). Results in Table 4A.

Figure 14. Ostrov Pyroxene. A) Ratioed Ostrov pyroxene spectra (Appendix 1.6, 2.6). B) Ostrov Pyroxene NBSR results consistent with LCP-enrichment. C) Ostrov pyroxene 1-, 2 μm band centers plotted against terrestrial pyroxene band centers [Adams, 1974,

Cloutis, 1991]. From bottom left to upper right, pyroxene composition goes from Mg-rich to Fe-rich to Ca-rich. Ostrov pyroxene plot as low-Ca, moderate Fe with some outliers. Results in Table 4B.

Figure 15. THEMIS Thermal Results. A) Alga THEMIS spectra from endmember regions. B) Reference endmember library spectra. Laboratory measured olivine spectra, Mars derived Surface Type 1 and 2 [Bandfield et al., 2000]. C) Ostrov THEMIS spectra from endmember regions. D) Alga DCS (9,6,4) highlighting the mafic mineralogy. E) Alga Peak Unit 1 endmember map. The endmember has the distinct feature at 11 μm consistent with the olivine lab spectra. F) Alga Peak Unit 2 endmember map. G) Alga Floor Units endmember map. H) Ostrov DCS (9,6,4) highlighting the mafic mineralogy. I) Ostrov Peak Unit 1 endmember map. J) Ostrov Peak Unit 2 endmember map. K) Ostrov Peak Unit 3 endmember map.

Datasets Used:

CRISM:

Alga: FRT00006415

Ostrov: FRT00017D02

HiRISE:

Alga: PSP_007573_1555, PSP_0007929_1555

Ostrov: PSP_017357_1530

CTX:

Alga:P18_007929_1555_XI_24S026W

Ostrov: P17_007639_1514_XN_28S027W

THEMIS:

Alga: I16914002

Ostrov: I07916004

Appendix:

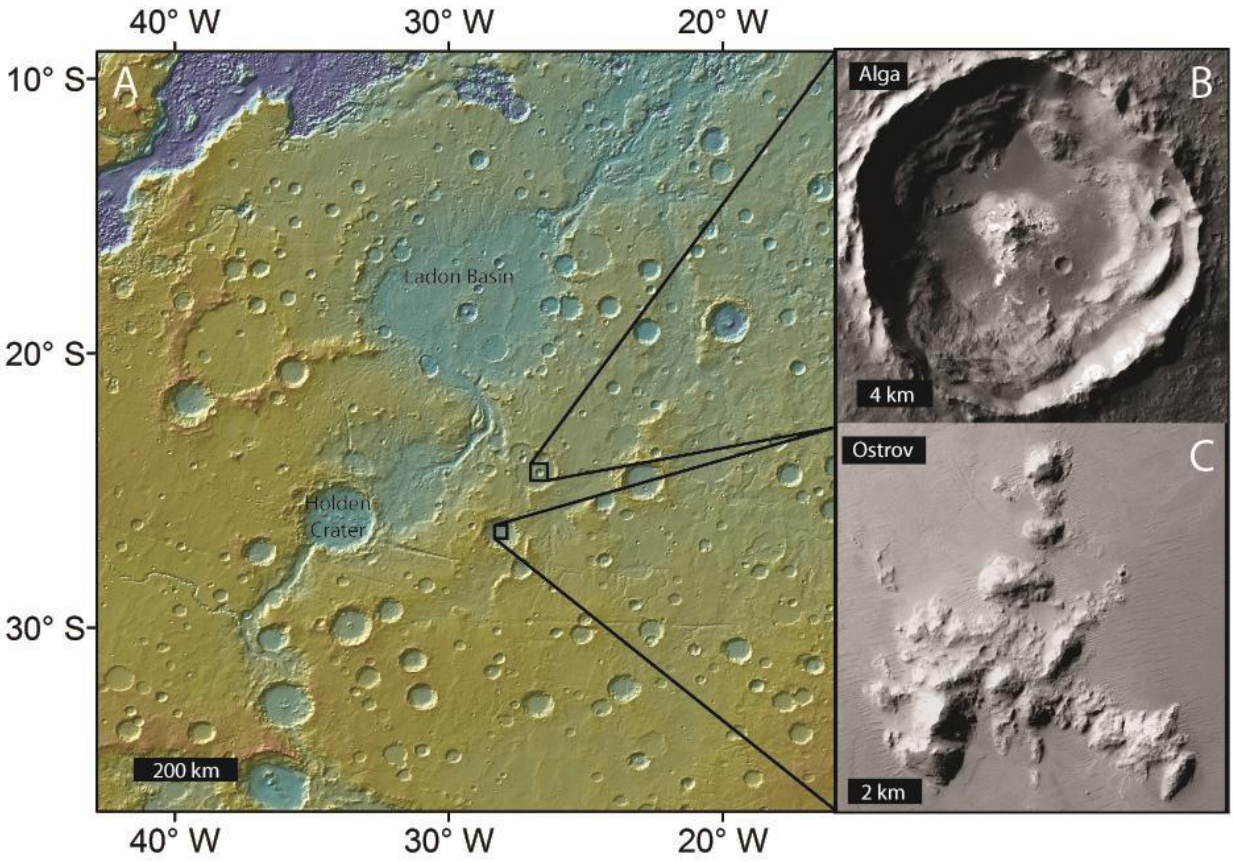

Chapter 1, Figure 1

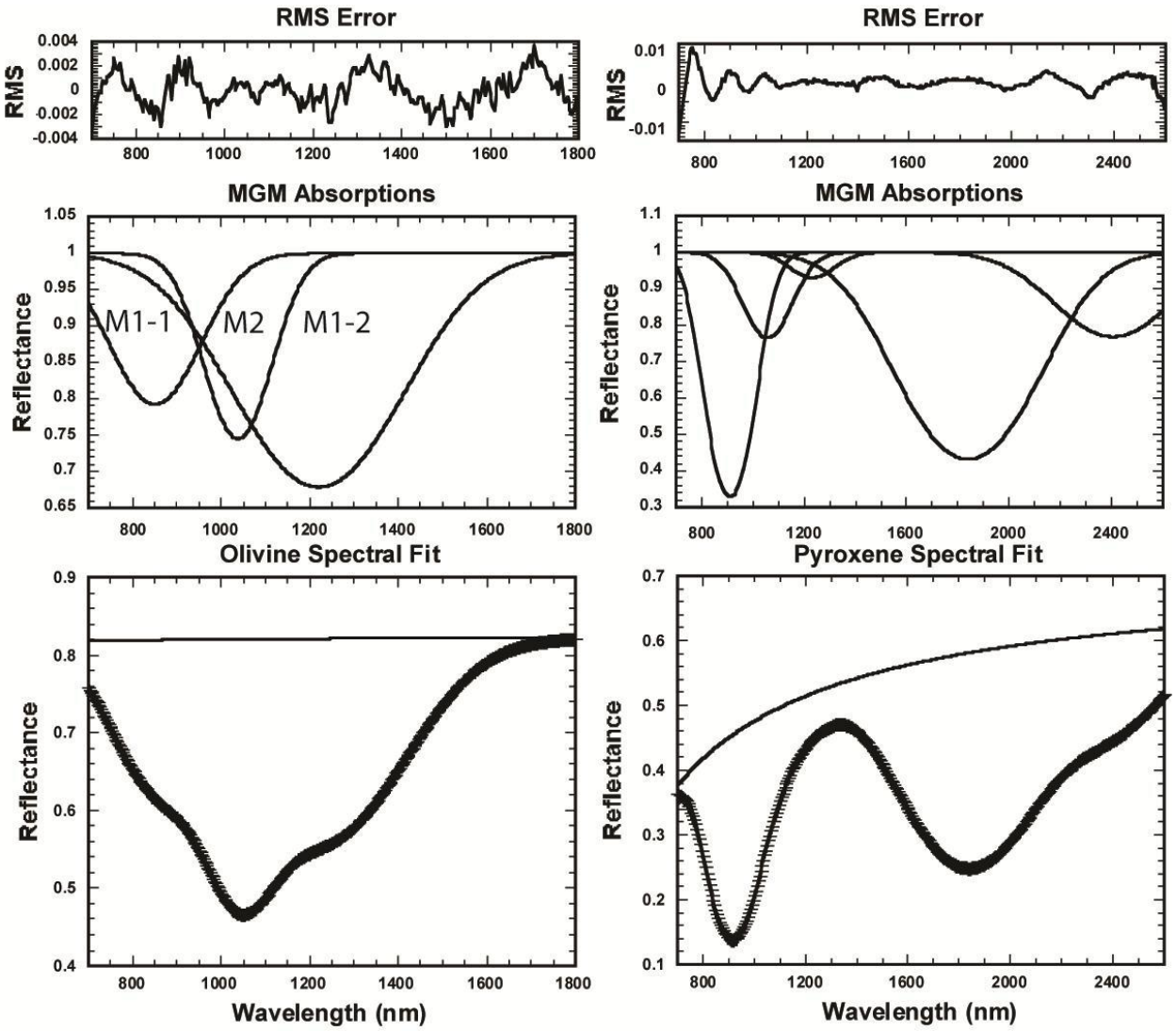

Chapter 1, Figure 2

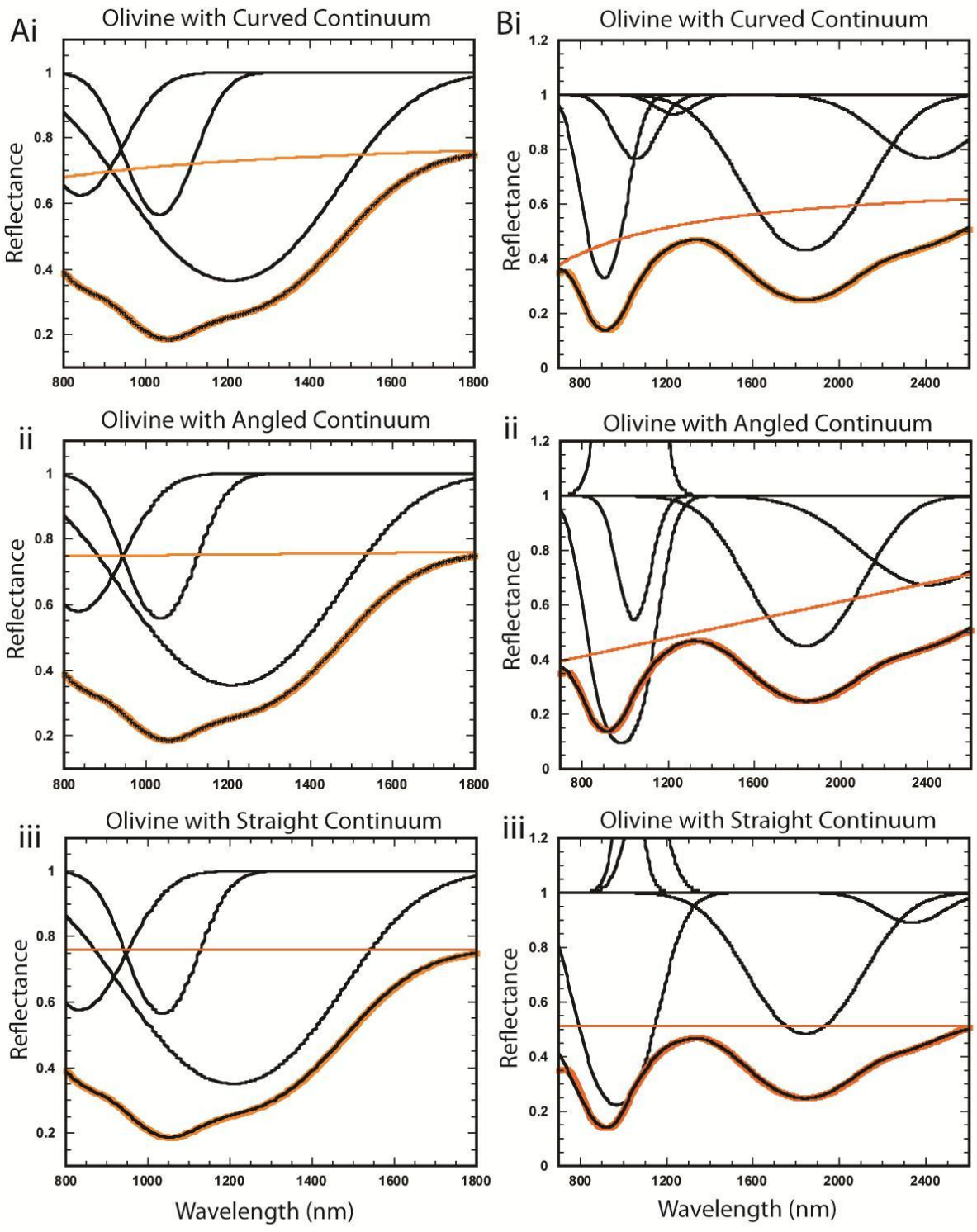

Chapter 1, Figure 3

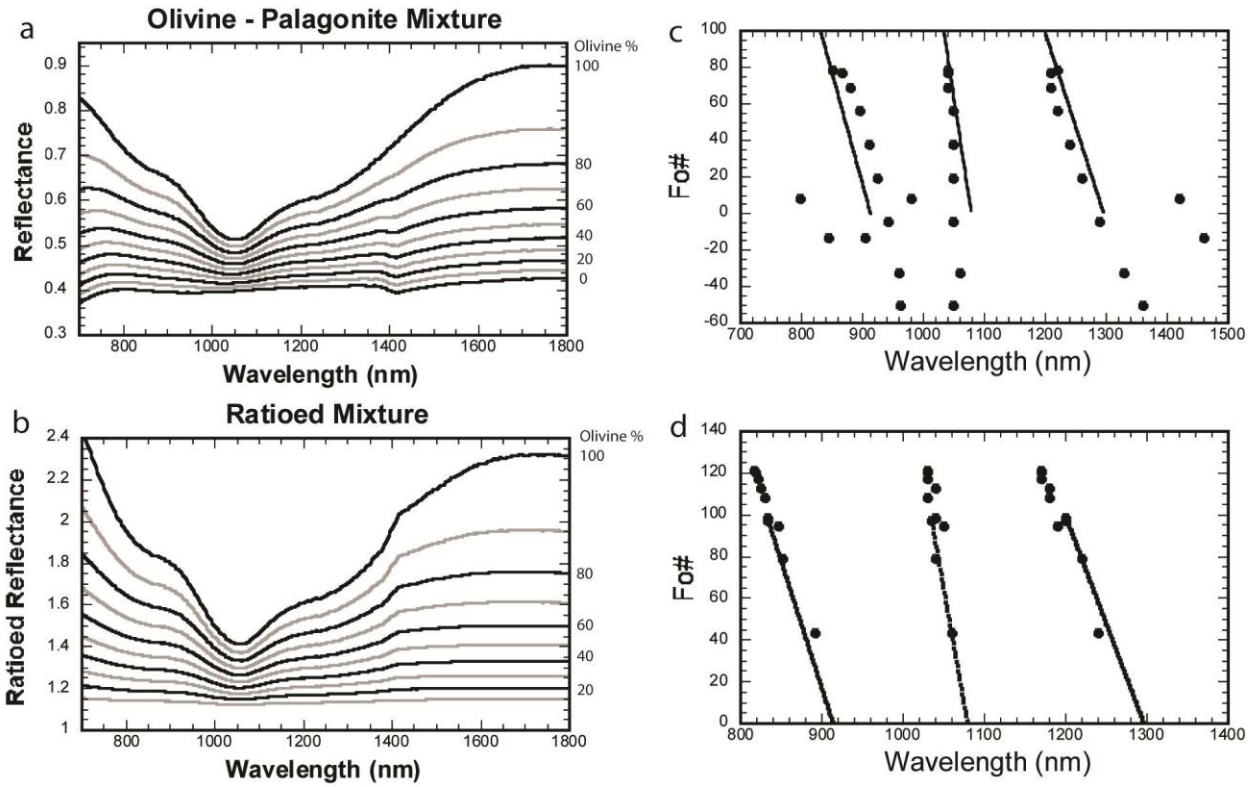

Chapter 1, Figure 4

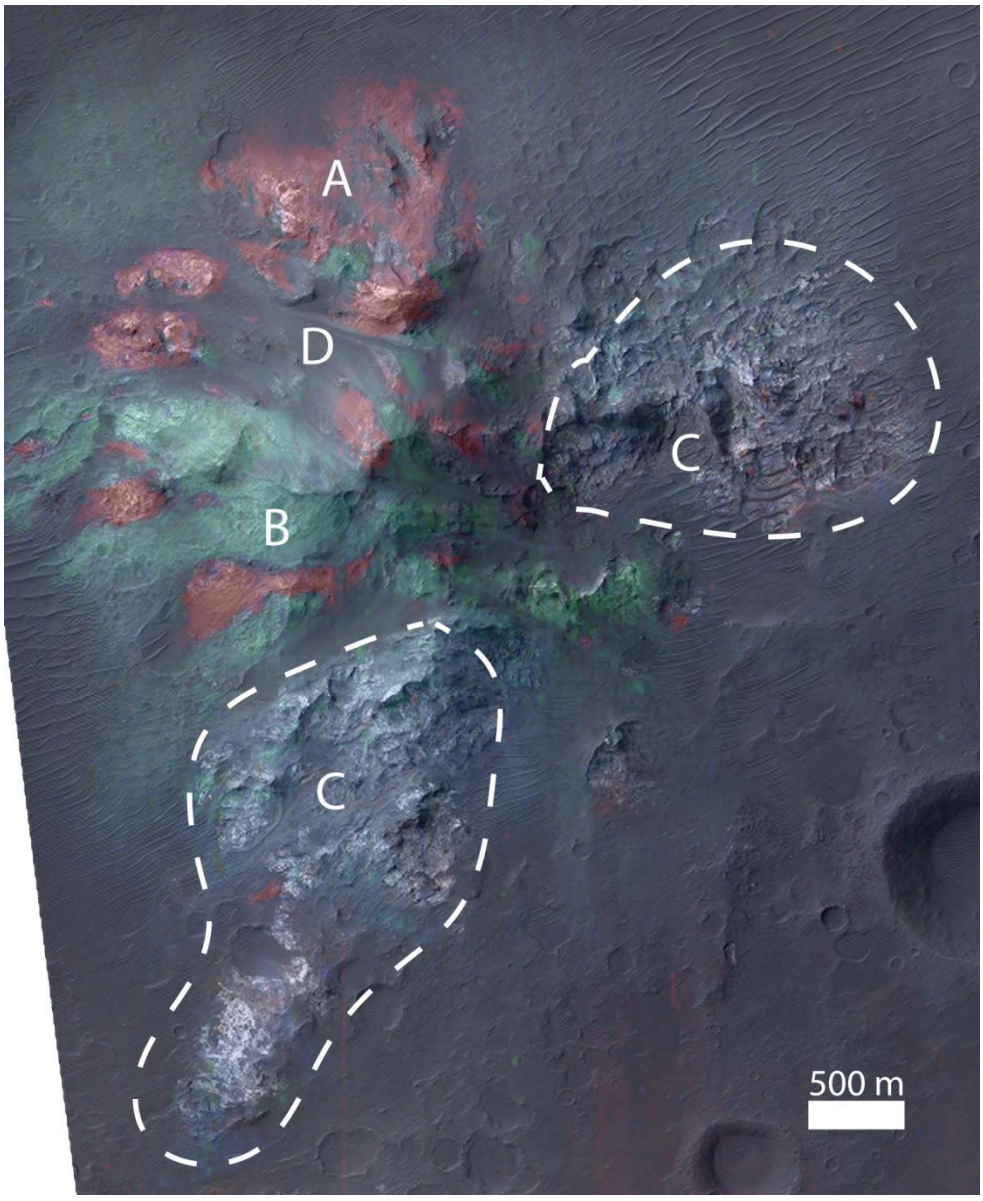

Chapter 1, Figure 5

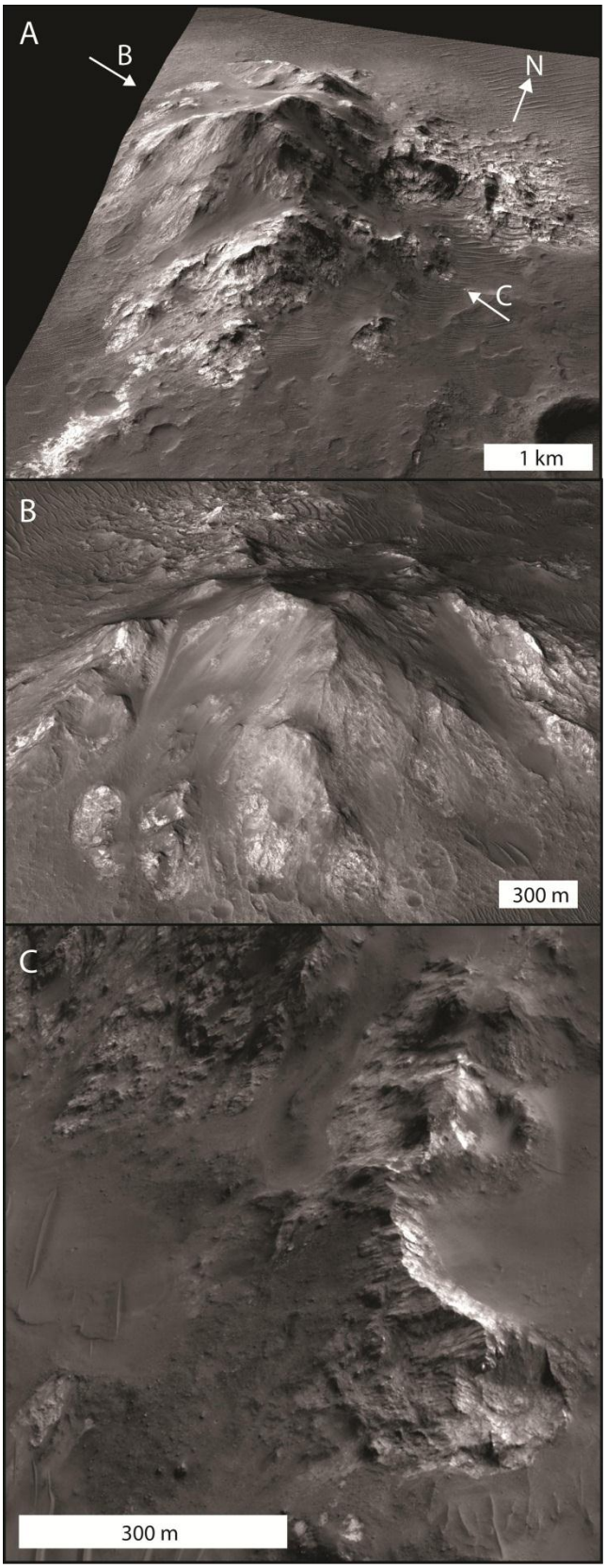

Chapter 1, Figure 6

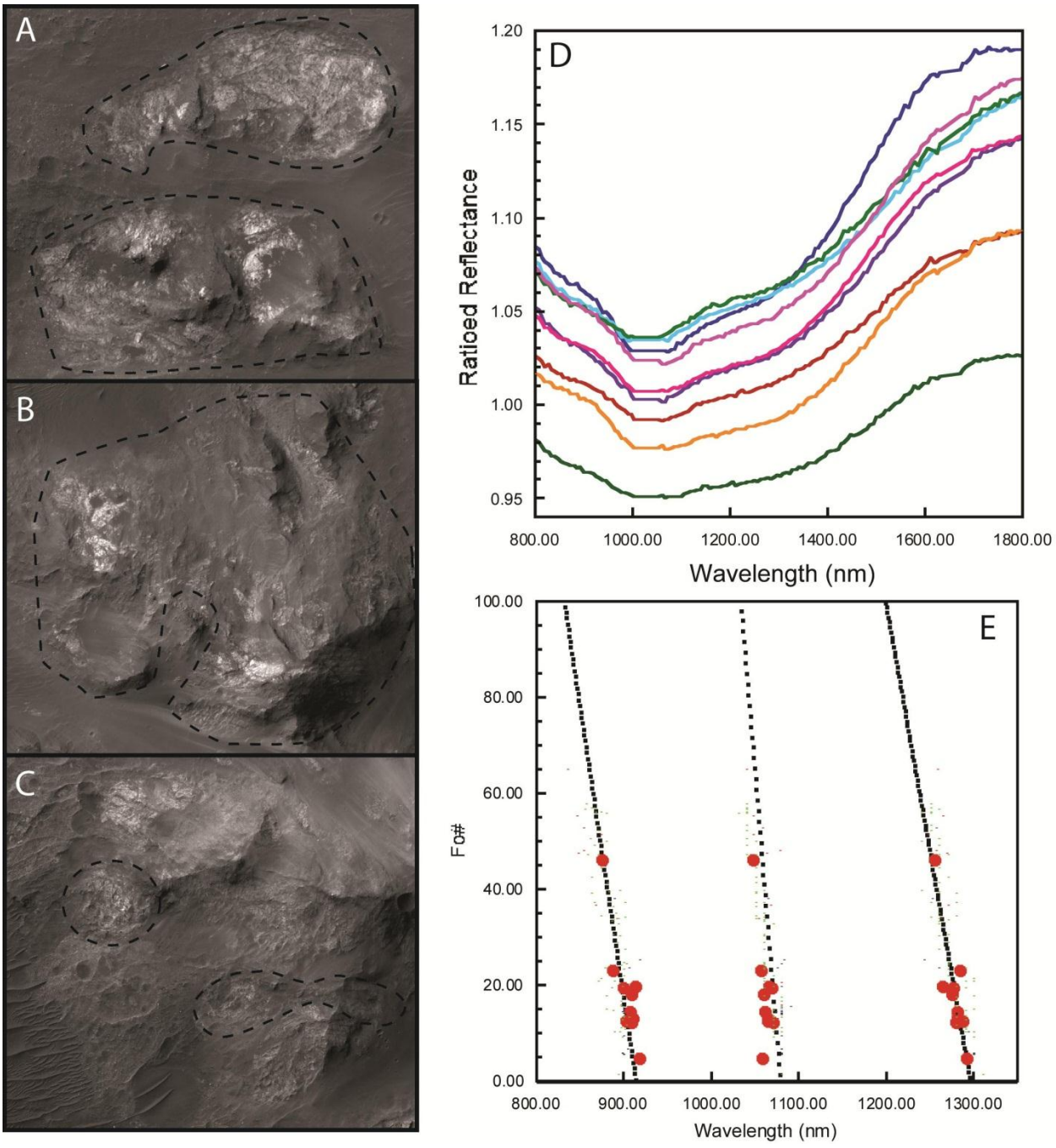

Chapter 1, Figure 7

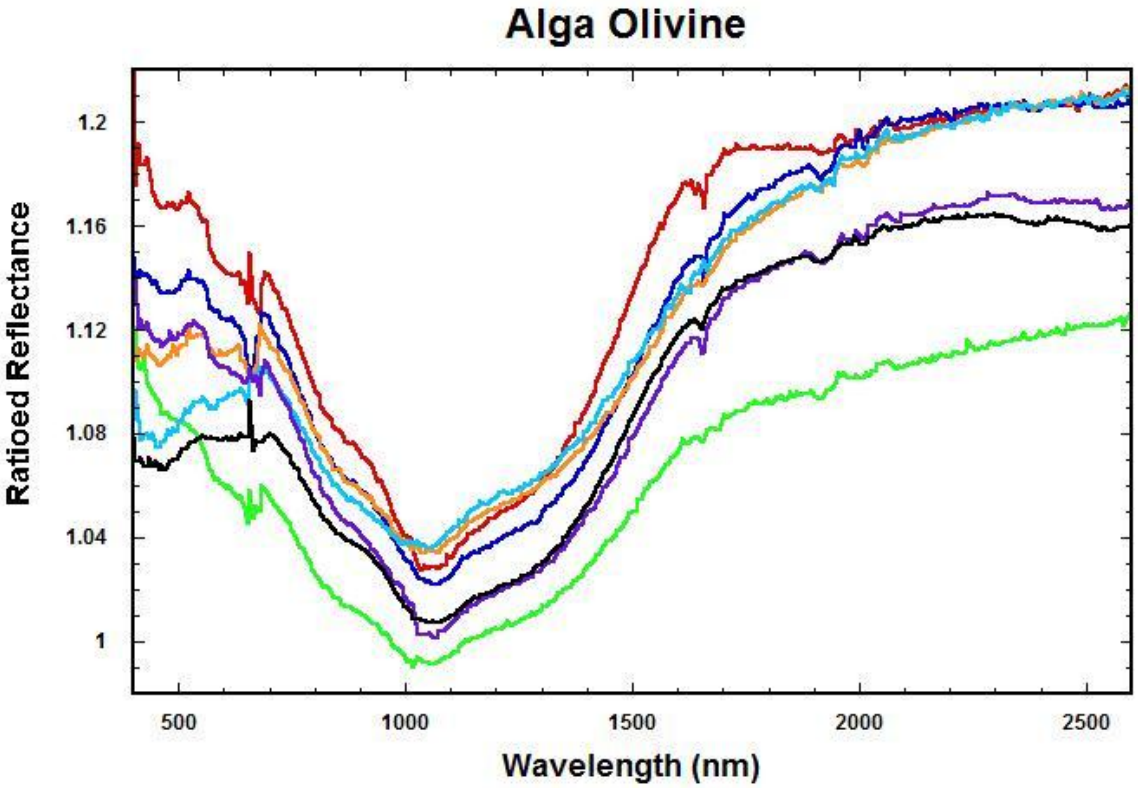

Chapter 1, Figure 7F

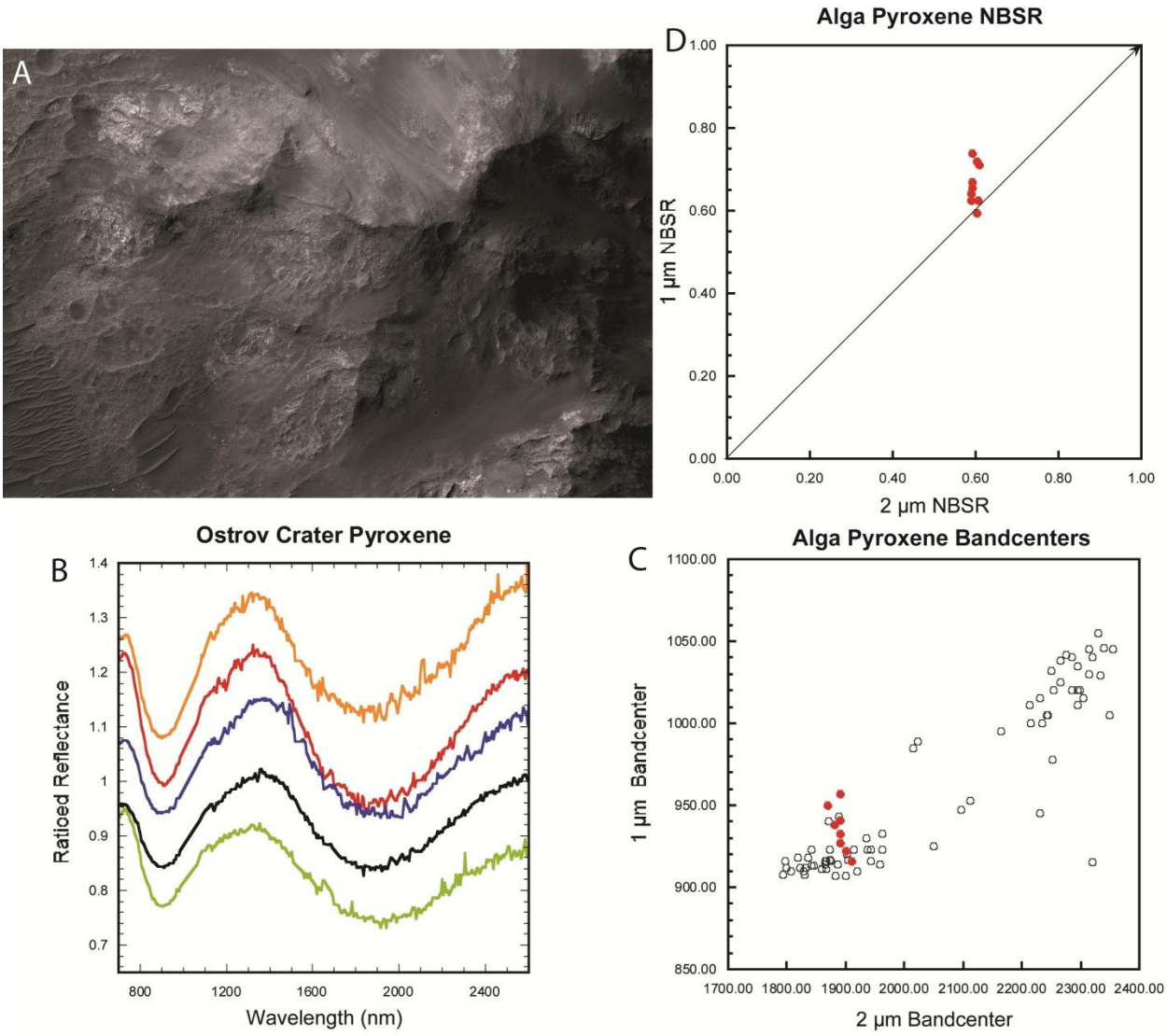

Chapter 1, Figure 8

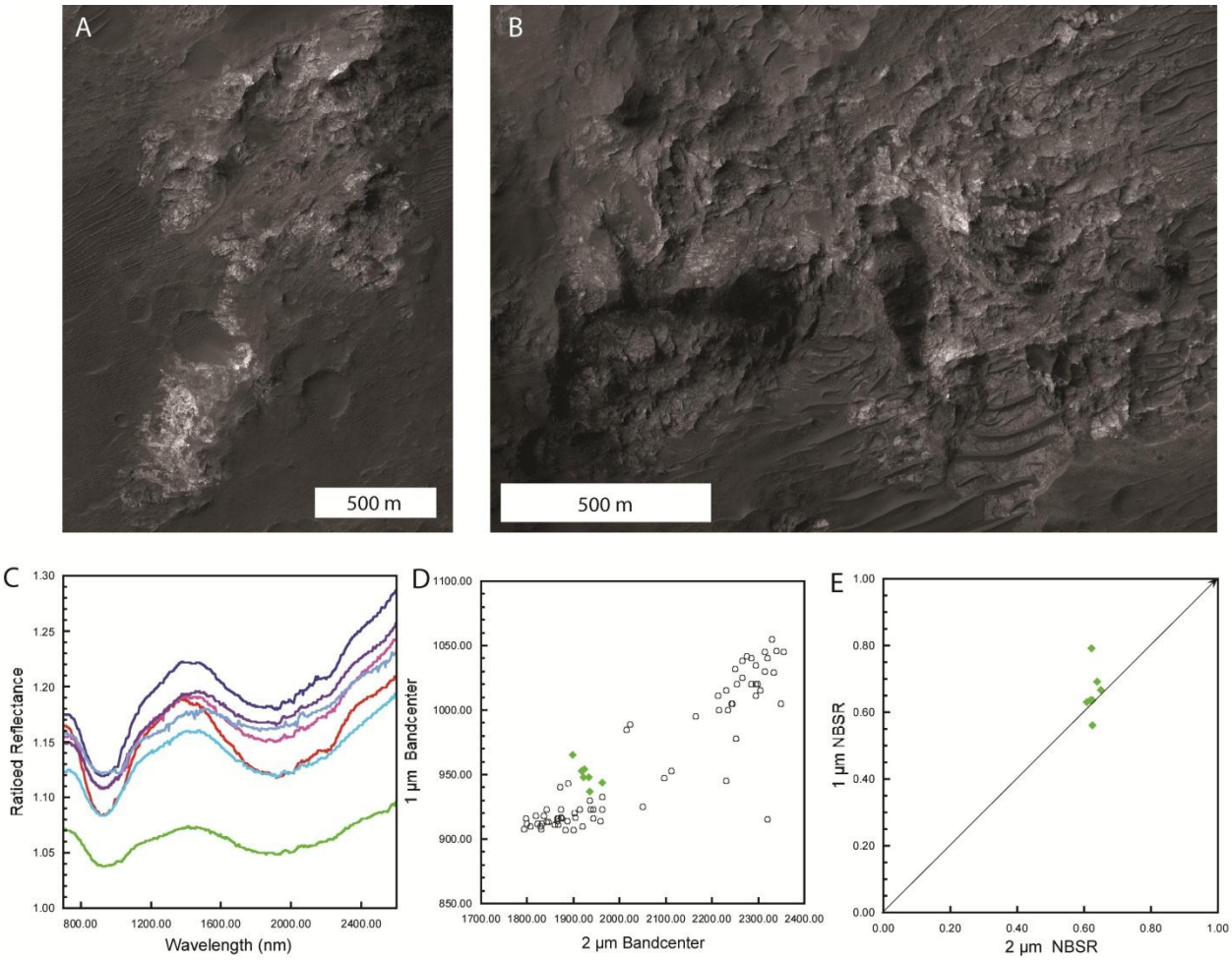

Chapter 1, Figure 9

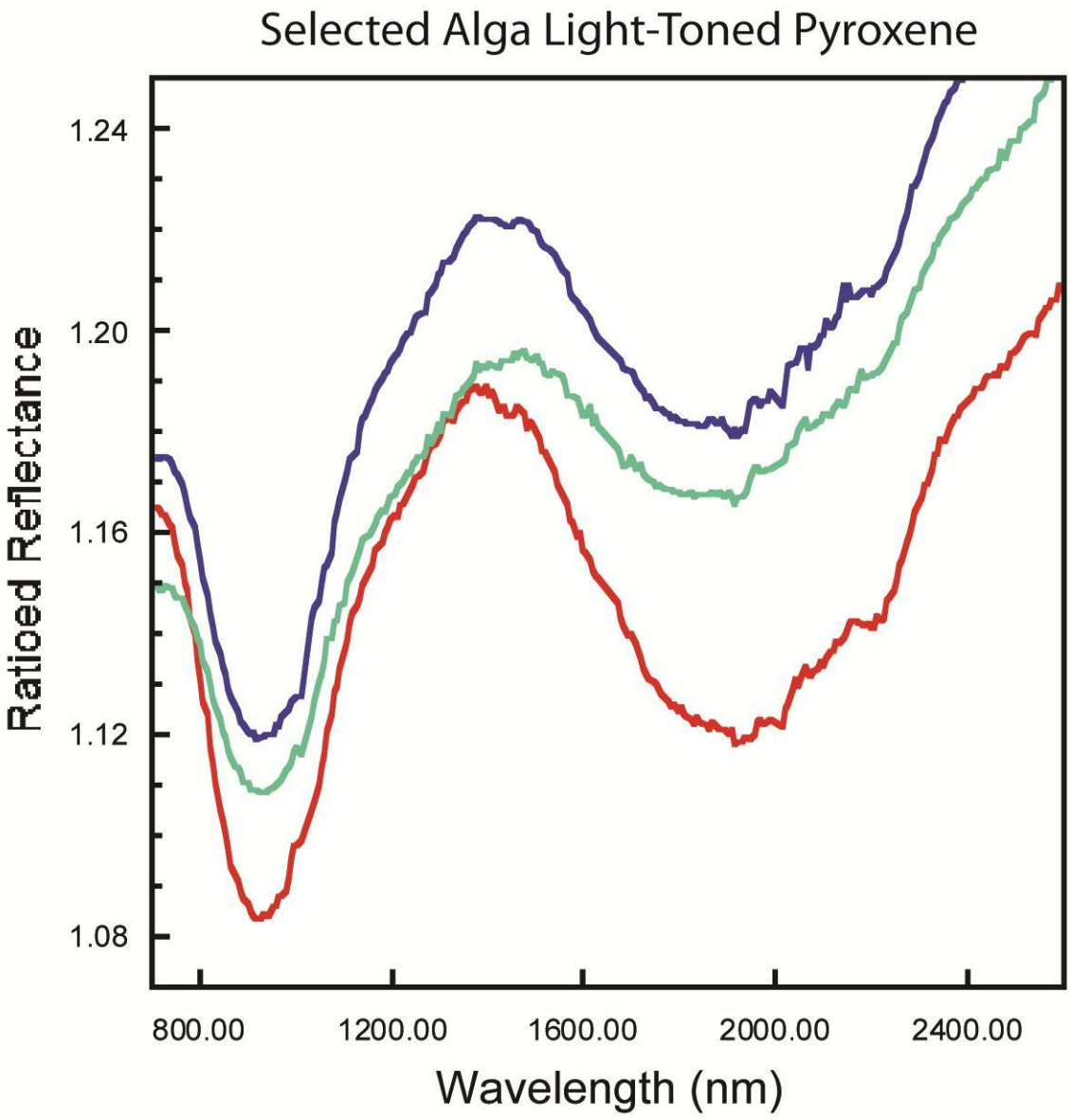

Chapter 1, Figure 10

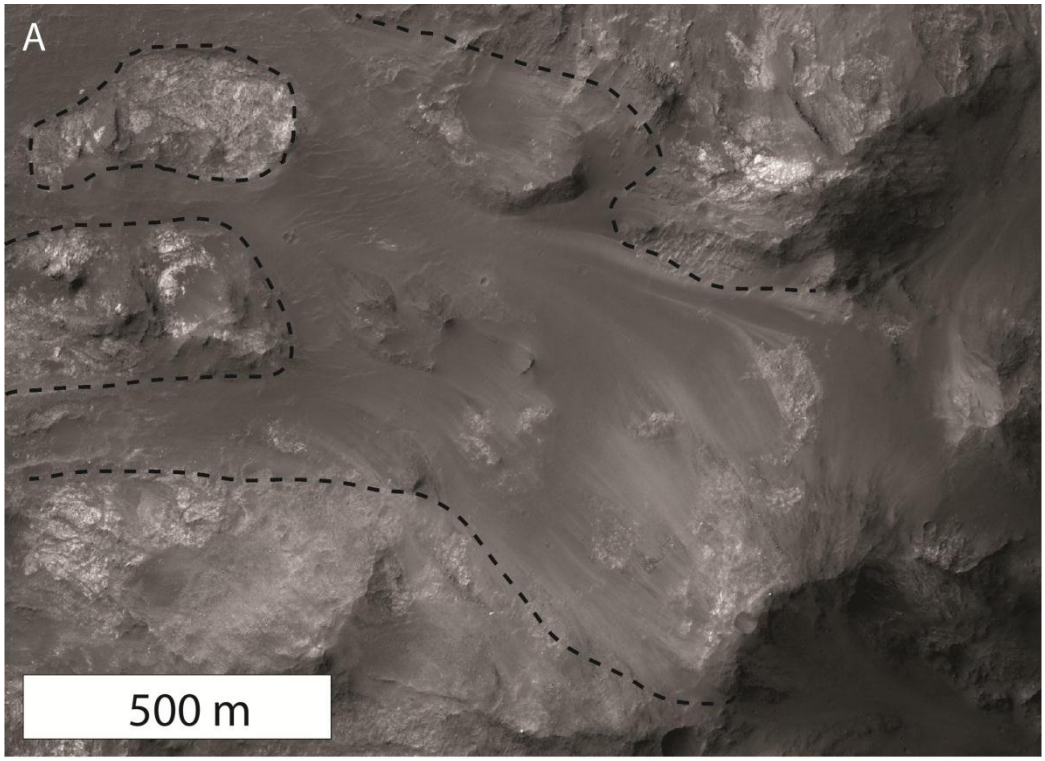

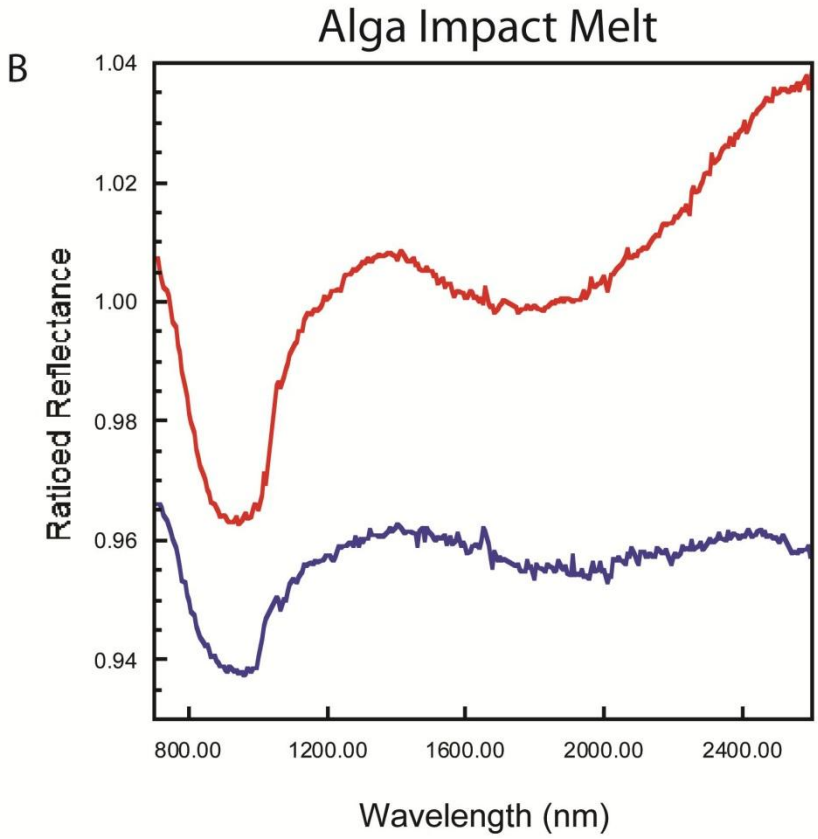

Chapter 1, Figure 11

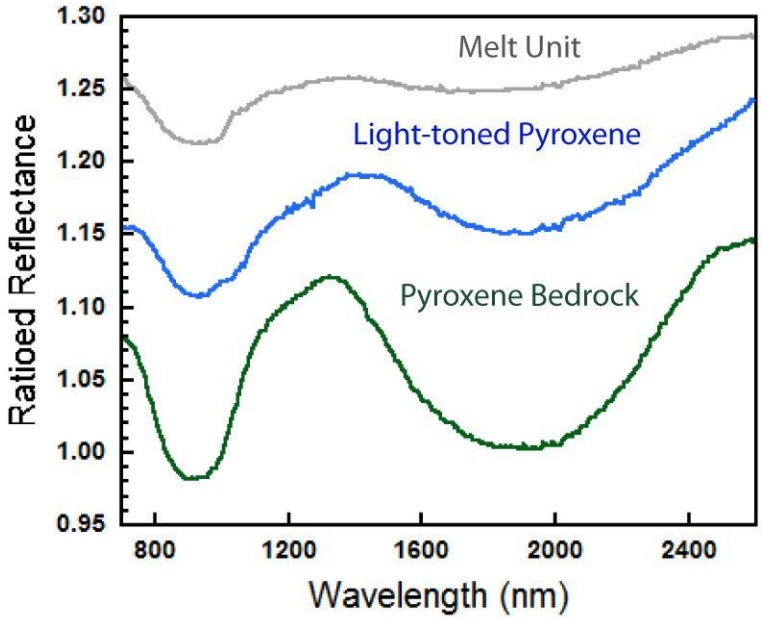

Chapter 1, Figure 12

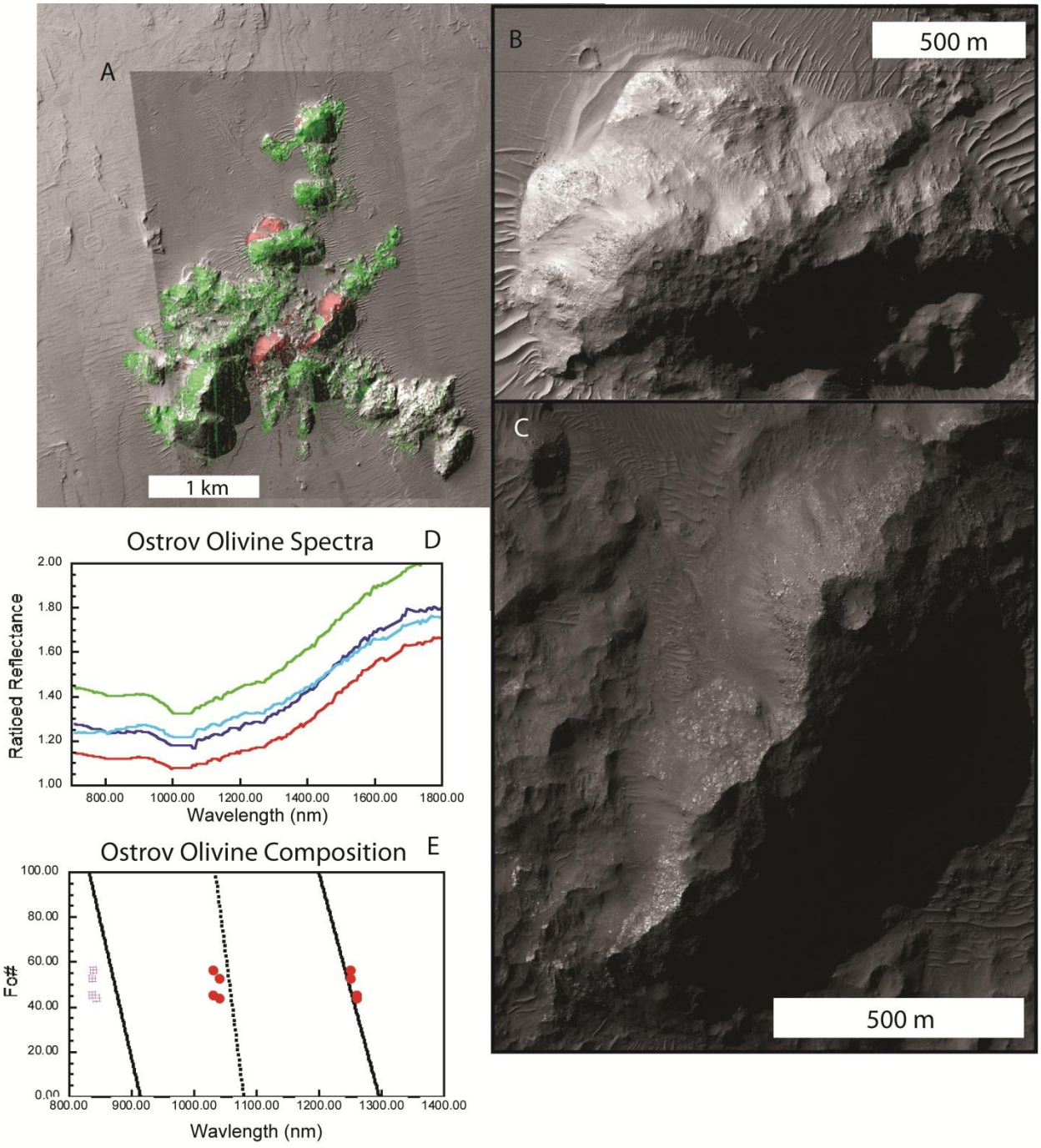

Chapter 1, Figure 13

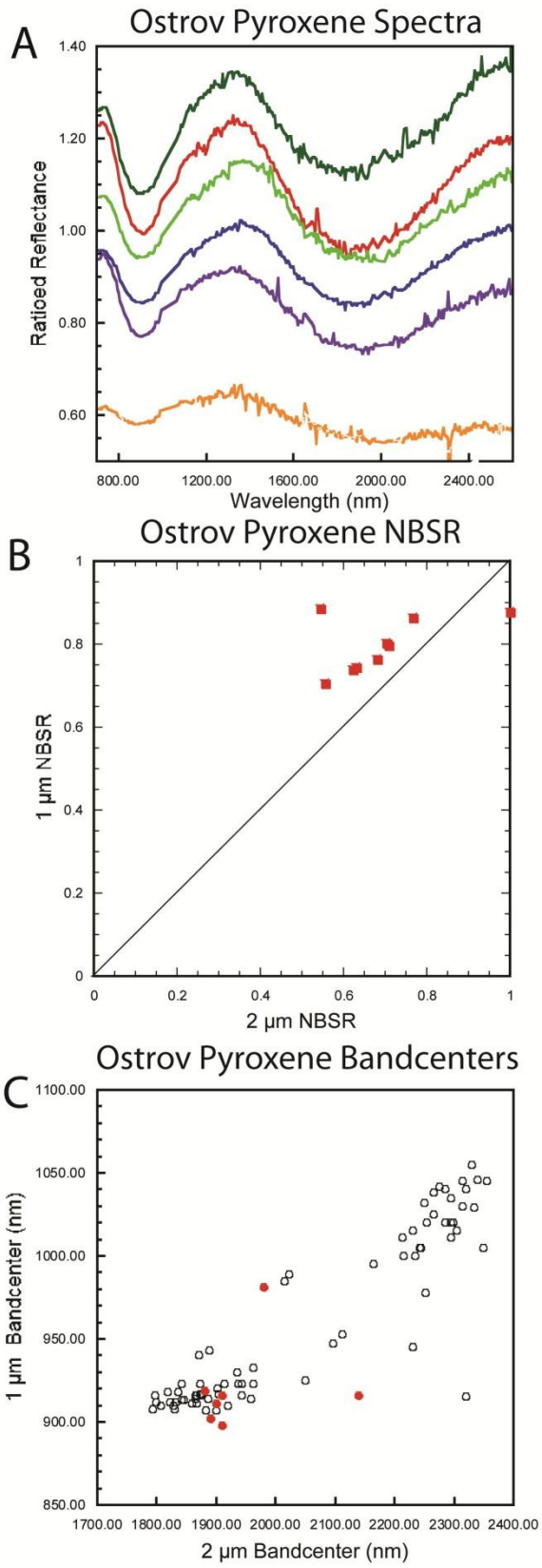

Chapter 1, Figure 14

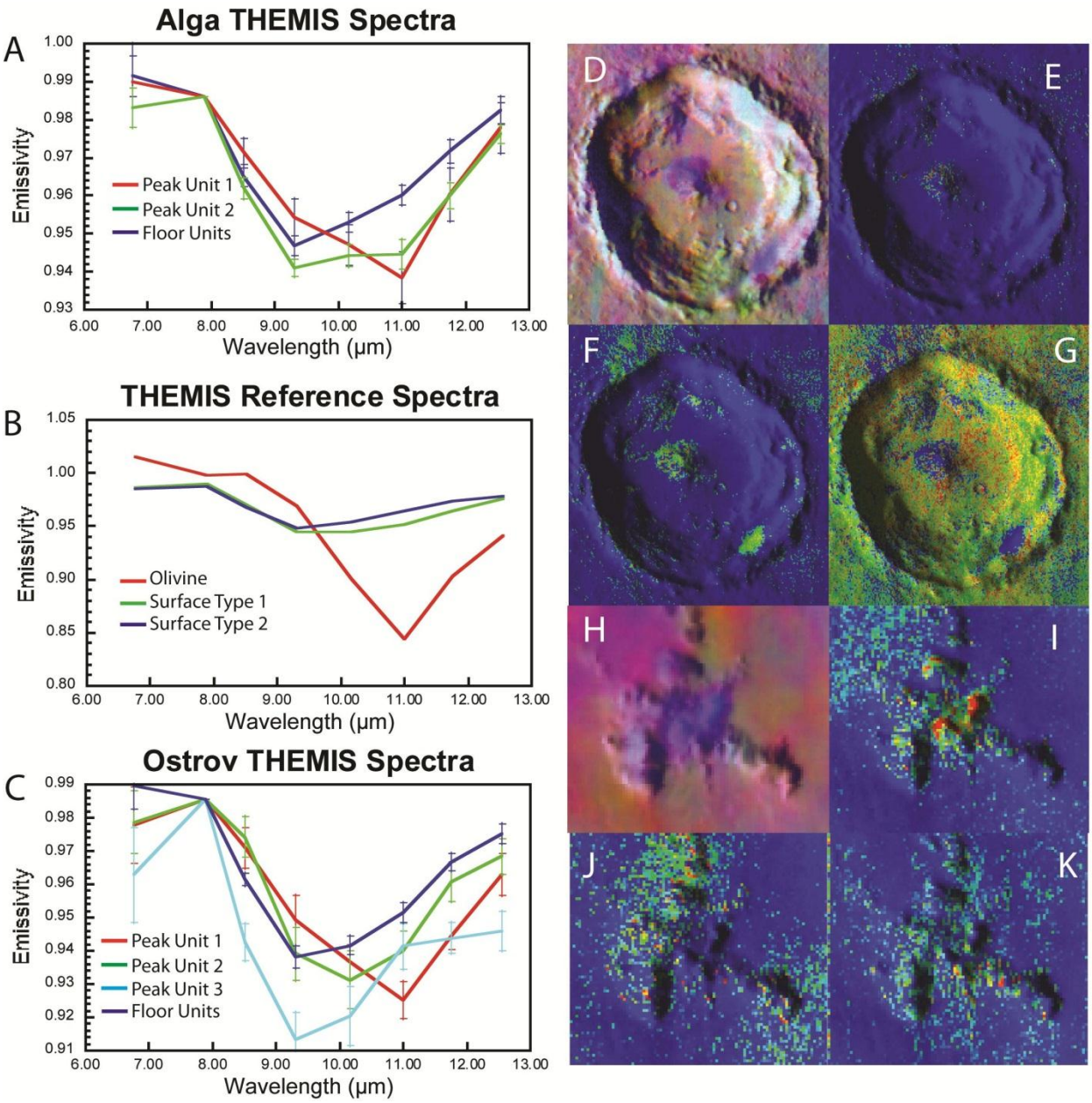

Chapter 1, Figure 15

Appendix 1: Un-projected CRISM FRT with selected Regions of Interest.

FRT00006415:

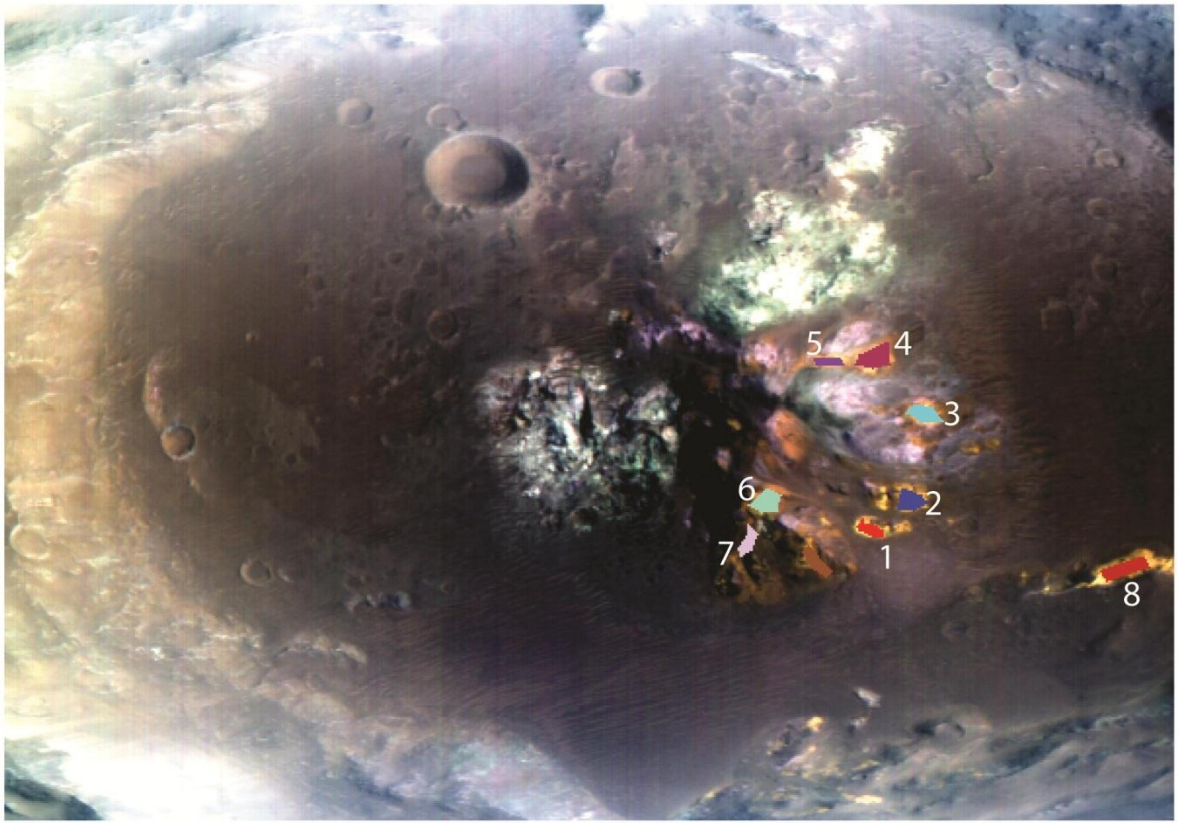

Appendix 1.1 Alga Olivine ROI

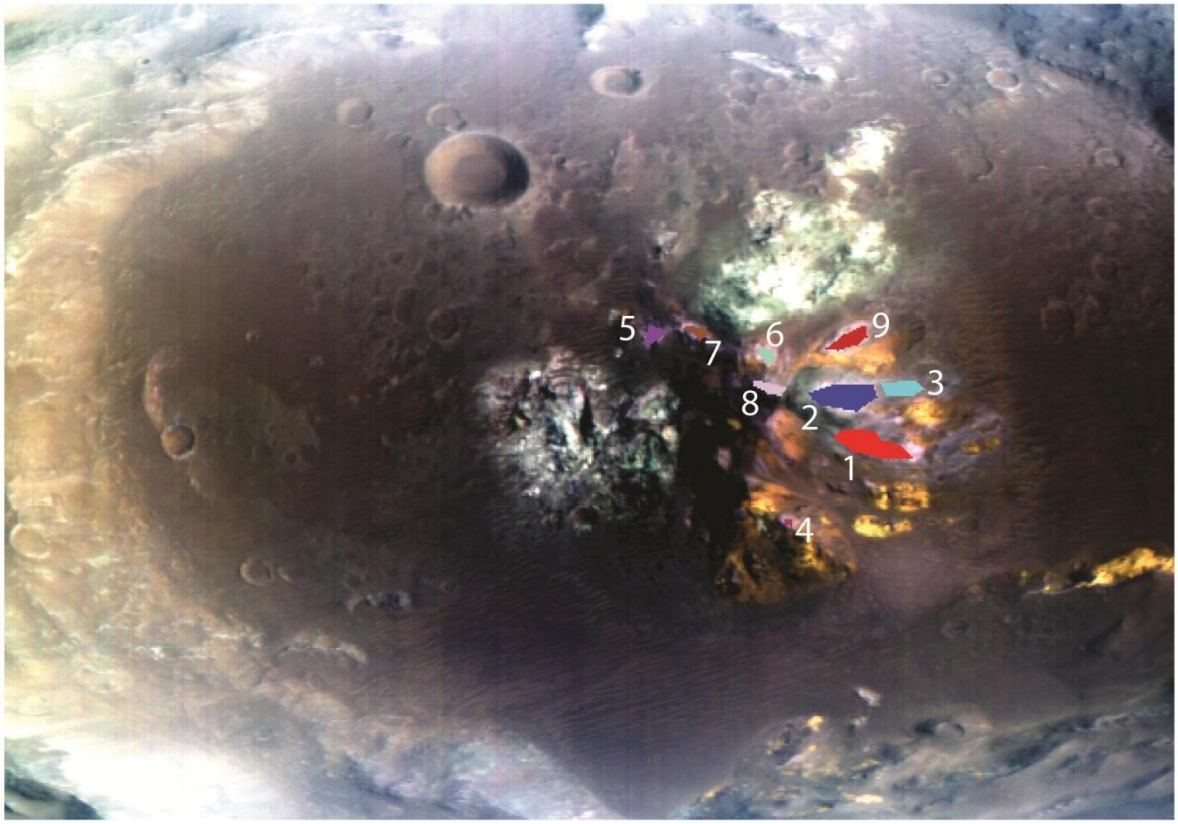

Appendix 1.2 Alga Pyroxene Bedrock ROI

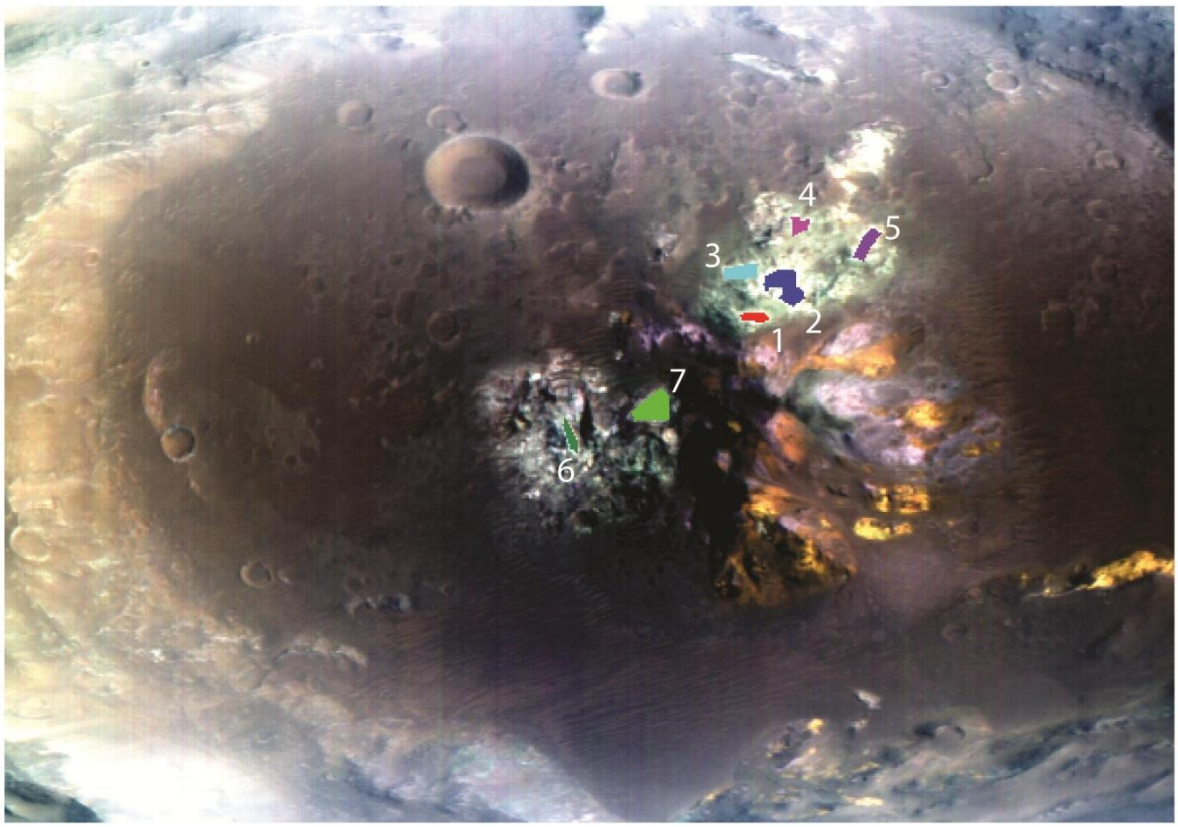

Appendix 1.3 Alga Light-toned Pyroxene ROI

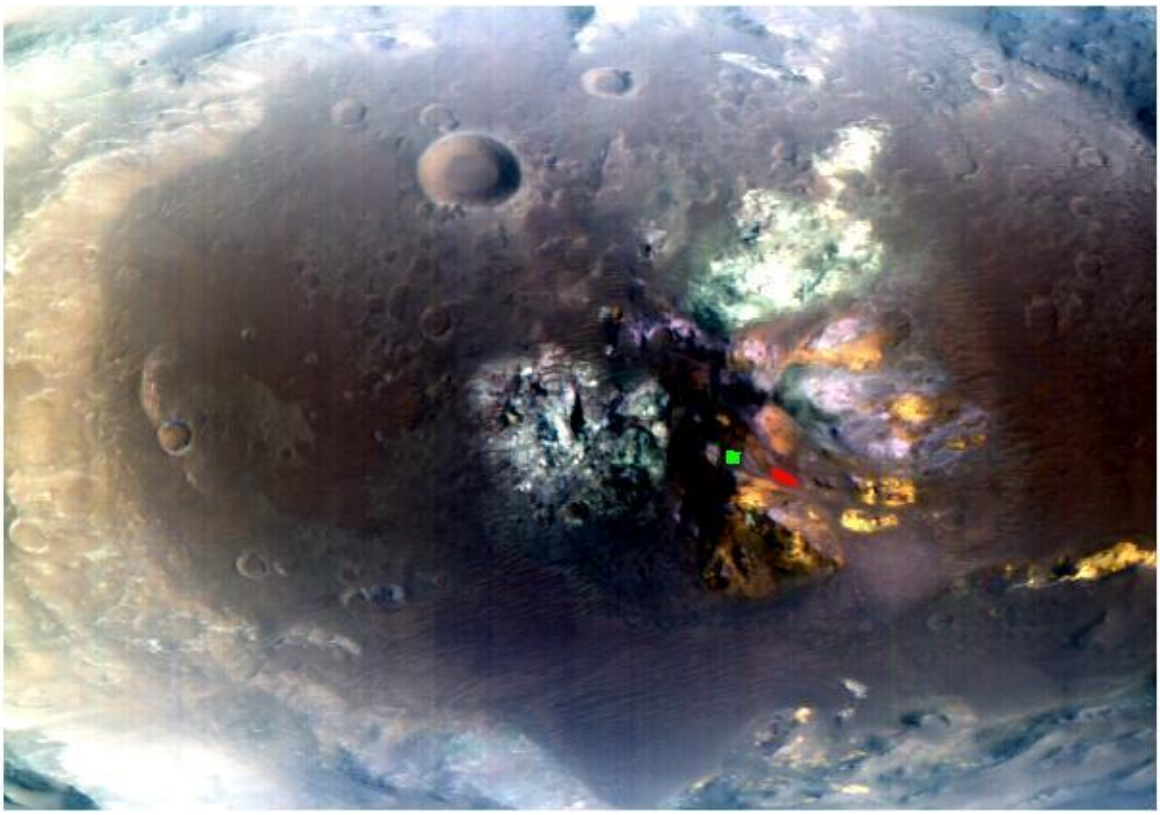

Appendix 1.4 Alga Melt ROI

FRT00017D02:

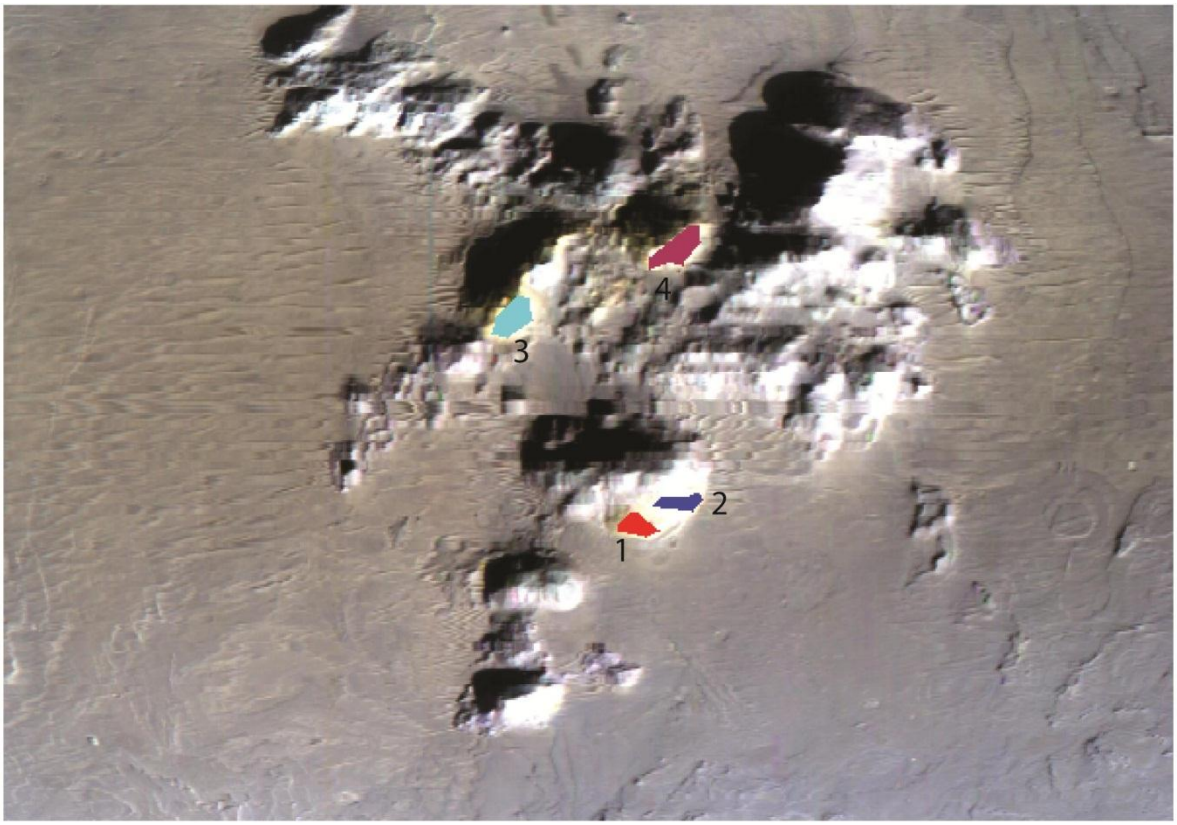

Appendix 1.5 Ostrov Olivine ROI

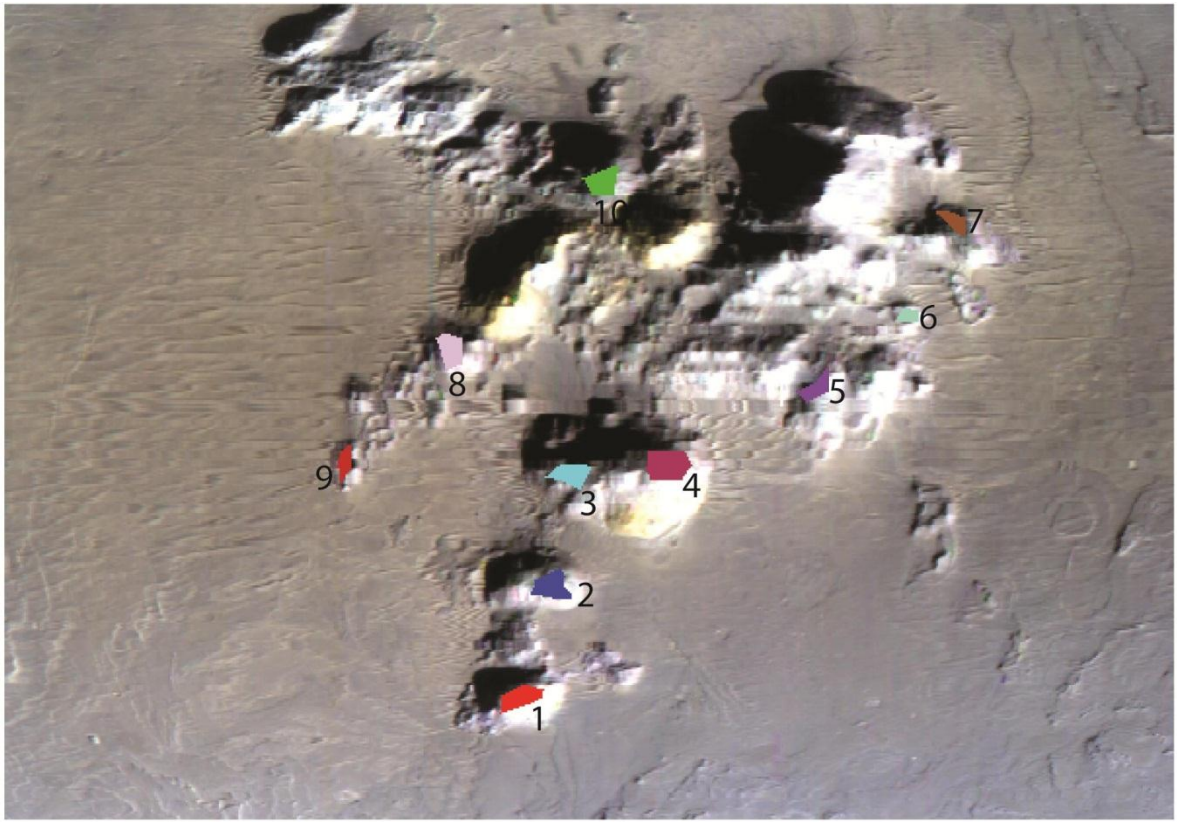

Appendix 1.6 Ostrov Pyroxene ROI

Appendix 2: List of Analyzed Regions of Interest. (d) indicates ratio denominator region. ROI center points and number of pixels listed. ROI are irregularly shaped and shown in Appendix 1.

FRT00006415

2.1

Alga Olivine	CenterX	CenterY	#Pixels
1	474	269	70
1d	476	333	172
2	497	254	113
2d	494	332	141
3	502	210	116
3d	502	332	145
4	478	180	157
4d	475	331	108
5	454	183	49
5d	458	334	84
6	422	255	133
6d	415	336	191
7	447	286	106
7d	449	335	99
8	414	275	81
8d	413	335	93
9	606	290	156
9d	604	323	278

2.2

Alga Pyroxene	CenterX	CenterY	#Pixels
1	474	226	349
1d	481	335	437
2	462	202	344
2d	464	336	350
3	492	197	133
3d	495	335	185
4	433	266	11
4d	433	339	42
5	365	170	66
5d	366	330	95
6	423	181	48
6d	427	339	63
7	388	169	45

7d	391	331	112
8	423	197	73
8d	426	339	139
9	466	172	123
9d	463	335	233

2.3

Alga Light-toned Pyroxene	CenterX	CenterY	#Pixels
1	416	160	55
1d	416	342	500
2	434	145	216
2d	436	334	751
3	408	137	120
3d	410	335	671
4	439	113	61
4d	440	338	612
5	473	123	98
5d	473	328	548
6	322	221	53
6d	324	339	543
7	364	205	212
7d	366	346	1658

2.4

Alga Melt	CenterX	CenterY	#Pixels
1	437	246	71
1d	443	339	696
2	411	235	41
2d	403	343	463

FRT00017D02

2.5

Ostrov Olivine	CenterX	CenterY	#Pixels
1	355	267	160
1d	360	399	791
2	378	255	146
2d	372	398	694
3	294	160	276

3d	283	403	702
4	377	126	299
4d	370	399	884

2.6

Ostrov Pyroxene	CenterX	CenterY	#Pixels
1	296	357	188
1d	298	406	477
2	311	297	199
2d	314	405	334
3	320	243	177
3d	319	404	315
4	372	237	302
4d	379	401	690
5	450	196	124
5d	445	396	491
6	495	160	58
6d	508	399	433
7	520	113	97
7d	511	399	526
8	260	179	179
8d	263	403	506
9	206	236	85
9d	209	404	189
10	337	91	176
10d	336	403	424

Chapter 2:

Spectroscopic Analysis of Martian Crater Central Peaks: 2. A Global Perspective on the Ancient Crust

J.R. Skok[1], J.F. Mustard[1], L.L Tornabene[2]

1. Department of Geological Sciences, Brown University

2. Department of Earth Sciences, University of Western Ontario

Abstract

The record of the earliest crust of Mars is expected to be preserved on this single plate planet, deeply buried under surface volcanics and altered minerals. Mars' extensive cratering history would have fractured and disrupted the upper layers of this ancient crust. Large impacts occurring after the main stage of surface alteration would have excavated this deeply buried material. We report the compositional analysis of unaltered mafic Martian crater central peaks with high-resolution spectral data that was used to characterize the presence, distribution and composition of mafic mineralogy. Reflectance spectra of mafic outcrops are modeled with the Modified Gaussian Model (MGM) to determine cation composition of olivine and pyroxene mineral deposits. Observations show that central peaks with unaltered mafic units are only observed in four general regions of Mars. Each mafic unit exhibits spectrally unmixed outcrops of olivine or pyroxene, indicating dunite and pyroxenite dominated compositions instead of basaltic composition common throughout much of the planet. Compositional analysis shows a wide range of olivine Fo# ranging from ~Fo_{60} to ~Fo_{5}. This variation is best explained by a high degree of fractionation in a slowly cooling, differentiating magma body. Pyroxene analysis shows that all the sites in the Southern Highlands are consistent with moderately Fe-rich, low-Ca pyroxene, likely pigeonite to ferrosilite. Mineral segregation in the ancient crust is most likely caused by cumulate crystallization and settling in a large lava lake or near-surface plutons. The global distribution of the deposits requires a powerful and global volcanic source, such as the hypothesized early Martian mantle overturn.

Introduction

The initial formation of a planetary crust is a critical stage in a planet's evolution. It can contain evidence of the last stages of planetary formation and gives a starting point for all subsequent crustal modification. The nature of this initial crust is difficult to address on Earth as plate tectonics has recycled all of the initially formed rocks. The lunar crust offers a well-studied primary crust [Taylor 1992], thought to be formed by plagioclase floatation from a magma ocean [Wood, 1970; Warren, 1990]. However, the small size and unique composition of the Moon makes it difficult to extrapolate this process to larger, wetter worlds. In this sense, Mars provides a valuable analog for the conditions of early terrestrial crusts with single-plate style of tectonics that would have preserved the ancient crustal material. Subsequent to planetary formation, Martian volcanism, alteration and impact cratering would obscure the ancient crust from surface observations. Recent high-resolution observations from the Mars Reconnaissance Orbiter (MRO) revel small, relatively compositionally pure outcrops of unaltered, igneous rocks that are exposed in crater central uplift structures as megablock fragments of this ancient crust. This ancient crust of Mars is the key to understanding the formation and early evolution of the planet.

The igneous composition of the current Martian surface has been studied by a number of investigations that use data from orbital, landed and laboratory instrumentation as described below. With the possible exception of the Martian meteorite ALH84001 [Mittlefehldt, 1994; Lapen et al., 2010] described below, all measurements of Martian primary lithologies are partially or entirely contaminated by volcanic and altered materials that formed after early planetary crustal formation. If the crustal blocks reported here are from this formational period, as hypothesized, then we cannot directly compare them to previous results. However the legacy

of observations of Martian igneous lithologies detail the diversity of Martian volcanic processes and sets the context for known Martian compositions.

Global surface mineralogy was analyzed with the Thermal Emission Spectrometer (TES) [Christensen et al. 1992] which mapped the presence and distribution of mafic minerals and igneous lithologies [e.g. Bandfield et al., 2000; Wyatt and McSween, 2002; Rogers et al., 2007; Koeppen and Hamilton, 2008]. Initial observations divided the primary crustal lithologies into a basaltic Surface Type 1 with 50% plagioclase feldspar, 25% clinopyroxene and 15% sheet silicates and an evolved Surface Type 2 with 35% plagioclase feldspar, 25% glass, 15% sheet silicates and 10% clinopyroxenes with a hemispherical division between the types [Bandfield et al., 2000]. Surface Type 2 has since been suggested to be the result of an alteration process [Wyatt and McSween, 2002; Ruff and Christensen, 2007]. Surface Type 1 has been further refined to show specific compositions unique to individual volcanoes and regions [Rogers et al., 2007]. Additional studies have shown compositional trends with time as younger terrains having a relative enrichment in high-calcium pyroxene (HCP) [Poulet et al., 2009; Skok et al., 2010] and a depletion in SiO_2 [Baratoux et al., 2011] hinting at the thermal evolution of the planet. Thermal infrared analysis of olivine exposures show that this mineral makes up approximately 10-20% of the aggregate surface abundance [Koeppen and Hamilton, 2008]. Olivine detections have seen a range of compositions with a concentration at intermediate to forsteritic compositions (Fo_{68}-Fo_{53}) [Koeppen and Hamilton, 2008; Hoefen et al., 2003] with some minor areas modeled with values as low as Fo_{39} and has high as Fo_{91} on a few basin rims. While TES provides the best available remote dataset to determine global lithologies, the large, 3 x 6 km pixel resolution limits the ability to resolve specific crustal outcrops with this dataset.

Our understanding of Martian surface mineralogy was further refined with visible and near infrared (VNIR) Observatoire pour l'Mine´ralogie, l'Eau, les Glaces, et l'Activite (OMEGA) observations (300 m to 5 km spatial resolution) mapping of iron-bearing igneous silicate mineralogy including high-calcium pyroxene (HCP), low-calcium pyroxene (LCP) and olivine [Mustard et al., 2005; Poulet et al., 2009]. The OMEGA observations confirm and extend many of the TES igneous results and greatly expand our understanding of the aqueous alteration of the crust [Bibring et al., 2006]. However the resolutions still result in large spatial averages of surface compositions.

Small scale surface compositions have been determined in select locations by in-situ analysis of Mars igneous samples with instrumentation on the Spirit Rover [Squyres et al., 2004; McSween et al., 2006]. An example is provided by the well-studied Gusev plains basalt known as Adirondack class that has an estimated modal mineralogy of approximately 25% olivine, 30% pyroxene with the remaining as plagioclase and accessory minerals. In these basaltic rocks the olivine's cation composition was determined to be intermediate to mildly fayalitic (Fo_{52-45}) from the alpha particle x-ray spectrometer (APXS) measurements and Fo_{60-35} based on the Miniature Thermal Emission Spectrometer (Mini-TES) [McSween et al., 2006]. The most detailed analysis of Martian crustal composition is provided by the study of Martian Meteorites [Mittlefehldt, 1994; Nyquist et al., 2001; McSween et al., 2002] These allow in-depth chemical analysis and a detailed history to be determined. Meteorite sampling has been skewed to only the most competent surface materials that can survive the ejection and landing on Earth and therefore nearly all are relatively young, igneous rocks. The majority of the samples have been classified as basaltic Shergottites and have ages that range from 175 Ma to 475 Ma [Nyquist et al., 2001 and references therein], indicating relatively recent Martian volcanic activity. However the

meteorites contain no contextual information, making it impossible to trace back the compositions to a particular region of Mars. Of particular interest is the meteorite, ALH84001, dated between 4.5 and 4.1 Gyr [Mittlefehldt, 1994; Nyquist et al., 2001; Lapen et al., 2010] depending on age determination method, it is the oldest sample of the Martian crust. The orthopyroxenite composition indicates the existence of early crustal processes capable of mineral segregation and may be a sample of a common early crustal component.

Current understanding of the initial formation of Mars is determined from isotopic and petrologic observations from Martian meteorites [Bertka and Fei, 1997; Debaille et al., 2007 and references within] and geophysical/geochemical modeling of planetary evolution [Borg and Draper, 2003; Elkins-Tanton et al., 2005]. Isotopic studies show that the initial formation of Mars would progress rapidly with core formation having been largely completed 12.4±4 Myr after solar system formation [Dabaille et al., 2007] while mantle evolution of source regions would be mostly completed within 100 Myr [Dabaille et al., 2007] (Figure 1). The details of this mantle evolution have been investigated with geophysical models. Elkins-Tanton et al., [2005] describe the results from an early magma ocean that would crystalize olivine and pyroxene cumulates, beginning with Mg-rich minerals and progressing to Fe-rich as the melt cools. The resulting density inversion would be corrected with a planetary scale mantle overturn. The volcanic activity resulting from the overturn event would be responsible for the formation of the bulk of the earliest crust of Mars. This overturn model predicts a global crustal dichotomy where shallow cumulate melting would lead to voluminous magma, low-Al, and high Fo#, while deep melts would lead to less magma, higher-Al and ~Fo_{70} [Elkins-Tanton et al., 2005]. These modeled predictions can now be tested with high-resolution spectroscopic images of the Martian surface.

Previous work [Chapter 1] has shown that Compact Reconnaissance Imaging Spectrometer for Mars (CRISM) spectroscopic analysis can be used to determine the cation composition of Fe-bearing mafic minerals. In that study, deep crustal exposures from Alga and Ostrov crater central peaks were analyzed for composition. Both central peaks have spatially distinct olivine- and pyroxene-dominated units with strong spectral signatures. At both sites, the pyroxene is consistent with a low-Ca and potentially high-Fe cation content and the olivine units range from fayalitic to intermediate Fo# values. Here we report on compositional determinations from 21 additional central peak exposures to investigate the nature of the Martian crust and compositional diversity across the planet (Figure 2). These observations are then integrated into a model for the formation of the ancient crust that can be used to refine and test future planetary formation models.

Methods

To develop the database of exposed, unaltered crust on Mars for analysis, we considered all potential central peak exposure observations. The survey initially considered the 150 sites included in the Crater Exposed Database [Tornabene et al., 2010] which are defined on the basis of High Resolution Imaging Science Experiment (HiRISE) [McEwen et al., 2007] and Context Imager (CTX) data [Malin et al., 2007]. Of these, 105 had CRISM full resolution targeted (FRT) image coverage. FRTs of central peaks were first examined with spectral summary parameter maps [Pelkey et al., 2007] that quickly summarize where likely exposures of unaltered crust exist. To confirm that in fact alteration minerals (identified on the basis of 1.9 μm H_2O combination tone) are absent and that crystalline igneous mafic minerals, olivine and/or pyroxene are present in bedrock exposures the areas highlighted in spectral summary parameters

were examined in detail with the full resolution spatial and spectral CRISM data. Observations with strong spectral signatures were then used to guide the selection of multipixel regions of interest (ROI). ROIs are selected based on regions highlighted in the mafic summary spectral parameters with associated ratio denominators selected in the same columns in a region of bland mafic parameters, typically in the crater floor.

CRISM. The primary compositional data for this analysis are observations from the CRISM VNIR hyperspectral imaging instrument [Murchie et al., 2007]. CRISM acquires FRT images at 18 meter per pixel spatial resolution and 544 spectral bands ranging from 0.32 – 4.0 μm. Additional observation modes are available but rarely used in this study. CRISM observations were corrected for instrumental artifacts and all data was processed into I/F [Murchie et al., 2007]. Atmospheric correction was determined with a volcano scan method developed and tested on ISM [Bibring et al., 1989] and OMEGA [Mustard et al., 2005] and detailed in McGuire et al., [2009]. The CRISM data is collected on a short wavelength S-detector (VNIR: 362-1053 nm) and a long wavelength L-detector (IR: 1002 -3920 nm). Full wavelength modeling requires detector coordination. Ratioed spectra were calculated for each detector independently, then joined by removing the overlapping spectral data (1000 nm – 1053 nm) from the S-detector and enacting a slight scaling factor on the S-detector data to match the joining point of the L-detector [Murchie et al., 2007]. The absolute value of the ratioed value is dependent on the relative albedo of the region of interest and denominator area and does not affect modeling as long as the values are consistent between detectors. Mafic mineral deposits are identified with mafic parameter maps that highlight spatial regions with characteristic spectral absorptions [Pelky et al., 2007; Salvatore et al., 2010]. The three parameters that were systematically applied were:

OLINDEX2:

$$\left(\left(\frac{RC1054-R1054}{RC1054}\right)*0.1\right)+\left(\left(\frac{RC1211-R1211}{RC1211}*0.1\right)+\left(\left(\frac{RC1329-R1329}{RC1329}\right)*0.4\right)+\left(\left(\frac{RC1474-R1474}{RC1474}*0.4\right)\right)\right) \quad (1)$$

LCPINDEX:

$$\left(\frac{R1330-R1050}{R1330+R1050}\right)*\left(\frac{R1330-R1815}{R1330+R1815}\right) \quad (2)$$

HCPINDEX:

$$\left(\frac{\mathrm{R1470-R1050}}{\mathrm{R1470+R1050}}\right)*\left(\frac{\mathrm{R1470-R2067}}{\mathrm{R1470+R2067}}\right) \quad (3)$$

Where R#### is the reflectance value at #### nm wavelength and RC#### denotes the value of a point at a wavelength of #### nm along a modeled line that follows the average slope of the spectrum. These parameters mapped spectral signatures characteristic of Olivine, LCP and HCP respectively. Average spectra were collected from regions of interests (ROI) of mineral deposits as defined by the mafic parameter. Average spectra were ratioed to a spectrally bland region in the same column of pixels, typically in the crater floor fill. This ratio technique is commonly used to suppress systematic errors and remove spectral features common to both regions.

MGM Method. Following the same methods detailed in Chapter 1 (Figure 3) the modified Gaussian method (MGM) [Sunshine et al., 1990; Sunshine and Pieters, 1993; Sunshine et al., 1998; Kanner et al., 2007] deconvolves overlapping absorptions of mafic mineral spectra into their fundamental absorption components. Individual absorption components are modeled as modified Gaussian distributions that mathematically describe the specific shape of electronic transition absorptions and are parameterized by a band center, band width, and band strength. Gaussians are defined as:

$$g(x) = s * \exp\left(-\frac{(x-\mu)^2}{2\sigma}\right) \quad (4)$$

where s is band strength, σ is the band width, and μ is the band center. The MGM superimposes several Gaussians onto a continuum to model the spectrum with known absorption features at fixed wavelengths due to specific electronic transitions.

Olivine Analysis. Olivine ($(Mg,Fe)_2SiO_4$) is a magnesium-iron silicate with a nesosilicate structure. It is spectrally identified in the near-infrared by a broad absorption centered near 1 μm that is the superposition of three overlapping absorptions due to electronic transitions in Fe^{2+} ions located in distorted octahedral crystal lattice sites [Burns 1970;1974;1993]. The exact band center of each of these absorptions is related to the relative proportion of Fe and Mg in the M1 and M2 sites with increasing Mg causing shorter wavelength absorptions and increasing Fe longer causing wavelength absorptions [Burns 1970; Sunshine and Pieters, 1998]. To avoid spectral considerations outside the diagnostic 1 μm band, we only model from 0.8 μm to 1.8 μm but visually check that there are no 2 μm features related to pyroxene. Three bands are used to model this absorption (Chapter 1. Table 1) with the resulting fitted bandcenters determining the composition [Sunshine and Pieters 1998; Isaacson et al., 2010]. The three bandcenters are fit to the laboratory determined compositional determination line to fit for least error to determine the composition of a given spectrum with the following relationship [Isaacson et al., 2010].

$$A = \left[\frac{1112.3}{1.2179^2} + \frac{2373}{2.2^2} + \frac{1335.9}{1.0309^2}\right] \quad (5)$$

$$B = \left(\frac{1}{1.2179^2} + \frac{1}{2.2^2} + \frac{1}{1.0309^2}\right) \quad (6)$$

$$Fo = B^{-1} * \left[A - \left(\frac{M1-1}{1.2179} + \frac{M2}{2.2} + \frac{M1-2}{1.0309}\right)\right] \quad (7)$$

A and B are constants that constrain the slope of the line that relates the composition as a function of band center for each of the olivine absorptions. M1-1, M2, and M1-2 are the bandcenters (in nm) for the three olivine absorptions. Fo is the cation composition ratio of Mg wt.% /(Mg wt.% + Fe wt.%) ranging from 0 (100% Fe) to 100 (100% Mg).

The formula can be modified to be fit to any two band inputs if needed. When modeling CRISM spectral data, we found that limiting analysis to the L detector data can produce more reliable results when there is a problem with the L+S detector alignment. The natural properties of the long wavelength M1-2 feature gives it the most wavelength variability per change in composition, meaning that small changes in bandcenters will have the least effect on the modeled composition making it the most stable feature band to fit [Sunshine et al., 1998]. For these reasons, we include the modeled fits both using all three olivine bands and alternatively only using the M2 and M1-2 bands. We find that in the 101 regions spectrally analyzed only three are at or more than 20 Fo units difference and only three regions (NA2, NP4, NP6) have a significant number of values greater than 10 units different. These three regions are the only ones where the S detector alignment may cause a significant effect on the compositional determination.

Pyroxene Analysis. Pyroxene ($(Ca,Mg,Fe)Si_2O_6$) is spectrally identified by absorptions at 1 and 2 μm with the band center slightly dependent on the Mg-Fe cation content and strongly dependent on the Ca content [Adams, 1974; Cloutis et al., 1986; Cloutis et al., 1991] and a weak 1.2 μm absorption. The pyroxene absorptions are caused by crystal field transitions of iron in octahedral coordination with the 1- and 2-μm absorptions due to the composition of the M2 crystallographic site causing distortion in the crystal structure based on the size of the cation

element. The 1.2 μm absorption due to molecular distortion in the M1 crystallographic site [Burns, 1993]. Pyroxene Ca content can be determined by modeling each absorption as a combination of endmember low-calcium and high-calcium pyroxene. Kanner et al. [2007] has shown that the ratio of endmember strengths is proportional to the relative composition of each endmember. Since pyroxene composition is spectrally distinguished by the Ca content, we refer to high-Ca (HCP) and low-Ca (LCP) compositions. This spectral determination does not distinguish structural variants of orthropyroxene (OPX) and clinopyroxene (CPX). However, in practice LCP strongly coincides with OPX while HCP coincides with CPX. Pyroxene compositions are modeled using 2 approaches. The first uses 5 absorptions (Chapter 1. Table 1), the LCP and HCP endmembers of both the 1 and 2 μm absorptions and an absorption at 1.2 μm used to provide a reliable fit but not used to determine composition. Ca content was determined by calculating the ratio of the modeled LCP endmember band strength and dividing by the total LCP and HCP strengths, (LCP/(LCP+HCP)) to determine the normalized band strength ratio (NBSR) [Kanner et al., 2007]. The NBSR was calculated for both the 1 and 2 μm absorptions. A NBSR value of 1.0 indicates there is only LCP while a value of 0.0 indicates only HCP, with intermediate values proportional to the relative Ca content. The calculation of the 2 μm NBSR is well constrained by the CRISM observation due to the lack of any competing absorption features in the 2 μm region. The 1 μm has several sources of error including spectral effects from iron oxides and small amounts of olivine plus S detector boundary issues. These issue lead to greater error in the reported 1 μm NBSR. Confidence in the 1 μm NBSR increases when it coincidences with the 2 μm NBSR as it should in natural pyroxenes. The second approach model pyroxene with two compositional bands, at 1 and 2 μm. This provides a systematic way to determine

absorption band centers. Band centers are used compare the Martian pyroxenes against classified terrestrial pyroxenes measured by Adams, [1974] and Cloutis and Gaffey, [1991].

Error Consideration. MGM was developed and tested by analyzing laboratory spectral measurements of well-characterized samples. Olivine compositional error occurs at two separate steps. The first is during the MGM spectral fitting process that models the CRISM spectra with the Gaussian absorptions. The model is running unit the RMS increase less than 10^{-5} with a successive iteration and is always lower than 10^{-2}. However, errors from slight varying in initial spectral parameters lead to an error of ~5 Fo# for olivine [Isaacson and Pieters 2011]. Additional errors are expected when applying the MGM to remote sensing data with lower signal-to-noise and additional spectral components. The second step is the calculation of Fo# from the modeled bandcenters. The composition is calculated as a least squares fitting to either 3 or 2 slopes. The greater difference between the laboratory determined slopes and actual data the larger the error in the compositional determination. This error is listed for all 3 slope fits (Table 3). A separate study applying the MGM to pyroxenes with laboratory and OMEGA data determined that the calcium content can be constrained to ±10% [Kanner et al., 2007].

Results

The spectral analysis of CRISM observed unaltered, well-exposed crater central peaks have yielded 23 sites (Table 1). The observed craters range in diameter from ~130 km to 7 km. When these observed sites are mapped, they naturally divide into four concentrated regions; North Argyre (NA), Northern Hellas (NH), Nili Fossae (NF) and the Northern Plains (NP) (Figure 2). While every crater has its own unique attributes, we describe one example from each

region in detail to highlight some of the observed diversity and then aggregate the compositions to look at global relationships.

North Argyre. The Northern Argyre (NA) region has so far yielded six central peaks that have well-defined, unaltered mafic spectra. Two of the craters in this region (Alga NA1 and Ostrov NA2) have been previously reported with spectral units mapped and analyzed [Chapter 1]. These examples displayed a clear lithologic distinction between olivine-bearing and pyroxene-bearing units, with olivine ranging from fayalitic compositions in Alga to intermediate compositions in Ostrov. The pyroxenes for both regions were consistent with a high-Fe, low-Ca composition.

Here we detail the characteristics of an additional example from this region, NA4, a 22 km diameter unnamed crater in the Northeast part of Ladon Basin (16.71°S, 28.14°W Figure 4, Figure 5) that is contained within CRISM observation FRT000097FF. This example highlights the difficulty in determining the original context of excavated peak material. The crater impacts into the Ladon Basin that was strongly modified and filled. The Ladon Basin itself sits on crust strongly modified by previous impact and volcanic processes. This makes it impossible to determine the original context and origin of the crustal material. Despite this, valuable composition and morphologic information are contained in the central peak occurrences. The central pit of NA4 is filled with aeolian materials, but the pit rim, particularly the northeastern portion, is comprised of mafic-bearing blocks. Light-toned olivine-bearing units form much of the northern and eastern rim, while pyroxene units dominate the western and southwest sides. Two olivine-bearing regions were successfully modeled with compositions of Fo_{20} and Fo_{16} (Table 3). These values are among the most fayalitic in this region but are comparable to the range from Alga Crater (NA1). Three pyroxene regions were modeled with 2 μm NBSR values

consistent at 0.56 (Table 4) with absorption bandcenters just above the LCP endmember values supporting the LCP enrichment of the pyroxene-bearing units.

North Hellas. The North Hellas (NH) region contains nine well-defined and exposed central peaks covering a wide spatial distribution. Here we describe one example, NH6, a relatively small (20 km) crater on the northern edge of Hellas Basin (31.43°S, 81.63°W Figure 6, Figure 7). The upper layers of the central peak, just below peak's apex are distinguished by a light-toned olivine-bearing lithology that is preferentially eroded from the darker surrounding material. The apex of the peak retains this darker material with a distinct pyroxene signature. One olivine region was successfully modeled yielding a three band fit with a composition of Fo_8 (Table 3). While this observation is the most Fe-rich olivine-bearing site from the Northern Hellas region, all are consistently fayalitic with a range from Fo_8 to Fo_{38} (Table 3). One pyroxene-bearing region from NH6 was modeled with an intermediate 1 μm NBSR (0.48) and LCP-rich 2 μm NBSR (0.73) (Table 4). While some variation does exist, the pyroxenes from the entire Northern Hellas region consistently show a moderate to high LCP enrichment.

Nili Fossae. The third region examined is the smallest current sample set with only two sites due to the high degree of alteration in this area [Ehlmann et al., 2009]. The Nili Fossae (NF) region is part of the Southern Highland terrain, located on the western edge of the Isidis basin and just south of the dichotomy border. The Nili Fossae region has been well examined due to spectrally well-exposed crustal exposures and a diverse geologic history [e.g.: Hoefen et al., 2003; Mangold et al., 2008; Fassett et al. 2005; Mustard et al., 2009; Ehlmann et al.; 2009]. Both examined sites are similar in size and each contains exposures of olivine and pyroxenes. Here we detail Hargraves (NF1) (20.76°N, 75.81°E Figure 8, Figure 9). The central pit structure is dominated by pyroxene-bearing bedrock with a few small olivine outcrops around the pit. Unlike

most of the other examples, the olivine-bearing material does not correlate to a clear albedo difference. The modeled olivine region in this central peak had a composition of Fo_{14}, while the range for the six modeled regions in NF have a range of Fo_{5-14}, again showing a strong fayalite enrichment. Pyroxene modeling of six regions in NF1 results in range of a 2 μm NBSR of 0.56-0.63 with a similar range for the 1 μm, again consistent with a slight enrichment in LCP.

Northern Plains. The North Plains (NP) region includes six craters with concentrations in Acidalia Planitia (NP1, NP2) and Utopia Planitia (NP3-NP6). Two sites, Kunowsky Crater (NP1) and Stokes Crater (NP5), are relatively large at 60 km, while the other four are 30 km or less, all of which are large enough to penetrate the Hesperian basalts that resurfaced the lowlands and that are estimated to be hundreds of meters thick [Head et al., 2002]. The four smaller craters all contain well-formed and preserved central peak structures surrounded in part by dark, olivine bearing dune materials. These are identified by the low albedo compared to the noticeably bright olivine bedrock units selected as regions of interest. In selecting regions of interest we choose spatially continuous mafic units based on parameter maps. With this method, central peaks in the Southern Highlands contained at most nine modeled olivine regions and in some cases only one or two regions. In contrast, the large NP craters, Kunowsky (NP1) and Stokes (NP5) have 17 and 21 olivine-bearing outcrops respectively.

Stokes Crater (NP5) (Figure 10, Figure 11, Figure 12) contains one of the more complex central peak structures examined in this study. The peak itself is offset to the north of center of the crater with depressions to the south and east of center. Large diffuse light-toned olivine-bearing units outcrop from the peak and edge of the southern basin. In between the olivine exposures on the peak are small pyroxene-bearing units with no distinctive morphology. The eastern depression contains dark olivine-bearing dunes underneath which are light-toned, highly

fractured megabreccia blocks with strong olivine signatures (Figure 10C). The 21 modeled olivine regions yield a diverse compositional range of $Fo_{15\text{-}65}$ ranging from mildly forsteritic to strongly fayalitic. The 2 μm pyroxene NBSR values for the 16 modeled regions range from 0.53-0.62 with values for the 1 μm absorption about 0.1 less (Table 2B). Stokes Crater fits into the pattern we are observing across the planet with light-toned olivine breccia interspersed with pyroxene bedrock units.

These examples show strong similarities among the observed central peak mafic units throughout all the regions. In all the locations we observed brecciated blocks with no evidence of spectral mixing. The observed olivine range from moderately forsteritic to strongly fayalitic and the pyroxene units are consistently enriched in LCP. Here we present the composition results of all the regions to determine any regional or global trends.

Nature of Olivine Compositional Trends. MGM modeling of the olivine regions from all of the sites show a wide range of values from Fo_5 to Fo_{70} (Figure 13, Table 3) with a mean value of Fo_{28} for all regions. This reinforces the Fe-rich fayalitic nature of the observed olivine units but highlights the diversity in the compositions. NA olivine-bearing units have a mean of $Fo_{34\pm23}$ (Figure 14). This region has the highest Fo of the four regions as well as the largest range. NH has a mean of $Fo_{18\pm7}$. The NH sites (Figure 15) are systematically fayalitic with only a small variation indicating a clear difference from the composition distribution in NA. NF has only 6 modeled regions and contains the most fayalitic values with a mean of Fo_{10} and a narrow 4 Fo unit range. The NP region (Figure 16) has a composition distribution similar to NA with a mean of $Fo_{32\pm15}$, and can be subdivided into the Acidalia and Utopia populations. The Acidalia region (NP1, NP2) has a range of $Fo_{11\text{-}58}$ with a mean of Fo_{43}, while Utopia (NP3, NP4, NP5, NP6) has a range of $Fo_{7\text{-}56}$ with a mean of Fo_{26}. The olivine in the Acidalia region is significantly more

Mg-rich than Utopia highlighting the regional differences that are emerging from the observations [Table 2A].

Pyroxene Bandcenter Analysis. Modeling the pyroxene absorptions with 2 absorptions to get bandcenter allow the comparison of regional compositions to terrestrial pyroxene values. Figure 17 plots the modeled bandcenters against a set of laboratory measured CPX and OPX [Adams, 1974; Cloutis et al., 1991]. The 2 μm bandcenters for the NF (Mean:1897 nm) and NA (Mean:1922 nm) regions are lowest and consistent with low-Ca, moderate-Mg pyroxene endmember (enstatite). The NH area pyroxenes have higher 2 μm bandcenters (Mean:1962 nm) indicating higher Fe content but still low-Ca (ferrosilite). The 2 μm bandcenters for the NP (Mean:1965 nm) have a wide spread but are generally elevated compared to the Southern Highland pyroxenes with many comparable to moderate Ca compositions (pigeonite).

Pyroxene NBSR Analysis. MGM modeling of the pyroxene unit spectra with five absorptions allow for the determination of the relative proportions of low and high-calcium pyroxene components by calculating the NBSR value for both the 1 and 2 μm absorptions (Figure 18, Table 4). This provides an additional composition consistency check as a well measured and modeled pyroxene should have consistent NBSR values for both absorptions. Here we observe an agreement between the 1 and 2 μm was within 0.04 for the Southern Highland sites and 0.08 for the Northern Lowland sites (Table 2B). Comparing between regions highlights additional regional differences in composition. The three regions in the Southern Highland show a consistent LCP enrichment while the NP sites has a noticeable HCP enrichment.

A final analysis presented here is the investigation of a compositional relationship to excavation depth. Figure 19 plots the range of measured compositions in red and approximate excavation depth (1/10 crater diameter) in blue as a function of crustal thickness [Neumann et

al., 2004]. Figure 19A plots olivine Fo# and Figure 19 B plots pyroxene 2 μm NBSR. No clear relationship is observed between composition, excavation depth or crustal thickness. This result is most likely explained by the complex Martian impact history that has well mixed the ancient crustal material vertically.

TES Thermal Constraints. A dedicated analysis of Martian central peaks with the TES thermal IR instrument is currently underway [Pan and Rogers, 2011]. While many of the craters and all of the spectral units detailed in this study are too small for TES analysis, two sites (NA3 and NH3) have been analyzed by Pan and Rogers [2011]. While the results are still preliminary, these two sites were grouped with several others with a similar thermal spectral response and classified as relatively feldspar rich with a collective compositional abundance of 32% Feldspar, 19% LCP, 17 % HCP, 0.1% Olivine and 14% High-silica phases with the remaining 18% as accessory phases and blackbody. The spatial resolution differences between instruments and the several central peak averages in this study make a direct comparison difficult but point out the significant feldspar component that is not characterized by CRISM observations and has potential for future development.

Discussion

Implications of Global Distribution. The selection of these 23 central peak structures was the result of considering CRISM-observed unaltered, mafic bearing central peaks. After identification and successful modeling of the mafic spectra extracted from the central peaks, the locations were plotted and the four regional groupings were identified (Figure 2). These resulting locations are possibly the result of several properties of the Martian surface or may provide deeper understanding of the nature of these exposed units. A similar spatial distribution is

observed in the overall distribution of the Crater Exposed Bedrock Database [Tornabene et al., 2010] that considers only the HiRISE morphology and not the mafic spectroscopy, indicating that is it more than just an effect of surface spectral quality. Several surface properties that may contribute to the observed distribution include; dust cover [Ruff and Christensen, 2002], crater density, bedrock exposures and outcrop surface refreshing rates, and the presence and pervasiveness of alteration. For example, the volcanically dominated areas of Tharsis and Elysium lack observations in this study due to the lack of preserved craters and high dust cover [Ruff and Christensen, 2002] of these elevated regions. However the notable absence of sites in Noachis and Arabia Terra are not easily explained. While conclusive evidence for this regional discrepancy is elusive, we offer several possible explanations assuming that the observation is real and not solely an artifact of the current CRISM FRT spatial coverage. One hypothesis is that the concentration around the main Martian basins (Argyre, Hellas, Isidis, and Utopia) is not coincidental and that the reported central peaks are excavating ejecta from these basins, potentially from the Martian mantle. Another possibility is that the regions outside of our listed sites are regions of heavy alteration, so that unaltered central peaks are no long observed there. This option is unlikely due to the correlation of the observations in the Crater Exposed Bedrock Database [Tornabene et al., 2010] which are based on morphology and not composition. A third possibility is that the regions without reported observations have lower abundance of well-exposed crustal bedrock. For instance, the lack of exposed mafics at southern mid-latitudes (30°S-60°S) may be due to mantling deposits covering the bedrock [Mustard et al., 2001]. This would explain the lack of observations to the south of Argyre and Hellas Basin and toward the polar regions. One final hypothesis is that the bedrock exposures we are describing are not globally distributed. It could be that the textures and morphologies we are documenting are

plutonic in origin and that we are observing the excavated remnants of large but localized volcanic plumes occurring below places like the North Argyre and North Hellas areas. Future mapping and additional understanding of the observed lithologies may help decide between these hypotheses.

Lithology Determination. Lithologic determination of the measured mafic regions in this study mirror the effort described in Chapter 1. Each of the central peaks has exposed blocks of olivine and/or pyroxene-bearing material with little evidence of spectral mixing. The olivine-bearing units are interpreted as dunites (though they are spectrally indistinguishable from olivine-plagioclase bearing troctolites) with a composition range from strongly fayalitic to moderately forsteritic. The pyroxene bearing units are interpreted as orthopyroxenites (again spectrally indistinguishable from a pyroxene-plagioclase bearing norite) with the NP exposures displaying a slight enrichement in Ca.

Crustal Formation. The complex cratering history of Mars makes it difficult to reconstruct the original stratigraphy of the exposed units, however only a few mechanisms are known to segregate mafic lithologies at kilometer scales. These include dunite channels in harzburgite as seen in ophiolites [Kelemen et al., 1995] and olivine deposition from komatiite surface flows [Walter, 1998] or melt fractionation of basin induced impact melts [Warren et al., 1996]. The first example has only been observed as a product of terrestrial plate tectonics in mid-ocean ridges, a feature not observed or expected on Mars. The second example would be unlikely to produce mineralogically segregated units thousands of meters thick as observed. The third option is viable and would potentially be difficult to distinguish from an internally erupted lava lake. The most commonly observed method for mineral segregation on Earth is a cumulate settling processes forming a layered mafic sequence. These features, well studied in variety of

terrestrial locations from the Bushveld complex in South Africa to the Skaergaard intrusion in Greenland [Cawthorn, 1996] can produce the observed Martian lithologies at the observed scales. One well studied example is the Bushveld Complex in South Africa [Cawthorn, 1996] which we briefly summarized in Figure 20. The Bushveld complex has been divided into four zones from top to bottom, Upper, Main, Critical and Lower. We will specifically focus on the Upper Zone, the one that would be the most likely to be excavated by impacts. This unit contains olivine that ranges from Fo_{63-5}, a similar range observed in the Mars observations presented here. Orthopyroxenes in the Upper zone range from a mg# 60-Mg#30 with most areas having values in the mid 50's mg#. The entire Bushveld complex is depleted in clinopyroxenes, again similar to our presented Mars observations. However, the Bushveld is only illustrative of the process that could have occurred on Mars. The Bushveld is the product of multiple igneous injections of basaltic magma and a complex history that would be impossible to resolve on Mars with current observations.

Several alternative possibilities could explain the observed compositions. These include that the basin forming impacts (Argyre, Hellas, Isidis, Utopia or Borealis [Andrews-Hanna et al., 2008]) excavated the mafic cumulates of the upper mantle. The post-overturn upper mantle predicted by Elkins-Tanton et al., [2005] would be Mg-rich olivine and pyroxene. Our measurements instead show a range of intermediate to low Mg#. Excavation of a stable or partially overturned mantle could produce consistent results but would be unlikely given the gravitational drive of the overturn for the former and the unlikely chance of only sampling the overturned remnants in the latter. Another option that we will explore in detail is the formation of an igneous secondary crust that would fit the modeled constraints of the overturn [Elkins-Tanton et al., 2005] and the crustal observations detailed here. The overturn would result in

diapirs of Mg-rich cumulates buoyantly rising through the early Martian mantle. These diapirs would have formed from the earliest Martian cumulates, dominated by forsterite (Mg_2SiO_4), enstatite ($MgSiO_3$) and potentially garnet. The rising cumulates would experience decompressional melting as the diapir passes the early Martian adiabat forming a partial melt. The initial melting would concentrate on minerals with incompatible elements and the most Fe-rich minerals. Rising diapirs would potentially encounter a proposed garnet-bearing mantle layer [Elkins-Tanton et al., 2005] at ~1050 km, providing a source of Al that would facilitate the eventual crystallization of a plagioclase component commonly observed in younger crusts on Mars [Bandfield et al., 2000]. Early crustal observations are consistent with low HCP and no garnet detections implying the partial melting of the diapirs past the CPX-out phase of 10% at low pressures [Walter, 1998]. The common observation of OPX and olivine suggest a partial melting in the 10-23% range [Parman, 2004]. The resulting melt would be less dense than the rising cumulate diapir and begin its own buoyant ascent to the surface. Current observations cannot distinguish between surface eruptions (Figure 21 Left) forming lava lakes or near surface intrusions (Figure 21 Right) forming the crust with serial magmatism [Longhi et al., 2003]. Observations only require that the magma bodies are large enough to fractionally crystalize into cumulate layers hundreds to thousands of meters thick and be close enough to the surface to be brecciated and excavated by impact craters. This model of crustal formation explains the observed mineralogically segregated lithologies, the Fe-rich but highly fractionated olivine compositions and the regional differences in composition values that are dependent on minor mantle chemical heterogeneities and varying diapir ascension histories. Future work can further refine the compositional determination and build up the spatial record and use this data to develop and test geophysical models of Martian planetary formation.

Conclusions

A planet wide survey of Martian central peaks with well exposed mafic outcrops and CRISM data results in 23 examples of deeply excavated Martian crust. The exposures are grouped into three regions in the Southern Highlands; Northern Argyre, Northern Hellas, Nili Fossae and several sites in the Northern Plains. In each of the exposures we observe olivine and/or pyroxene-bearing outcrops with little spectral evidence of mineral mixing in the VNIR. This indicates that the deep crust is comprised of mineralogically segregated units. Olivine outcrops show a wide range of compositions ranging from strongly fayalitic to moderately forsteritic. Pyroxene outcrops in the Southern Highlands show an enrichment in LCP with the Northern Argyre and Nili Fossae regions being relatively more Mg-rich than the North Hellas sites and the Northern Plains.

The deep crust compositional observations are best explained by a crustal formation model that segregates mafic minerals into cumulate layers. The global distribution of these materials indicates a planetary scale volcanic process. The most reasonable driver of such an event would be the decompression partial melting of rising diapirs of Mg-rich mantle cumulates in an early planetary overturn process. This crustal formation process would result in a compositionally stratified ancient crust that would be brecciated, incorporated with subsequent volcanics and aqueous alteration to create the crust we observe today.

Acknowledgements

We are very grateful for the fine work of the NASA MRO project team and the fine job by the CRISM Science Operations Center (SOC). This work was supported by NASA through a subcontract with the Applied Physics Lab at Johns Hopkins University.

References:

Adams, J.B., (1974), Visible and near-infrared diffuse reflectance: Spectra of pyroxenes as applied to remote sensing of solid objects in the Solar System. *J. Geophys. Res.,* 79, 4829-4836.

Andrews-Hanna, J.C. et al., (2008), The Borealis basin and the origin of the martian crustal dichotomy. Nature, 453, 1212-1215, doi:10.1038/nature007011.

Bandfield et al. (2000), A Global view of Martian Surface Compositions from MGS-TES. *Science,* 287, 1626, DOI: 10.1126/science.287.5458.1626.

Baratoux et al., (2011), Thermal history of Mars inferred from orbital geochemistry of volcanic provinces. *Nature*, 475, 7355, 254.

Bibring et al. (1989), Results from the ISM experiment. *Nature*, 341, 591-593, doi:10.1038/341591a0.

Bibring et al., (2006), Global Mineralogical and Aqueous Mars History Derived from OMEGA/Mars Express Data. *Science*, 312, 400, doi:10.1126/science.1122659.

Bertka, C.M. and Y. Fei (1997), Mineralogy of the Martian interior up to core-mantle boundary pressures. *J. Geophys. Res.,* 102, B3 5251-5264.

Borg, L.E and D.S. Draper (2003), A petrogenetic model for the origin and compositional variation of the martian basaltic meteorites. *Met. & Planet. Sci*. 38, 1713-1731.

Burns, R.G., (1970), Crystal field spectra and evidence of cation ordering in olivine minerals, *Am. Mineral*., 55, 1608-1632.

Burns, R.G., (1974), The polarized spectra of iron in silicates: Olivine a discussion of neglected contributions from Fe2+ ions in M(1) sites, *Am. Mineral*., 59, 625-629.

Burns, R. G. (1993), *Mineralogical Applications of Crystal Field Theory*, 2nd ed., 551 pp., Cambridge University Press, Cambridge.

Cawthorn, R.G. (ed.) (1996) *Layered Intrusions*. Elsevier, Amsterdam, Netherlands.

Christensen, P.R. et al., (1992), Thermal emission spectrometer experiment – Mars Observer mission. *J. Geophys. Res.*, 97,E5, 7719-7734.

Cloutis, E. A., M. J. Galley, T. L. Jackowski, and R. L. Reed (1986), Calibrations of phase abundance, composition, and particle size distributions for olivine-orthopyroxene mixtures from reflectance spectra, *J. Geophys. Res.*, 91, pp. 11,641-11,653.

Cloutis, E.A., Gaffey, M.J. (1991), Pyroxene spectroscopy revisited: Spectral composition corrwlations and relationship to geothermometry. *J. Geophys. Res.*, 96, 22809-22826.

Debaille, V., Brandon, A.D., Yin, Q.Z., and B. Jacobsen, (2007), Coupled ^{142}Nd-^{143}Nd evidence for a protracted magma ocean in Mars. *Nature*, 450, 525-528, doi:10.1038/nature06317.

Debaille, V., Brandon, A.D., O'Neill, C.O., Yin, Q.-Z., and B. Jacobsen (2009), Early martian mantle overturn inferred from isotopic composition of nakhlite meteorites. *Nature Geosci.*, 2, 548-552.

Ehlmann, B. L., et al. (2009), Identification of hydrated silicate minerals on Mars using MRO-CRISM: Geologic context near Nili Fossae and implications for aqueous alteration, *J. Geophys. Res.*, 114, E00D08, doi:10.1029/2009JE003339.

Elkins-Tanton, L. T., Hess, P.C., and E. M Parmentier (2005), Possible formation of ancient crust on Mars through magma ocean processes. *J. Geophys. Res*., 110, E12S01, doi:10.1029/2005JE002480.

Fassett, C.I. and J.W. Head III (2005), Fluvial sedimentary deposits on Mars: Ancient deltas in a crater lake in the Nili Fossae region. GRL, 32, L14201, doi:10.1029/2005GL023456.

Gaffey, S. J., (1986), Spectral reflectance of carbonate minerals in the visible and near-infrared (0.35-2.55 microns): Calcite, aragonite, and dolomite, *Am. Mineral*., 71, 151-162.

Head et al., (2002) Northern lowlands of Mars: Evidence for widespread volcanic flooding and tectonic deformation in the Hesperian Period. *J. Geophys. Res.*, 107, E1, 5003.

Hiroi, T. and S. Sasaki (2001), Importance of space weathering simulation products in compositional modeling of asteroids: 349 Dembowska and 449 Aeternitas as examples. Met. Planet. Sci., 36, 1587-1596.

Hoefen et al., (2003), Discovery of Olivine in the NiliFossae Region of Mars. Science, 302, 627, DOI:10.1126/science.1089647.

Isaacson, P.J. and C.M. Pieters (2010), Deconvolution of lunar olivine reflectance spectra: Implications for remote compositional assessment. *Icarus*, 210, 1, 8-13.

Isaacson, P. J., et al. (2011), Remote compositional analysis of lunar olivine-rich lithologies with Moon Mineralogy Mapper (M3) spectra, *J. Geophys. Res.*, 116, E00G11, doi:10.1029/2010JE003731.

Jones et al., (2011), A geomorphic analysis of Hale crater, Mars : The effects of impact into ice-rich crust. Icarus. 211, 259-272.

Kanner, L. C., J. F. Mustard, A. Gendrin (2007), Assessing the limits of the Modified Gaussian Model for remote spectroscopic studies of pyroxenes on Mars. *Icarus* 187 442-456, doi:10.1016/j.icarus.2006.10.025 14.

Kelemen et al. (1995), Extraction of mid-ocean-ridge basalt from the upwelling mantle by focused flow of melt in dunite channels. *Nature*. 375, 747-753.

Koeppen, W. C., and V. E. Hamilton (2008), Global distribution, composition, and abundance of olivine on the surface of Mars from thermal infrared data. *J. Geohpys. Res.,* 113, E05001.

Lapen et al. (2010), A Younger Age for ALH84001 and Its Geochemical Link to Shergottite Sources in Mars. Science, 328, 347-351.

Longhi, J., A new view of lunar ferroan anorthosites: Post magma ocean petrogenesis, J. Geophys. Res., 108(E8), 5083,doi:10.1029/2002JE001941, 2003.

Malin, M. C., et al. (2007), Context Camera Investigation on board the Mars Reconnaissance Orbiter, *J. Geophys. Res.,* 112, E05S04, doi:10.1029/2006JE002808.

Mangold, et al. (2008), Identification of a new outflow channel on Mars in Syrtis Major Planum using HRSC/MEx data. Planet & Sp. Sci., 56, 1030-1042.

McEwen et al. (2007), Mars Reconnaissance Orbiter's High Resolution Imaging Science Experiment (HiRISE). *J. Geophys. Res.*, **112**, E05S02, doi:10.1029/2005JE002605.

McGuire, et al., (2009), An improvement to the volcano-scan algorithm for atmospheric correction of CRISM and OMEGA spectral data. *Planet. Space Sci.*, 57, 809-815.

McSween, H. Y. (2002), The rocks of Mars, from far and near. *Met. Planet. Sci*., 37, 7-25.

McSween, H. Y., et al. (2006), Characterization and petrologic interpretation of olivine-rich basalts at Gusev Crater, Mars,J. Geophys. Res., 111, E02S10, doi:10.1029/2005JE002477.

Mittlefehldt, D. W., (1994), ALH84001, a cumulate orthopyroxenite member of the martian meteorite clan. *Meteoritics*. 29, 214-221.

Melosh (1989), *Impact cratering: A geologic process.* Oxford University Press.

Murchie, S., et al. (2007), Compact Reconnaissance Imaging Spectrometer for Mars (CRISM) on Mars Reconnaissance Orbiter (MRO). *J. Geophys. Res*., 112, E05S03, doi:10.1029/2006JE002682.

Mustard, J. F., and J. M. Sunshine (1995), Seeing through the dust: Martian crustal heterogeneity and links to the SND meteorites, *Science*, 267, 1623–1626, doi:10.1126/science.7886449.

Mustard et al., (2001) Evidence for recent climate change on Mars from the identification of youthful near-surface ground ice. Nature, 412, 6845, 411-414.

Mustard et al. (2005), Olivine and Pyroxene Diversity in the Crust of Mars. *Science*, 307, 1594 doi: 10.1126/science.1109098.

Mustard et al. (2007), Mineralogy of the Nili Fossae region with OMEGA/Mars Express data: 1. Ancient impact melt in the Isidis Basin and implications for the transition from the Noachian to Hesperian. *J. Geophys. Res.*, 112, E08S03, doi:10.1029/2006JE002834.

Mustard, J.F. et al., (2008), Hydrated silicate minerals on Mars observed by the Mars Reconnaissance Orbiter CRISM instrument. *Nature.* 454, 305-309.

Mustard, J. F., B. L. Ehlmann, S. L. Murchie, F. Poulet, N. Mangold, J. W. Head, J.-P. Bibring, and L. H. Roach (2009), Composition, Morphology, and Stratigraphy of Noachian Crust around the Isidis basin, *J. Geophys. Res.*, 114, E00D12, doi:10.1029/2009JE003349.

Neumann, G. A., M. T. Zuber, M. A. Wieczorek, P. J. McGovern, F. G. Lemoine, and D. E. Smith (2004), Crustal structure of Mars from gravity and topography, *J. Geophys. Res.*, 109, E08002, doi:10.1029/2004JE002262.

Nyquist, L.E., Bogard D. D., Shih C-Y., Greshake A., Stoffler, D., and O. Eugster (2001), Ages and geologic histories of martian meteorites. *Space Sci. Rev.*, 96, 105-164.

Pan, C. and D. Rogers (2011), Thermal infrared study of central uplifts of Martian impact craters. AGU Fall Meeting P31D-1721.

Parman, S.W. and T.L. Grove (2004), Harzburgite melting with and without H2O: Experimental data and predictive modeling. *J. Geophys. Res.*, 109, B02201, doi:10.1029/2003JB002566.

Pelkey, S. M., et al. (2007), CRISM multispectral summary products: Parameterizing mineral diversity on Mars from reflectance, *J. Geophys. Res.*, 112, E08S14, doi:10.1029/2006JE002831.

Poulet, F., J.-P. Bibring, Y. Langevin, J. F. Mustard, N. Mangold, M. Vincendon, B. Gondet, P. Pinet, J.-M. Bardintzeff, and B. Platevoet (2009), Quantitative compositional analysis of Martian mafic regions using MEx/OMEGA reflectance data: 1. Methodology, uncertainties and examples of application, *Icarus*, 201, 69–83.

Rogers, A. D., and P. R. Christensen (2007), Surface mineralogy of Martian low-albedo regions from MGS-TES data:Implications for upper crustal evolution and surface alteration, *J. Geophys. Res.*, 112, E01003, doi:10.1029/2006JE002727.

Ruff, S. W., and P. R. Christensen, (2002) Bright and dark regions on Mars: Particle size and mineralogical characteristics basedon Thermal Emission Spectrometer data, *J. Geophys. Res.*, 107(E12), 5127, doi:10.1029/2001JE001580.

Ruff, S. W., and P. R. Christensen (2007), Basaltic andesite, altered basalt, and a TES-based search for smectite clay minerals on Mars, *Geophys. Res. Lett.,* 34(L10204), doi:10.1029/2007GL02960

Salvatore, M. R., J. F. Mustard, M. B. Wyatt, and S. L. Murchie (2010), Definitive evidence of Hesperian basalt in Acidalia and Chryse planitiae, *J. Geophys. Res.,* 115, E07005, doi:10.1029/2009JE003519.

Squyres, S. W., et al. (2004), The Spirit Rovers Athena Science Investigation at Gusev Crater, Mars. *Science*, 305, 794, DOI: 10.1126/science.3050794.

Skok, J. R., J. F. Mustard, S. L. Murchie, M. B. Wyatt, and B. L. Ehlmann (2010), Spectrally distinct ejecta in Syrtis Major, Mars: Evidence for environmental change at the Hesperian-Amazonian boundary, *J. Geophys. Res.*, 115, E00D14, doi:10.1029/2009JE003338.

Sunshine, J.M., Pieters, C.M., and S.F. Pratt (1990), Deconvolution of mineral absorption bands: An improved approach. *J. Geophys. Re*s., 95, 6955-6966.

Sunshine, J.M. and C.M. Pieters (1993), Estimating modal abundances from modified from spectra of natural and laboratory pyroxene mixtures using the modified Gaussian model. *J. Geophys. Res*., 98, 9075-9087.

Sunshine, J.M. and C.M. Pieters (1998), Determining the composition of olivine from reflectance spectroscopy. *J. Geophys. Res*., 103, 13675-13688.

Taylor, S. R. (1992), Solar System Evolution: A New perspective, 307 pp., Cambridge Univ. Press, New York.

Tornabene et al. (2010), A crater-exposed bedrock database for Mars with applications for determining the composition and structure of the upper crust. 41st LPSC, Houston, TX.

Walter, M.J. (1998), Meeting of Garnet Peridotite and the Origin of Komatiite and Depleted Lithosphere. *J. Petrology*, 39, 1, 29-60.

Warren, P.H. (1990), Lunar Anorthosites and the Magma-Ocean Plagioclase-Flotation Hypotheses: Importance of Feo Enrichment in the Parent Magma. *Am. Min*., 75, 46-58.

Warren, P. H., Claeys, P., and Cedillo-Pardo, E., (1996), Mega-impact melt petrology (Chicxulub, Sudbury, and the Moon): Effects of scale and other factors on potential for fractional crystallization and development of cumulates, *in* Ryder, G., Fastovsky, D., and

Gartner, S., eds., The Cretaceous-Tertiary Event and Other Catastrophes in Earth History: Boulder, Colorado, Geological Society of America Special Paper 307.

Wilde et al. (2001), Evidence from detrital zircons for the existence of continental crust and oceans on the Earth 4.4 Gyr ago. *Nature*, 409, 175-178.

Wood, J.A., Dickey, J.S., Marvin, U.B., Powell, B.N., (1970), Lunar anorthosites and a geophysical model of the Moon. *Proc. Apollo 11 Lunar Sci. Conf.* 1, 965–988, 16.

Wyatt, M.B. and H.Y. McSween (2002), Spectral evidence for weathered basalt as an alternative to andesite in the northern lowlands of Mars. *Nature*, 417, 263-266.

Tables

Table 1: Details from each of the central peak structures reported in this study. Column Key: Code: Central peak designation for this project. Letters refer to region, NA: North Argyre, NH: North Hellas, NF: Nili Fossae, NP: Northern Plains. Number is based on analysis order. Name: Name of crater where available, **bold** name indicates that the examined cater is an unnamed crater within the larger named crater in bold. CRISM_ID: Is a concatenation of CRISM FRT information as: Obs Year_Obs Day_Obs Hexidecimal ID. Longitude has positive values going east. Diameter is the average diameter of the observed crater. Olivine and Pyroxene are marked if that mineral has been modeled at that site.

Code	Name	CRISM ID	Latitude	Longitude	Diameter	Olivine	Pyroxene
NA1	Alga Crater	2007_167_6415	-24.34	-26.65	18	O	P
NA2	Ostrov Crater	2010_099_17D02	-26.51	-28.09	70	O	P
NA3	Hale Crater	2009_066_117BC	-35.58	-36.43	130	O	P
NA4	**Ladon Basin**	2008_018_97FF	-16.71	-28.14	22	O	P
NA5	**Kasimov Crater**	2008_186_B5BE	-24.93	-22.78	7	O	-
NA6		2009_042_10FE8	-31.41	-16.66	37	-	P
NH1		2009_042_C2A5	-25.78	34.42	39	-	P
NH2		2008_032_9BCF	-24.26	43.47	22	-	P
NH3		2008_248_C554	-18.74	62.63	50	O	P
NH4		2009_231_147FB	-21.53	44.75	42	O	P
NH5		2011_173_1EB32	-19.32	64.03	31	-	P
NH6		2011_176_1EBA0	-31.43	81.63	20	O	P
NH7		2010_086_177F9	-6.23	93.63	26	-	P
NH8		2007_286_82E8	-15.75	96.87	35	O	P
NH9		2008_245_C4D0	-31.29	108.67	73	-	P
NF1	Hargraves	2008_185_B573	20.76	75.81	62	O	P
NF2		2009_044_110B7	20.22	69.42	50	O	P
NP1	Kunowsky Crater	2008_013_9610	56.86	-9.23	62	O	P
NP2		2010_127_18A06	52.64	15.24	25	O	P
NP3		2008_242_C417	59.84	135.80	30	O	-
NP4		2008_232_C16F	55.58	139.65	26	O	-
NP5	Stokes Crater	2008_155_ADA4	55.65	171.35	63	O	P
NP6		2010_093_17AA1	66.42	144.06	29	O	-

Table 2A: Summary of Modeled Olivine Composition Results. Region; Number of modeled spectra in the region; Range of modeled values; Mean modeled composition of all regions; Standard deviation of modeled compositions. Table summarizes full results in Table 3.

Region	# Regions	Fo# Range	Fo# Mean	Fo# S.D.
NA Olivine	18	7-70	34	23
NH Olivine	15	8-38	18	7
NF Olivine	6	5-14	10	4
NP Olivine	87	7-58	32	15

Table 2B. Summary of Modeled Pyroxene Composition Results. Region; Number of modeled spectra in the region; Mean 1 µm NBSR values; Standard deviation of 1 µm NBSR values; Mean

2 μm NBSR values; Standard deviation of 2 μm NBSR values. Table summarizes full results in Table 4.

Region	# of Regions	1 μm NBSR Mean	1 μm NBSR S.D.	2 μm NBSR	2 μm NBSR S.D.
NA Pyroxene	32	0.65	0.14	0.62	0.09
NH Pyroxene	46	0.56	0.09	0.60	0.07
NF Pyroxene	12	0.55	0.08	0.59	0.02
NP Pyroxene	30	0.46	0.07	0.54	0.09

Table 3. List of Modeled Olivine Regions, Bandcenters and Compositions. Column 1:Region ID Region:Region#:ROI #, 2: Olivine M1-1 band, 3: Olivine M2 band, 4:Olivine M1-2 band, 5: Olivine least squares fit composition calculated from M1-1, M2, and M1-2 bands, 6: Least squares fitting error for three band fit, 7: Olivine least squares fit composition for M2 and M1-2 bands, 8: Absolute difference between 3 band and 2 band compositions.

North Argyre Olivine Unit	M1-1	M2	M1-2	3-Band Comp (Fo#)	Comp Fitting Error	2-Band Comp (Fo#)	Comp Difference
NA1_1	877	1046	1257	45	160	46	1
NA1_2	899	1072	1282	16	3	15	1
NA1_3	889	1063	1290	18	270	11	7
NA1_4	901	1069	1298	7	172	2	5
NA1_5	902	1069	1293	9	87	6	3
NA1_6	897	1067	1289	14	91	10	3
NA1_7	902	1067	1285	14	43	14	0
NA1_8	900	1079	1281	14	44	13	1
NA1_9	896	1064	1276	22	26	23	1
NA2_1	843	1035	1264	59	1408	44	15
NA2_2	836	1035	1254	68	1172	53	15
NA2_3	838	1031	1251	70	1123	56	13
NA2_4	837	1034	1263	63	1653	45	18
NA4_1	900	1080	1268	20	190	23	3
NA4_2	897	1080	1279	16	86	14	2

NA5_1	835	1040	1258	65	1340	47	18
NA5_2	891	1053	1263	34	135	38	4
NA5_3	874	1048	1247	51	62	53	2

North Hellas Olivine Unit	M1-1	M2	M1-2	3-Band Comp (Fo#)	Comp Fitting Error	2-Band Comp (Fo#)	Comp Difference
NH3_1	895	1074	1294	10	151	4	7
NH3_2	899	1075	1285	13	20	11	2
NH3_3	898	1080	1281	14	82	12	3
NH3_4	899	1080	1281	14	74	12	2
NH4_1	903	1077	1269	20	144	24	4
NH4_2	899	1080	1280	15	71	13	1
NH4_3	899	1081	1279	15	82	13	2
NH4_4	899	1081	1279	15	84	13	1
NH4_5	901	1078	1279	14	47	14	0
NH4_6	897	1088	1276	16	292	13	3
NH4_7	891	1078	1269	25	123	23	2
NH6_1	907	1073	1289	8	5	8	0
NH8_1	888	1065	1252	38	97	42	4
NH8_2	905	1075	1260	24	341	32	8
NH8_3	917	1083	1243	25	1653	43	18

Nili Fossae Olivine Unit	M1-1	M2	M1-2	3-Band Comp (Fo#)	Comp Fitting Error	2-Band Comp (Fo#)	Comp Difference
NF1_1	900	1080	1280	14	67	13	1
NF2_1	904	1075	1293	7	26	4	3
NF2_2	900	1082	1295	5	124	-1	6
NF2_3	899	1080	1280	14	76	13	2
NF2_4	901	1079	1280	14	52	13	1
NF2_5	898	1083	1296	6	183	-1	7

Northern Plains Olivine Unit	M1-1	M2	M1-2	3-Band Comp (Fo#)	Comp Fitting Error	2-Band Comp (Fo#)	Comp Difference
NP1_1	861	1039	1263	51	661	43	8
NP1_2	873	1045	1263	44	285	41	3
NP1_3	887	1055	1266	34	78	35	1
NP1_4	855	1039	1257	57	587	48	8
NP1_5	856	1040	1254	58	466	50	7
NP1_6	867	1044	1246	56	106	56	0
NP1_7	879	1051	1244	50	82	55	5
NP1_8	866	1044	1260	49	355	44	5
NP1_9	870	1041	1252	52	246	52	0
NP1_10	887	1052	1262	36	122	39	3
NP1_11	867	1034	1251	56	436	56	0
NP1_12	883	1050	1261	39	121	41	1
NP1_13	881	1048	1260	41	173	42	1
NP1_14	863	1037	1251	57	360	55	2
NP1_15	866	1039	1248	57	252	56	0
NP1_16	874	1044	1240	56	141	61	5
NP1_17	899	1061	1273	23	78	27	3
NP2_1	900	1068	1286	14	34	12	1
NP2_2	889	1062	1285	21	198	15	5
NP2_3	896	1076	1291	11	114	5	6
NP3_1	874	1059	1298	21	1107	6	16
NP3_2	885	1062	1291	19	419	10	9
NP3_3	905	1071	1282	13	9	15	2
NP3_4	898	1070	1295	9	148	4	6
NP3_5	903	1074	1284	12	1	11	0
NP3_6	898	1074	1287	13	31	10	3
NP3_7	899	1079	1283	13	57	11	3
NP3_8	895	1077	1292	10	142	4	7
NP3_9	871	1061	1301	21	1378	3	18
NP3_10	888	1069	1303	10	607	-2	12

NP4_1	874	1051	1278	34	511	26	8
NP4_2	862	1049	1279	39	953	25	14
NP4_3	858	1043	1270	47	861	36	12
NP4_4	863	1047	1273	43	709	32	11
NP4_5	886	1064	1263	33	1	33	0
NP4_6	871	1047	1258	47	181	45	3
NP4_7	887	1074	1293	15	337	4	10
NP5_1	896	1063	1272	24	23	26	2
NP5_2	892	1058	1269	29	73	31	2
NP5_3	888	1062	1268	30	9	30	1
NP5_4	870	1043	1250	53	164	53	0
NP5_5	901	1065	1249	34	441	45	11
NP5_6	894	1067	1256	33	139	38	6
NP5_7	894	1055	1260	34	150	40	6
NP5_8	897	1080	1279	16	93	14	2
NP5_9	896	1061	1262	30	82	35	5
NP5_10	901	1069	1270	21	53	25	4
NP5_11	899	1079	1280	15	56	13	2
NP5_12	898	1080	1280	15	81	13	2
NP5_13	901	1063	1262	28	187	35	8
NP5_14	898	1071	1276	19	2	20	1
NP5_15	898	1076	1277	17	34	17	1
NP5_16	896	1064	1243	40	435	50	11
NP5_17	879	1043	1237	56	253	64	8
NP5_18	901	1058	1246	37	547	50	13
NP5_19	890	1055	1261	35	90	39	4
NP5_20	899	1065	1268	25	64	29	5
NP5_21	904	1064	1265	24	169	32	7
NP6_1	857	1049	1290	36	1770	17	19
NP6_2	878	1076	1314	7	1478	-14	21
NP6_3	864	1058	1299	26	1691	5	20
NP6_4	873	1065	1308	15	1512	-5	20

Table 4. Pyroxene Observation Table. MGM fits of pyroxene spectra. LCP and HCP bandcenters and NBSR were determined by 5 Gaussian modeling. NBSR is calculated from bandstrengths (LCP/(LCP+HCP). 1 and 2 μm bandcenters determined by 3 Gaussian modeling.

North Argyre Pyroxene	1 µm LCP Bandcenter	1 µm LCP Banddepth	1 µm HCP Bandcenter	1 µm HCP Banddepth	1 µm NBSR	2 µm LCP Bandcenter	2 µm LCP Banddepth	2 µm HCP Bandcenter	2 µm HCP Banddepth	2 µm NBSR	1 µm Bandcenter	2 µm Bandcenter
NA1_1	889	-0.11	1075	-0.05	0.67	1760	-0.12	2145	-0.08	0.59	933	1893
NA1_2	886	-0.12	1064	-0.07	0.63	1746	-0.14	2138	-0.10	0.59	938	1884
NA1_3	893	-0.09	1075	-0.05	0.66	1757	-0.10	2152	-0.07	0.59	941	1892
NA1_4	890	-0.11	1075	-0.06	0.64	1751	-0.13	2133	-0.09	0.59	941	1886
NA1_5	889	-0.10	1078	-0.04	0.72	1773	-0.12	2135	-0.08	0.60	922	1896
NA1_6	896	-0.08	1068	-0.06	0.59	1759	-0.14	2131	-0.09	0.60	957	1890
NA1_7	892	-0.10	1080	-0.04	0.71	1769	-0.12	2132	-0.08	0.61	927	1891
NA1_8	893	-0.08	1065	-0.03	0.74	1782	-0.10	2148	-0.07	0.59	916	1909
NA1_9	894	-0.11	1082	-0.06	0.63	1743	-0.13	2129	-0.08	0.61	950	1867
NA2_1	901	-0.23	1099	-0.06	0.79	1801	-0.21	2142	-0.11	0.65	918	1892
NA2_2	899	-0.16	1086	-0.05	0.76	1850	-0.17	2199	-0.08	0.68	898	1912
NA2_3	902	-0.15	1110	-0.05	0.74	1912	-0.26	2528	-0.16	0.62	827	1892
NA2_4	903	-0.16	1103	-0.04	0.80	1839	-0.17	2183	-0.07	0.70	911	1904
NA2_5	896	-0.20	1083	-0.05	0.80	1841	-0.16	2162	-0.07	0.71	916	1911
NA2_6	898	-0.20	1078	-0.07	0.74	1775	-0.19	2168	-0.11	0.63	919	1877
NA2_7	901	-0.10	1151	-0.04	0.71	1936	-0.22	2517	-0.18	0.56	916	2141
NA2_8	891	-0.22	1078	-0.03	0.86	1834	-0.16	2142	-0.05	0.77	902	1887
NA2_9	920	-0.15	1077	-0.02	0.88	1894	-0.12	2299	0.00	1.00	981	1979
NA2_10	900	-0.15	1141	-0.02	0.89	1908	-0.25	2563	-0.21	0.54	805	1875
NA3_1	905	-0.02	1082	0.00	0.84	1779	-0.06	2164	-0.03	0.64	921	1882
NA4_1	920	-0.08	1075	-0.03	0.70	1809	-0.09	2200	-0.07	0.56	957	1954
NA4_2	913	-0.07	1084	-0.03	0.67	1792	-0.07	2192	-0.06	0.56	961	1941
NA4_3	906	-0.06	1088	-0.05	0.54	1783	-0.08	2181	-0.07	0.56	997	1932
NA6_1	904	-0.02	1080	-0.03	0.46	1872	-0.04	2285	-0.03	0.58	994	1991
NA6_2	921	-0.02	1074	-0.03	0.46	1850	-0.05	2236	-0.03	0.61	1005	1964
NA6_3	919	-0.02	1075	-0.02	0.47	1850	-0.04	2232	-0.03	0.59	1005	1987
NA6_4	923	-0.06	1120	-0.07	0.49	1744	-0.10	2165	-0.07	0.59	999	1876
NA6_5	916	-0.05	1112	-0.05	0.50	1762	-0.08	2158	-0.06	0.60	990	1890
NA6_6	899	-0.02	1081	-0.02	0.41	1906	-0.03	2340	-0.04	0.47	994	2100
NA6_7	920	-0.05	1115	-0.05	0.51	1792	-0.07	2180	-0.04	0.62	994	1901
NA6_8	906	-0.07	1105	-0.09	0.46	1735	-0.13	2150	-0.10	0.57	1021	1919
NA6_9	915	-0.03	1088	-0.04	0.47	1749	-0.07	2155	-0.05	0.57	1001	1892

North Hellas Pyroxene	1 µm LCP Bandcenter	1 µm LCP Banddepth	1 µm HCP Bandcenter	1 µm HCP Banddepth	1 µm NBSR	2 µm LCP Bandcenter	2 µm LCP Banddepth	2 µm HCP Bandcenter	2 µm HCP Banddepth	2 µm NBSR	1 µm Bandcenter	2 µm Bandcenter
NH1_1	957	-0.07	1183	-0.06	0.54	1761	-0.10	2222	-0.08	0.57	1014	1939
NH1_2	948	-0.07	1192	-0.09	0.44	1749	-0.11	2177	-0.07	0.61	1098	1955
NH1_3	930	-0.05	1109	-0.07	0.42	1756	-0.11	2193	-0.10	0.52	1016	1955
NH1_4	921	-0.01	1060	-0.02	0.35	1837	-0.06	2208	-0.04	0.59	1010	1957
NH2_1	920	-0.08	1075	-0.03	0.70	1809	-0.09	2200	-0.07	0.56	957	1954
NH2_2	913	-0.07	1084	-0.03	0.67	1792	-0.07	2192	-0.06	0.56	961	1941
NH2_3	906	-0.06	1088	-0.05	0.54	1783	-0.08	2181	-0.07	0.56	997	1932
NH3_1	918	-0.04	1073	-0.03	0.54	1827	-0.08	2216	-0.07	0.54	983	1984
NH3_2	905	-0.05	1082	-0.05	0.54	1800	-0.11	2180	-0.09	0.56	986	1952
NH3_3	900	-0.06	1085	-0.05	0.57	1782	-0.10	2165	-0.08	0.56	978	1935
NH3_4	909	-0.06	1083	-0.05	0.56	1803	-0.11	2184	-0.08	0.56	983	1953
NH3_5	907	-0.06	1083	-0.05	0.55	1796	-0.11	2192	-0.09	0.54	989	1958
NH3_6	907	-0.01	1084	-0.02	0.38	1811	-0.03	2239	-0.02	0.58	1015	1977
NH3_7	906	-0.02	1079	-0.04	0.40	1804	-0.07	2215	-0.06	0.56	1025	1950
NH3_8	894	-0.03	1086	-0.03	0.47	1845	-0.09	2242	-0.07	0.56	989	1984
NH3_9	898	-0.02	1060	-0.02	0.54	1859	-0.07	2235	-0.06	0.55	965	2004
NH3_10	905	-0.06	1085	-0.05	0.53	1793	-0.10	2182	-0.08	0.56	991	1945
NH3_11	900	-0.07	1080	-0.06	0.52	1781	-0.09	2180	-0.08	0.55	991	1941
NH3_12	895	-0.06	1081	-0.05	0.54	1784	-0.09	2183	-0.08	0.55	980	1945
NH3_13	913	-0.03	1083	-0.01	0.71	1869	-0.06	2246	-0.05	0.55	932	2008
NH3_14	910	-0.03	1069	-0.01	0.68	1879	-0.05	2255	-0.04	0.56	935	2013
NH3_15	901	-0.06	1084	-0.05	0.53	1782	-0.10	2176	-0.08	0.56	988	1933
NH4_1	912	-0.04	1080	-0.04	0.52	1814	-0.06	2219	-0.04	0.60	993	1927
NH4_2	904	-0.06	1097	-0.05	0.51	1784	-0.06	2199	-0.04	0.61	978	1893
NH4_3	893	-0.05	1089	-0.05	0.51	1784	-0.08	2195	-0.05	0.62	994	1892
NH4_4	925	-0.05	1069	-0.02	0.70	1868	-0.08	2219	-0.06	0.60	956	1982
NH4_5	777	-0.07	1023	-0.07	0.47	1813	-0.09	2256	-0.07	0.55	955	1997
NH4_6	854	-0.08	1203	-0.06	0.57	1961	-0.11	2467	-0.04	0.74	957	1984
NH4_7	901	-0.01	1082	-0.01	0.57	1859	-0.03	2283	-0.02	0.56	847	1993

NH5_1	922	-0.07	1128	-0.04	0.64	1851	-0.08	2190	-0.03	0.71	960	1917
NH5_2	921	-0.06	1121	-0.03	0.64	1844	-0.06	2192	-0.03	0.69	960	1919
NH5_3	917	-0.06	1101	-0.03	0.69	1861	-0.06	2180	-0.03	0.69	952	1937
NH5_4	903	-0.02	1079	-0.02	0.56	1900	-0.03	2301	0.00	0.86	992	1961
NH5_5	911	-0.04	1080	-0.01	0.73	1866	-0.04	2275	-0.02	0.71	937	1924
NH5_6	921	-0.07	1129	-0.05	0.56	1809	-0.06	2183	-0.05	0.58	982	1936
NH5_7	915	-0.04	1088	-0.05	0.47	1811	-0.07	2191	-0.05	0.56	996	1956
NH5_8	920	-0.04	1095	-0.03	0.62	1896	-0.05	2236	-0.02	0.75	967	1950
NH5_9	923	-0.05	1104	-0.03	0.61	1850	-0.04	2207	-0.02	0.65	976	1947
NH6_1	900	-0.03	1087	-0.03	0.48	1872	-0.02	2291	-0.01	0.73	970	2011
NH7_1	901	-0.01	1080	-0.01	0.60	1900	-0.04	2300	-0.02	0.66	971	1977
NH8_1	910	-0.05	1086	-0.03	0.60	1937	-0.03	2279	-0.02	0.60	937	2010
NH8_2	873	-0.04	1075	-0.04	0.49	1949	-0.03	2329	-0.04	0.46	996	2171
NH9_1	853	-0.08	1010	-0.09	0.47	1753	-0.24	2224	-0.19	0.56	923	1335
NH9_2	857	-0.08	1062	-0.03	0.70	1817	-0.13	2344	-0.11	0.56	882	1341
NH9_3	923	-0.08	1022	-0.03	0.75	1724	-0.14	2159	-0.11	0.55	938	1340
NH9_4	912	-0.09	1031	-0.05	0.62	1812	-0.15	2274	-0.12	0.55	952	1335

Nili Fossae Pyroxene	1 µm LCP Bandcenter	1 µm LCP Banddepth	1 µm HCP Bandcenter	1 µm HCP Banddepth	1 µm NBSR	2 µm LCP Bandcenter	2 µm LCP Banddepth	2 µm HCP Bandcenter	2 µm HCP Banddepth	2 µm NBSR	1 µm Bandcenter	2 µm Bandcenter
NF1_1	854	-0.08	1019	-0.05	0.61	1750	-0.11	2104	-0.08	0.57	894	1886
NF1_2	891	-0.06	1064	-0.04	0.61	1755	-0.09	2121	-0.06	0.58	947	1897
NF1_3	795	-0.07	1038	-0.06	0.54	1787	-0.09	2304	-0.06	0.63	866	1886
NF1_4	856	-0.08	1044	-0.06	0.56	1769	-0.09	2190	-0.07	0.58	928	1922
NF1_5	896	-0.09	1095	-0.04	0.69	1754	-0.09	2168	-0.07	0.56	943	1920
NF1_6	879	-0.08	1071	-0.05	0.62	1769	-0.10	2166	-0.07	0.58	948	1918
NF2_1	922	-0.03	1110	-0.04	0.42	1794	-0.06	2229	-0.04	0.60	1063	1898
NF2_2	922	-0.08	1141	-0.07	0.52	1734	-0.10	2137	-0.07	0.60	1039	1818
NF2_3	909	-0.04	1078	-0.03	0.59	1781	-0.07	2179	-0.06	0.56	969	1934
NF2_4	920	-0.03	1064	-0.02	0.56	1771	-0.06	2194	-0.05	0.57	969	1911
NF2_5	940	-0.07	1168	-0.09	0.44	1769	-0.09	2203	-0.06	0.61	1156	1828
NF2_6	906	-0.03	1097	-0.04	0.43	1816	-0.04	2236	-0.03	0.62	1045	1946

Northern Plains Pyroxene	1 µm LCP Bandcenter	1 µm LCP Banddepth	1 µm HCP Bandcenter	1 µm HCP Banddepth	1 µm NBSR	2 µm LCP Bandcenter	2 µm LCP Banddepth	2 µm HCP Bandcenter	2 µm HCP Banddepth	2 µm NBSR	1 µm Bandcenter	2 µm Bandcenter
NP1_1	918	-0.04	1118	-0.05	0.46	1762	-0.06	2192	-0.04	0.59	1012	1880
NP1_2	917	-0.06	1131	-0.06	0.48	1736	-0.08	2173	-0.06	0.59	1017	1882
NP1_3	911	-0.02	1075	-0.04	0.40	1789	-0.06	2201	-0.05	0.55	1012	1946
NP1_4	920	-0.02	1063	-0.02	0.48	1814	-0.06	2201	-0.04	0.58	988	1945
NP1_5	913	-0.02	1083	-0.03	0.41	1767	-0.05	2206	-0.04	0.59	1017	1882
NP1_6	907	-0.01	1087	-0.02	0.36	1774	-0.04	2215	-0.03	0.62	1032	1878
NP1_7	913	-0.03	1103	-0.05	0.37	1745	-0.09	2170	-0.06	0.60	1035	1876
NP1_8	913	-0.02	1084	-0.04	0.38	1786	-0.07	2181	-0.05	0.58	1026	1921
NP1_9	911	-0.02	1091	-0.03	0.42	1782	-0.06	2176	-0.04	0.57	1020	1923
NP2_1	877	-0.10	1068	-0.11	0.48	1939	-0.06	2302	-0.11	0.36	967	2194
NP2_2	900	-0.04	1079	-0.03	0.53	1904	-0.05	2279	-0.06	0.42	972	2141
NP2_3	908	-0.04	1076	-0.05	0.46	1901	-0.07	2318	-0.12	0.37	984	2208
NP2_4	874	-0.08	1084	-0.09	0.46	2004	-0.06	2377	-0.13	0.34	958	2287
NP2_5	906	-0.03	1077	-0.02	0.59	1897	-0.03	2321	-0.08	0.29	920	2267
NP5_1	918	-0.04	1118	-0.05	0.46	1762	-0.06	2192	-0.04	0.59	1012	1880
NP5_2	917	-0.06	1131	-0.06	0.48	1736	-0.08	2173	-0.06	0.59	1017	1882
NP5_3	911	-0.02	1075	-0.04	0.40	1789	-0.06	2201	-0.05	0.55	1012	1946
NP5_4	920	-0.02	1063	-0.02	0.48	1814	-0.06	2201	-0.04	0.58	988	1945
NP5_5	913	-0.02	1083	-0.03	0.41	1767	-0.05	2206	-0.04	0.59	1017	1882
NP5_6	907	-0.01	1087	-0.02	0.36	1774	-0.04	2215	-0.03	0.62	1032	1878
NP5_7	913	-0.03	1103	-0.05	0.37	1745	-0.09	2170	-0.06	0.60	1035	1876
NP5_8	913	-0.02	1084	-0.04	0.38	1786	-0.07	2181	-0.05	0.58	1026	1921
NP5_9	911	-0.02	1091	-0.03	0.42	1782	-0.06	2176	-0.04	0.57	1020	1923
NP5_10	920	-0.03	1112	-0.04	0.48	1758	-0.07	2160	-0.05	0.59	1012	1886
NP5_11	914	-0.03	1097	-0.04	0.43	1756	-0.07	2167	-0.05	0.61	1017	1877
NP5_12	909	-0.01	1073	-0.01	0.53	1824	-0.06	2241	-0.05	0.55	980	1969
NP5_13	902	-0.01	1079	-0.01	0.52	1899	-0.03	2301	-0.02	0.53	987	2052
NP5_14	905	-0.11	1097	-0.08	0.56	1745	-0.16	2142	-0.12	0.57	940	1907
NP5_15	917	-0.06	1088	-0.05	0.53	1807	-0.12	2206	-0.10	0.55	1002	1969
NP5_16	912	-0.03	1082	-0.02	0.60	1784	-0.06	2184	-0.04	0.57	967	1922

Figure Captions

Figure 1. Planetary Formation Model. The best accepted model of Martian crustal formation combines our understanding of lunar formation, modeling of mineral crystallization and isotopic constraints from Martian meteorites. A) Initial formation began with solar system condensation and accretion of meteoritic material. B) Energy from impacts and differentiation would melt silicates forming a deep magma ocean and the segregation of metallic core. C) Crystallization of the magma ocean would begin with Mg-enriched olivine and later pyroxenes that would be denser than the melt and forming a cumulate pile at the bottom of the magma ocean and result in an increasingly Fe-rich magma. D) Crystallization would end with Fe-rich olivine and pyroxenes above a garnet layer stable at depths of 1050 km. The water content of the magma would tend to suppress plagioclase formation. E) The mineral crystallization sequence would create a density inversion that would be corrected with an overturn that is likely to be continuous with the crystallization of the Fe-enriched minerals. The displacement of the Mg-rich minerals toward stratigraphically higher regions with lower pressure would result in decompression partial melting. The final stages of this process, occurring after the majority of the magma ocean has crystalized, would extrude on the ancient Martian surface and form the bulk of the martian crust. (Based on Debaille et al., [2009] and Elkins-Tanton et al., [2005])

Figure 2. Map of Analyzed Sites. Twenty-three sites have spectra of unaltered mafic materials that can be modeled with the MGM. The result of this selection process is a natural grouping in four general regions, North Argyre (NA), North Hellas (NH), Nili Fossae (NF) and Northern

Plains (NP). Red marks have only olivine outcrops, green symbols have only pyroxene outcrops, black symbols have both olivine and pyroxene outcrops. (MOLA background).

Figure 3. MGM Example. A) MGM run on laboratory Olivine with Fo_{96} (Relab sample: C3PO53). Left top) RMS error between the observed spectra and modeled fit. Left Middle) Three olivine absorptions with fitted positions, widths, and strengths. Initial positions, depths and widths are listed in Table 1**.** Left Bottom) Olivine spectra (cross hatched points) with fit (black line) and curved continuum (thin black line). B) MGM run on laboratory Pyroxene (Relab Sample: c1xp23). Right top) RMS error between the observed spectra and modeled fit. Right middle) Five absorptions with fitted positions, widths, and strengths. Right Bottom) Pyroxene spectra (cross hatched points) with fit (black line) and curved continuum (thin black line).

Figure 4. North Argyre example region. Inset) Ladon Basin context with arrow pointing to crater that contains this central pit structure. A) NA4 is one of the few sites that have a central pit. (CTX) B) Mineral map showing mafic deposits on central pit structure. (CRISM FRT00097FF Parameter Map R:Olindex2 G:LCPindex B:HCPindex on CTX)

Figure 5. NA4 Spectra Top) Ratioed Olivine Spectra. Bottom) Ratioed Pyroxene Spectra

Figure 6. North Hellas example region. A) NH6 is a classic central peak structure with a ring of light-toned olivine and a peak of pyroxene-bearing material. B) CRISM Projected RGB. Observation is 10 km across at center. R:2.5 μm G:1.5 μm B:1 μm (FRT0001EBA0) C)

CRISM projected mineral map showing mafic deposits on central pit structure. CRISM Parameter Map R:Olindex2 G:LCPindex B:HCPindex. From CRISM: FRT0001EBA0.

Figure 7. NH6 Spectra Top) Ratioed Olivine Spectra. Bottom) Ratioed Pyroxene Spectra. From CRISM: FRT0001EBA0.

Figure 8. Nili Fossae example region. A) NF1 CTX overview of Hargraves crater. B) CRISM projected mineral map showing mafic deposits on central pit structure. Observation is 10 km across at center. R:Olindex2 G:LCPindex B:HCPindex C) CRISM Projected RGB. R:2.5 μm G:1.5 μm B:1 μm (FRT0000B573).

Figure 9. NF1 Spectra Top) Ratioed Olivine Spectra. Bottom) Ratioed Pyroxene Spectra. From CRISM: FRT0000B573.

Figure 10. Northern Plains example region. A) NP5 Context image of Stokes Crater (CTX) B) CTX view of central peak. Light-toned small clasts in upper right are classic olivine-bearing breccias. Lower right light material are olivine bearing particulate material not used for olivine analysis. C) CRISM projected mineral map showing mafic deposits on central pit structure. Observation is 10 km across at center. R:Olindex2 G:LCPindex B:HCPindex (CRISM FRT0000ADA4) D) CRISM projected RGB. R:2.5 μm G:1.5 μm B:1 μm (CRISM FRT0000ADA4)

Figure 11. NP5 Top) Light-toned olivine-bearing breccias exposed in the depression just east of the Stokes Crater center. Bottom) Pyroxene-bearing bedrock material exposed north of the Stokes Crater center. HiRISE: ESP_016980_2360

Figure 12. NP5 Spectra Top) Ratioed Olivine Spectra. Poor registration from the S detector are unable to resolve the 1 μm pyroxene absorption, causing increased error with three band olivine fitting. This is a case when the two band fits would provide more confident results. Bottom) Ratioed Pyroxene Spectra. From CRISM:FRT0000ADA4.

Figure 13. All Outcrop Olivine Distribution. Plot shows the modeled composition for all examined olivine regions. Data in Table 3. Left) Three band fit. Right) M2 and M1-2 band fit. Lower right bar shows limit of expected propagated error of each point.

Figure14. Argyre Olivine Outcrop Distribution. Data in Table 3 Left) Three band fit. Right) M2 and M1-2 band fit. Lower right bar shows limit of propagated error of each point.

Figure15. Hellas Olivine Outcrop Distribution. Data in Table 3 Left) Three band fit. Right) M2 and M1-2 band fit. Lower right bar shows limit of propagated error of each point.

Figure 16. Northern Plains Olivine Outcrop Distribution. Data in Table 3 Left) Three band fit. Right) M2 and M1-2 band fit. Lower right bar shows limit of propagated error of each point.

Figure 17. Pyroxene Bandcenters: 1-, 2 µm bandcenters of all pyroxene regions plotted against terrestrial pyroxene bandcenters [Adams, 1974, Cloutis, 1991] by region. From bottom left to upper right, pyroxene composition goes from Mg-rich to Fe-rich to Ca-rich. Plot of modeled pyroxene bandcenters plotted against terrestrial laboratory measured bandcenters. Significant variation exists on 1 µm axis while 2 µm axis is well modeled. While variation exists in each region, averages vary from low-Fe, low-Ca toward high-Fe, high-Ca in the order of North Argyre, North Hellas, Nili Fossae, and Northern Plains. Data in Table 4.

Figure 18. Pyroxene NBSR. LCP/(LCP+HCP) Band depths. NBSR for all modeled pyroxene observations, colored by region. Significant variance exists on the 1 µm axis while 2 µm NBSR shows regional differences. In order of decreasing LCP, the regions rank North Argyre, North Hellas, Nili Fossae and Northern Plains. Data summarized Table 2 and detailed in Table 4.

Figure 19. Depth Map with crustal thickness: A) Plot Olivine Fo# (Red) and crater excavation depth (blue) as a function of crater thickness (black) [Neumann et al., 2003].

B) Plot Pyroxene NBSR (Red) and crater excavation depth (blue) as a function of crustal thickness (black) with the key below. [Neumann et al., 2003].

1	NH4
2	NH8
3	NH1
4	NH9
5	NH2
6	NH7
7	NA2
8	NA6
9	NH3
10	NA3
11	NF2

12	NH5
13	NA1
14	NA5
15	NF1
16	NA4
17	NP5
18	NH6
19	NP4
20	NP6
21	NP2
22	NP3
23	NP1

Figure 20. Schematic of the Bushveld Layered Igneous Intrusion. Large magma volumes lead to cumulate layering and high fractionation causes a diverse range of mafic compositions [Cawthorn, 1996]. Impact brecciation of the Upper Zone would access fayalite to intermediate olivine-bearing material and moderate-Fe, low-Ca pyroxene-bearing material as observed on Mars.

Figure 21. Proposed model of crustal formation. Bottom) Mantle density instabilities would lead to overturn with rising diapirs of Mg-rich minerals. Decompression melting would preferentially melt the Fe-rich faction which would buoyantly rise faster than the diapir. Large volume eruptions would cool slowly and stratify into cumulate layers. Bottom Left) illustrates magma eruptions as lava lakes. Bottom Right) illustrates pluton cooling/serial magmatism. Top) Extensive cratering would brecciate cumulate layers, mixing and excavating mafic lithologies.

Datasets:

NA:

HiRISE:PSP_006782_1630

CTX:P15_006782_1637_XN_16S028W

CRISM:FRT000097FF

NH:

HiRISE:ESP_016219_1485

CTX:P21_009072_1468_XI_33S278W

CRISM:FRT00001EBA0

NF:

HiRISE:PSP_009639_2010

CTX:P21_009072_2025_XN_22N284W

CRISM:FRT0000B573

NP:

HiRISE:ESP_019604_2360;ESP_018048_2360;ESP_016980_2360

CTX: P20_008686_2356_XN_55N188W;P12_005825_2359_XI_55N188W

CRISM:FRT0000ADA4

Chapter 2, Figure 1

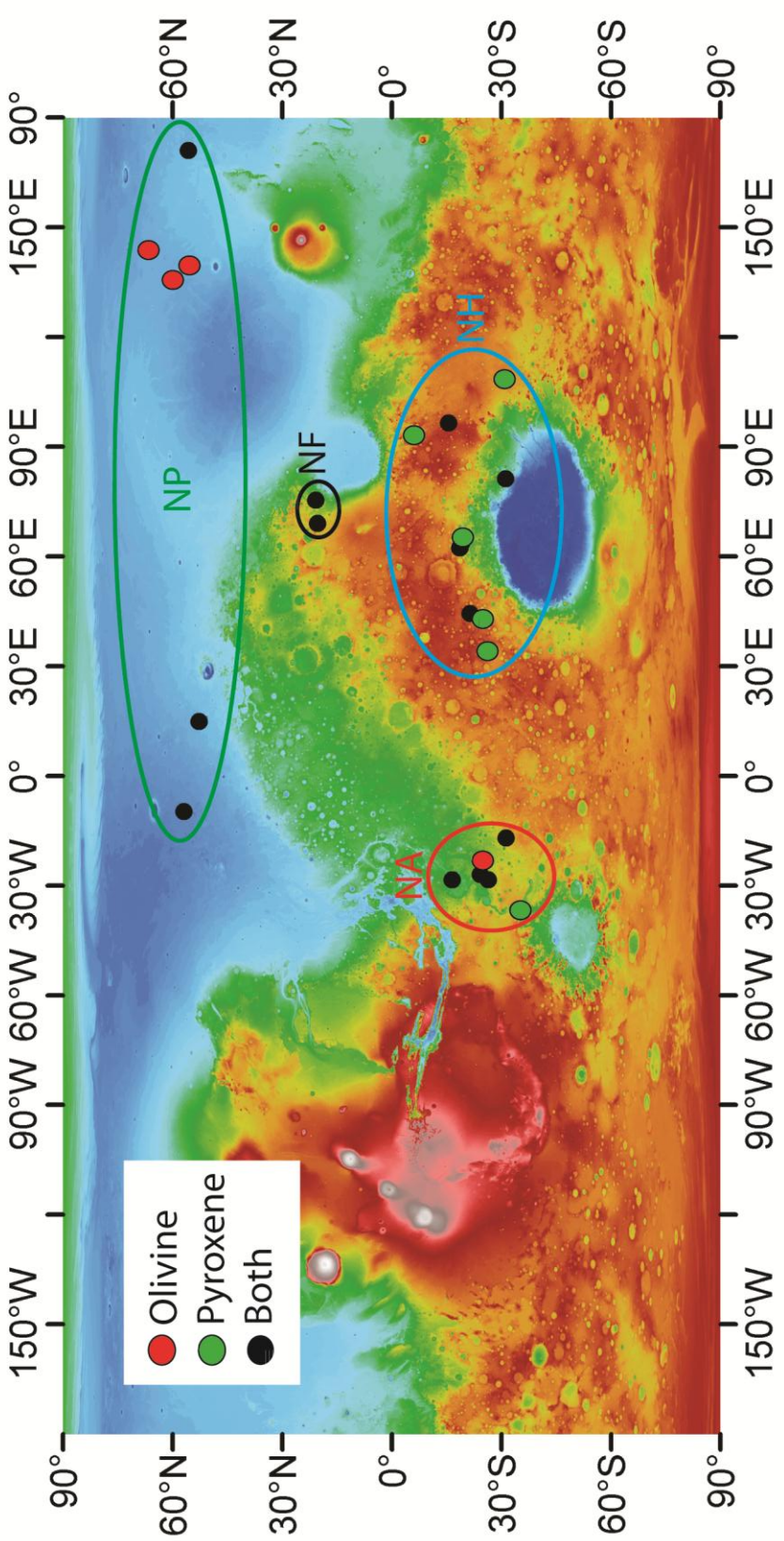

Chapter 2, Figure 2

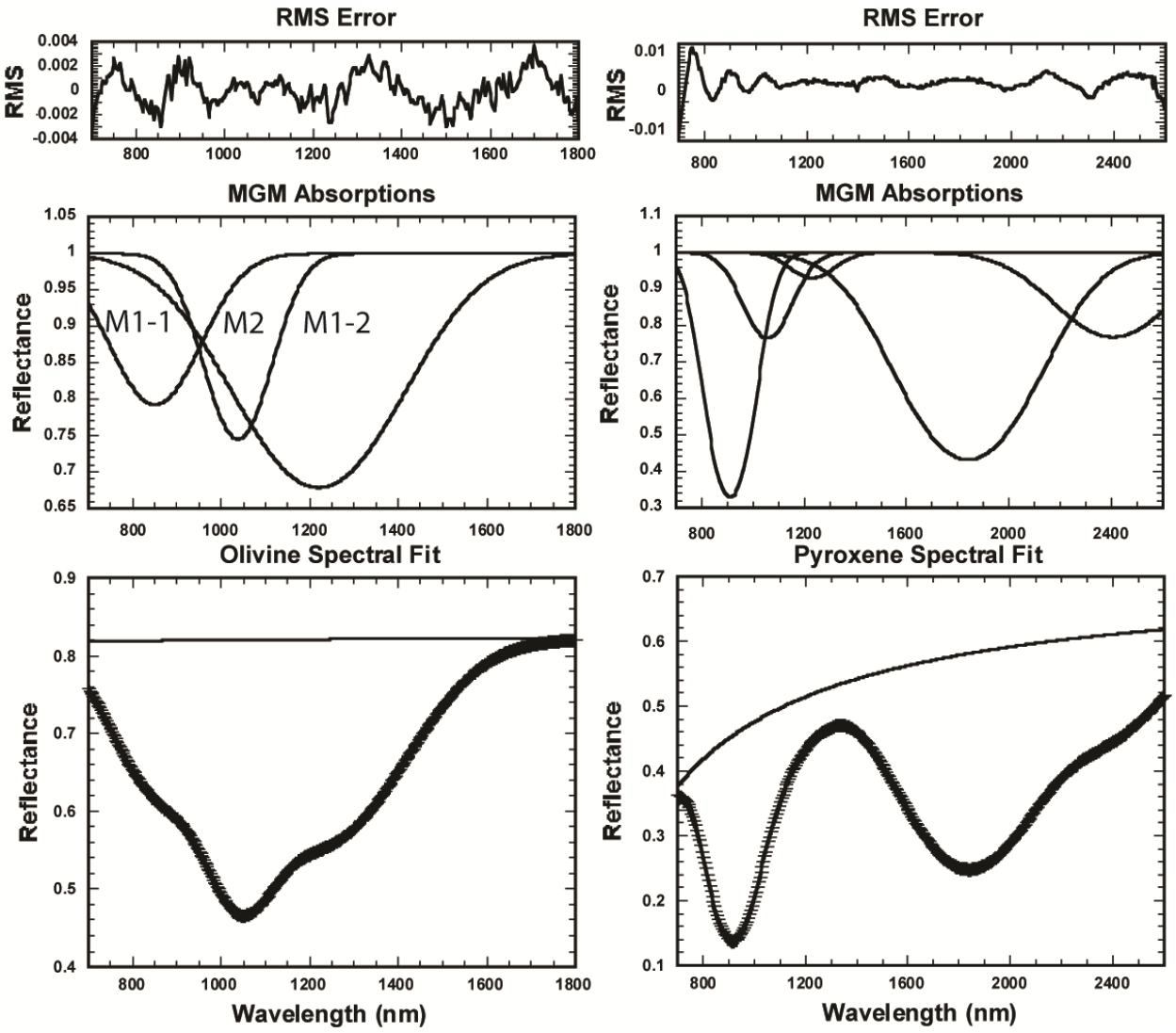

Chapter 2, Figure 3

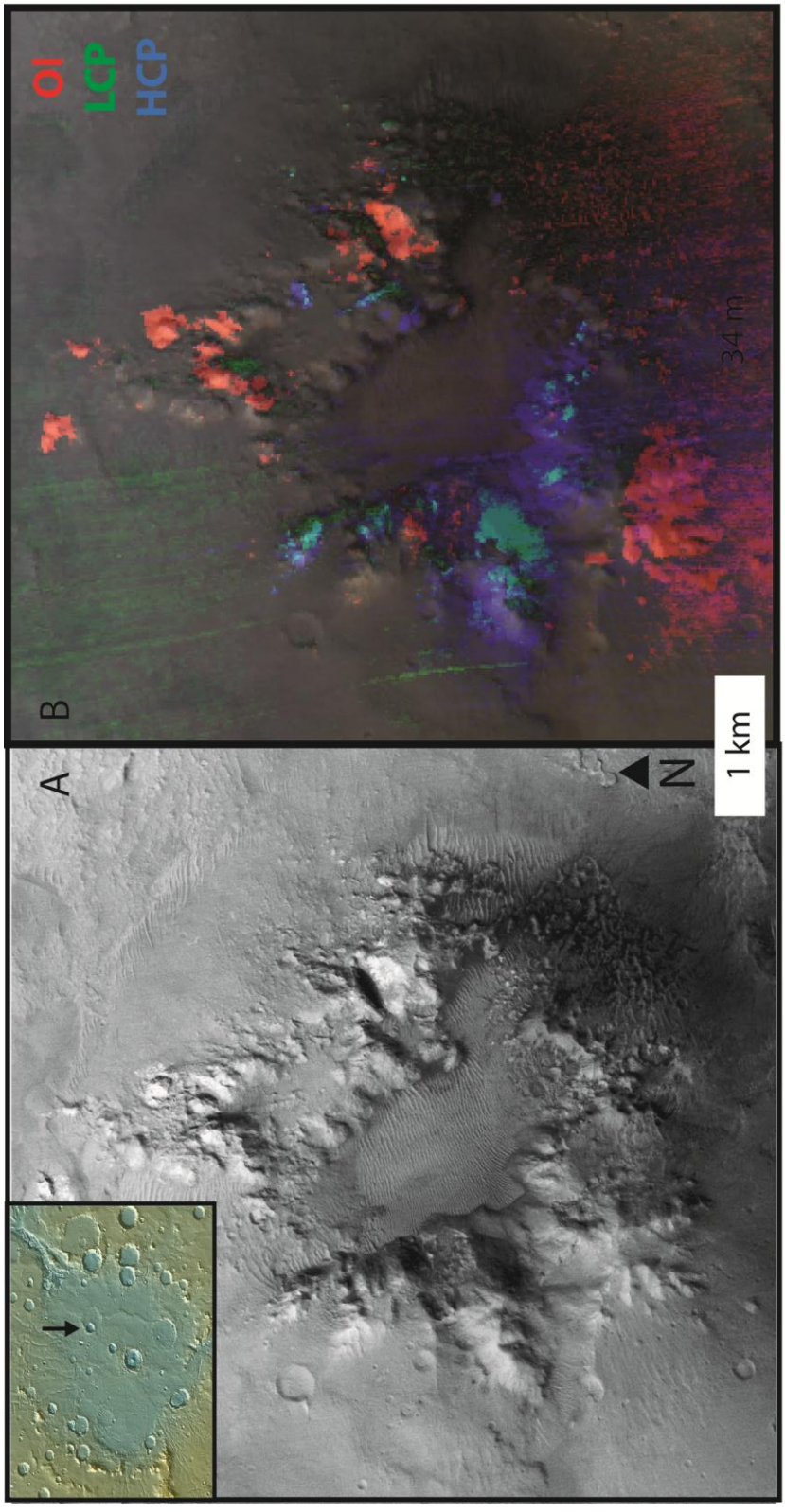

Chapter 2, Figure 4

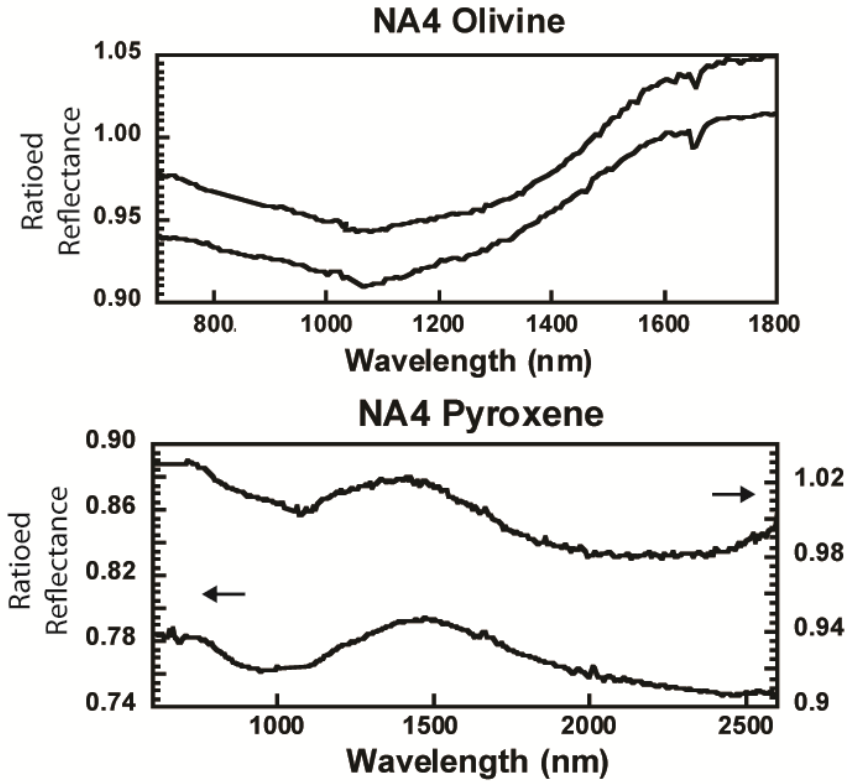

Chapter 2, Figure 5

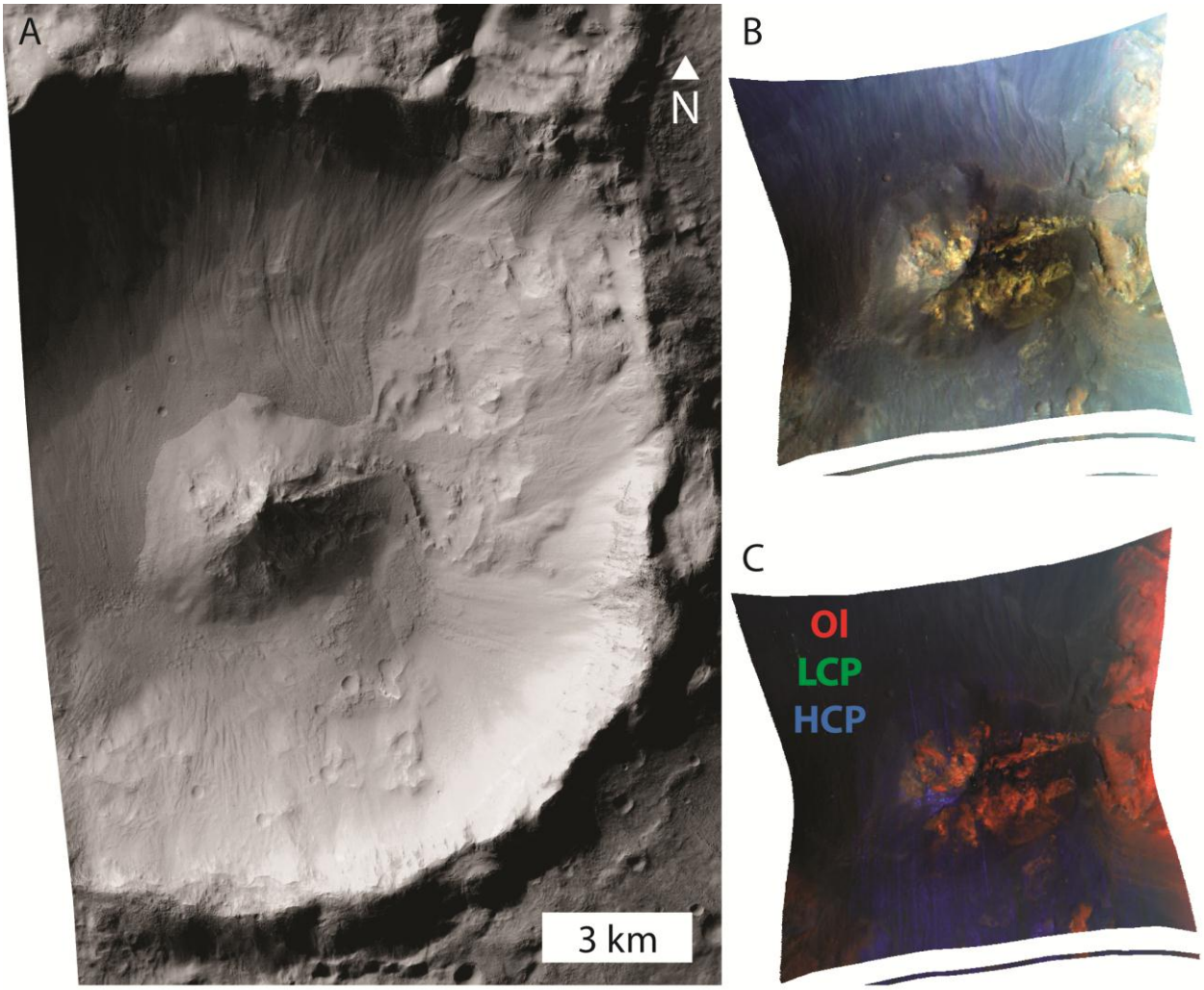

Chapter 2, Figure 6

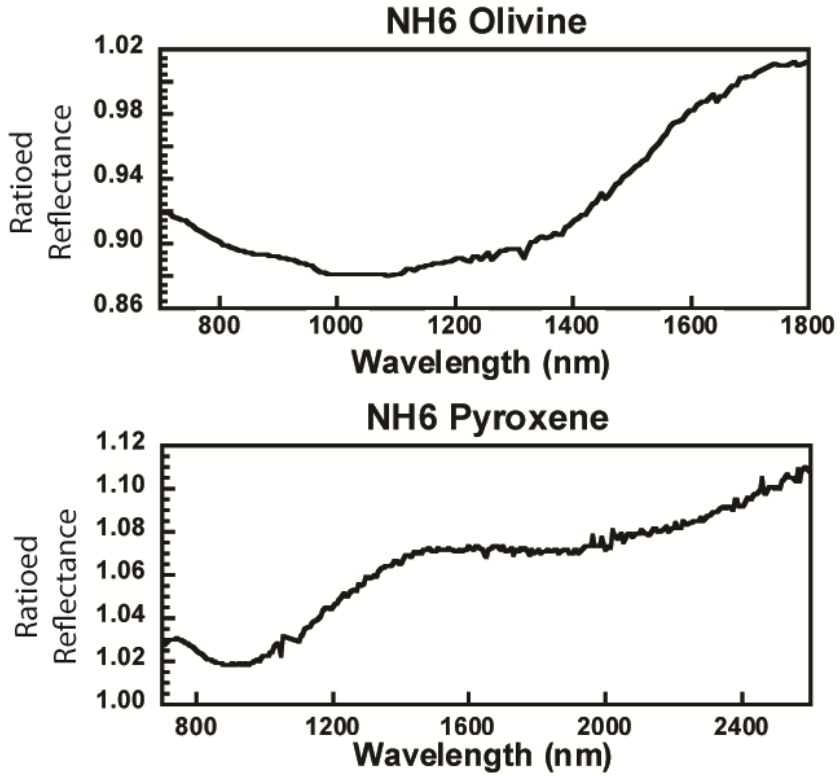

Chapter 2, Figure 7

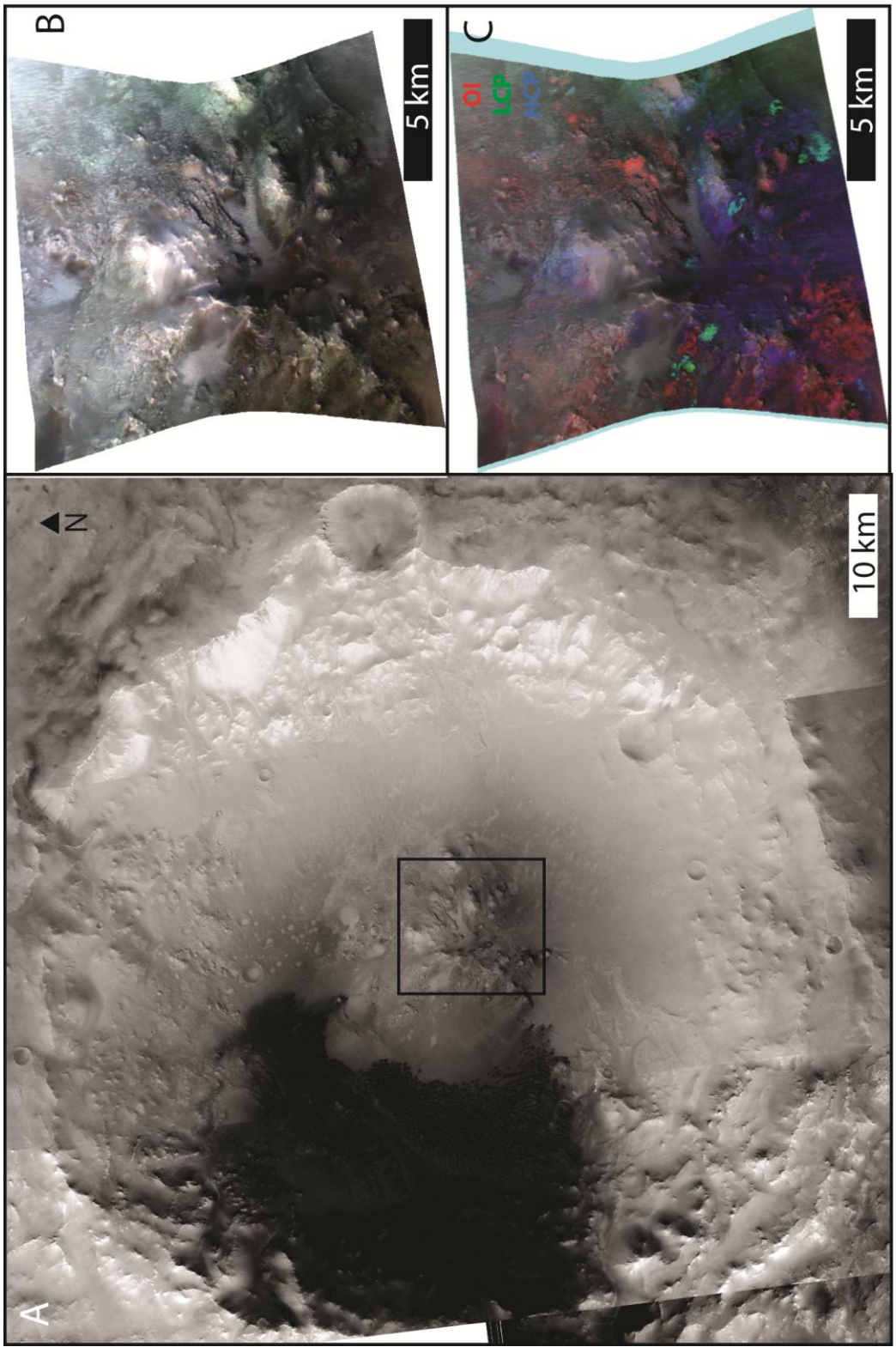

Chapter 2, Figure 8

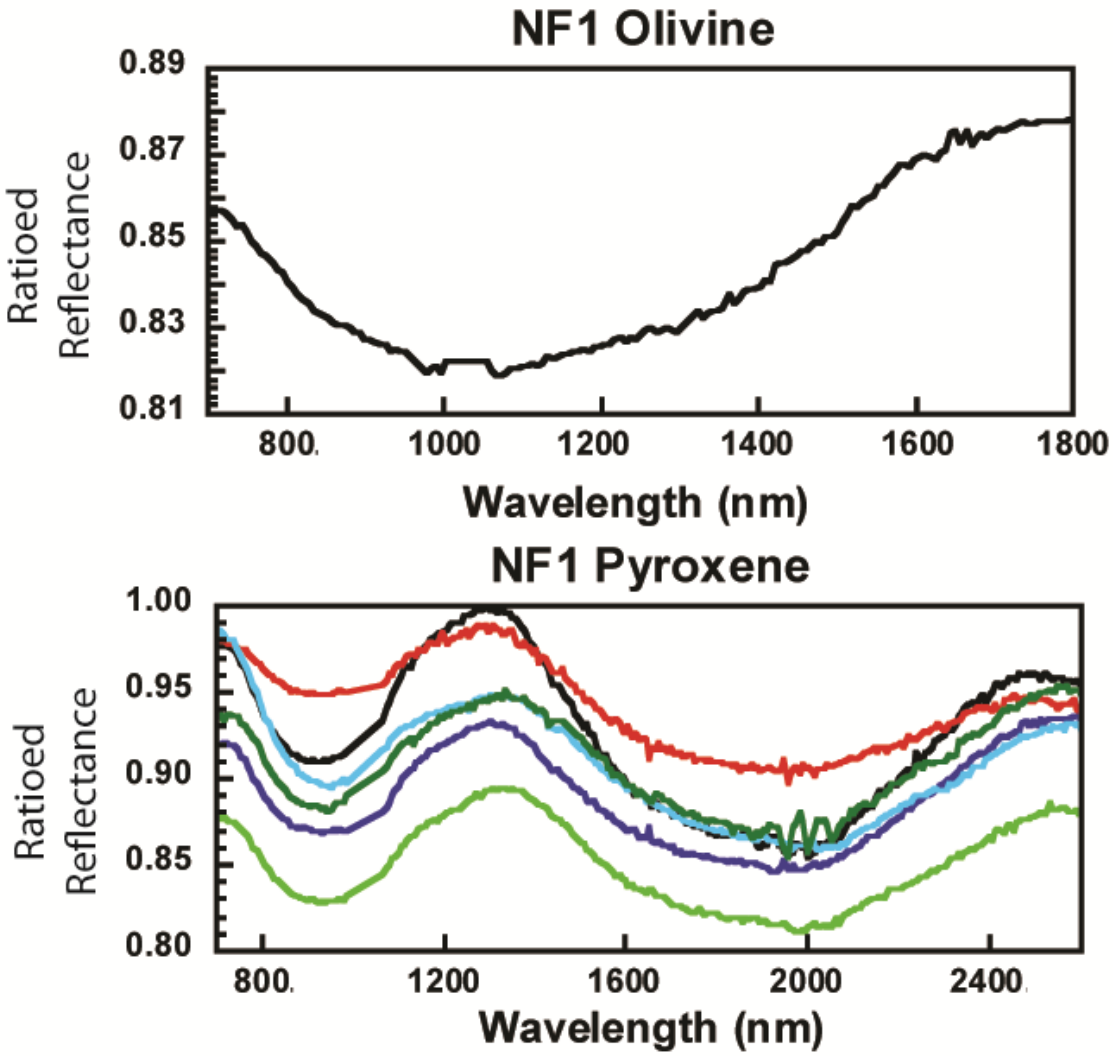

Chapter 2, Figure 9

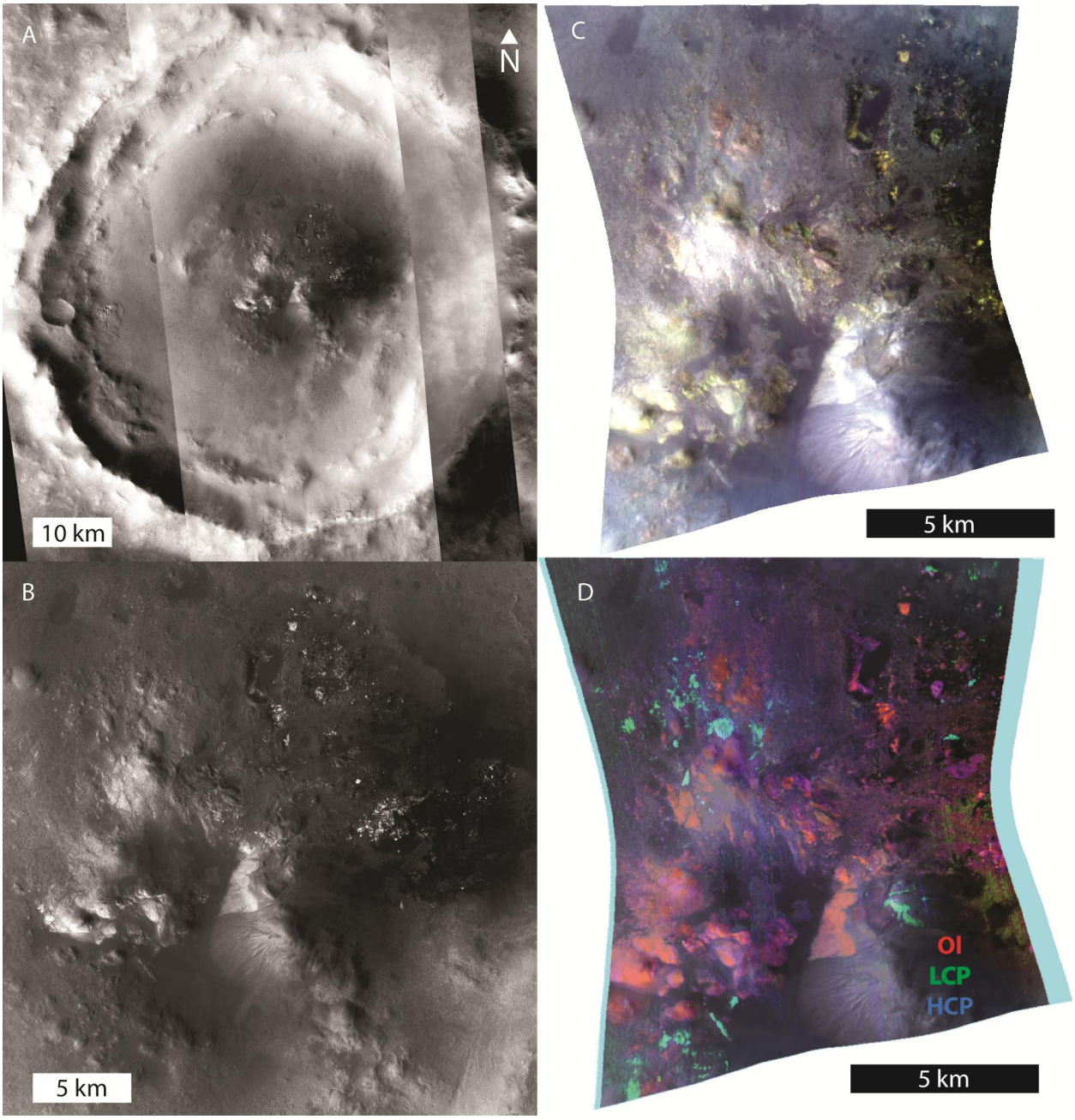

Chapter 2, Figure 10

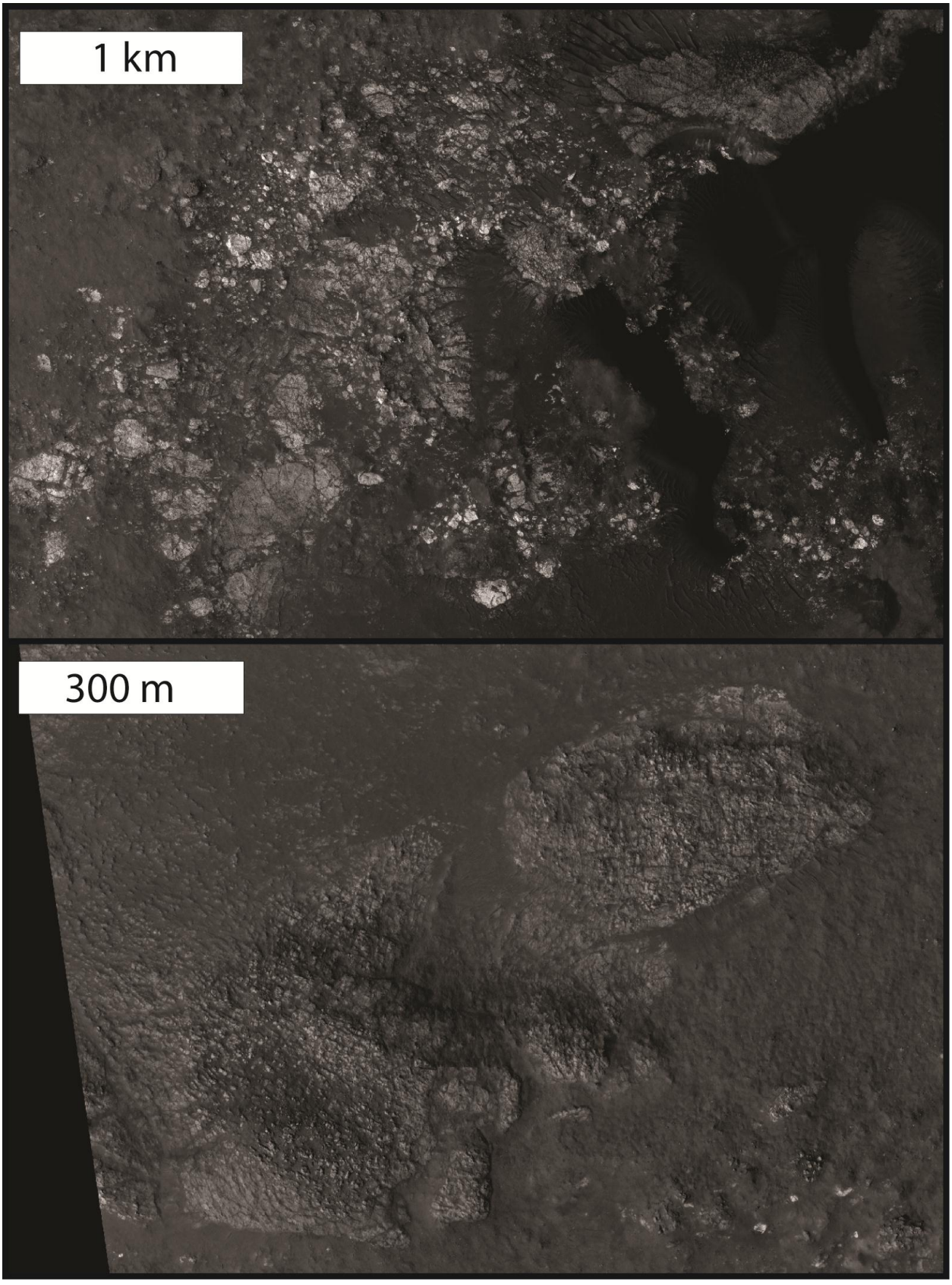

Chapter 2, Figure 11

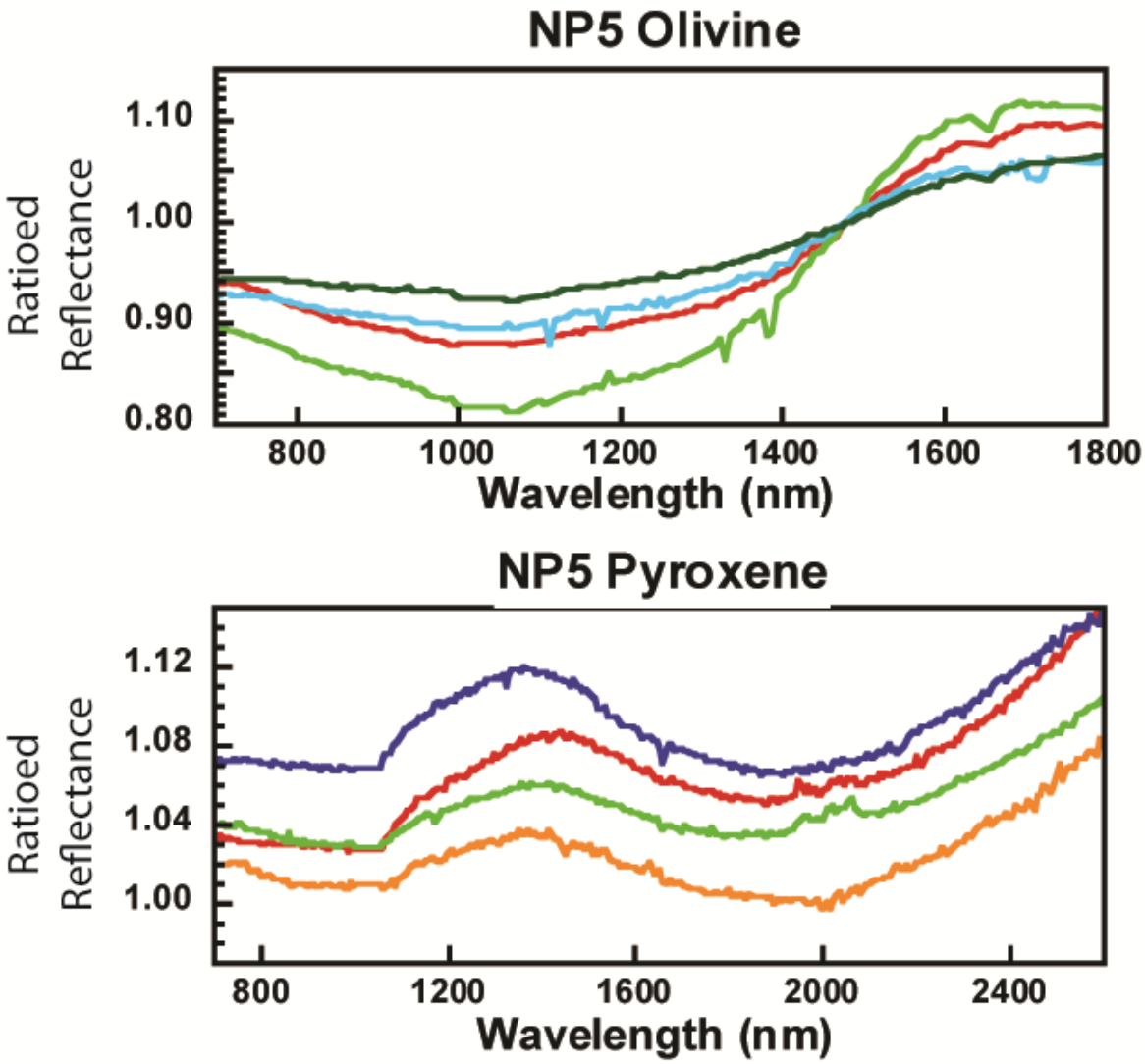

Chapter 2, Figure 12

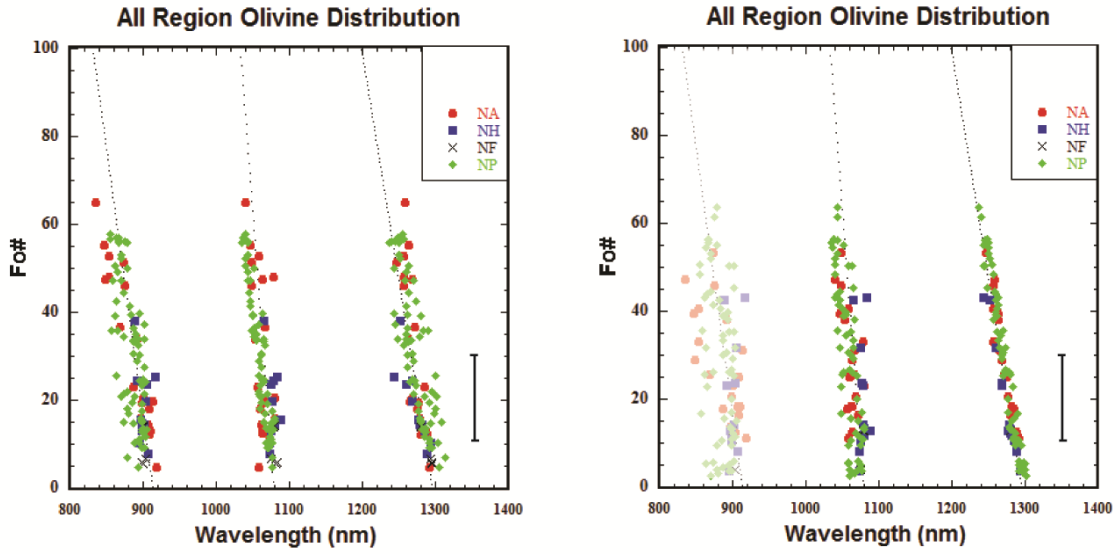

Chapter 2, Figure 13

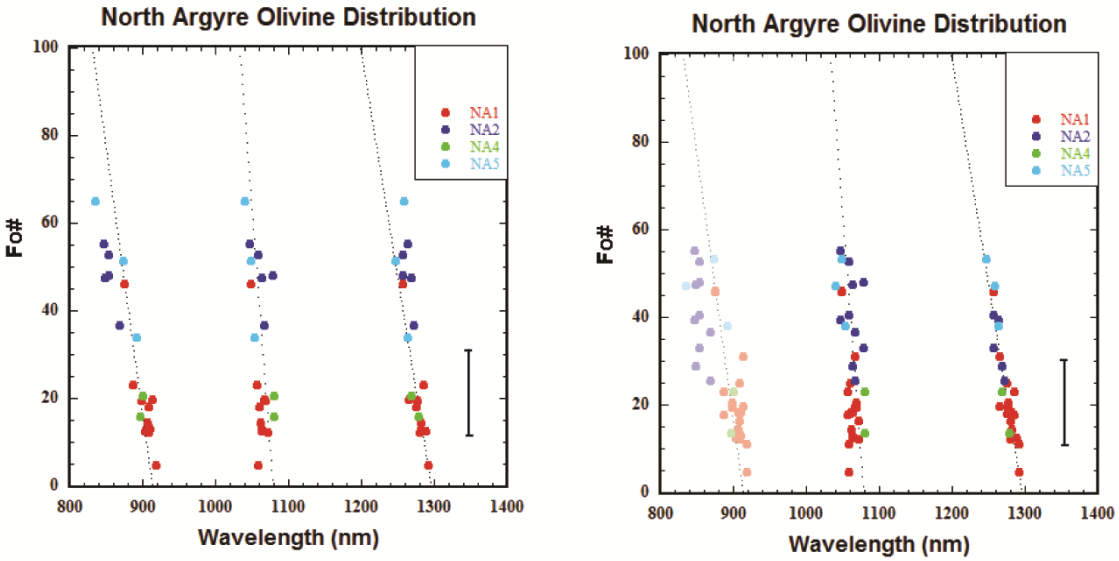

Chapter 2, Figure 14

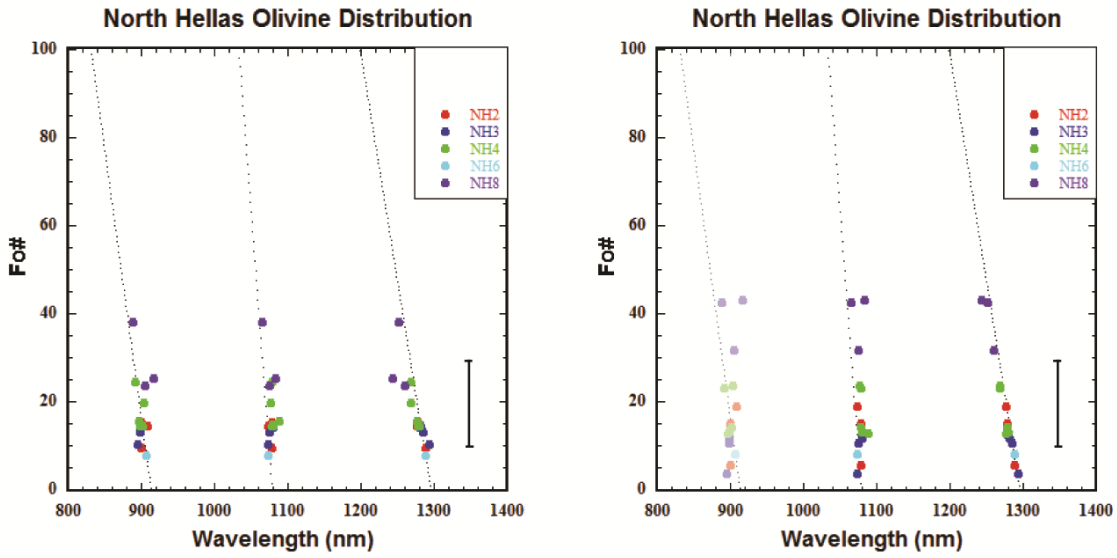

Chapter 2, Figure 15

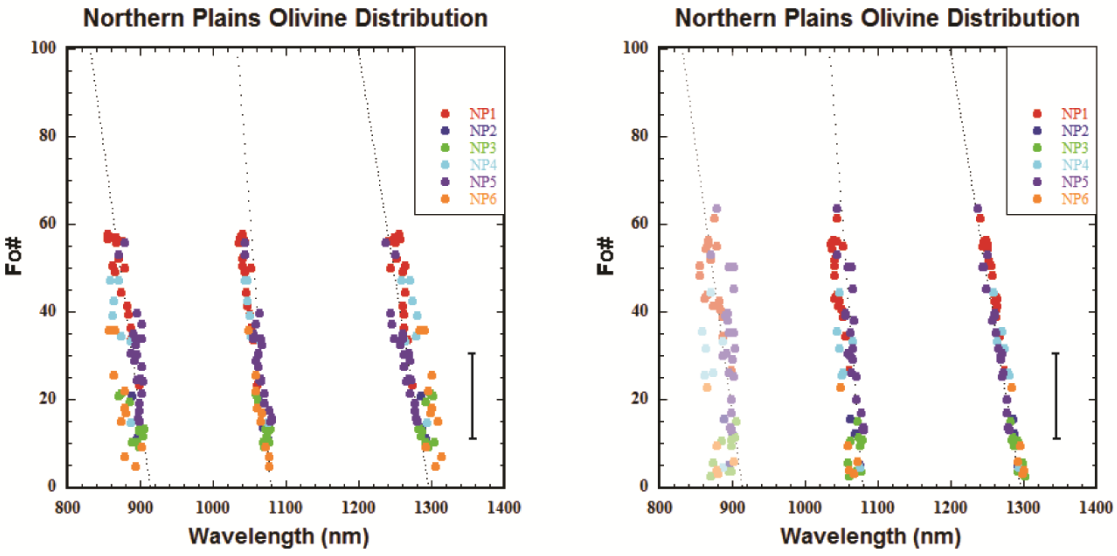

Chapter 2, Figure 16

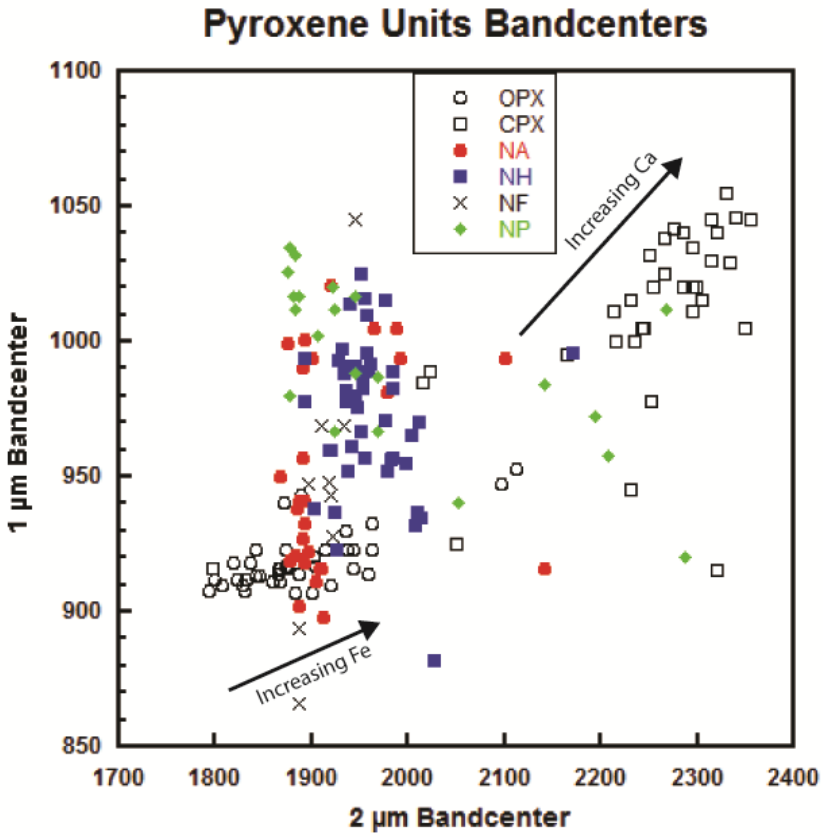

Chapter 2, Figure 17

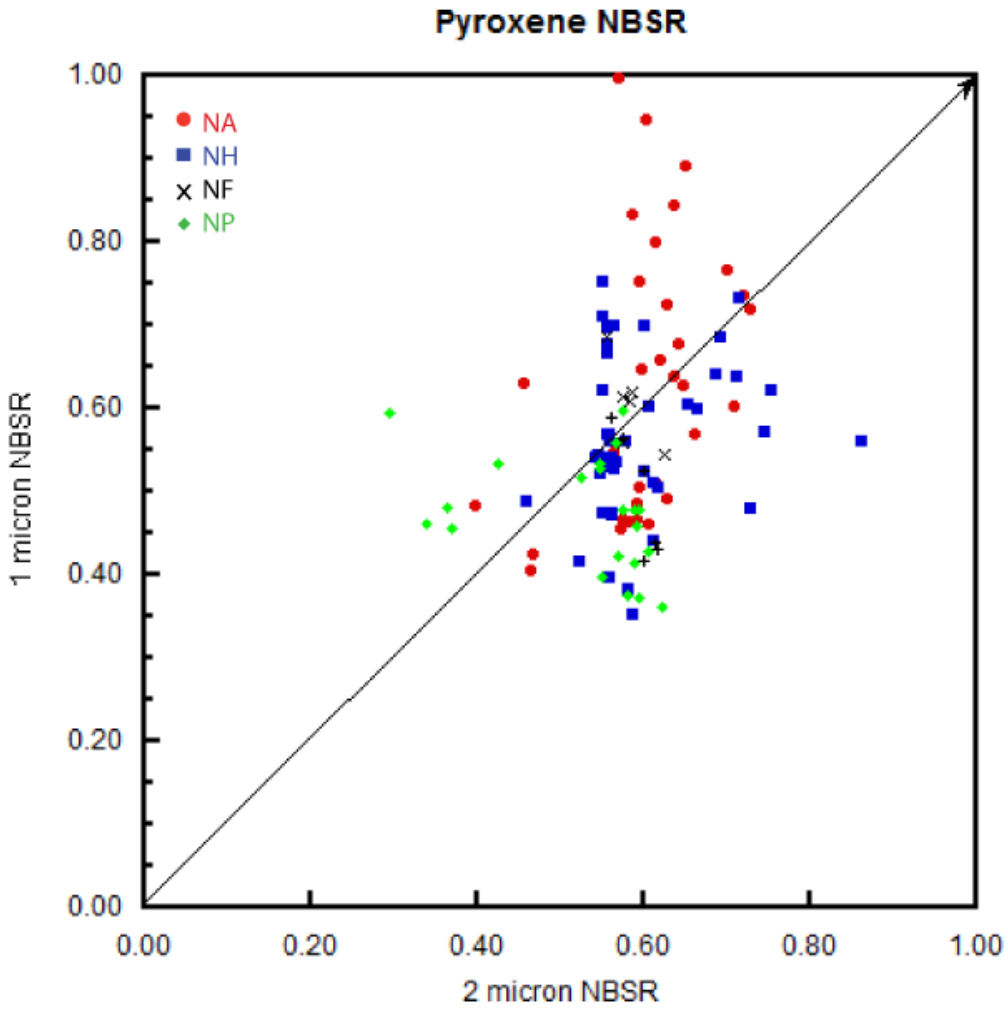

Chapter 2, Figure 18

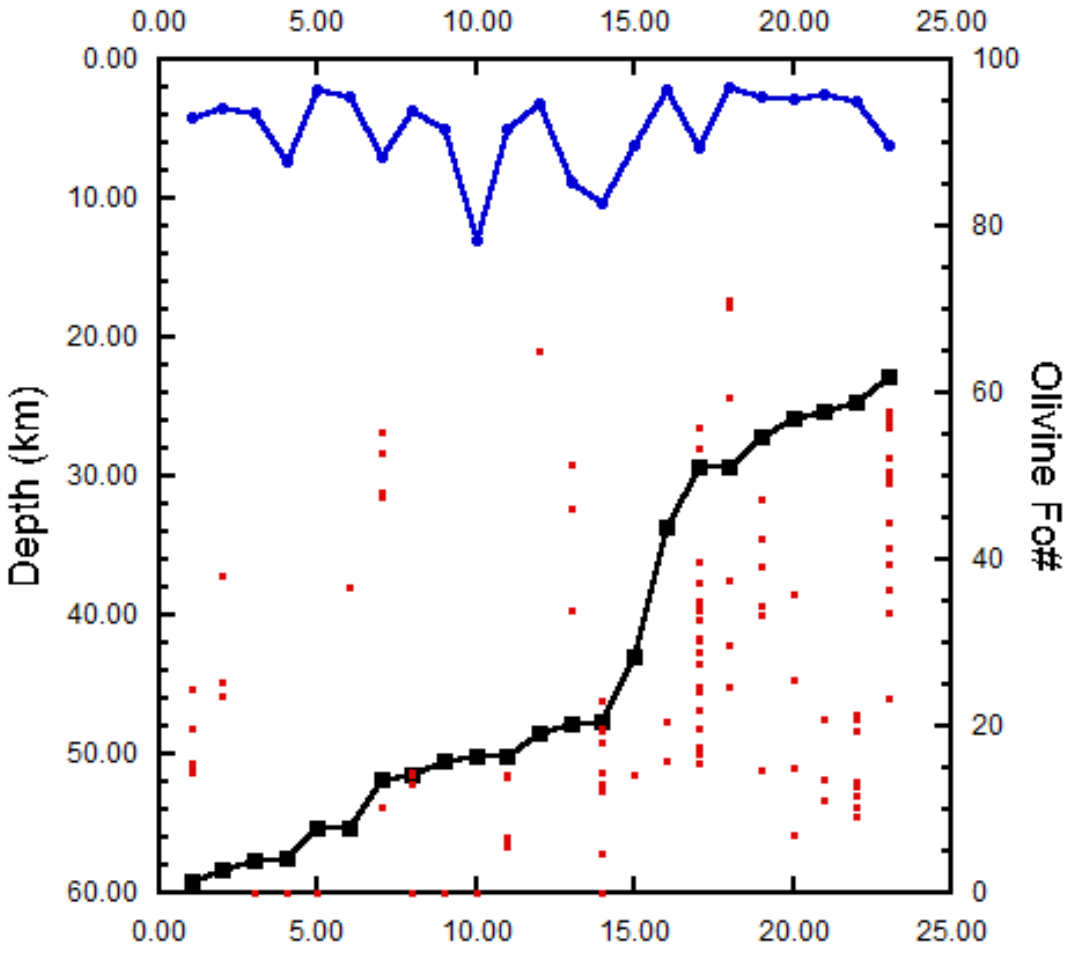

Chapter 2, Figure 19A

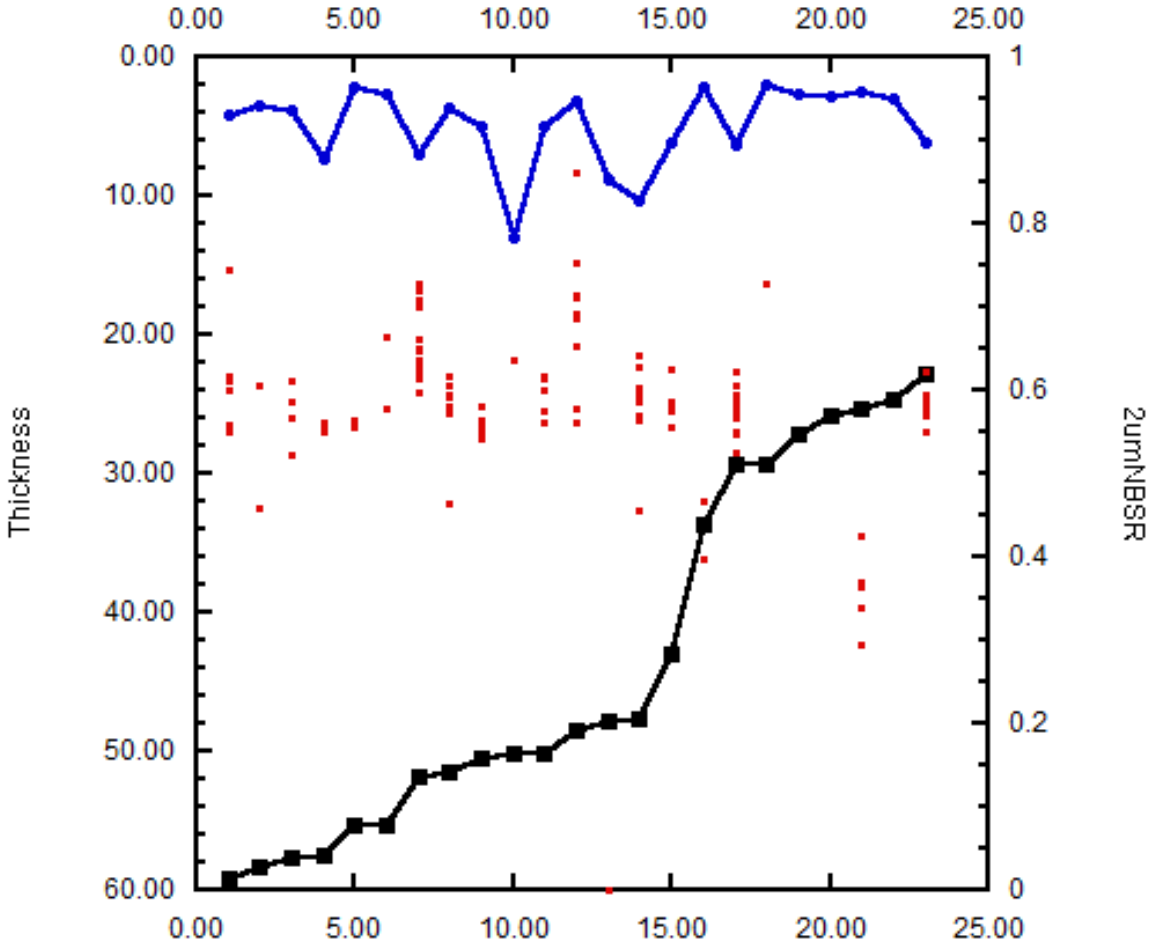

Chapter 2, Figure 19B

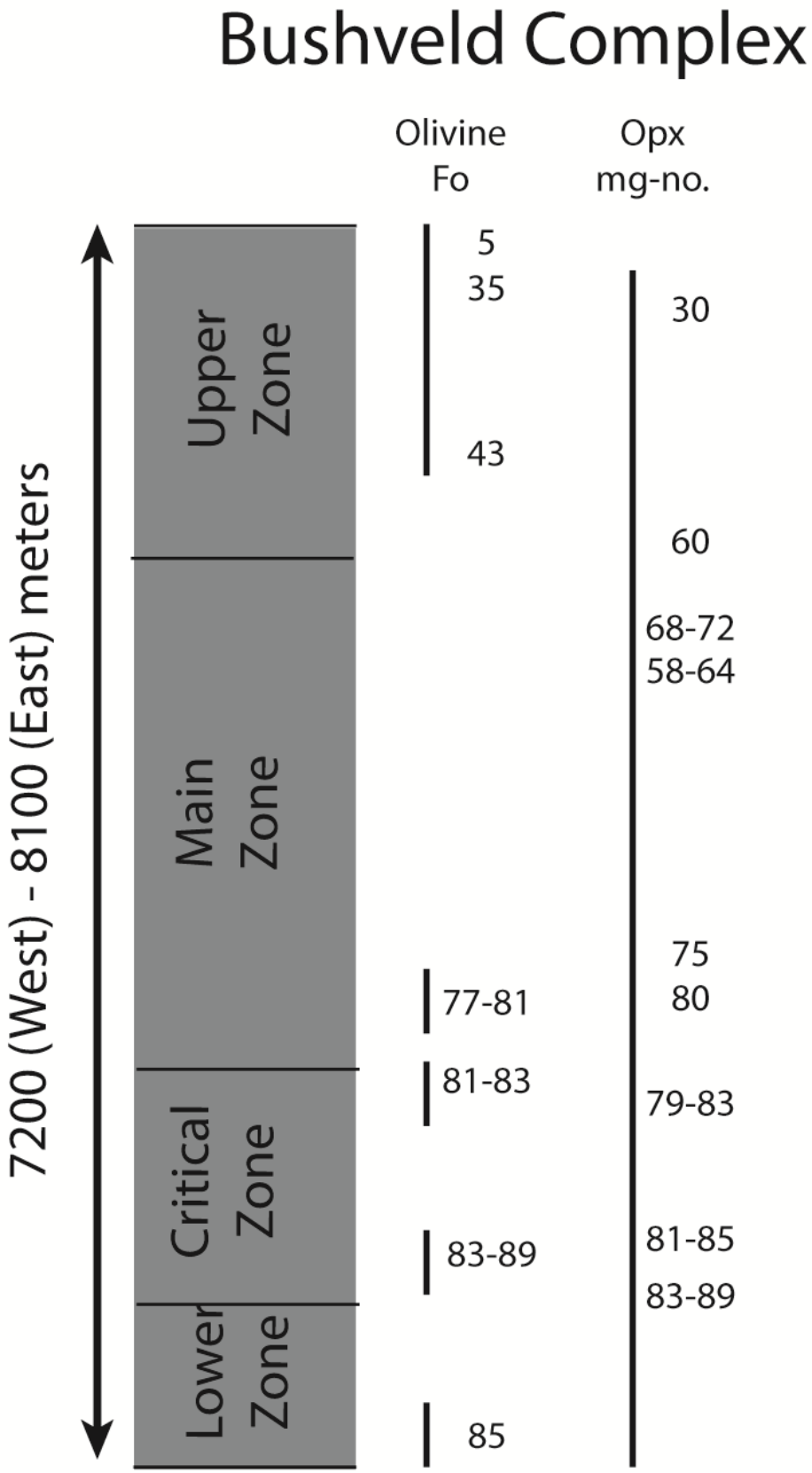

Chapter 2, Figure 20

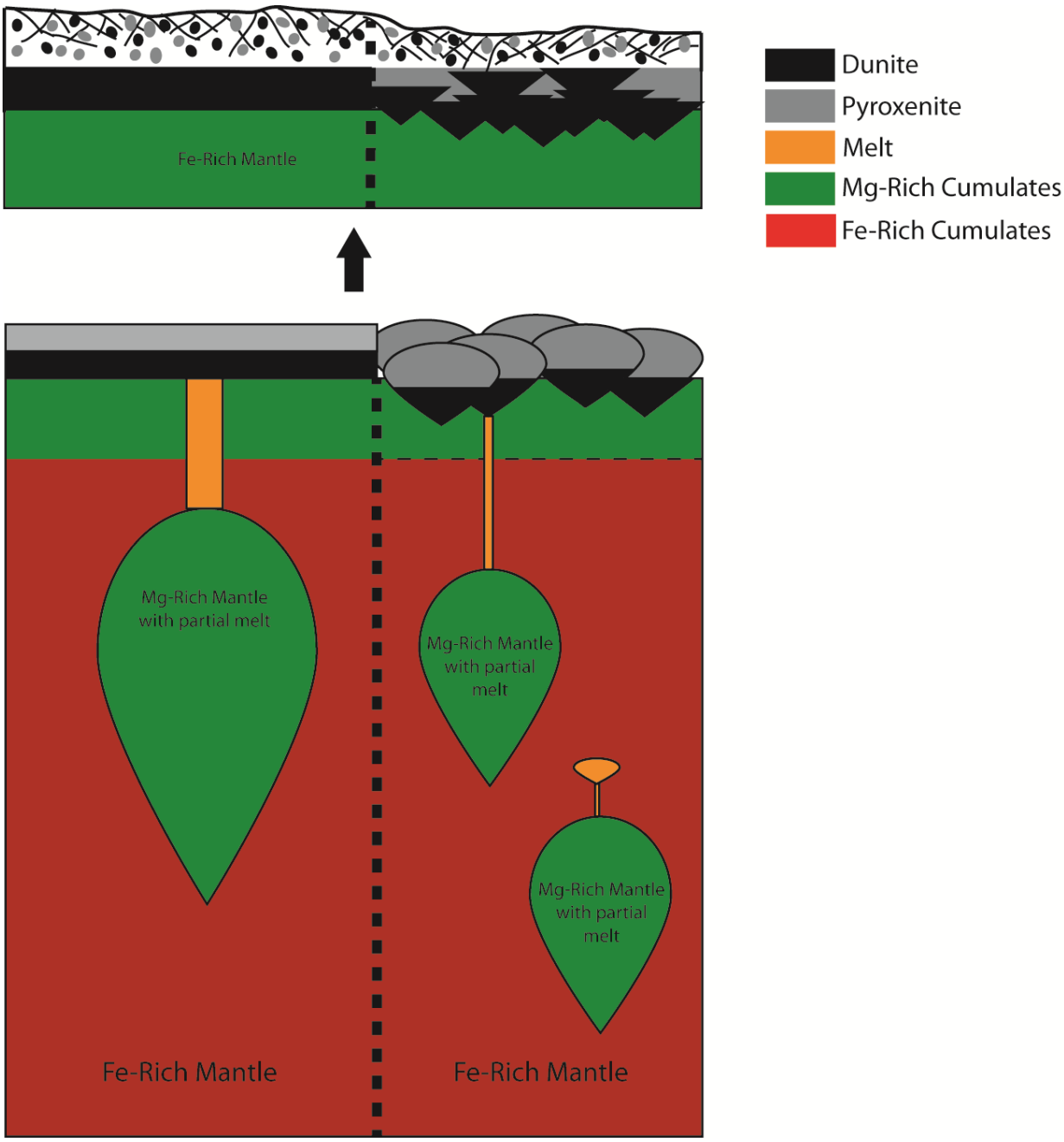

Chapter 2, Figure 21

Appendix 1.

FRT00006415 Alga Olivine	CenterX	CenterY	#Pixels
1	474	269	70
1d	476	333	172
2	497	254	113
2d	494	332	141
3	502	210	116
3d	502	332	145
4	478	180	157
4d	475	331	108
5	454	183	49
5d	458	334	84
6	422	255	133
6d	415	336	191
7	447	286	106
7d	449	335	99
8	414	275	81
8d	413	335	93
9	606	290	156
9d	604	323	278

Pyroxene	CenterX	CenterY	#Pixels
1	474	226	349
1d	481	335	437
2	462	202	344
2d	464	336	350
3	492	197	133
3d	495	335	185
4	433	266	11
4d	433	339	42
5	365	170	66
5d	366	330	95
6	423	181	48
6d	427	339	63
7	388	169	45
7d	391	331	112
8	423	197	73
8d	426	339	139
9	466	172	123
9d	463	335	233

Pyroxene2	CenterX	CenterY	#Pixels
1	416	160	55
1d	416	342	500
2	434	145	216
2d	436	334	751
3	408	137	120
3d	410	335	671
4	439	113	61
4d	440	338	612
5	473	123	98
5d	473	328	548
6	322	221	53
6d	324	339	543
7	364	205	212
7d	366	346	1658

FRT00017D02

Olivine	CenterX	CenterY	#Pixels
1	355	267	160
1d	360	399	791
2	378	255	146
2d	372	398	694
3	294	160	276
3d	283	403	702
4	377	126	299
4d	370	399	884

Pyroxene	CenterX	CenterY	#Pixels
1	296	357	188
1d	298	406	477
2	311	297	199
2d	314	405	334
3	320	243	177
3d	319	404	315
4	372	237	302
4d	379	401	690
5	450	196	124
5d	445	396	491
6	495	160	58
6d	508	399	433
7	520	113	97
7d	511	399	526
8	260	179	179
8d	263	403	506
9	206	236	85
9d	209	404	189
10	337	91	176
10d	336	403	424

FRT000117BC

Pyroxene	CenterX	CenterY	#Pixels
1	72	143	477
1d	70	394	438
2	91	104	42
2d	92	174	221
3	87	147	46
3d	88	177	97
4	283	50	600
4d	281	103	257
5	273	30	77
5d	275	102	108
6	235	97	203
6d	218	9	218

FRT0000B5BE	CenterX	CenterY	#Pixels
1	513	249	107
1d	503	17	391
2	528	216	302
2d	535	24	515
3	473	219	94
3d	478	17	231

FRT000097FF							
Olivine	CenterX	CenterY	#Pixels	Pyroxene	CenterX	CenterY	#Pixels
1	261	197	185	1	418	158	356
1d	264	398	752	1d	424	386	615
2	304	308	109	2	354	127	79
2d	310	398	531	2d	356	58	347

FRT00010FE8	CenterX	CenterY	#Pixels
1	170	128	186
1d	169	59	459
2	135	141	273
2d	139	64	832
3	131	120	58
3d	132	65	434
4	279	193	339
4d	293	52	464
5	242	209	746
5d	245	53	615
6	162	173	473
6d	165	60	550

7	212	195	699
7d	215	59	713
8	327	287	124
8d	328	63	713
9	323	109	173
9d	326	64	326

FRT0000C2A5

Pyroxene	CenterX	CenterY	#Pixels
1	276	223	123
1d	275	45	2534
2	54	271	203
2d	54	87	1215
3	253	335	40
3d	256	39	1217
4	365	223	108
4d	383	51	2245

FRT000082E8

Olivine	CenterX	CenterY	#Pixels
1	171	155	534
1d	168	369	2620
2	96	263	175
2d	122	265	239
3	101	328	48
3d	104	375	2085
4	68	215	114
4d	37	230	37
5	117	206	40
5d	76	202	80
6	80	172	29
6d	236	189	195
7	270	229	54
7d	247	274	235
8	212	239	47
8d	254	367	4965

FRT0000C554

Olivine	CenterX	CenterY	#Pixels	Pyroxene	CenterX	CenterY	#Pixels
1	354	10	29	1	309	132	51
1d	357	68	245	1d	313	87	631
2	470	37	82	2	332	162	67
2d	467	106	230	2d	333	85	418

3	484	325	261	3	307	174	82
3d	481	198	276	3d	312	86	435
4	543	390	275	4	336	199	159
4d	543	46	748	4d	329	87	390
5	366	306	90	5	364	211	262
5d	378	108	470	5d	366	106	838
6	103	351	250	6	356	106	1092
6d	116	58	1091	6d	408	268	448
7	63	328	317	7	399	343	127
7d	73	61	1041	7d	406	194	387
8	220	397	168	8	416	348	302
8d	214	64	638	8d	422	193	445
9	407	33	163	9	470	362	117
9d	424	147	852	9d	472	193	208
				10	299	373	824
				10d	311	86	872
				11	235	238	592
				11d	248	77	770
				12	234	288	640
				12d	238	81	770
				13	176	250	557
				13d	176	250	737
				14	204	232	384
				14d	205	81	732
				15	318	395	215
				15d	322	88	420

FRT00001EB32

Pyroxene	CenterX	CenterY	#Pixels
1	449	143	86
1d	453	386	604
2	452	230	692
2d	460	377	1228
3	468	306	595
3d	474	375	845
4	370	232	107
4d	370	408	110
5	405	280	78
5d	407	396	314
6	307	223	112
6d	307	392	469
7	263	260	101
7d	269	394	378

8	180	220	231
8d	168	377	682
9	193	204	80
9d	199	400	95

FRT000147FB

Olivine	CenterX	CenterY	#Pixels	Pyroxene	CenterX	CenterY	#Pixels
1	587	173	643	1	555	238	43
1d	573	385	2563	1d	564	394	436
2	567	504	210	2	504	162	121
2d	575	384	1499	2d	521	395	877
3	587	242	118	3	488	233	20
3d	591	386	952	3d	498	396	643
4	582	265	132	4	457	335	100
4d	589	385	933	4d	461	400	360
5	545	289	564	5	418	356	37
5d	547	384	2082	5d	419	400	179
6	425	250	184	6	213	330	124
6d	423	400	564	6d	217	36	693
7	509	240	123	7	85	343	75
7d	514	387	892	7d	87	144	850
8	527	233	88	8	146	297	53
8d	532	387	751	8d	150	182	333
9	412	322	75	9	110	314	132
9d	409	400	344	9d	111	223	530
10	383	341	425	10	140	395	77
10d	382	401	460	10d	154	235	383
11	346	362	53				
11d	346	396	224				
12	358	77	436				
12d	377	398	1126				
13	355	143	256				
13d	368	395	947				
14	347	177	500				
14d	356	397	626				
15	306	290	157				
15d	311	401	169				

FRT0001EBA0

Olivine	CenterX	CenterY	#Pixels
1	351	211	1114
1d	346	44	1399
2	388	186	197

2d	389	45	561
3	300	267	90
3d	306	45	450
4	390	242	401
4d	377	39	1312
5	238	148	570
5d	241	33	523
6	245	227	696
6d	263	349	2048
7	247	192	196
7d	247	353	857
8	372	164	516
8d	397	316	1268

FRT000177F9			
Pyroxene	CenterX	CenterY	#Pixels
1	312	167	417
1d	312	23	932
2	247	136	468
2d	250	17	320
3	224	88	266
3d	223	16	349
4	235	44	29
4d	235	18	80
5	256	35	30
5d	257	16	99
6	269	275	221
6d	272	16	536
7	354	242	504
7d	362	373	363

FRT0000C4D0			
Olivine	CenterX	CenterY	#Pixels
1	332	196	64
1d	331	53	73
2	386	204	125
2d	390	84	512
3	464	161	71
3d	468	84	530
4	344	342	81
4d	353	63	119
5	257	360	90
5d	237	87	449

6	406	312	461
6d	419	87	692

FRT0000B573

Olivine	CenterX	CenterY	#Pixels	Pyroxene	CenterX	CenterY	#Pixels
1	504	32	1786	1	494	174	335
1d	470	262	2392	1d	495	253	615
2	186	270	510	2	551	216	248
2d	181	240	175	2d	548	274	441
3	110	363	133	3	370	193	82
3d	114	410	261	3d	372	153	137
4	216	54	117	4	276	114	303
4d	225	171	187	4d	278	176	365
5	509	212	450	5	204	20	394
5d	508	256	474	5d	211	125	404
6	593	255	173	6	131	53	71
6d	602	182	271	6d	121	306	130
7	596	55	846				
7d	598	180	455				

FRT000110B7

Olivine	CenterX	CenterY	#Pixels	Pyroxene	CenterX	CenterY	#Pixels
1	303	246	126	1	170	193	1322
1d	297	455	578	1d	166	437	2674
2	267	282	144	2	260	115	105
2d	260	454	391	2d	260	453	332
3	308	373	130	3	112	216	67
3d	303	453	372	3d	117	440	398
4	363	353	190	4	286	60	33
4d	365	451	253	4d	287	27	104
5	464	280	66	5	332	61	56
5d	463	455	210	5d	332	126	420
6	582	218	105	6	368	64	66
6d	583	450	381	6d	368	131	149
7	645	191	117	7	433	85	132
7d	622	410	222	7d	435	116	74
				8	471	180	49
				8d	469	114	53

FRT00009610

Olivine	CenterX	CenterY	#Pixels	Pyroxene	CenterX	CenterY	#Pixels
1	349	131	288	1	457	143	23

1d	371	495	2573	1d	458	187	360
2	336	150	171	2	98	51	75
2d	340	499	1081	2d	112	373	921
3	352	88	26	3	181	83	92
3d	357	505	945	3d	176	384	800
4	125	57	569	4	36	447	105
4d	151	509	1133	4d	40	400	461
5	162	86	272	5	104	436	110
5d	184	521	838	5d	108	375	774
6	149	24	444	6	206	413	101
6d	160	515	810	6d	208	389	145
7	200	61	358	7	578	46	68
7d	229	513	660	7d	581	106	231
8	214	204	177	8	614	50	42
8d	232	514	452	8d	615	107	294
9	250	222	213	9	418	63	113
9d	255	514	432	9d	421	129	347
10	283	208	79				
10d	303	514	648				
11	296	223	65				
11d	313	511	631				
12	286	185	110				
12d	306	513	564				
13	259	282	43				
13d	267	512	396				
14	244	291	134				
14d	256	516	613				
15	198	282	141				
15d	202	521	284				
16	182	295	146				
16d	193	516	430				
17	404	418	39				
17d	410	502	658				

FRT0000C417

Olivine	CenterX	CenterY	#Pixels
1	152	144	410
1d	159	503	940
2	118	152	643
2d	119	502	929
3	53	168	585
3d	54	499	599
4	94	216	408

4d	111	499	1007
5	85	145	223
5d	96	497	637
6	114	195	199
6d	101	496	676
7	88	249	131
7d	93	495	326
8	105	265	212
8d	102	496	351
9	157	323	282
9d	166	499	637
10	258	332	63
10d	259	495	128

FRT0000ADA4

Olivine	CenterX	CenterY	#Pixels	Pyroxene	CenterX	CenterY	#Pixels
1	197	400	73	1	439	394	309
1d	195	526	326	1d	436	25	600
2	200	409	42	2	193	107	228
2d	195	526	231	2d	193	54	1405
3	176	503	50	3	449	49	37
3d	175	531	172	3d	448	27	182
4	47	265	38	4	467	31	28
4d	56	458	229	4d	467	47	68
5	180	365	28	5	578	406	157
5d	182	475	55	5d	584	492	410
6	184	358	20	6	384	386	88
6d	190	504	85	6d	380	34	1465
7	275	160	159	7	507	333	77
7d	282	37	1072	7d	515	499	370
8	456	343	152	8	514	381	27
8d	459	167	743	8d	517	502	114
9	459	90	158	9	472	446	56
9d	457	168	543	9d	471	508	70
10	475	316	76	10	496	425	56
10d	484	506	350	10d	499	499	209
11	504	274	285	11	530	424	18
11d	511	502	896	11d	533	497	192
12	518	301	818	12	456	35	27
12d	523	508	1144	12d	544	7	80
13	244	438	100	13	526	33	52
13d	236	522	357	13d	525	6	69
14	432	452	392	14	98	370	58

14d	436	27	838	14d	103	496	161
15	321	227	150	15	78	436	22
15d	331	153	584	15d	79	494	46
16	349	314	172	16	146	531	24
16d	348	156	469	16d	141	512	198
17	38	142	56				
17d	39	11	115				
18	43	161	69				
18d	44	12	112				
19	56	334	207				
19d	57	483	246				
20	599	90	208				
20d	596	481	1244				
21	555	110	337				
21d	563	487	1739				
22	531	190	482				
22d	544	486	1378				

FRT00018A06

Olivine	CenterX	CenterY	#Pixels	Pyroxene	CenterX	CenterY	#Pixels
1	455	235	291	1	250	378	143
1d	454	68	1918	1d	244	34	647
2	419	225	415	2	250	459	67
2d	427	66	2720	2d	252	36	520
3	431	262	888	3	403	351	87
3d	437	72	2744	3d	416	57	1744
4	214	251	2254	4	400	278	52
4d	214	41	2697	4d	407	63	638
5	296	327	243	5	476	412	813
5d	312	50	1270	5d	482	66	4094
6	276	358	415	6	344	314	23
6d	293	51	1191	6d	344	88	450
7	306	374	1070	7	139	170	39
7d	312	53	1505	7d	137	48	751
8	335	329	160				
8d	3447	60	1128				

FRT0000C16F

Olivine	CenterX	CenterY	#Pixels
1	179	154	167
1d	181	46	214
2	213	168	111
2d	216	47	105

3	195	188	125
3d	201	46	137
4	196	174	112
4d	200	46	90
5	198	153	78
5d	205	46	72
6	210	197	68
6d	218	47	110
7	171	168	82
7d	177	46	143

FRT0000CF27			
Olivine	CenterX	CenterY	#Pixels
1	404	278	442
1d	405	509	504
2	402	208	148
2d	407	509	240
3	399	248	164
3d	408	509	264
4	379	217	332
4d	388	508	281
5	370	175	256
5d	388	508	391
6	371	144	215
6d	390	509	318

Chapter 3:

Evidence for a Post-Noachian Fluvial System in the Northeast Syrtis Major Region, Mars.

J.R. Skok[1], J.F. Mustard[1]

1. Department of Geological Sciences, Brown University

Abstract

The mineralogy, morphology and geology of the region northeast of Syrtis Major records the diverse and changing history of early Mars in a well-exposed environment. The region contains a stratigraphic record that spans the period of formation of phyllosilicate-bearing Noachian crust, altered under neutral pH conditions, to the more acidic, sulfate depositing, Hesperian period dominated by volcanic processes. The active fluvial history is woven into this period of transition. Geomorphic evidence along the northeast Syrtis boundary supports the existence of a Hesperian fluvial system that is sourced in the Hesperian basalts and terminates in the Isidis Basin. Detailed analysis of this system constrains the local fluvial history and further describes the key exposures in the northeast Syrtis region.

Introduction

The northeast edge of the Syrtis Major complex on the western edge of the Isidis Basin (Figure 1) on Mars, straddles the boundary between the Noachian crustal exposures of Nili Fossae [Mustard et al., 2009; Ehlmann et al., 2009] and the Hesperian volcanics of Syrtis Major [Hiesinger and Head, 2004]. This boundary is suggested to mark a global change in igneous, alteration and fluvial activity [Bibring et al., 2006]. The diversity of geologic processes and mineralogical units represented in the region make it a complicated but vital region to understand. The oldest preserved local unit is the altered Noachian crustal bedrock that forms the plains to the north of Syrtis Major. The region was then shaped by the formation of the Isidis impact basin. The basin formation created the regional slopes and topography that influences later processes. Olivine-bearing units were then emplaced throughout the region but always

stratigraphically above the altered bedrock as either impact melts [Mustard et al., 2007] or picritic lava flows [Tornabene et al., 2008]. This was followed by development of the Nili Fossae [Wichman and Schultz, 1989] that cut the olivine-bearing units [Mustard et al., 2007; 2009] and the formation of Jezero Crater and the subsequent fluvial activity forming the crater lake and deposited phyllosilicate-bearing deltas [Fassett and Head, 2005; Ehlmann et al., 2008a; Schon et al., 2012]. The olivine-bearing unit was then partially altered to a magnesium carbonate-bearing assemblage [Ehlmann et al., 2008b]. And extensive surface leaching occurred in the altered basement units to create zones of kaolinite. The beginning of the Hesperian saw a major shift in Mars climate leading to the development of sulfate layers and volcanic eruptions of basaltic lava flows that make up the Syrtis Major shield. The nature of the sulfate unit formation is still debated with basin deposition, groundwater precipitation and contact alteration of volcanic flows as possible alternatives [Ehlmann and Mustard, 2012].

The last major unit to be emplaced in the region is the Syrtis Major volcanic lavas that cap the local stratigraphy to the immediate southwest of our study region [Schaber et al., 1982; Hiesinger and Head, 2004]. The study of Syrtis Major's eastern edge cliff forming morphology and the knobby terrain transition from Syrtis Major to the Vastitas Borealis suggests that the lavas may have encountered a volatile rich unit, such as an ice sheet [Ivanov and Head, 2003]. The presence of ice deposits at mid-latitudes is predicted at times of high planetary obliquity [e.g.: Head et al., 2003] during the recent Amazonian and would be more likely during a wetter time on Mars.

The emplacement of the Syrtis volcanics was followed by a final period of fluvial activity described in this paper and in Mangold et al., [2008]. Mangold et al. [2008] described the presence of a channel deeply etched into the Syrtis basalts. This channel and several related

nearby fluvial features would have required a significant source of water to create the observed morphology. This study focuses on the detailed analysis of another set of Hesperian aged geomorphic features that are similar to those described in Mangold et al. [2008] located on the edge of the northeast Syrtis scarp (Figure 2). Previous analyses have overlooked this fluvial system. An in-depth analysis of this fluvial system can constrain locally derived water required to flow in the mid to late Hesperian and further understand the geologic history of the geologically important northeast Syrtis region.

Methods

All data for this analysis are maintained in an ArcMap GIS database and the mapping uses the Thermal Emission Imaging System (THEMIS) [Christensen et al., 2004] daytime infrared global mosaic with 256 pixels per degree baselayer [Christensen et al., 2004]. Surface morphology was assessed using a combination of ~6 m/pixel images from the Context Camera (CTX) instrument aboard the Mars Reconnaissance Orbiter (MRO) spacecraft [Malin et al., 2007], and the 100 m/pixel global mosaic of daytime infrared (IR) images from the THEMIS instrument aboard the Mars Odyssey spacecraft. Detailed morphology was also investigated using ~0.25 m/pixel images from the High Resolution Imaging Science Experiment (HiRISE) instrument aboard MRO [McEwen et al., 2007]. Topographic information was determined regionally with MOLA gridded topography with a resolution of 128 pixels per degree [Zuber et al., 1992] and locally with CTX derived digital elevation models (DEM). CTX DEMs were produced with the NASA Ames Stereo Pipeline software [Broxton et al., 2011]. Overlapping images were selected with moderate to high incidence angle from orbits on either side of the

targeted site to provide perspective on the topographic features. The images are first aligned using an automatic alignment algorithm built into the software. Next each pixel is correlated to the corresponding pixel of the other image creating a disparity map. A sub-pixel refining method is then employed to smooth out instrument artifacts. Finally, using instrument information contained in the Integrated Software for Imagers and Spectrometers (ISIS) database on each planetary camera, the elevation of each point is triangulated based on the known position of the spacecraft and the disparity of each pixel pair. This result is then used to construct the DEM used in this analysis. This method is still in the research stage and was developed generally to work with as many planetary datasets as possible [Broxton et al., 2011].

Topographic analysis of fluvial systems is limited by the requirement that analysis is performed on modern topography and not during the time of activity. It is difficult to constrain if and how the landscape may have changed in the interim and is largely assumed here to be unchanged unless observations require an alternative. In such a case, the required topography is mentioned and possible explanations for the change are considered.

Crater counts were performed on a 6 meter/pixel CTX Mosaic with the publicly available CraterTools ArcMap toolkit [Kneissl et al., 2010]. Crater count ages are based on the crater production functions described by Hartmann and Neukum [2001]. Composition information was determined from data obtained by the Compact Reconnaissance Imaging Spectrometer for Mars (CRISM) visible and near-infrared (VNIR) hyperspectral imaging instrument [Murchie et al., 2007]. CRISM acquires full resolution targeted (FRT) images at 18 meter per pixel spatial resolution and 544 spectral bands ranging from 0.32 – 4.0 μm.

Results

The recorded fluvial history of the northeast Syrtis region can be divided into two main periods. The first is defined by the Jezero Crater open basin lake and preserved delta [Fassett and Head, 2005; Ehlmann et al., 2008a] and dated near 3.7 Ga [Fassett and Head, 2008] and pre-dates the Hesperian volcanics that embay the lacustrine deposits [Goudge et al., 2011]. The second post-dates the Hesperian volcanics, with sources within the volcanic terrains and is explored here. Many of the geomorphic features from this second fluvial episode have been described by Mangold et al. [2008], but an in-depth look at similar geomorphic features located on volcanic scarp of northeast Syrtis region has not been performed until now. We break down the observations into three parts [Figure 2; upland channels (blue), basin depression (blue shade), outlet channel (green)] and describe each in turn with implications for the fluvial and geologic history of the region.

A subtle system of channels is apparent on top of a broad lava flow emplaced in the early Hesperian (3.75-3.8 Ga) [Hiesinger and Head, 2004; Skok et al., 2010] (Figure 3). The exact location of the system origins are difficult to determine due to the subtle geomorphic features that define this unit. The features form braided shallow channels that follows a flat 7 km wide basaltic lava flow that previously floored a local topographic low surrounded by older Noachian material (Figure 3, lower left). Just before the features leave the basaltic unit, it encountered a large flat region (Figure 3, upper right) where the channel spreads out and divides into two main directions and additional minor ones. One major system is directed to the south while the other one leads to the east toward the Isidis Basin. The eastern system eroded a channel through 3.5 km of basaltic volcanics while the southern system eroded through 4.2 km of basaltic materials, cutting channels into the volcanic cliffs. As the eastern system comes off the volcanic plateau it

encounters a boxwork texture of light-toned sulfate bearing material and erodes a channel that leads to the basin depression.

Basin Depression. As the plateau channels leave volcanic plains the formation agent may have collected in an apparent basin centered at 17.6°N 76.6°E (Figure 4). At one time this basin would have drained via an east-west channel with a highest elevation of -2330 meters which would have been the lake elevation when the channel was active. However in the current topography, the lowest outlet is a 3 km wide region to the southeast that would have provided flow for fill above the -2430 meter crest point, 100 meters lower than the water height that would have activated the east-west outlet channel (Figure 4). The southeast channel shows no indication of fluvial morphology or modification and is inferred only on the basis of MOLA topography. This southeast channel is floored by loose particulate material that appears to have been derived from adjacent cliff forming volcanics with no evidence of fluvial morphology.

The basin depression is ellipsoidal with an elongate east-west axis (Figure 4). When the east-west channel was active, the lake would have approximate dimensions of ~27 km by ~17 km with a maximum depth near 200 m. If the southeast outlet channel was active the lower shoreline and depth would form a lake 22 km by 8 km and 100 m maximum depth.

The basin fill unit is distinct and has an spatial extent that coincides with the topographic contour line that is enclosed by the current basin topography and not the one that would have been active during active channel formation (Figure 4). The basin depression is largely covered with a rough textured, crater retaining material (Figure 5, Figure 6). The edges of this basin fill material exposes a finely layered, relatively light-toned, olivine and magnesium carbonate ($MgCO_3$) -bearing material (Figure 7, Figure 8). Similar light-toned material is observed in a 500

m impact crater in the basin fill unit, indicating that the carbonates underlie the ~40 m thick basin unit (Figure 5). The origin of the basin fill material is unknown and could be an isolated, competent volcanic unit, a lithified fluvial or aeolian depositional unit. Alternatively, it does bear compositional similarities to a regional olivine bearing unit that is suggested to be part of an ejecta unit from the Isidis basin formation [Mustard et al., 2007]

*Outlet Channel***.** The proposed basin at one time emptied though an outlet channel that flowed to the east (Figure 9). This channel can be easily traced for 48 km, as it drops ~750 m from an elevation of -2330 m at the basin rim to -3100 m elevation. The channel begins with a well-defined and preserved path and a width of ~500 m. After the first ~7 km the channel morphology becomes complex and shows signs of braiding or multiple channel forming episodes. Sections of the channel have not been well preserved, indicating inherently weak surface materials or an active subsequent geologic history. The remainder of the channel is well defined with sharp sides. Much of the length of the channel is floored with aeolian material that forms ripples that are consistently perpendicular to the channel walls.

The channel terminates abruptly near -3100m as it enters the edge of Isidis Basin. Though the exact reason for channel termination is not clear, the slope in this region is slightly less than the rest of the path and the flow may have lost the potential required for down cutting erosion.

Crater Counting. Crater counts were performed to constrain the absolute and relative timing of the main features of this fluvial system. Some of the major regional events have been well examined including the Isidis impact at 3.96 Ga [Werner, 2005] and emplacement of the Syrtis Major volcanics between 3.8 and 3.75 Ga [Hiesinger and Head, 2004, Werner, 2005] and

Jezero fluvial valley network formation at 3.74 Ga [Fassett and Head, 2008]. We report crater counting results for some of the smaller units that are directly related to the described fluvial system. The source region fluid etched morphology is superimposed on the Syrtis Major volcanic surface. We date these volcanics to check against the accepted Syrtis Major ages and to provide a maximum age of fluvial activity. This unit (Figure 10 Yellow Outline, Figure 11 Upper Right) provides an age of 3.41 Ga (+0.09 -0.21) from a counting area of 280 km^2. This unit is morphologically related to the Syrtis Major flows but dates a few hundred million years younger than the main edifice [Hiesinger and Head, 2004], but is coincident with the volcanics that resurfaced Jezero at 3.50 (+0.11 -0.61) (Figure 10 Purple Outline, Figure 11 Lower Right) [Goudge et al., 2012]. This age is after the formation of the Jezero open basin lake as the unit embays the Jezero lacustrine deposits [Fassett and Head, 2005; Ehlmann et al., 2008a; Schon et al., 2012] and predates the fluvial deposit described in this chapter. The younger age could be the result of long lived volcanic feature with late forming distal flows or an artifact of a relatively small counting area. Crater counting of the dark basin filling material (Figure 10 Red outline, Figure 11 Lower Left) yields an age of 1.29 Ga (+0.20 -0.22) from a counting area of 190 km^2. The area is too small to have a strong confidence in the exact number but is does constrain the basin fill unit to having a shorter surface exposure age than the surrounding volcanics potentially indicating surface erosion or a covering unit. The Noachian plains contain the basin and outlet channels (Figure 10 Blue outline, Figure 11 Upper Left). This area is highly textured and eroded and contains a number of different units. Rather than try to date individual stratigraphic layers within this area we chose to select an aggregate area that would provide an approximate exposure age for the surface. Crater counting yielded an age of 3.71 Ga (+0.06, -0.11) on a counting area of 3000 km^2. While the Noachian material that forms most of this area is likely

even older, this age constrains the surface exposure age, indicating that this surface was mostly in place 200 Ma after the Isidis impact and has not encountered substantial erosion since that time.

Discussion

The system described here is very most likely carved by flowing water that formed the etched channels on the volcanic plains, eroded back the volcanic cliffs, pooled in the basin and then carved the eastern outlet channel. Some of the morphologic features could have had other origin sources. The source region channels could have been the product of the volcanic emplacement process and the outlet channel could have been carved by thermal erosion similar to lunar sinuous rilles [Hurwitz et al., 2012]. However the persistence of the basin depression , the braided channels and specific morphology suggest that is system is the result of a fluvial erosive process.

The morphologic mapping, topographic analysis and crater counting have revealed several notable observations about this fluvial system and the surrounding region. The first significant observation is the cause of the cliff forming volcanics in this region. The basin depression at the base of the Syrtis volcanics is most reasonably the product of the regional topography that resulted from the Isidis Basin formation. Yet the volcanic flows are 500 m higher than the basin 4 km to the south and 900 m higher 9 km to the west with a 12° average slope on the volcanic edge. The relatively flat nature of the volcanic flows suggests low viscosity lavas that should have flowed over and filled the basin if they had encountered the modern topography. Instead, something must have impeded the volcanic flows near their current

position. A ~1 km thick ice sheet would be capable of halting the volcanic flows (Figure 13), forming the edge effects described by Ivanov and Head [2003] and provide the volatiles required for the contact alteration hypothesis for formation for the sulfate deposits [Ehlmann and Mustard, 2012]. Subsequent climate change could make the ice unstable at these latitudes during interglacial periods and sublime away leaving the current observed topography.

Following the emplacement of the Syrtis Major volcanics in the early Hesperian, a water source must have been available to drive and erode the observed fluvial system. Mangold et al., [2008] described several potential sources for the outlet channel to the south of our study region. Suggested sources include subsurface out flows that result from aquifer over pressurization, possibly from volcanic heating or impact fracturing of overlaying units or the raising of subsurface water tables [Andrews-Hanna et al., 2007]. Alternatively, periodic orbital changes could lead to additional high obliquity, low latitude ice deposits in the region. Basal melting of this ice could provide the fluids required to carve the observed morphology. A widespread surface source would explain the diffuse nature of the fluvial morphology on the volcanics and the lack of well-defined point source of the origin. The volume of water from this source would have to be large enough to fill the basin to a least 200 m depth to activate the eastern outlet channel, even after being divided into several directions on the source volcanics (Figure 3). While the presence of surface fluid flow is documented in the mapped source morphology, the contribution of ground water into the basin is likely but unconstrained with current observations.

The basin depression is defined by the observation of topographic contour lines that close around the depression. The highest contour that completely encloses the basin topography is -2450 m. However, the eastern outlet channel that was formed has a head elevation of -2330 m. Current topography would lead to basin out flow through the 3 km wide passage to the southeast.

Therefore the passage must have been blocked in order to force the basin to fill with an additional 120 m of water to activate the eastern channel. We offer three possible scenarios to explain this inconsistency. The first is that the current topography is not representative of the topography during fluvial activity. Regional or local subsidence could have shifted the local topography enough to affect the boundaries of the paleolake shore. Specifically, the out flow of a large aquifer could have this effect. However, this would have to happen after the emplacement of the volcanics and would be expected to cause more fractures and cracking if it was this significant. The second scenario is that the passage was blocked by a continuation of the sulfate and mafic cap unit observed to the west of the passage to the sulfate mesa to the immediate east. Since we do not observe any fluvial morphology associated with this passage or major erosional remnants of this unit, it is unlikely that the material was remove by hydrologic erosion. The material could have collapsed and been removed by aeolian processes after the fluvial activity had ended, though this would not explain why the erosion did not remove the sulfate mesa to the east of the passage. One final scenario is that the current passage topography existed during the time of fluvial activity but that it was during a time of mid-latitude ice deposits. The presence of an ice dam could block this passage and force out flow through the eastern passage. The presence of regional ice units would then coincide with an atmospheric source for the fluvial activity. The sublimation of the dam would remove evidence of the passage blockage without leaving traces of material. None of these scenarios has compelling evidence for its selection, but the lack of erosional features in the southeast passage would best be explained by the ice dam hypothesis.

Based on the observations stated above, a possible chronology would have required at least two periods of local ice deposits. The first would have been during the emplacement of the

Syrtis Major volcanics to cover and preserve the basin as a topographic low. After the volcanics have cooled, another period of ice deposits could have sourced the fluvial system while blocking the southeastern passage. The first ice period would require ice at least 1 km thick to stop the volcanic flows in the current configuration. However, during the time of active fluvial activity the ice cover of the basin would have had to be thinner to not overwhelm the drainage system and instead allow for fluid accumulation and discharge though the outlet channel. Given the long history of Mars, it is likely that this region experienced a series of separate ice deposits that may have driven or modified this system.

Within the current enclosed basin contour is the dark-toned basin fill material. The unit has steep edges with roughly layered light-toned olivine with magnesium carbonate spectral signatures. Similar carbonates have been observed throughout the region [Ehlmann et al., 2009, Mustard et al., 2009] and are not considered unique to the basin. The basin fill unit, however is unique to the basin. Its presence could be explained by late stage volcanism partially filling in the local low, or it could be a depositional unit from the fluvial actively. The water flowing off the source region volcanics had significant erosional potential, with several kilometers of volcanics eroded where the streams flowed over the cliffs. These volcanic materials could have been eroded by the fluvial activity and then deposited in the basin on top of the existing carbonates. This leads to mineral stability issues. The waters would have flowed through the sulfate layers at the base of the source region volcanics potentially becoming acidic in the process. Acidic waters have the potential to dissolve the carbonate minerals expressed throughout the basin. The current exposure of the carbonates suggests that the fluids remained with a neutral pH despite interaction with the sulfate units; the duration of fluvial activity wasn't

long enough to dissolve the carbonates; or that the carbonates were buried during fluvial activity and only recently exposed.

Conclusions

The Hesperian-aged fluvial system located on the edge northeast Syrtis boundary records important late stage geologic events that are vital to understanding the full geologic history of the region. This system represents the second distinct episode of fluvial activity in the region; with the first defined by the Jezero open basin crater lake at 3.74 Ga [Fassett and Head, 2008]. This second episode is constrained to occur after the early Hesperian emplacement of Syrtis Major volcanics. The fluvial system is defined by the observation of high elevation lineated erosional features on the basalts that indicate the system's source, a topographic basin that indicates fluvial storage and an outlet channel flowing toward the low elevation Isidis Basin. The absence of clear source morphology suggests an atmospheric origin of the system's water, such as snow or ice deposits. The observation of the outlet channel is not consistent with current topography and would require either significant erosion on the southeast edge of the basin or the existence of a temporary ice dam, further constraining the geologic history of the region. The combination of these observations contribute to a more dynamic and detailed understanding of the late-stage geology in the northeast Syrtis region.

References:

Andrews-Hanna., J.C., Phillips, R.J., and M.T. Zuber (2007), Meridiani Planum and the global hydrology of Mars. *Nature*, 446, doi:10.1038/nature05594.

Baker, V.R. (1982), *The Channels of Mars.* Austin: Texas University Press.

Bibring et al., (2006), Global Mineralogical and Aqueous Mars History Derived from OMEGA/Mars Express Data. *Science*, 312, 400, doi:10.1126/science.1122659.

Broxton, M. J. and L. J. Edwards. (2008), The Ames Stereo Pipeline: Automated 3D Surface Reconstruction from Orbital Imagery. Lunar and Planetary Science Conference 39, abstract #2419.

Christensen et al., (2004), The Thermal Emission Imaging System (THEMIS) for the Mars 2001 Odyssey Mission. *Space Sci. Rev.*, 110, 85-130.

Ehlmann et al. (2008a) Clay minerals in delta deposits and organic preservation potential on Mars. *Nat. Geo.*, 1, 355-358.

Ehlmann et al. (2008b) Orbital Identification of Carbonate-Bearing Rocks on Mars. *Science*, 322, 1828-1832.

Ehlmann, B. L., et al. (2009), Identification of hydrated silicate minerals on Mars using MRO-CRISM: Geologic context near Nili Fossae and implications for aqueous alteration, *J. Geophys. Res.*, 114, E00D08, doi:10.1029/2009JE003339.

Ehlmann, B.L. and J.F. Mustard (2012) An in-situ record of major environmental transitions on early Mars at Northeast Syrtis Major. *GRL* In submission

Fassett, C.I. and J.W. Head III (2005), Fluvial sedimentary deposits on Mars: Ancient deltas in a crater lake in the Nili Fossae region. *GRL*, 32, L14201, doi:10.1029/2005GL023456.

Fassett, C.I. and J.W. Head III (2008), The timing of martian network activity: Constraints from buffered crater counting. *Icarus*, 195, 61-89.

Goudge, T.A. et al. (2012), Constraints on the History of Open-Basin Lakes on Mars from the Timing of Volcanic Resurfacing. 43rd LPSC, Houston, TX.

Hartmann, W.K. and G. Neukum (2001), Cratering Chronology and the Evolution of Mars. *Space Sci. Rev.*, 96, 165-194.

Hartmann, W.K., (2005) Martian cratering 8: Isochron refinement and the chronology of Mars. *Icarus* 174, 294-320.

Hiesinger, H., and J. W. Head III (2004), The Syrtis Major volcanic province, Mars: Synthesis from Mars Global Surveyor data, *J. Geophys. Res.*, 109, E01004, doi:10.1029/2003JE002143.

Head et al. (2003), Recent ice ages on Mars. *Nature*, 426,797-802.

Hurwitz, D. M., J. W. Head, L. Wilson, and H. Hiesinger (2012), Origin of lunar sinuous rilles: Modeling effects of gravity, surface slope, and lava composition on erosion rates during the formation of Rima Prinz, J. Geophys. Res., 117, E00H14, doi:10.1029/2011JE004000.

Ivanov, M. A., and J. W. Head III, (2003) Syrtis Major and Isidis Basin contact: Morphological and topographic characteristics of Syrtis Major lava flows and material of the Vastitas Borealis Formation, *J. Geophys. Res.*, 108(E6), 5063, doi:10.1029/2002JE001994.

Kneissl T., van Gasselt S., Neukum G., (2010), Map-projection-independent crater size-frequency determination in GIS environments - New software tool for ArcGIS, *Planetary and Space Science.*

Malin, M. C., et al. (2007), Context Camera Investigation on board the Mars Reconnaissance Orbiter, *J. Geophys. Res.*, 112, E05S04, doi:10.1029/2006JE002808.

Mangold, et al. (2008), Identification of a new outflow channel on Mars in Syrtis Major Planum

using HRSC/MEx data. *Planet & Sp. Sci.*, 56, 1030-1042.

McEwen et al. (2007), Mars Reconnaissance Orbiter's High Resolution Imaging Science Experiment (HiRISE). *J. Geophys. Res.*, **112**, E05S02, doi:10.1029/2005JE002605.

Mustard et al. (2007), Mineralogy of the Nili Fossae region with OMEGA/Mars Express data: 1. Ancient impact melt in the Isidis Basin and implications for the transition from the Noachian to Hesperian. *J. Geophys. Res.*, 112, E08S03, doi:10.1029/2006JE002834.

Mustard, J. F., B. L. Ehlmann, S. L. Murchie, F. Poulet, N. Mangold, J. W. Head, J.-P. Bibring, and L. H. Roach (2009), Composition, Morphology, and Stratigraphy of Noachian Crust around the Isidis basin, *J. Geophys. Res.*, 114, E00D12, doi:10.1029/2009JE003349.

Mustard et al. (2001) Evidence for recent climate change on Mars from the identification of youthful near-surface ground ice. *Nature*, 412, 6845, 411-414.

Schaber, G. G., Syrtis Major, a low relief volcanic shield, *J. Geophys. Res.*, 87, 9852-9866, 1982.

Schon, S.C., et al., (2012) An overfilled lacustrine system and progradational delta in Jezero crater , Mars: Implications or Noachian climate. *Planetary and Space Science.*, doi:10.1016/j.pss.2012.02.003.

Skok, J. R., J. F. Mustard, S. L. Murchie, M. B. Wyatt, and B. L. Ehlmann (2010), Spectrally distinct ejecta in Syrtis Major, Mars: Evidence for environmental change at the Hesperian-Amazonian boundary, *J. Geophys. Res.*, 115, E00D14, doi:10.1029/2009JE003338.

Tanaka, K., (1986), The Stratigraphy of Mars. *J. Geophys. Res*., 91, B13, E139-E158.

Tornabene, L. L., J. E. Moersch, H. Y. McSween Jr., V. E. Hamilton, J. L. Piatek, and P. R. Christensen (2008), Surface and crater-exposed lithologic units of the Isidis Basin as mapped by coanalysis of THEMIS and TES derived data products, *J. Geophys. Res.*, 113, E10001, doi:10.1029/2007JE002988.

Wichman, R.W. and P.H. Schultz (1989), Sequence and Mechanisms of Deformation Around the Hellas and Isidis Impact Basins on Mars. *J. Geophys. Res.*, 94, B12, 17,333-17,357.

Zuber, M.t., D.E. Smith, J.W. Head, D.O. Muhleman, S.C. Solomon, J.B. Garvin, J.B. Abshire, and J.L. Bufton (1992), The Mars Observer laser altimeter investigation, *J. Geophys. Res.*, 97, 7781-7797.

Werner, S. C. (2005), Major aspects of the chrono-stratigraphy and geologic evolutionary history of Mars, Ph.D. dissertation, Cuvilier, Berlin.

Figure Captions

Figure 1. Left) Regional context of the northeast Syrtis region. The geologic history of the region has been influenced by the formation of the Isidis Basin and the subsequent tectonic opening of the Nili Fossae fault zones. The region is located at the Northern edge of the Early Hesperian Syrtis Major volcanic flows. (MOLA) Right) Jezero Crater is a well preserved open basin lake with a developed fluvial delta system with layered phyllosilicates. Lava flows to the south were emplaced in the early Hesperian Syrtis Major eruption which overlay extensive sulfates deposits. (THEMIS Daytime IR).

Figure 2. Map of hydrologic system on the edge of northeast Syrtis. Etched source fluvial morphology is mapped in blue, outlet channels are mapped in green. Cyan shaded contour (-2450 m) indicates the highest level fully enclosed by the current basin topography. Red contour (-2350 m) indicates minimum lake level required to activate the eastern outlet channel. (CTX mosaic)

Figure 3. Example of source region terrain with lightly eroded braided channels on volcanic materials. Upper Right Inset) CTX mosaic shows the source flow features leaving the volcanics that were deeply eroded by significant flow. Source fluvial morphology is divided mainly between the east and south channels with minors features directed to the north. Bottom Left Inset) Braided erosional grooves in fluvial source region.

Figure 4. Basin topography. The topographic low that forms the lake basin in this fluvial system. The interior, contour (-2450 m) shows the current topographic boundary of the basin that would flow to the southeast, there is little evidence for fluvial activity for this route and it may have formed from aeolian erosion or collapse. The exterior contour (-2350 m) shows the topographic

boundary that would have activated the eastern outlet channel. (MOLA topography on CTX imagery)

Figure 5. Basin mineralogy. Same contours as Figure 4 (Interior: -2450 m, Exterior: -2350 m). Background has CRISM RGB (R: 2.5μm, G: 1.5 μm, B: 1.0 μm) on CTX. Basin fill unit coincides with edges of blue contour line with magnesium carbonate (Bight Green in CRISM stamp) exposed around the edges of the fill units.

Figure 6. HiRISE view of basin fill unit. The unit is highly textured and retains craters. Fill unit is spectrally non-distinct but is surrounded by light-toned, layered olivine and magnesium carbonate deposits (Figure 7). Carbonates underlie the fill unit and are exposed around the edges of a 500 m crater (inset) on the basin fill, constraining the fill unit thickness to ~40 m.

Figure 7. Detailed HiRISE view of edge of fill unit with light-toned, layered olivine and magnesium carbonate-bearing deposits around the edge.

Figure 8. CRISM ratioed reflectance of magnesium carbonate ($MgCO_3$) on edge of basin fill units. (FRT000199C7). Laboratory magnesite spectra for comparison (LACB03B). Spectra identified by characteristic absorption features at 2.32 and 2.51 μm.

Figure 9. OutletChannel Morphology. Mapped outlet channel with multiple routes. Inset) Close up look at channel with defined walls, floor ripples and possible evidence of multiple out flows (right edge).

Figure 10. Crater counted regions. Areas where crater counts were performed and the calculated ages using chronologies from Hartmann and Neukum, [2001]. Yellow is Syrtis Major volcanic plains, Purple is Jezero volcanics, Blue are the Noachian plains, Red is the basin fill unit.

Figure 11. Cumulative crater counting plots. A) The Noachian Plains encompass the nominal landing ellipse. Extensive erosion and exhumation have created several crater populations with a noticeable inflection point at ~800 m. We calculate the age with the larger, more stable crater population. B) The lava flows offer a well preserved crater collecting surfacing. C) Basin Depression shows the youngest determined range in the region. Young age may be due to recent sedimentation or exhumation to reduce crater population. D) Interior volcanic deposits inside Jezero bracket fluvial activity and correspond with Syrtis lava flows [Goudge, personal communications].

Figure 12. Proposed ice sheet limits during time of Syrtis Major emplacement. “J” marks Jezero Crater to the immediately northeast of our study site. Top) Extent of Early Hesperian ice sheet that protected the basin topographic lows on the Noachian plains. Bottom) Topography with dotted line indicating the cliff forming edge of the Syrtis Major volcanics.

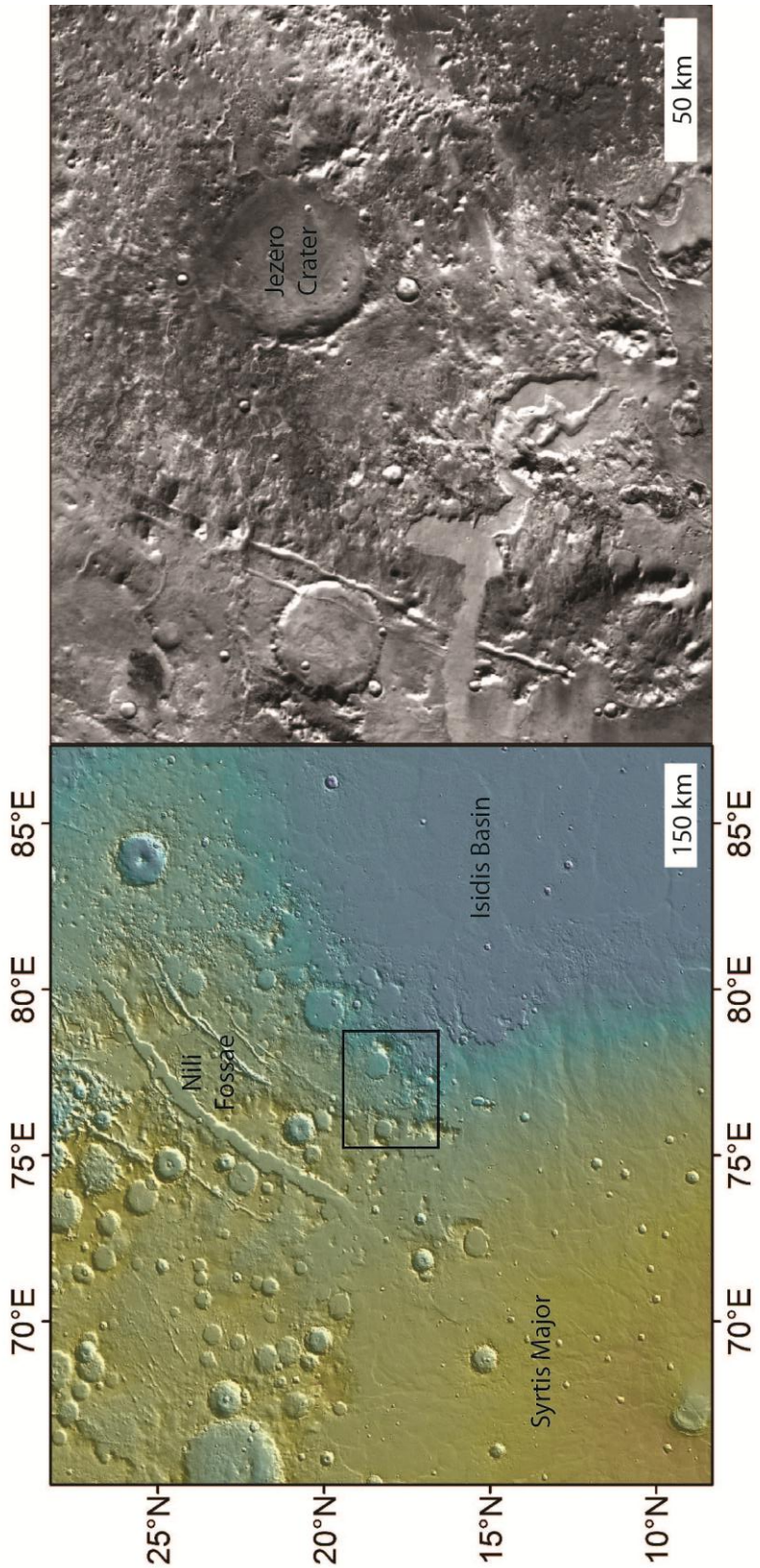

Chapter 3, Figure 1

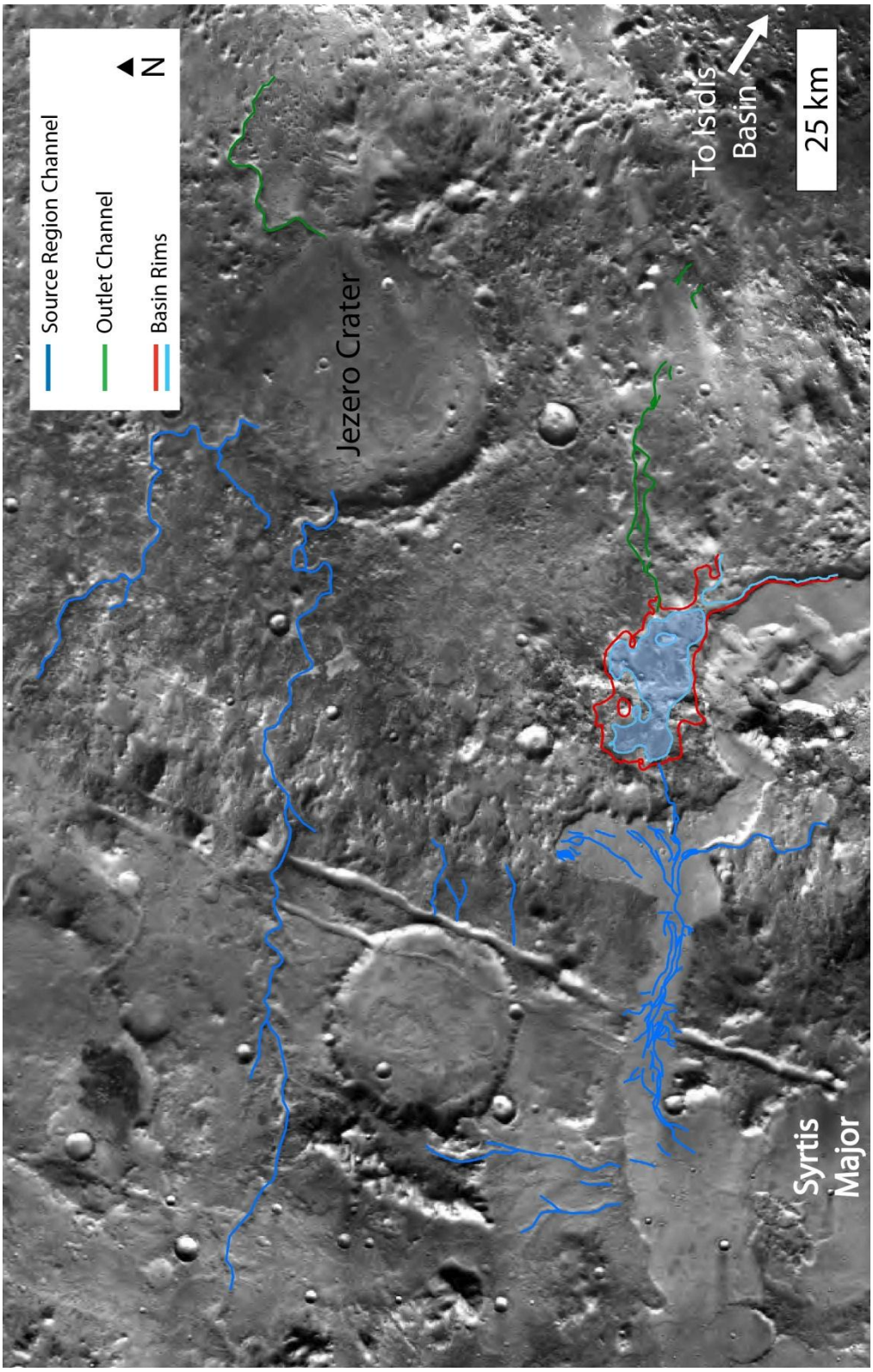

Chapter 3, Figure 2

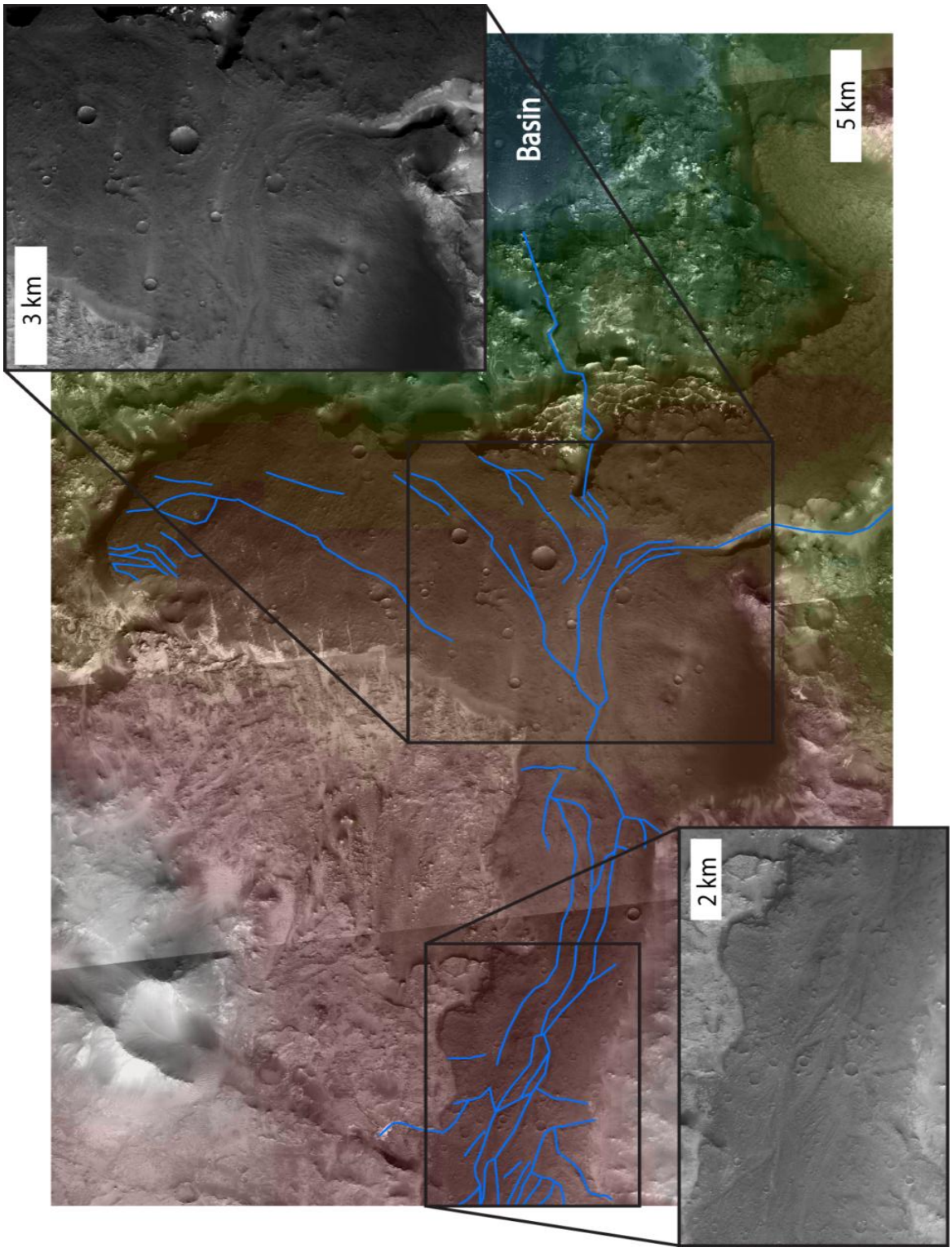

Chapter 3, Figure 3

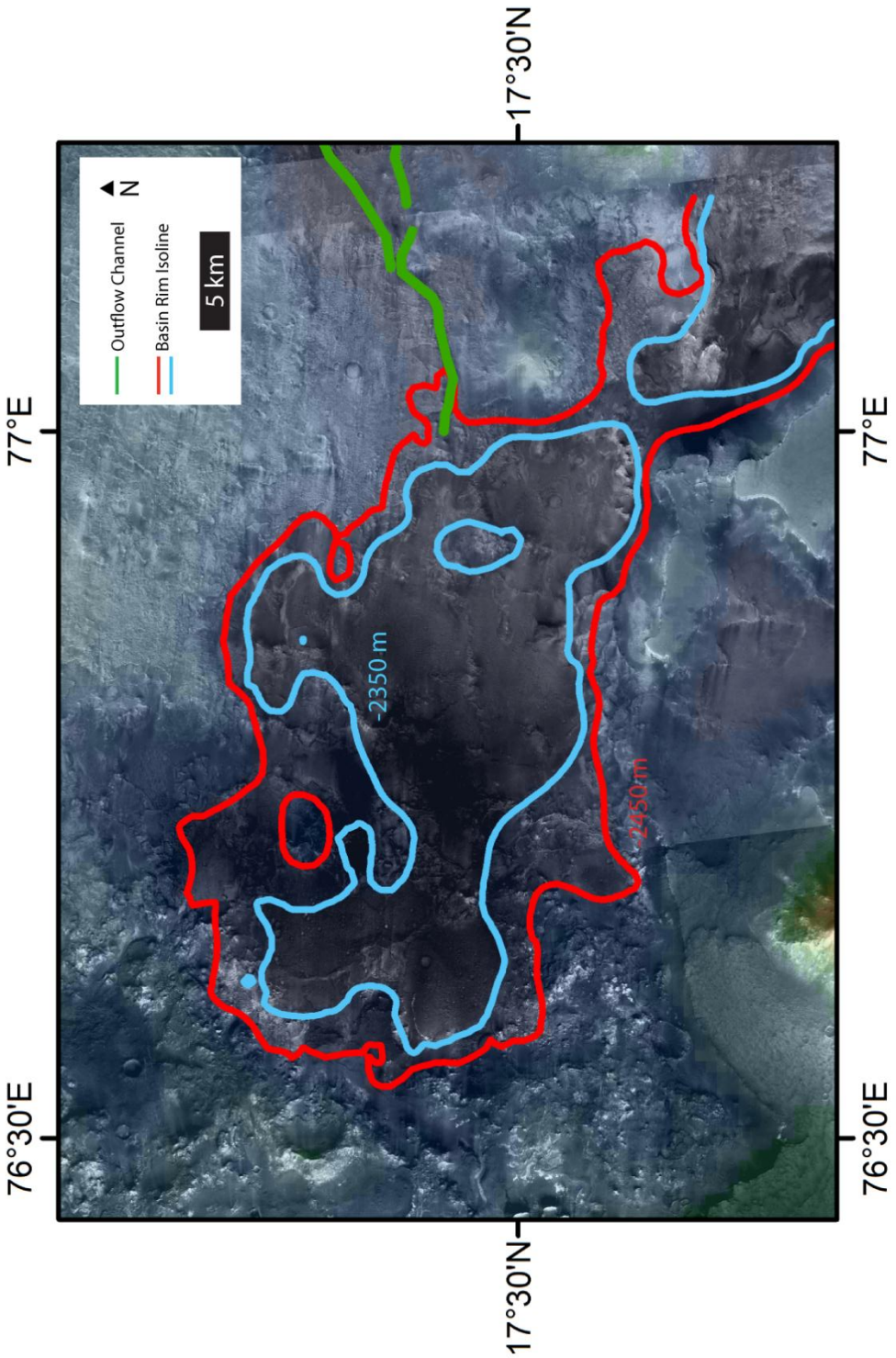

Chapter 3, Figure 4

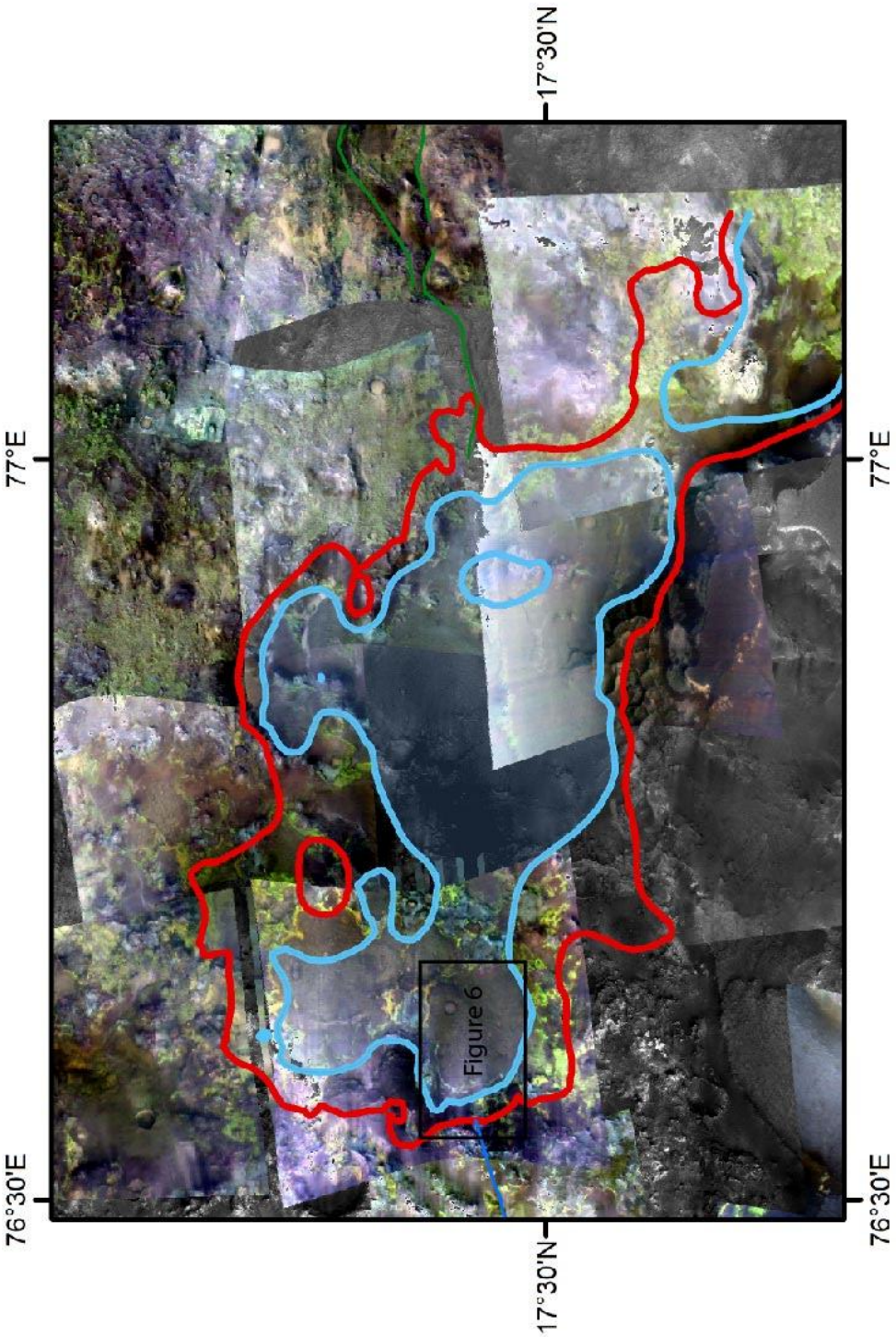

Chapter 3, Figure 5

Chapter 3, Figure 6

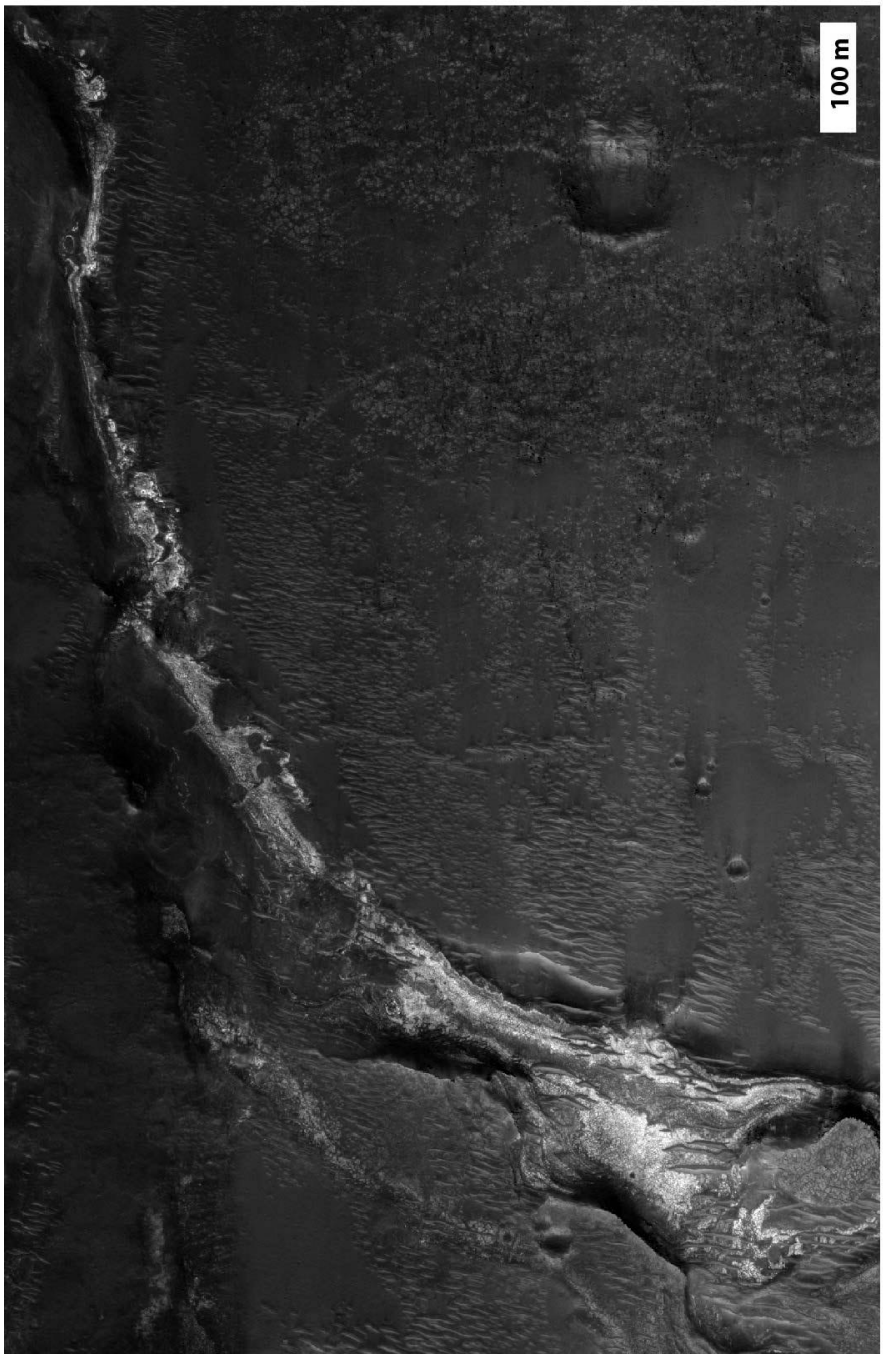

Chapter 3, Figure 7

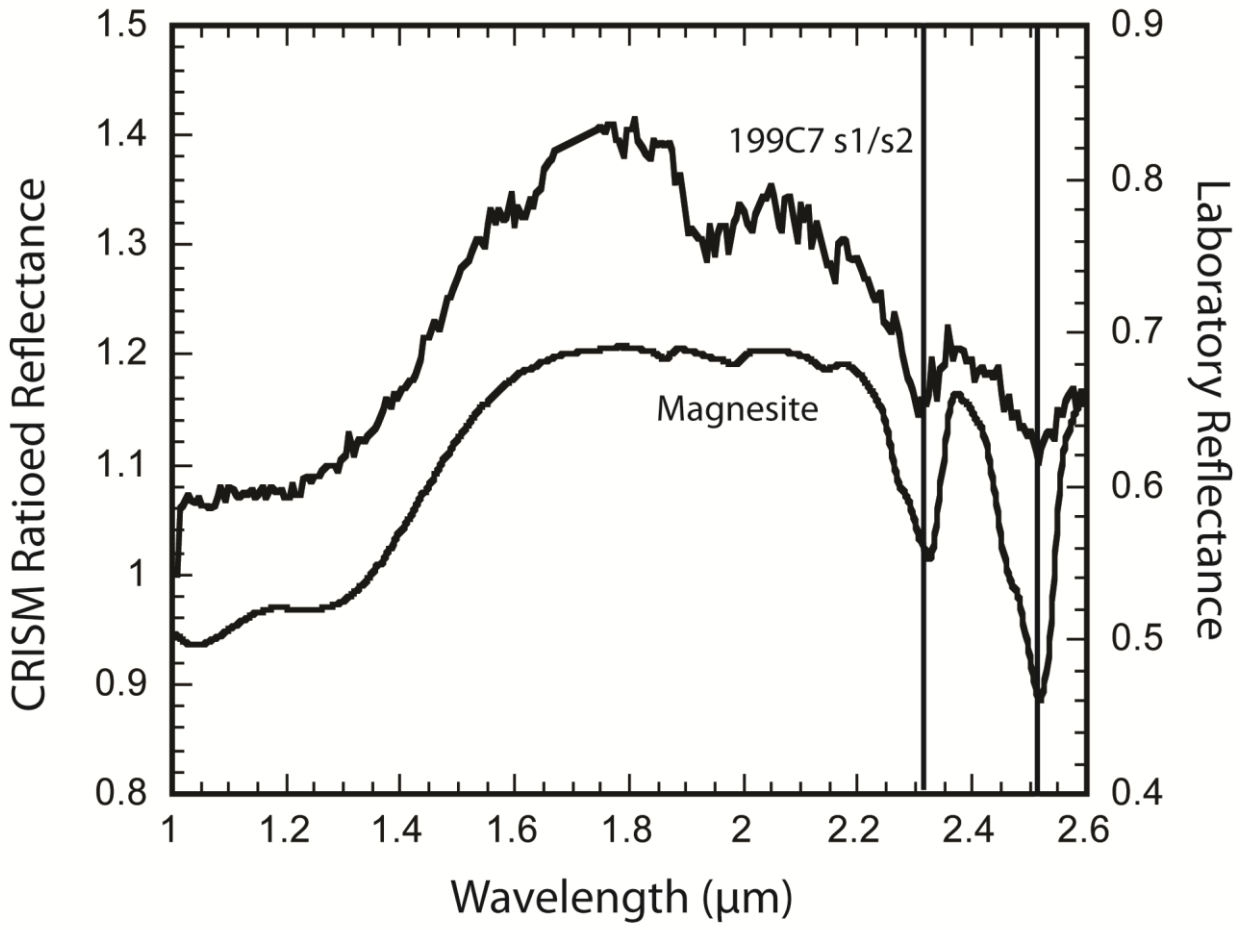

Chapter 3, Figure 8

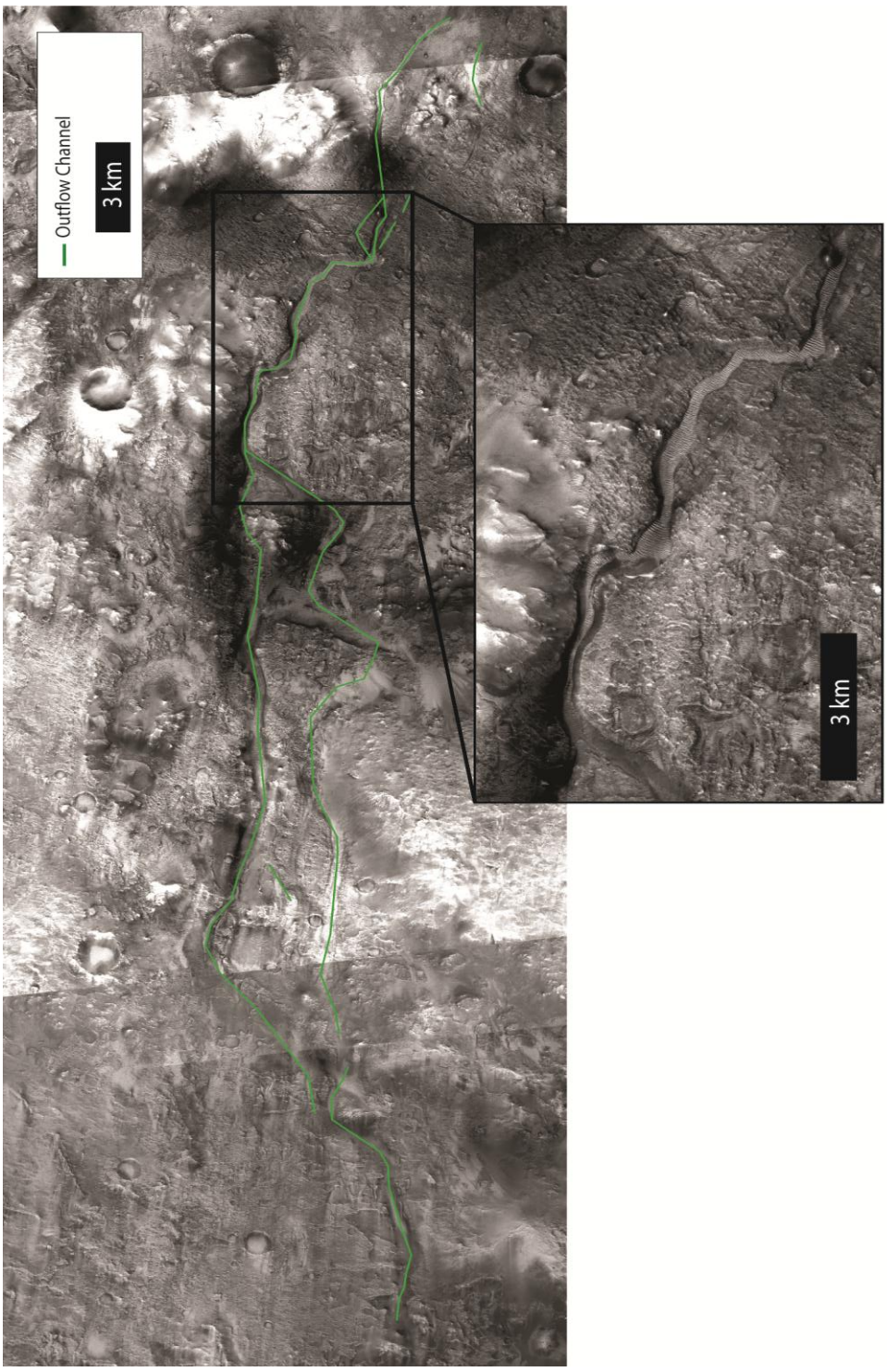

Chapter 3, Figure 9

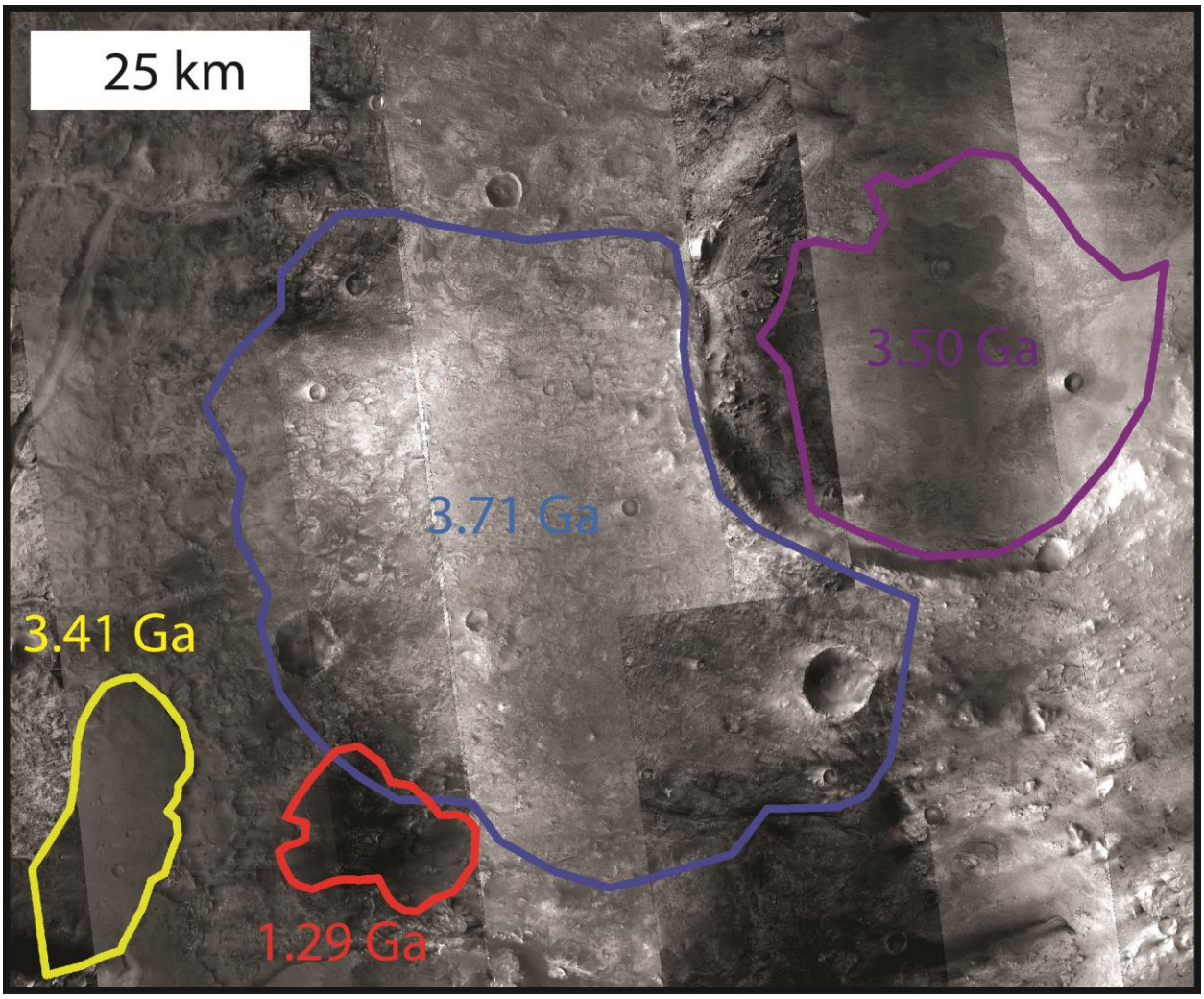

Chapter 3, Figure 10

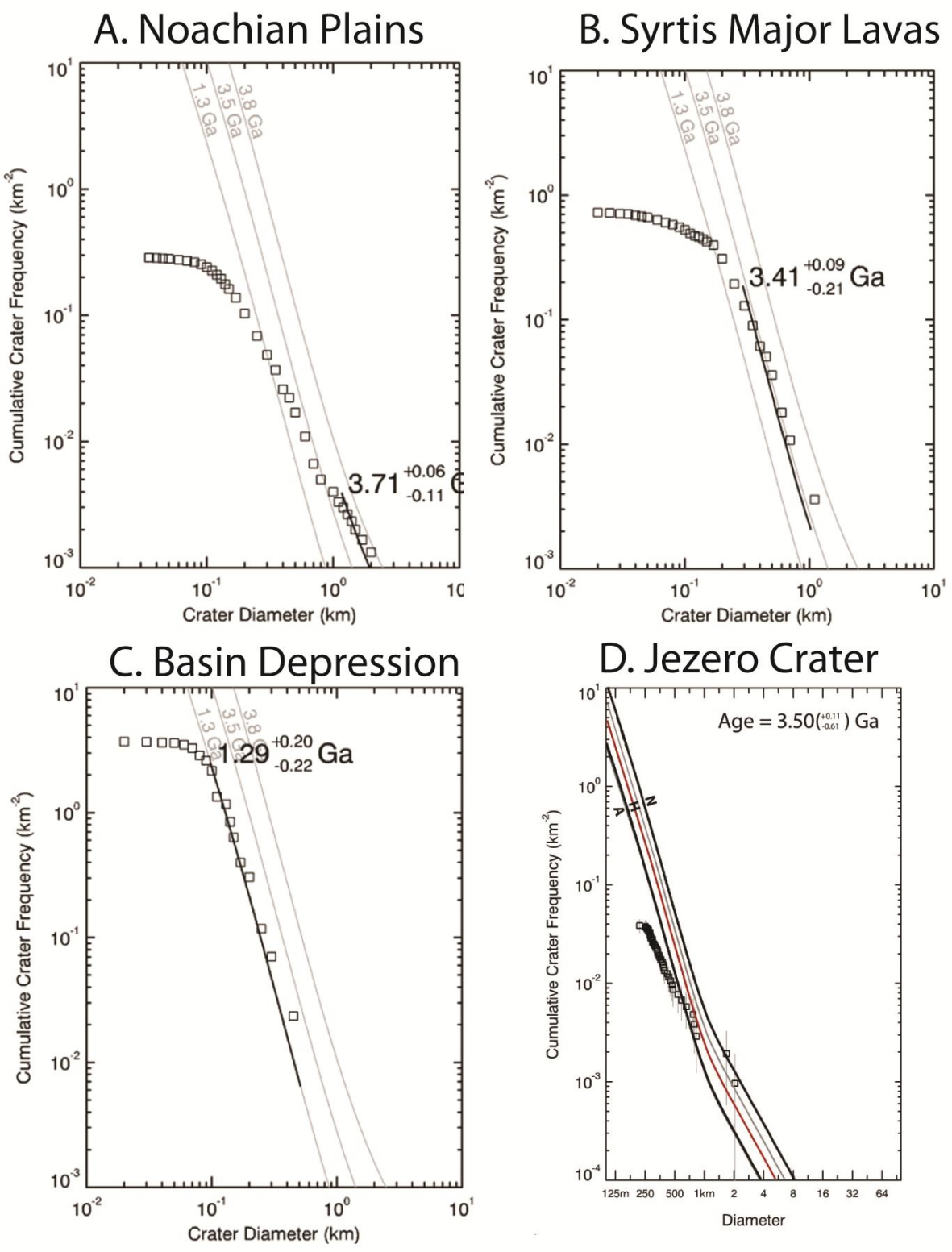

Chapter 3, Figure 11

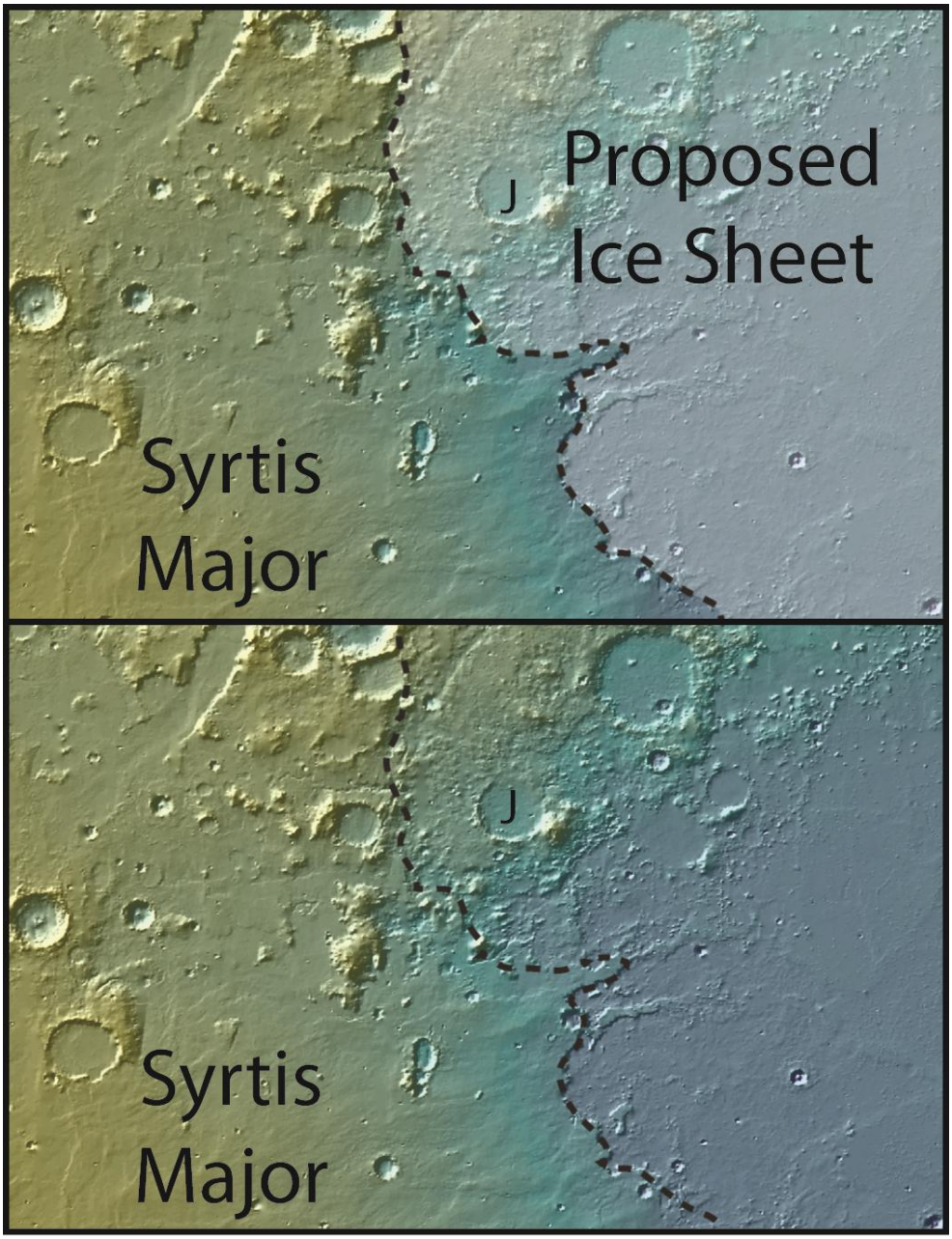

Chapter 3, Figure 12

Chapter 4:

Evolved Volcanism and Hydrothermal Deposits in the Nili Patera Caldera of Syrtis Major.

J.R. Skok[1], J.F. Mustard[1], B.L. Ehlmann[2], R.E. Milliken[3], S.L. Murchie[4]

1. Department of Geological Sciences, Brown University

2. Division of Geological and Planetary Sciences, California Institute of Technology

3. Department of Civil Engineering and Geological Sciences, University of Notre Dame

4. Applied Physics Laboratory, Johns Hopkins University

Expanded on Publication in:

Nature Geoscience, 31 Oct. 2010

Abstract

The Syrtis Major complex is a large well-preserved and relatively dust free early Hesperian volcanic center. The complex erupted in several phases and formed multiple superimposed calderas. Nili Patera is the youngest and northern most caldera and contains evidence of a late stage evolved lava flow. Within this caldera we focus on an isolated 100 m tall cone and a related light-toned lava flow with a dacitic composition. On and around the cone and dacite flow are numerous light-toned deposits. These deposits are spectrally identified as Si-OH (silica) bearing. Silica deposits in this volcanic context are evidence of a late stage and well-preserved hydrothermal system. While similar mineralogy can be produced by a number of formation mechanisms, the deposits are associated with topographic mounds suggesting a hot spring formational environment. Volumes of the mounds combined with observations of analog systems on Earth have been used to constrain the formation duration to be on the order of 1,000 and 100,000 years with a required minimum amount of water of 6-15 km^3. The history of active water, thermal energy and the preservation properties of silica deposits make this system an ideal place to search for signs of Martian habitability.

Introduction

The Syrtis Major volcanic complex on Mars is a type example of Hesperian plains volcanism (Figure 1). Crater statistics of the complex indicates formation in the Early Hesperian with major resurfacing completed by 3.7-3.8 Ga [Hiesinger and Head 2004; Skok et al. 2010]. Spectroscopic observations in the thermal infrared (TIR) and visible and near-infrared (VNIR) constrain the modal mineralogy and show the rocks to be consistent with an olivine-bearing

basaltic lava that is enriched in high-calcium pyroxene [Mustard et al., 1997; Baratoux et al., 2007; Rogers and Christensen, 2007; Poulet et al., 2009]. Near the center of Syrtis Major are two named calderas, Nili and Meroe Patera, at the northern and southern ends of an elongated depression that indicate multiple caldera formation episodes [Schaber, 1982; Crumpler et al. 1996; Hiesinger and Head 2004]. The Nili Patera caldera (Figure 2) hosts a 100 m high degraded cone on the northeastern side of its floor and a spatially related lighter-toned lava flow to the west of the cone. The Nili Patera volcanic cone is unique in its region and is the only local late-stage volcanic feature with significant topography, possibly indicating a more viscous Si-rich composition or the eruption of material to create a cinder cone. TIR spectral properties of this flow have been interpreted as either due to a glassy dacitic composition or possibly a high-Si glass alteration product [Christensen et al., 2005]. On the west side of the cone a moderately sloping flank with streaks of varying albedo likely results from downslope movement of materials. The east side of the cone has been removed likely either by an explosive eruptive process or extensive erosion.

Observations of this volcanic cone and lava flow with the Compact Reconnaissance Imaging Spectrometer for Mars (CRISM) on the Mars Reconnaissance Orbiter (MRO) show that many of the small exposures of light-toned materials exhibit distinct spectroscopic signatures consistent with a hydrated silica deposit. Although silica has been detected at several other locations on Mars [Squyres et al., 2008; Milliken et al., 2008; Ehlmann et al., 2009; Ruff et al., 2011], this is the first time it has been observed in close geologic context with a well-preserved volcanic source. The pristine condition of this source allows us to confidently determine the deposit volumes and spatial extent with remote observations. These observations are combined

in the context of terrestrial hydrothermal systems to better characterize the deposits and the underlying system.

Methods

Spectral Identification. Observations from the CRISM instrument provide the fundamental observations of these cone deposits that were used to make the alteration mineral detection. The CRISM imaging spectrometer measures solar reflectance in the VNIR wavelength region (0.36-3.92 μm) with a full spatial resolution of ~18 m/pixel [Murchie et al. 2007]. CRISM data are calibrated to radiance and divided by the solar spectrum, giving I/F values. Simple photometric and atmospheric corrections are then performed on a pixel-by-pixel basis by first dividing by the cosine of the incidence angle and then dividing by a scaled atmospheric transmission spectrum obtained via the volcano scan method [McGuire et al., 2009]. The reported distribution of silica deposits is based on the mapping of overtone and combination tone absorptions using spectral parameter BD2200 [Pelkey et al., 2007]. The parameter highlights regions of interest that are then validated by examination of spectral ratios. For the Nili Patera cone, the spectral parameter map of the 2.2 μm combination tone correlates to light-toned surface deposits. Mineral detections were made with the following custom parameter that was developed to increase the signal to noise and highlight the featured deposits:

$$1 - 2 * \left(\frac{average(2190-2250)}{average(2050-2130)+average(2360-2430)}\right) \quad (1)$$

Where average(####-####) is the average values of the 10 CRISM spectral bands between the wavelength list as ####.

CTX & HiRISE DEM Production. Overlapping Context Imager (CTX) [Malin et al. 2007][ID:P04_002427_1888_XI_08N292W; P18_008255_1888_XN_08N292W] and High Resolution Imaging Science Experiment (HiRISE) imaging data [ID:ESP_013582_1895; ESP_020940_1895] were processed with the Ames Stereo Pipeline software [Broxton et al. 2011]. Overlapping images were selected with moderate to high incidence angle from orbits on either side of the targeted site to provide perspective on the topographic features. The images are first aligned using an automatic alignment algorithm built into the software. Next each pixel is correlated to the corresponding pixel of the other image creating a disparity map. A sub-pixel refining method is then employed to smooth out instrument artifacts. Finally, using instrument information contained in the ISIS database on each planetary camera, the elevation of each point is triangulated based on the known position of the spacecraft and the disparity of each pixel pair. This result is then used to construct the DEM used in this analysis.

Analog Methods. Hydrothermal system properties were determined from measured dimensions of the deposits and the application of terrestrial analog observational values. Deposit spatial dimensions were determined from CTX and HiRISE projected data. Deposit height was determined from a CTX derived DEM focusing on the mound deposit immediately south of the volcanic cone. Spatial Analyst tools in the ArcGIS software suite were used to determine the deposit volumes. Deposits were assumed to be pure silica with a density of 2600 kg/m^3. Current estimates do not account for potential silica porosity. Density and volume can be used to calculate the mass of each deposit and determine the mass per area (kg/m^2). This value (mass per area), when divided by the observed terrestrial deposition rates, determined by Tolber et al.

[2008] (Table 1), provide the time required for deposit formation. Terrestrial observations of the SiO_2 content of fluids provide a range of values to determine water and magma volumes. The mass of each deposit was then converted into SiO_2 molar values to determine molar H_2O required for a range of concentrations and provide the minimum water required for observed deposits assuming complete deposition of dissolved silica.

Examination of the Puna Dacite analog [Teplow et al., 2009] in Hawaii provide analog values to estimate, in a similar geologic setting, the minimum dacite and basaltic magmatic volumes. These estimates are based on the assumption that the hydrothermal water that was used in silica deposition was sourced from differentiation of the magma chamber. With this assumption, we use the terrestrial analog Hawaiian dacite value of 2.44% H_2O content and the determination that each unit of dacite melt would require 75 parts basalt source melt [Teplow et al., 2009]. The estimates based on these analogs are minimum values that assume all of the magmatic waters deposited SiO_2 at the surface at the analog concentrations.

Results

Spectral Results. The light-toned deposits identified on and around the Nili Patera cone (Figure 3) are characterized by a deep, broad asymmetric absorption near 2.2 μm when ratioed to surrounding volcanic surfaces (Figure 4). The band depth of this feature is 3-4%, and the exact band center shifts from 2.21 to 2.25 μm depending on the particular deposit. Ratioed spectra of the light-toned deposits also show a very broad absorption centered near 3 μm. Large area averages show 1.4 and 1.9 μm absorptions that are just detectable above the level of noise in the data (Figure 4c).

A broad absorption near 2.21 μm is caused by a combination tone (–OH stretch and Si-OH bend) that produces overlapping absorptions at 2.21 μm and 2.26 μm caused by isolated Si-OH and H-bound Si-OH, respectively [Anderson and Wickersheim, 1964; Goryniuk et al., 2004]. These are distinct from narrower Al-OH features near 2.2 μm in aluminum phyllosilicates [Milliken et al., 2008]. Laboratory silica samples also typically exhibit absorption features near 1.4 μm due to the OH bend overtone near 1.38-1.39 μm and H_2O combination tones from 1.41-1.46 μm [Anderson and Wickersheim, 1964; Goryniuk et al., 2004] as well as a 1.9-μm H_2O combination tone [Goryniuk et al., 2004].

The Nili Patera detections are spectrally distinctive from detections of opaline silica and a similar broad 2.2 μm absorption elsewhere on Mars because of comparatively weak 1.4- and 1.9-μm hydroxyl- and water-related absorption features [Goryniuk et al., 2004]. Laboratory experiments have shown that dehydration of silica can decrease the strength of H_2O-related absorptions either through heating [Milliken, 2006] or exposure to Mars-like atmospheres [Cloutis et al., 2009]. Additional constituents in the deposits such as metal oxides may also obscure the shorter wavelength vibrational absorptions, and may also be responsible for the enhanced short wavelength (<1.5 um) broad absorption in unratioed spectra (Figure 4c). Fe- and Ti- oxides have been shown to co-occur with hydrated silica precipitates in terrestrial settings as micron-scale coatings [Cloutis et al., 2009; Chemtob et al., 2009]. The asymmetrical shape, strength, width, and position of the 2.21 μm absorption, the presence of an enhanced 3.0 μm feature, and the presence but weakness of the 1.4 and 1.9 μm absorptions lead to the identification of weakly hydrated amorphous silica for the spectrally distinct phase. However it is important to note that from the current spectral observations we cannot conclusively determine if this deposit formed as a typical hydrated silica that subsequently lost much of the H_2O, if the

distinctive spectral properties represent an original characteristic of silica, or if the hydration features are merely being obscured by other constituents.

Silica Distribution and Morphology. Initial reporting of the silica deposits identified only the proximal deposits adjacent to the volcanic cone [Skok et al., 2010]. These are located to the south and west of the cone and near the cone's summit (Figure 5). Confirmed individual silica deposits range in area from 0.21 km^2 to the 18 meter/pixel resolution limit of the CRISM instrument. The largest deposit is on the western flank of the cone and radiates from a high point at 290 m elevation in a fan shape down to the cone base at 230 m (Figure 6). HiRISE imagery of this deposit (Figure 3c) indicates that the silica material is a diffuse deposit mixed with mobile surface material which preferentially fills in the topographic lows. Because of the location and morphology of this cone-flank silica deposit, we infer that it preserves the original setting of silica formation, with the fan shape of the deposit resulting from the precipitation of silica from surface fluid flows. The silica deposits located on the light-toned volcanic flow on the floor of the Nili Patera caldera are smaller and are circular or semi-circular in shape, possibly indicating localized source vents (Figure 3d). Directly south of the cone is a 20 m high circular deposit (South Mound) that is brightest in the center and fades outwards. Additional silica deposits occur just to the west of the cone's summit ridge. These deposits are exposed in several constant elevation layers with just a thin band visible among the volcanic slope debris.

The second area with confirmed SiO_2 spectra are the distal deposits extending ~7 km north-south (Figure 7A, B). This light-toned region is roughly concentric to the cone and is continuous except for a ~400 meter gap near the center of length. Farther to west, on the edge of the dacite flow, 14 km from the cone is an additional region of light-toned features. These appear morphologically similar to the distal units but do not currently have spectral observations to

confirm the composition. Additional silica identifications are seen 11.5 km to the Southwest of the cone (Figure 7C, D). These deposits are noticeably less pristine, but potentially better spectrally exposed, than the proximal deposits, and are exposed only on the outside edges of highly modified small (~350 m) impact structures.

DEM Analysis of Mound Height. The production of a DEM from stereo CTX and HiRISE imagery provided a more detailed look at the scale of the silica mounds. Here we focus on one of the best defined examples, the South Mound deposit (Figure 8). This deposit has a clear topographic expression associated with a silica spectra identification that forms a roughly conical shape. A profile (Figure 8D) shows that the deposit is on the slope of the volcanic cone. Measuring from the average base elevation to the apex of the deposit yields a total height of ~20 m. The well expressed nature of this deposit is unique as many of the other deposits tend to be more aerially extensive and less vertically pronounced compared to the surrounding terrain. This led us to use the height value in future calculations of deposit volume.

Discussion

Formation Mechanisms. The formation of silica deposits has been extensively studied in a wide variety of environments on Earth. Silica sinter precipitated from fluids is typically associated with hydrothermal systems [Rodgers et al., 2004; Preston et al., 2008], but spatial extensive regions with silica can also be produced by several mechanisms including acid-fog alteration [Schiffman et al., 2006] or as alteration products from the weathering of ash or volcanic materials [McLennan, 2003]. Many of these mechanisms have been considered for various Martian environments [e.g.: Milliken et al., 2008; Ruff et al., 2011] and we describe the

various options in terms of the Nili Patera geologic context. We list the following mechanisms separately but recognize that some combination may apply.

The first possibility is that the silica signature is the result of a silica-rich surface coating analogous to those found in the Ka'u desert in Hawaii [e.g., Minitti et al., 2007; Chemtob et al., 2010]. These coatings are formed as acid-sulfate solutions leach away divalent and trivalent cations leaving a silica-rich coating several μm thick. The strong association of the observed silica deposits in Nili Patera with mounds several meters high suggest that the silica deposits are not purely surficial, however if the coatings were widespread, the mounds could be the locations of best exposure.

A second mechanism is an acid-sulfate leaching process where H_2S fumarole emissions produce low pH solutions that alter the materials around volcanic vents. The alteration mobilizes the cations leaving behind silica enrichment [e.g., White et al., 1988]. This mechanism is typically in and around an active fumarole vents, but the silica material can be redistributed post-formation by aeolian processes. Again, this mechanism would not directly explain the association with the mound structures other than a wide spread feature that is best exposed with high standing topography.

In addition to these high temperature formation mechanisms, silica deposits can be formed by low-temperature processes. Prominent among these is acid-fog alteration that dissolves the oxide components of the basaltic surface and precipitates amorphous silica [Tosca et al., 2004]. This process can potentially effect the large areas seen in Nili Patera, however the process often continues to deposit jarosite and other sulfates that are not detected spectrally at this site and do not account for the observed fan morphology on the flank deposit or the association with topographic mounds.

A final mechanism for silica formation is the precipitation of silica sinters from fluids in a hot spring or geyser-like environment. This process is common in most terrestrial volcanic fields with active groundwater flow and would explain the strong correlation between silica detections and the mound topography. The precipitation from a fluid would also best explain the fan shaped silica deposit on the southwest flank of the Nili Patera cone. While this mechanism is probable for the proximal deposits, the distal deposits imply that the either the hydrothermal fluid ascent could occur at a distance away from the cone or that the heat within the dacite lava flow would be enough to drive localized alteration systems to form these deposits with alteration fluids sourced from magmatic waters or ground water from the surrounding Noachian crust.

Insight from Earth Analogs. The production of topographic DEM with CTX and HiRISE observations allow for a detailed view of the dimensions of the described silica deposits. Integrating these measurements with observations from terrestrial analog silica system can constrain key properties of the system. Silica deposition has been well studied in a variety of terrestrial volcanic centers. Measuring the rate of silica deposition in analog sites can provide initial constraints on the understanding of the deposition of a similar feature on Mars. We here summarize the work by Tobler et al. [2008] detailing the silica deposition rates in Icelandic hydrothermal systems. The study placed trays of glass slides in water runoff from volcanically driven hydrothermal system. The trays were left for periods ranging from days to years depending on the deposition rate. The mass of deposited silica and elapsed time allowed determination of silica precipitation rates. These values were then presented with characteristic properties of the fluids (Table 1).

Applying terrestrial values to a Martian system requires caution and a clear understanding of the fundamental differences in the systems. Where Iceland is a relatively wet terrain with

abundant rainfall and water runoff, Mars during the time of silica deposition was likely water limited with conditions unstable for standing surface water [Haberle et al., 2001]. In the Iceland analog sites, silica precipitation was a function of SiO_2 concentration, temperature, pH, and salinity. On Mars the controlling factor was most likely the rate of fluid flow, as surface water would quickly evaporate under Martian atmospheric conditions causing the complete deposition of the fluid's dissolved SiO_2 content.

Another terrestrial analog used to constrain the Martian system is the Puna dacite found on the island of Hawaii [Teplow et al., 2009]. The Hawaiian volcanic hotspot is a good analog to the entire Syrtis Major complex with its basaltic composition and multiple eruptive events. Hawaii is a much better analog than the usual subduction arc volcanics that produces most terrestrial dacite deposits. In 2005, drilling on Kilauea Lower East Rift Zone (KLERZ) encountered a dacitic melt composition at a depth of 2488 m [Teplow et al., 2009]. This composition is very rare on Hawaii and indicates a high degree of fractionation to concentrate the silica component. A similar fractionation process would have had to occur in Syrtis Major and erupted in one of the last volcanic episodes. While the formation of this Puna melt is still being researched, the initial analysis provides two values that can constrain the volcanic eruptions in Syrtis Major. In the Puna dacitic melt, the H_2O fraction is measured at 2.44 wt.% and the magma fractionation required 75 parts parent basalt to concentrate one unit of dacite [Teplow et al., 2009]. These values are used below to constrain the volcanic history of the Syrtis Major volcanic complex.

Mound Volume Determination. The CTX and HiRISE DEM of the Nili Patera caldera and silica deposits confirms and quantifies the observations that the South Mound is on a topographic mound structure and that every observed silica deposit on the caldera floor has some

topographic expression. We initially focus on the South Mound as it isolated from other deposits and is particularly well-preserved. Figure 8 shows a north-south transect on the southern margin of the volcanic cone and across the South Mound. The silica mound is superimposed on the slope of the cone and so we estimate the height from the mound peak to the distance halfway between the upper and lower slope. This yields a height of 20 meters with a base area mapped at ~30,000 m^2. These dimensions yield a conical volume of ~200,000 m^3. Our initial calculations assume the mounds are essentially pure SiO_2, with a density of 2,600 kg/m^3. This yields a total mass of ~$5.19x10^8$ kg and a mass per area of ~17,300 kg/m^2. This can be combined with the measured silica deposition rates from the Iceland analog. Plugging in rates (Table 1) on both the high (20 kg/yr m^2) and low (0.2 kg/yr m^2) end of natural systems, we get a range of 870 yrs to 87,000 yrs to deposit the observed material (Table 2).

We can use the measured deposit volumes to also constrain the fluids required for deposition. The ~$5.19x10^8$ kg of the South Mound deposit yields $8.66x10^9$ mols SiO_2. The Iceland analog site had SiO_2 concentrations that range from 300-700 p.p.m. At 700 p.p.m., we require $1.23x10^{13}$ mols of H_2O or 0.22 km^3 and for 300 p.p.m, we require $2.89x10^{13}$ mols H_2O or 0.52 km^3. These estimates assume that the SiO_2 component of the fluids were fully deposited. This is consistent with surface conditions that have long been unstable for liquid water and no visible fluvial features around the deposits. These constraints can be expanded to include the rest of the silica deposits in Nili Patera. Mapping shows a total silica area of ~84,700 m^2. While many of these are not clearly resolved in the DEM to get individual volumes, where observed they do correspond to topographic mounds. Since background topography overwhelms silica mound height, we have not been able to use analytical techniques to determine volume of collective silica deposit. Instead we estimate volume given a general height of 20 m (measured

from South Mound) and approximate a cone shape of the mound, we get 5.65×10^6 m^3 of material yielding 1.47×10^{10} kg of SiO_2. This estimate is on the higher limit due to the well expressed nature of South Mound type example. We calculate 2.44×10^{11} mols of SiO_2 requiring 3.49×10^{14} mols H_2O or 6.29 km^3 at 700 p.p.m SiO_2 and 8.15×10^{14} mols H_2O or 14.7 km^3 at 300 p.p.m (Table 2). Again, this is the minimum water required at the given concentrations to explain the observed deposits.

The hydrothermal waters responsible for the silica deposits have two possible origins; ground waters activated by the volcanic heat (a potential fluid source region from Chapter 3) or magmatic waters segregated by magma differentiation (Figure 9). Current observations cannot distinguish between either possibilities, but each carries its own implications. In the ground water hypothesis, sufficient water (at least 6-14 km^3) would have to be available in volcanic rock that makes up the caldera floor. This water could have been transported in as precipitation or ice deposits [Forget et al., 2006], or sourced from a hydrated Noachian crust that is below and around the sunken caldera. If the fluids are entirely from a magmatic source, then we can constrain the magma content of this last stage of Syrtis Major volcanism. Invoking the Hawaiian Puna dacite as an analog, the dacite magma is 2.44 wt% H_2O with 75 times more basalt than dacite to allow the fractionation. Assuming that all the water is separated out of the dacite and reaches the surface to form the silica deposits, the low silica concentration (15 km^3 H_2O) yields 230 km^3 dacite and 52,000 km^3 basalt, while the high silica concentration (6 km^3 H_2O) yields 100 km^3 dacite and 7,400 km^3 basalt (Table 3). Since it is unlikely that all the magmatic water would have been separated and activated into the silica deposits, these would be minimum estimates.

Implication for Habitability. The search for extraterrestrial life is one of the ultimate goals for science and our space exploration program. This effort is currently manifested on Mars as the search for habitable environments. In this regard, volcanically driven hydrothermal systems have been extensively studied for their biologic capacity [Segerer et al., 1993]. The fluid, heat and nutrient-rich environment are ideal for many types of organisms and often foster the evolution of extremophiles that are well adapted at survival in extreme environments. Previous work has also suggested that volcanic vents could be the site of the origin for life on Earth [Nisbet and Sleep, 2001]. Given this abundant collection of evidence on Earth, it is very likely that if organisms suited to hydrothermal vents were available in the active system in Nili Patera, that they would have been able to survive in that environment. The next logical question is if this system had the opportunity to contact or form life?

Without substantial evidence, we speculate on plausible scenarios for life on Mars and the implications for the Nili Patera hydrothermal system. One possibility is that life on Mars may have originated on an early, warm, wet Mars as it did on Earth. Then as Mars cooled and dried and the active hydrosphere receded into the deep subsurface, the biosphere (primarily microbial is crustal pore spaces) would have followed it into the crust, were it remains a vertically segregated from the surface by a global cryosphere layer [Clifford and Parker, 2001]. This hypothesis could be tested with a sample extraction from a depth of several kilometers, far beyond current technological capabilities. However volcanics, such as those at Syrtis Major would have been sourced in the mantle and had to penetrate the buried hydrosphere. Magmatic heat would have melted the bounding cryosphere and may have provided a fluid rich conduit from the hydrosphere to source the surface deposits. In this scenario, the Nili Patera deposits could have tapped into a pre-existing subsurface biosphere and provide a suitable habitable

microenvironment ranging from the deep biosphere to the surface deposits for the duration of the hydrothermal system.

An alternate scenario is that if life did not exist in a preexisting global layer, could the hydrothermal system in Nili Patera have had time to develop life? The development of life is a very challenging problem. The organic building blocks of life seem to be readably synthesized given the right materials and energy [Miller and Urey, 1959], but the exact pathway to self-replicating life is unknown. However, as we have demonstrated earlier, at rates similar to natural silica deposition rates on Earth, the Nili Patera deposits would have required 1,000's-100,000's years to form with significant water and energy inputs. These estimates are based only on the preserved, observed deposits that occurred after all volcanic resurfacing. It is likely that the process was active throughout the length of active volcanism with only the last stage now observed. While it is unknown if these timescales are enough for life to evolve, it is likely that they would have been among the best opportunities available on Mars. Given these observations, these hydrothermal deposits are one of the best locations on Mars to have developed and preserved evidence of life or at the very least, signs of a once habitable environment.

Conclusions

The Silica deposits in the Nili Patera Caldera are the best preserved volcanically driven hydrothermal system on Mars and the only one initially identifiable from orbit. The hydrothermal determination is confirmed by the correlation of a 2.2 μm absorption feature with all the light-toned deposits on and around the Nili Patera volcanic cone. This absorption feature is best explained the diagnostic Si-OH bond. The related 1.9 μm molecular H_2O band and 1.4

μm combination tones are weak but also observed. These silica deposits are spatially related to the volcanic cone and the associated dacite lava flow. Morphologically, the deposits occur in semicircular or fan shape orientations consistent with point origins given the local slopes. The inspection of HiRISE analglyphs and analysis of CTX derived DEMs allow the determination of the volume of the silica mounds with individual deposits recorded in the range of several hundred thousand cubic meters. Comparison to terrestrial depositional rates and conditions can constrain the time component and water volume required with realistic values of 1000-100,000 yrs and 6-15 km^3 of water. The identification of a volcanically driven hydrothermal system has important astrobiological implications. The abundant heat and water required by the system could create a microenvironment conducive for the survival of life and potentially the requirements for its formation. The strong preservation properties of silica make this location a candidate for the search for past Martian life.

Acknowledgments

This work is supported by CRISM investigation on MRO under contract from JPL. Thanks to the MRO team for data collection, Ingrid Spitale for HiRISE acquisition, and Steve Ruff, Melissa Rice, Dick Morris and Kim Seelos for discussion and analysis help. Tim Goudge with HiRISE DEM.

References:

Amador, E.S and J.L Bandfield (2011), Mars Aqueous Mineralogy: A Comparison of Thermal-Infrared and Visible/Near-Infrared Spectral Data. Exploring Mars Habitability Conf.

Anderson, J. H., Jr., and K. A. Wickersheim (1964), Near infrared characterization of water and hydroxyl groups on silica surfaces, *Surf. Sci.*, **2**, 252– 260, doi:10.1016/0039-6028(64)90064-0.

Baratoux, D., P. Pinet, A. Gendrin, L. Kanner, J. Mustard, Y. Daydou, J. Vaucher, and J.-P. Bibring (2007), Mineralogical structure of the subsurface of Syrtis Major fom OMEGA observations of lobate ejecta blankets, *J. Geophys. Res.,* 112, E08S05, doi:10.1029/2007JE002890.

Broxton et al. (2011), The Ames Stereo Pipeline: NASA's Open Source Automated Stereogrammetry Software A part of the NASA NeoGeography Toolkit. http://ti.arc.nasa.gov/tech/asr/intelligent-robotics/ngt/stereo/.

Chemtob, S.M., Jolliff, B. L., Rossman, G.R., Eiler, J.M. and R. E. Arvidson (2009), Silica coatings in the Ka'u Desert, Hawaii, a Mars analog terrain : A micromorphogical, spectral, chemical and isotopic study. *J. Geophys. Res.***115** E04001 doi:10.1029/2009JE003473.

Christensen, P.R., N.S. Gorelick, G.L. Mehall, and K.C. Murry, THEMIS Public Data Releases, Planetary System node, Arizona State University, http://themis-data.asu.edu.

Christensen, P.R. et al. (2005), Evidence for magmatic evolution and diversity on Mars from infrared observations. *Nature*, **436**, 7050, 504-509.

Clifford, S.M. and T.J. Parker (2001) The Evolution of the Martian Hydrosphere: Implications for the Fate of a Primordial Ocean and the Current State of the Northern Plains. *Icarus*, 154, 40-79.

Cloutis, E.A., et al. (2009), Spectral Reflectance Diversity of Silica-Rich Materials: Insights into Structure and Petrogenesis and Implications for Mars. Workshop on Modeling Martian Hydrous Environments. Houston, TX.

Crumpler, L. S., J. W. Head III, and J. C. Aubele (1996), Calderas on Mars: Characteristics, structure, and associated flank deformation, *Geol. Soc. Spec. Pub.*, **110**, 307– 348.

Ehlmann, B. L. et al. (2009), Identification of hydrated silicate minerals on Mars using MRO-CRISM: Geologic context near Nili Fossae and implication for aqueous alteration. *J. Geophys. Res.,***114**, E00D08, doi:10.1029/2009JE003339.

Farmer, J.D and Des Marais, D.J. (1999), Exploring for a record of ancient Martian life. *J. Geophys. Res.*, **104**, E11 26977-26995.

Forget, F, Haberle, R.M., Montmessin, F., Levrard, B., and J.W. Head, (2006) Formation of Glaciers on Mars by Atmospheric Precipitation at High Obliquity. Science, 311 , 368-371.

Goryniuk, M. C., B. A. Rivard, and B. Jones (2004), The reflectance spectra of opal-A (0.5–25 um) from the Taupo Volcanic Zone: Spectra that may identify hydrothermal systems on planetary surfaces. *Geophys. Res. Lett.***31**, L24701, doi:10.1029/2004GL021481.

Haberle, R. M., C. P. McKay, J. Schaeffer, N. A. Cabrol, E. A. Grin, A. P. Zent, and R. Quinn (2001), On the possibility of liquid water on present-day Mars, *J. Geophys. Res.*, 106, 23,317–23,326, doi:10.1029/2000JE001360.

Hiesinger, H., and J. W. Head III (2004), The Syrtis Major volcanic province, Mars: Synthesis from Mars Global Surveyor data. *J. Geophys. Res.*, **109**. E01004,

Malin et al. (2007), Context camera investigation on board the Mars Reconnaissance Orbiter., *J. Geophys. Res.*,**112**, E05S04, doi :10.1029/2006JE002808.

Marion, G.M., Catling, D.C., Crowley, J.K. and J.S. Kargel (2011), Modeling hot spring chemistries with applications to martian silica. Icarus. 212, 629-642.

McEwen et al. (2007), Mars Reconnaissance Orbiter's High Resolution Imaging Science Experiment (HiRISE). *J. Geophys. Res.*, **112**, E05S02, doi:10.1029/2005JE002605.

McGuire, et al., (2009), An improvement to the volcano-scan algorithm for atmospheric correction of CRISM and OMEGA spectral data. *Planet. Space Sci.*, 57, 809-815.

McLennan, S. M. (2003), Sedimentary silica on Mars, *Geology*, **31**, 4, 315-318.

Miller, S.L. and H.C. Urey (1959) Organic compound synthesis on primitive earth. Science, 130, (3370), 245-251.

Milliken, R.E. (2006), Estimating the Water Content of Geologic Materials Using Near-Infrared Reflectance Spectroscopy: Applications to Laboratory and Spacecraft Data. Ph.D Dissertation, Brown University.

Milliken, R.E. et al. (2008), Opaline silica in young deposits on Mars. *Geology*, **36**, 11, 847-850.

Minitti, M. E., C. M. Weitz, M. D. Lane, and J. L. Bishop (2007), Morphology, chemistry, and spectral properties of Hawaiian rock coatings and implications for Mars, J. Geophys. Res., 112, E05015, doi:10.1029/2006JE002839.

Moratto, Z. M., M. J. Broxton, R. A. Beyer, M. Lundy, and K. Husmann. 2010. Ames Stereo Pipeline, NASA's Open Source Automated Stereogrammetry Software. Lunar and Planetary Science Conference 41, abstract #2364. [ADS Abstract].

Morris et al. (2008), The Hydrothermal System at Home Plate in Gusev Crater, Mars: Formation of High Silica Material by Acid-Sulfate Alteration of Basalt, LPSC.

Murchie, S.L., et al. (2007), Compact Reconnaissance Imaging Spectrometer for Mars (CRISM) on Mars Reconnaissance Orbiter (MRO), *J. Geophys. Res.*,**112**, E05S03, doi :10.1029/2006JE002682.

Mustard, J.F., Murchie, S.M., Erard, S. and J. Sunshine (1997), In situ compositions of Martian volcanics: Implications for the mantle. *J. Geophys. Res*. **102** E11, 25605-25615.

Mustard et al., (2009), Composition, Morphology, and Stratigraphy of Noachian Crust around the Isidis basin. *J. Geophys. Res.*,**114**, E00D12 doi:10.1029/2009JE003349.

Nisbet, E.G. and N.H. Sleep (2001) The habitat and nature of early life. *Nature*, **409**, 1083- 1091.

Pelkey, S.M. et al. (2007), CRISM multispectral summary products: Parameterizing mineral diversity on Mars from reflectance. *J. Geophys. Res.***112**, E08S14, doi:10.1029/2006JE002831.

Preston, L.J., Benedix, G.K., Genge, M.J., and M.A. Sephton (2008), A multidisciplinary study of silica sinter deposits with applications to silica identification and detection of fossil life on Mars. *Icarus*, **198**, 331-350.

Poulet, F., J.-P. Bibring, Y. Langevin, J. F. Mustard, N. Mangold, M. Vincendon, B. Gondet, P. Pinet, J.-M. Bardintzeff, and B. Platevoet (2009b), Quantitative compositional analysis of

Martian mafic regions using MEx/OMEGA reflectance data: 1. Methodology, uncertainties and examples of application, *Icarus,* **201**, 69–83.

Rogers, A.D. and P.R. Christensen (2007), Surface mineralogy of Martian low-albedo regions from MGS-TES data: Implications for upper crustal evolution and surface alteration. *J. Geophys. Res.***112** E01003 doi:1029/2006JE002727.

Rodgers, K.A. et al. (2004), Silica phases in sinters and residues form geothermal fields of New Zealand, *Earth Sci. Rev.*,**66**, 1 – 61.

Ruff, S.W., et al. (2008), The Nature and Distribution of Silica at Home Plate in Gusev Crater, Mars: Evidence for a Hydrothermal System, 39th LPSC.

Ruff, S. W., et al. (2011), Characteristics, distribution, origin, and significance of opaline silica observed by the Spirit rover in Gusev crater, Mars, *J. Geophys. Res*., 116, E00F23, doi:10.1029/2010JE003767.

Schaber, G. G., Syrtis Major, a low relief volcanic shield, *J. Geophys. Res.*, 87, 9852-9866, 1982.

Schiffman, P., Zierenberg, R., Marks, N., Bishop, J.L., and M.D. Dyar, et al. (2006), Acid-fog deposition at Kilauea volcano : A possible mechanism for the formation of siliceous-sulfate rock coatings on Mars. *Geology*, **34**, 11, p. 921.

Seelos, K. D., et al. (2010), Silica in a Mars Environment: Ka'u Desert, Kilauea Volcano, Hawaii. *J. Geophys. Res.,* **115** E00D15 doi:10.1029/2009JE003347.

Segerer et al., (1993), Life in hot springs and hydrothermal vents. Origins of Life and Evolution of Biospheres, Springer Netherlands, 23.

Skok, J. R., J. F. Mustard, S. L. Murchie, M. B. Wyatt, and B. L. Ehlmann (2010), Spectrally distinct ejecta in Syrtis Major, Mars: Evidence for environmental change at the Hesperian-Amazonian boundary, *J. Geophys. Res.*, 115, E00D14, doi:10.1029/2009JE003338.

Skok, J.R. et al. (2010), Silica deposits in the Nili Patera caldera on the Syrtis Major volcanic complex on Mars. Nat. Geo., 3, 838-841, doi:10.1038/NGEO990.

Squyres, S. W. et al. (2008), Detection of Silica-Rich Deposits on Mars.*Science*, **320**.

Teplow et al., (2009) Dacite Melt at the Puna Geothermal Venture Wellfield, Big Island of Hawaii. *GRC Trans.,* 33, 989-994.

Tobler et al., (2008), In-situ grown silica sinters in Icelandic geothermal areas. *Geobiology*, 6, 481-502, DOI:10.1111/j.1472-4669.2008.00179.x.

Tosca, N.J., McLennan, S.M., Lindsley, D.H. and M.A.A. Schoonen (2004), Acid-sulfate weathering of synthetic Martian basalt : The acidfog model revisited. *J. Geophys. Res.***109**, E05003 doi :10.1029/2003JE002218.

Werner, S., (2009), The global martian volcanic evolutionary history. *Icarus*, **201**, 44-68.

White, D. E., R. A. Hutchinson, and T. E. C. Keith (1988), The geology and remarkable thermal activity of Norris Geyser Basin, Yellowstone National Park, U.S. Geol. Surv. Prof. Pap., 1456.

Tables

Table 1. Tobler et al. [2008] determination of Icelandic silica sinter growth rate and system properties.

Site	Silica Deposition Rate (kg m^{-2} yr^{-1})	Temperature (°C)	pH	$[SiO2]_{tot}$ ppm	Salinity %
Geysir 1	0.2	70-96	9	363	0.05
Geysir 2	0.7	76-82	8.7	372	0.05
Hveragerdi	0.7	66-74	9.1	304	0.04
Geysir 3	1.4	61-70	9	372	0.05
Svartsengi	9.7	42	7.7	250	2.56
Krafla	19.5	80	10	603	0.06
Reykjanes	304	75	7.5	695	4.67

Table 2. Calculated hydrothermal system properties based on measured deposit dimensions and application of terrestrial analog values.

	Southern Mound	**Proximal Deposits**
Mound Area	30,000 m^2	850,000 m^2
Mass/Area	17,000 kg/m^2	Same
Deposition Time with Rate 3 (0.2kg yr^{-1} m^{-2})	100,000 yrs	Same
Deposition Time with Rate 2 (20 kg yr^{-1} m^{-2})	1000 yrs	Same
Deposition Time with Rate 1 (305 kg yr^{-1} m^{-2})	60 yrs	Same
Water Volume (700 ppm SiO_2)	0.2 km^3	6 km^3
Dacite Volume (700 ppm SiO_2)	3.5 km^3	100 km^3
Basalt Volume (700 ppm SiO_2)	260 km^3	7440 km^3
Water Volume (300 ppm SiO_2)	0.5 km^3	15 km^3
Dacite Volume (300 ppm SiO_2)	8.2 km^3	230 km^3
Basalt Volume (300 ppm SiO_2)	610 km^3	52080 km^3

Figures Captions

Figure 1: Regional Context. A) MOLA elevation of the Syrtis Major Volcanic complex (outlined in black). Nili Patera is the youngest and northern most caldera in the volcanic system. B) Nili Patera caldera with CRISM coverage. Black dashed line is the profile of Figure 9.

Figure 2: Image of the Nili Patera caldera in Syrtis Major. a) CTX grayscale imagery with THEMIS DCS (Bands 9,7,5) overlay. Pink THEMIS regions corresponds with Si-rich TES deconvolution. b) Zoom in of cone structure. Arrows point out the largest of the deposits discussed in this paper, however all the bright areas to the left of the arrows show similar spectral features where large enough to fit a CRISM pixel. (CTX:P04_002427_1888_XI_08N292W; THEMIS:I09472026; CRISM:FRT000082EE, FRT00010628)

Figure 3. CRISM and HiRISE observations of silica deposits.a) CRISM RGB composite of Nili Patera cone with deposits. Large black ellipse indicates large field with many discrete deposits, small black ellipse indicates summit deposits. Blue circle, green and red arrows correspond to the deposit spectra shown in Figure 3 (R: 2.4 μm, G: 1.5 μm, B: 1.1 μm). (CRISM: FRT00010628) B) Custom 2.2 μm parameter map with green indicating detections. C) HiRISE image of flank deposit. D) HiRISE image of floor deposit to the south of the cone. (HiRISE:ESP_013582_1895)

Figure 4. Mineral deposit spectra showing strong 2.21 μm absorption band indicative of Si-OH. a) Average ratioed spectra from region of interest that includes all bright deposits (magenta in 2b). Possible detection of weak water absorptions at1.4 and 1.9 μm. Laboratory spectra of silica

coated basalt is shown for comparison [Chemtob et al., 2009]. Note the similar 2.2 μm Si-OH absorption. b) Ratioed spectra from regions in indicated in Figure 3. Detection is identified by characteristic absorption at 2.2 μm. c) Calibrated spectra of deposit 1 and the corresponding denominator spectra. The primary difference is the absorption feature at 2.2 μm present in the deposit but absent in the denominator.

Figure 5. Locations of silica deposits in the Nili Patera Caldera. The proximal deposits have been previously reported [Skok et al. 2010] and are mineralogically confirmed with CRISM spectra. Of these deposits, the south mound is best resolved and is used as the basis of the reported mound height determinations. The light-toned distal deposit have weak spectral signatures consistent with silica (Figure 8). Composition of these deposits are likely to be similar to be the proximal deposits but are not included in total area calculations until additional spectral confirmation. The edge deposits have textural and morphological similarities to the proximal and distal deposits but have not been spectrally imaged for confirmation. The southwest deposits are spectrally confirmed as silica-bearing with both with CRISM and THEMIS observations [Amador et al., 2011] and are isolated from the other deposits showing the potential extent of hydrothermal activity.

Figure 6. A) 3D perspective view of the Nili Patera cone and silica deposits (5x vertical exaggeration). All silica deposits are location either on the volcanic cone or the associated dacite flow surrounding the cone and spreading out to the West. Deposits occur in a thin band on the western side of the cone summit and on southern flanks of the cone. Spectral and morphological

studies of Syrtis Major repeatedly confirm it basaltic composition and low lava viscosity. The elevated topography of this volcanic cone is unique throughout the Syrtis Major complex indicating a more viscous composition than the basaltic complex, supporting a siliceous composition of the cone. (CRISM FRT00010628 color on CTX DEM). B) HiRISE on HiRISE DEM of southern portion of volcanic cone. South Mound is on the caldera floor in the foreground to the right of center. Fan shape deposit in on the volcanic cone flank to the left of center. Silica material is sourced on the cone and is deposited downslope. View toward north. (5x vertical exaggeration). C) Close up of South Mound. View toward north. (5x vertical exaggeration).

Figure 7. South mound profile and volume determination, North is at the top of each image. A) HiRISE color of South Mound displaying semi-circular deposit with a concentration of material at the center of the mound. B) Color DEM with topolines of southern slope of the volcanic cone with the South Mound. C) Associated CTX image with profile shown in D. D) Topography profile of southern flank of volcanic cone and South Mound silica deposit. This deposit is superimposed on the volcanic slope but has a median height of approximately 20 m.

Figure 8. Distal Silica Spectral Confirmation. A) Volcanic cone and north section of dacite flow. B) Ratioed spectra of distal deposits show characteristic 2.2 μm Si-OH absorption features. (Spectra from HRS0000C6D7) C) Southwest edge of dacite flow with light-toned silica deposits. D) Ratioed spectra of distal deposits show characteristic 2.2 μm Si-OH absorption features. (Spectra from FRT000082EE).

Figure 9. East-West profile of Nili Patera Caldera with volcanic cone and proposed caldera schematic (Transect is shown in dotted line in Figure 1). Late stage evolved eruption formed cone and dacitic flows. Thermally driven waters rise to the surface to deposit silica deposits. Water may be sourced from 1) Magmatic waters differentiated from evolved magmas or 2) surrounding hydrated Noachian crust or buried hydrosphere.

Datasets:

CRISM:

FRT000082EE

HRS0000C6D7

FRT000010628

HiRISE:

ESP_013582_1895

ESP_014149_1890

ESP_019585_1890

ESP_020940_1895

ESP_005684_1890

ESP_019740_1890

CTX:

P20_008980_1869_XI_06N291W

P18_008255_1888_XN_08N292W

P17_007609_1883_XN_08N293W

P17_007543_1881_XN_08N290W

P21_009191_1895_XN_08N292W

P16_007398_1893_XN_09N292W

P11_005262_1884_XI_08N291W

P04_002427_1888_XI_08N292W

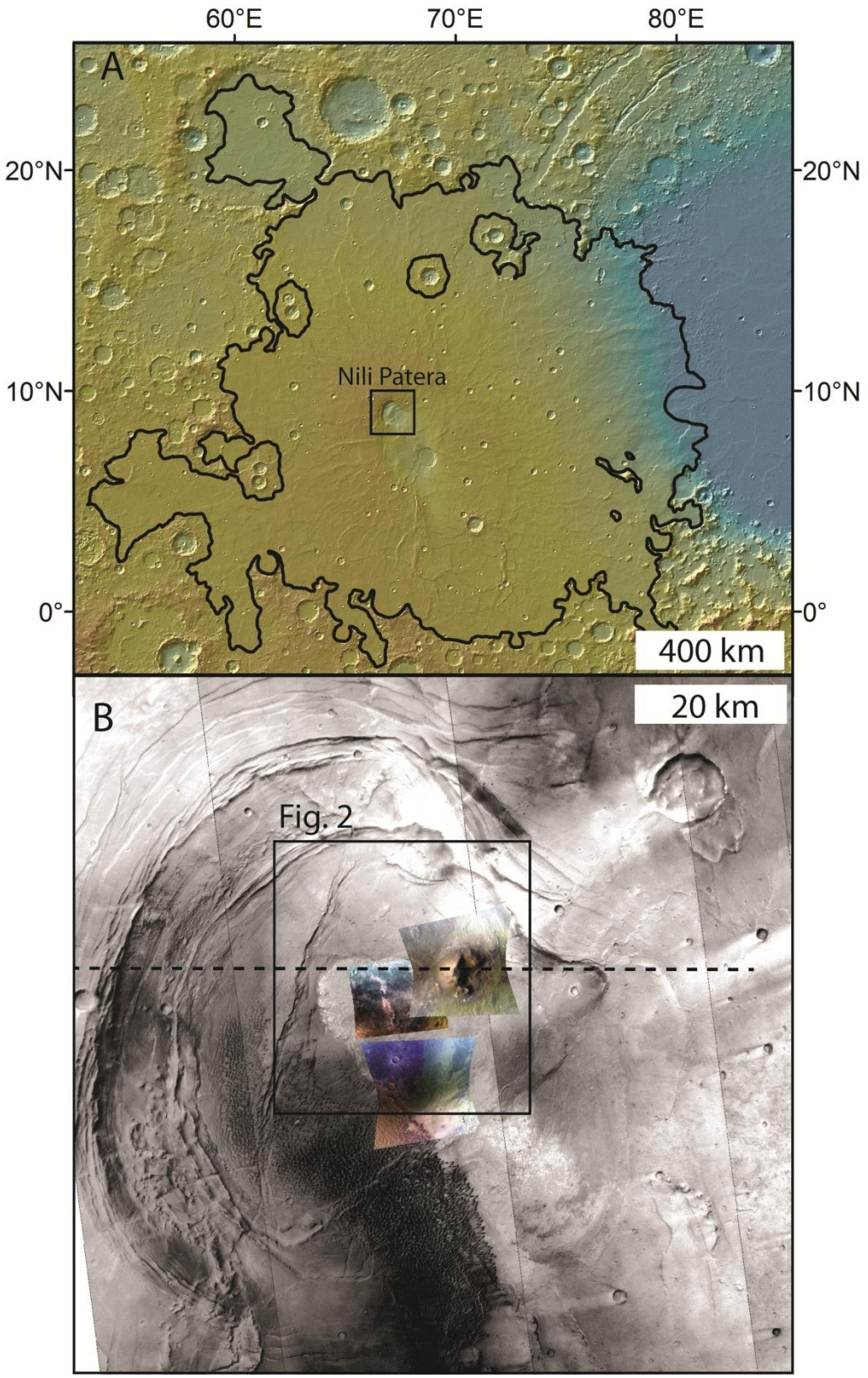

Chapter 4, Figure 1

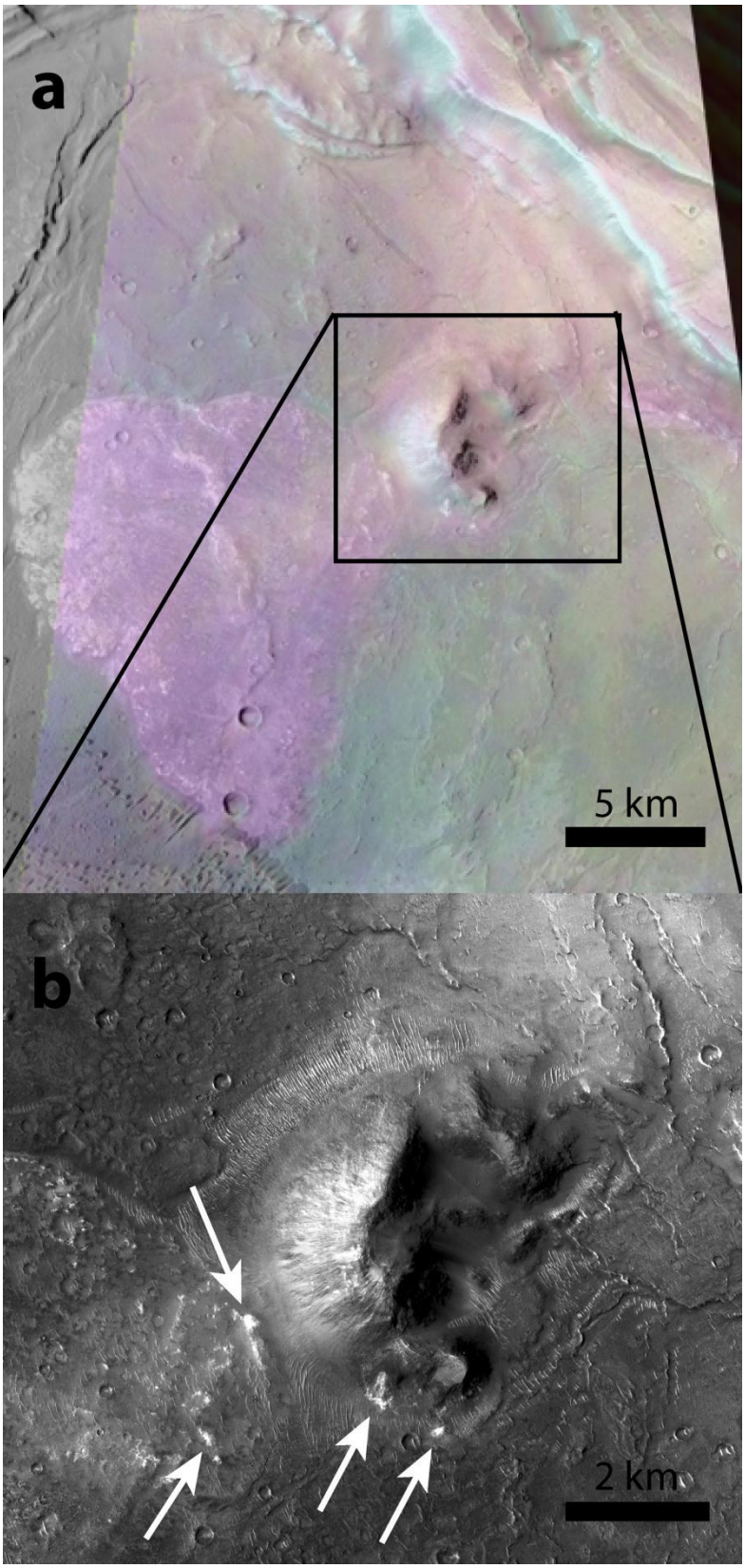

Chapter 4, Figure 2

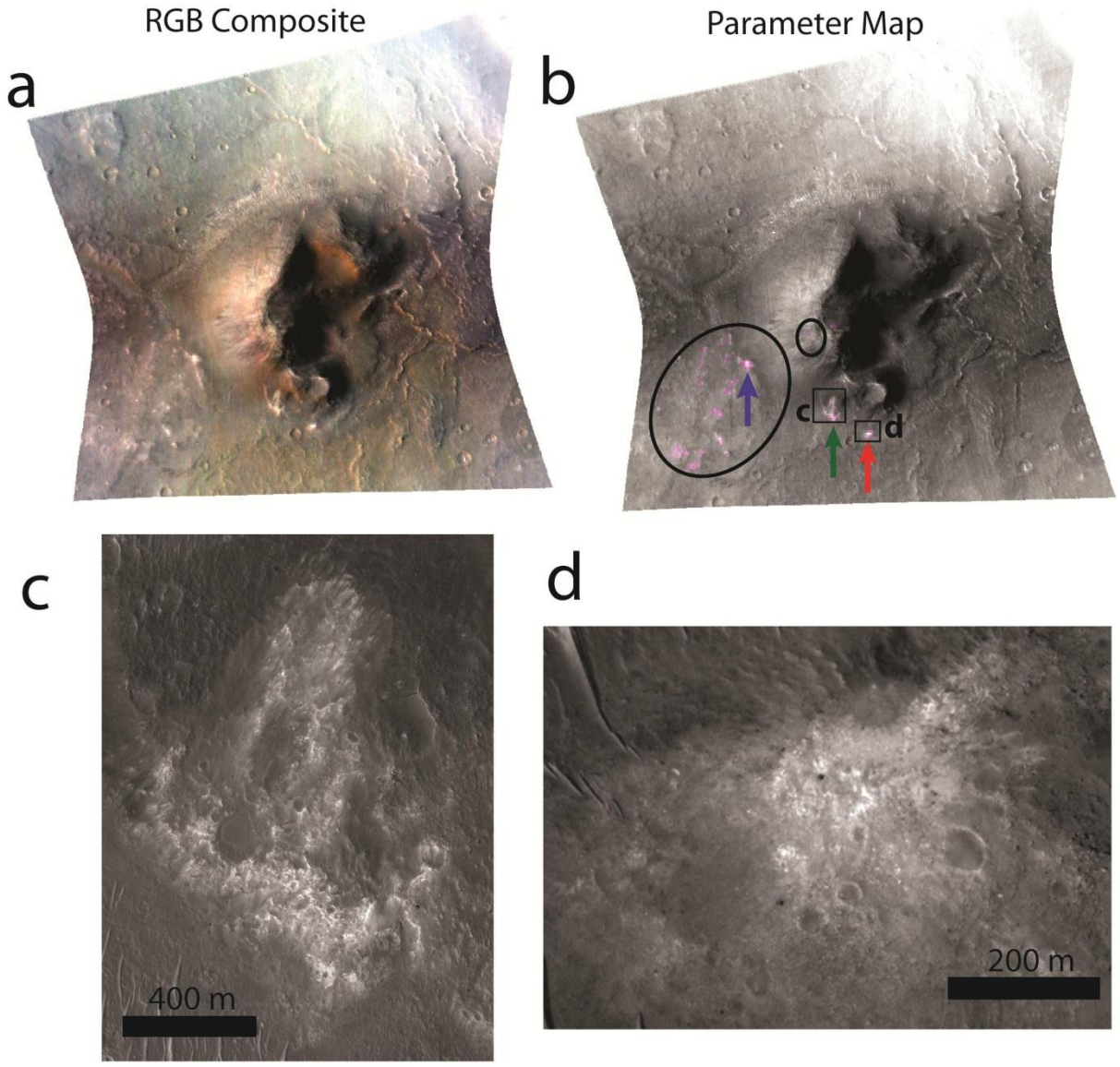

Chapter 4, Figure 3

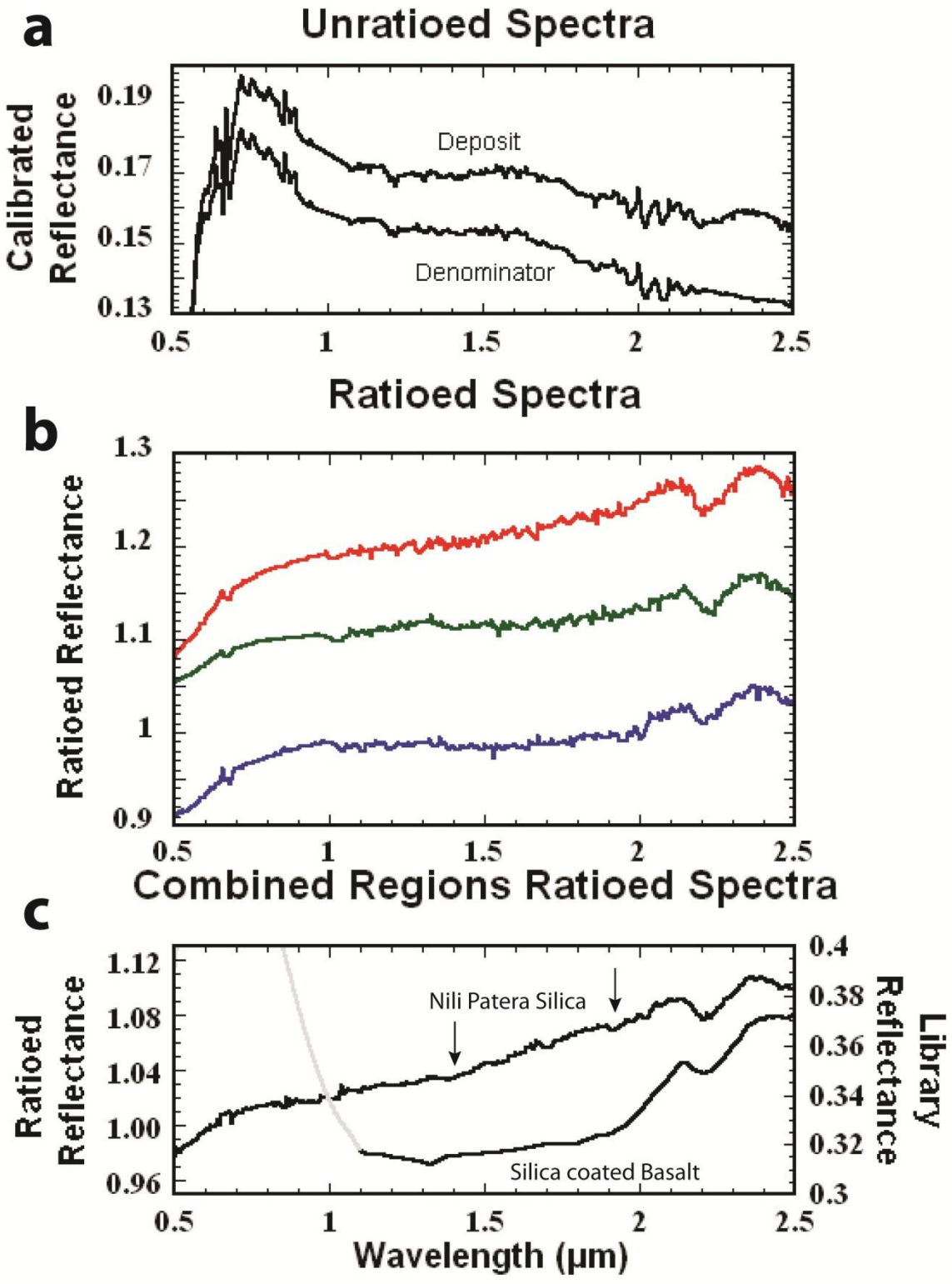

Chapter 4, Figure 4

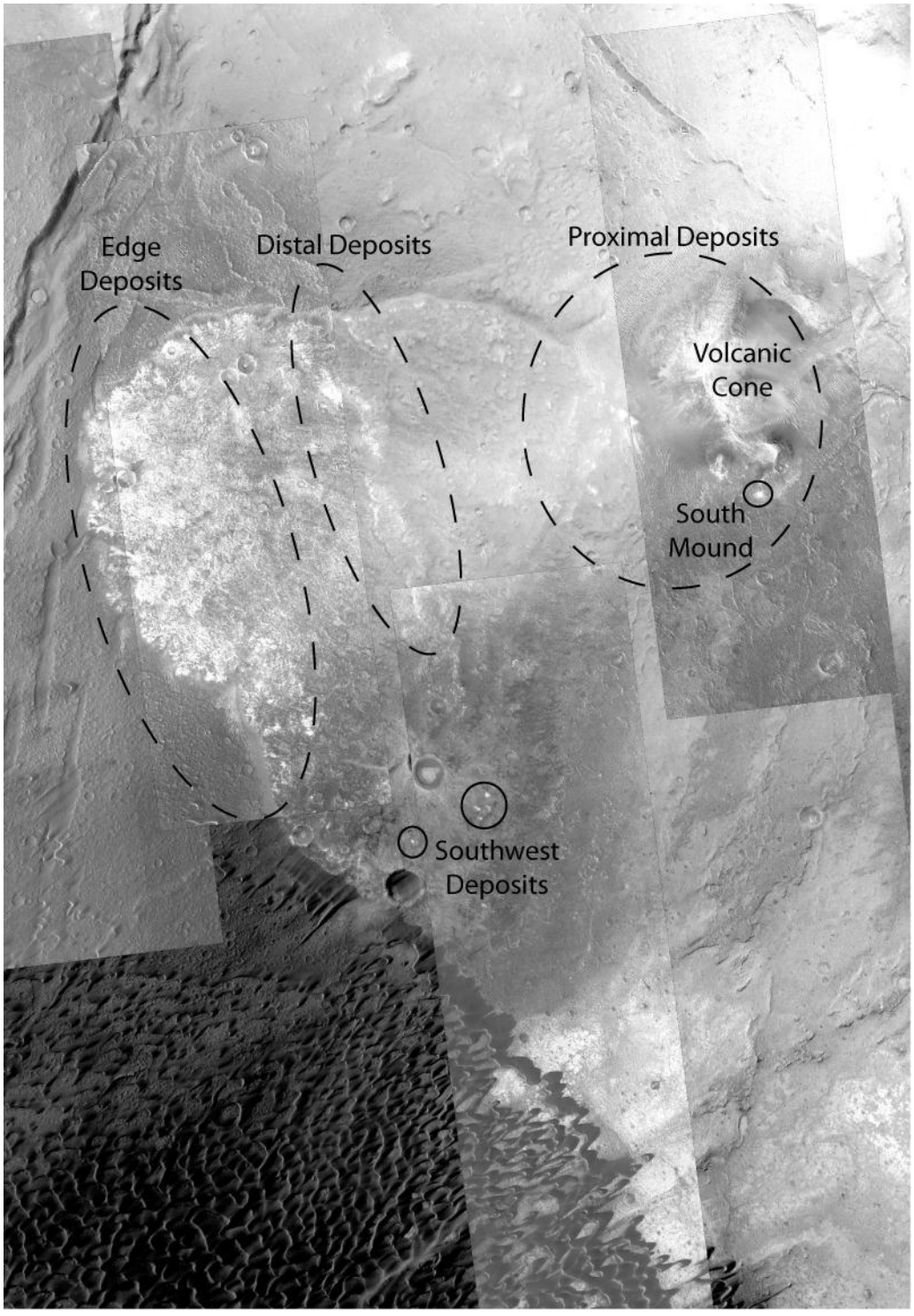

Chapter 4, Figure 5

Chapter 4, Figure 6A

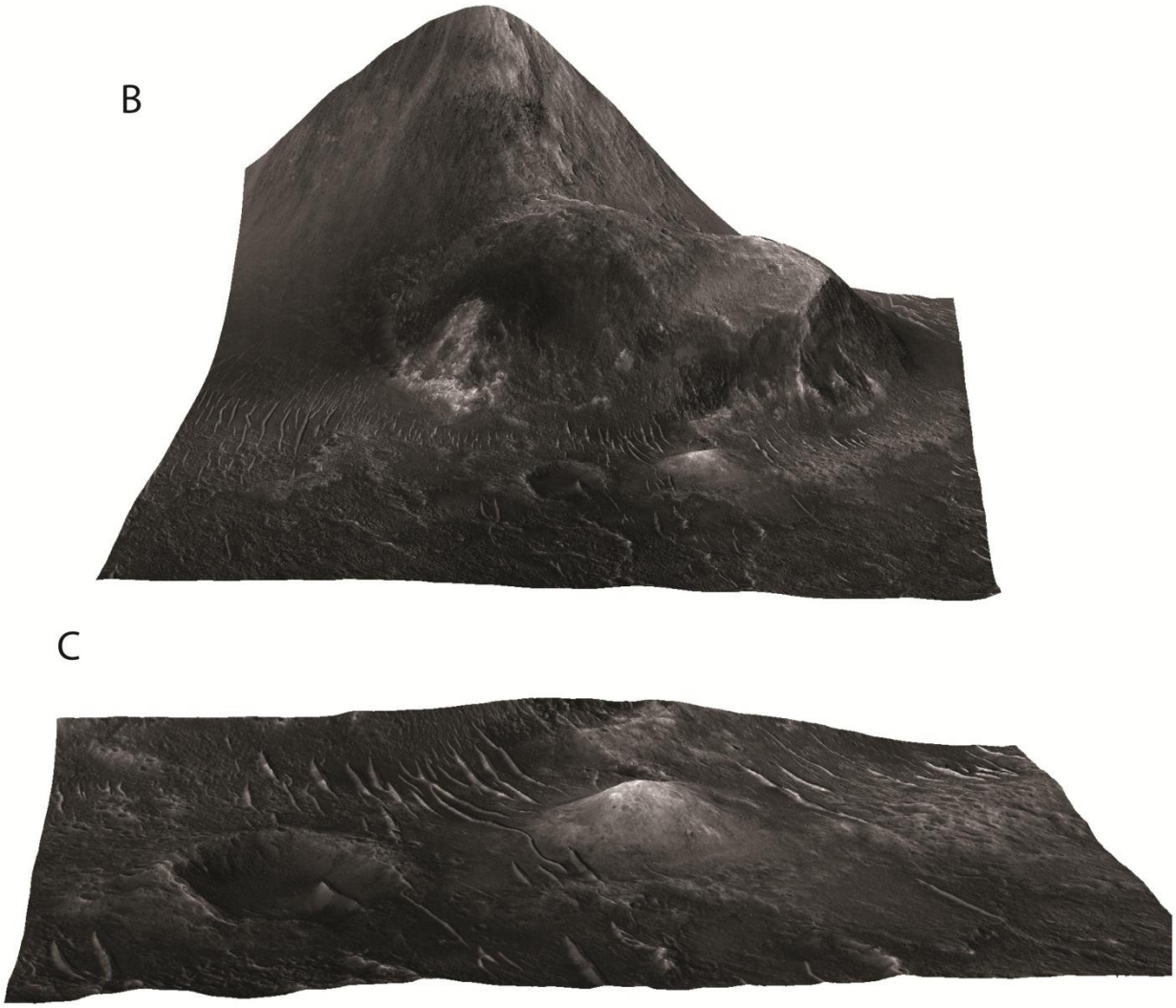

Chapter 4, Figure 6

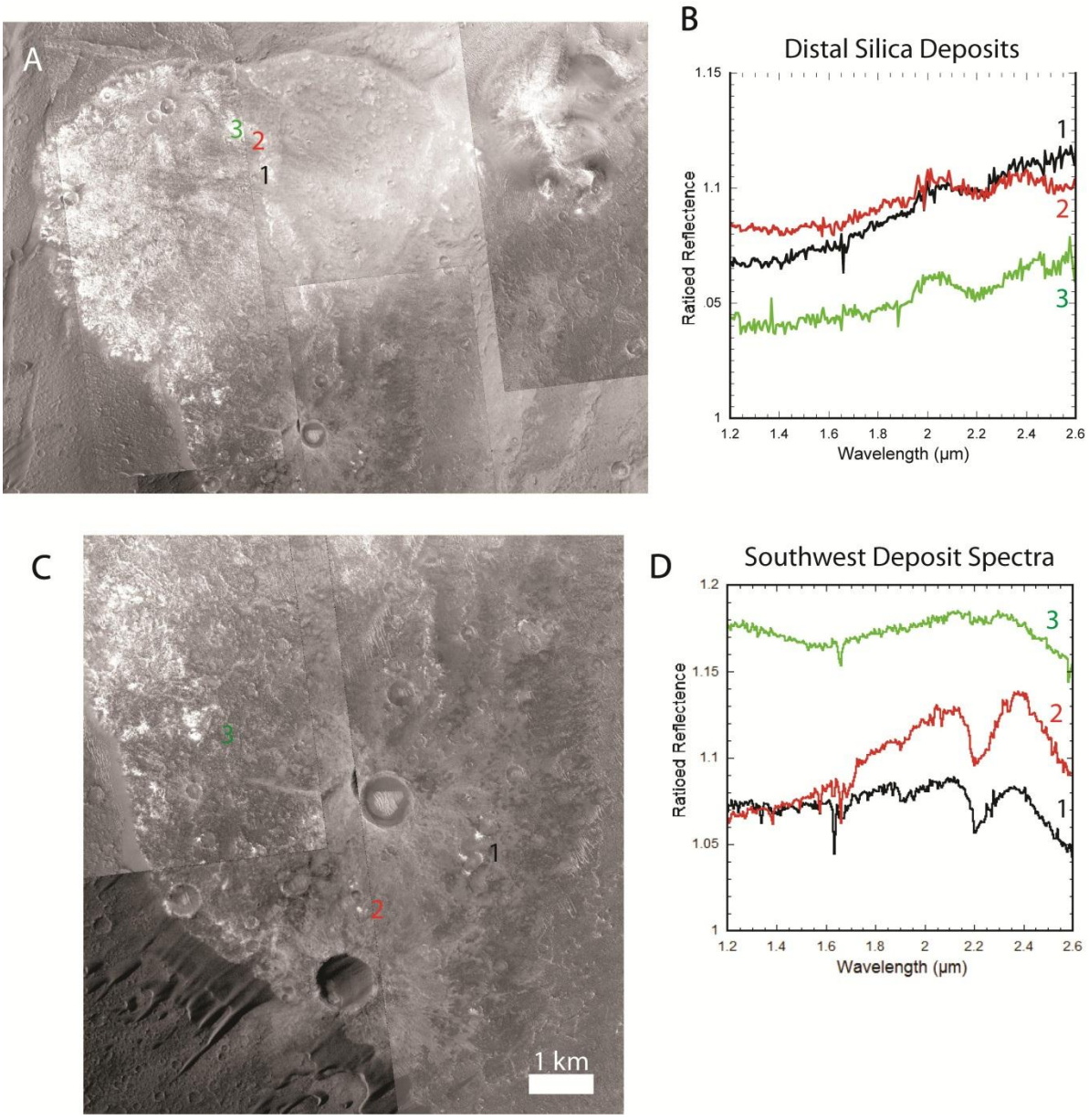

Chapter 4, Figure 7

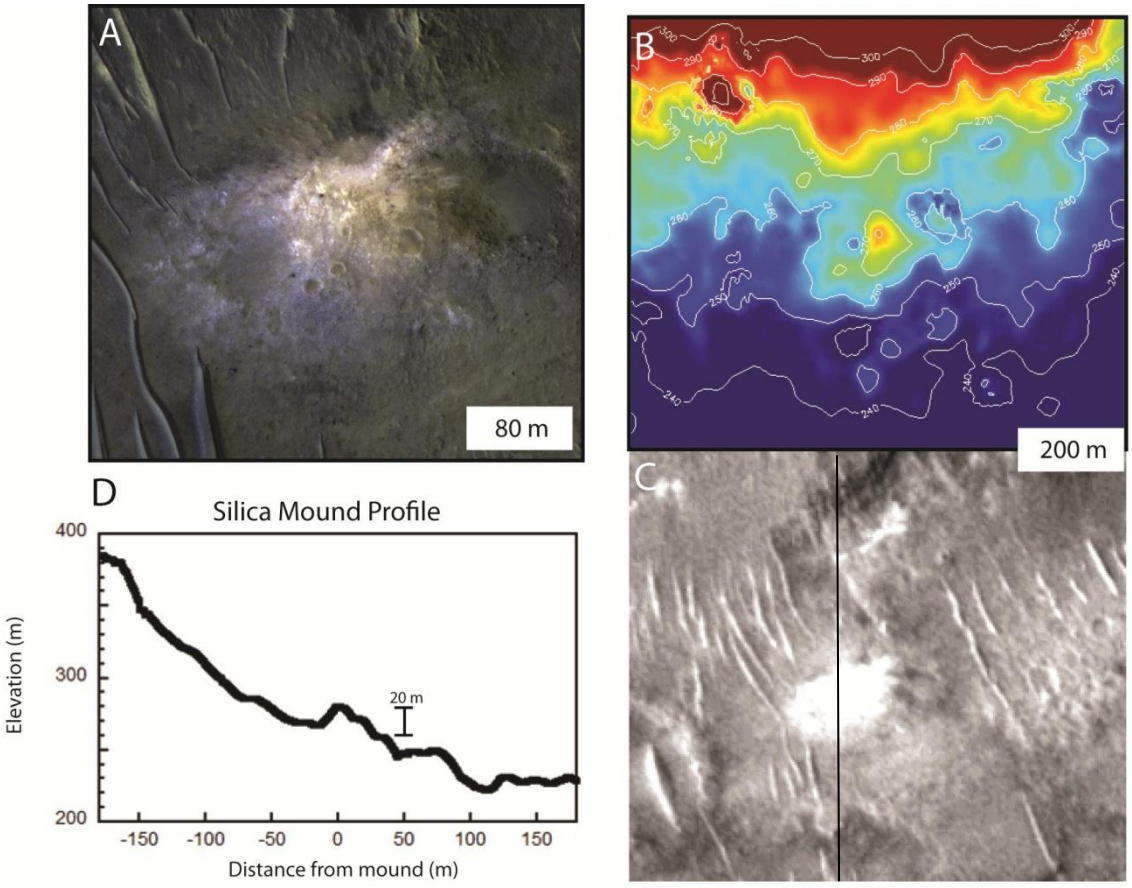

Chapter 4, Figure 8

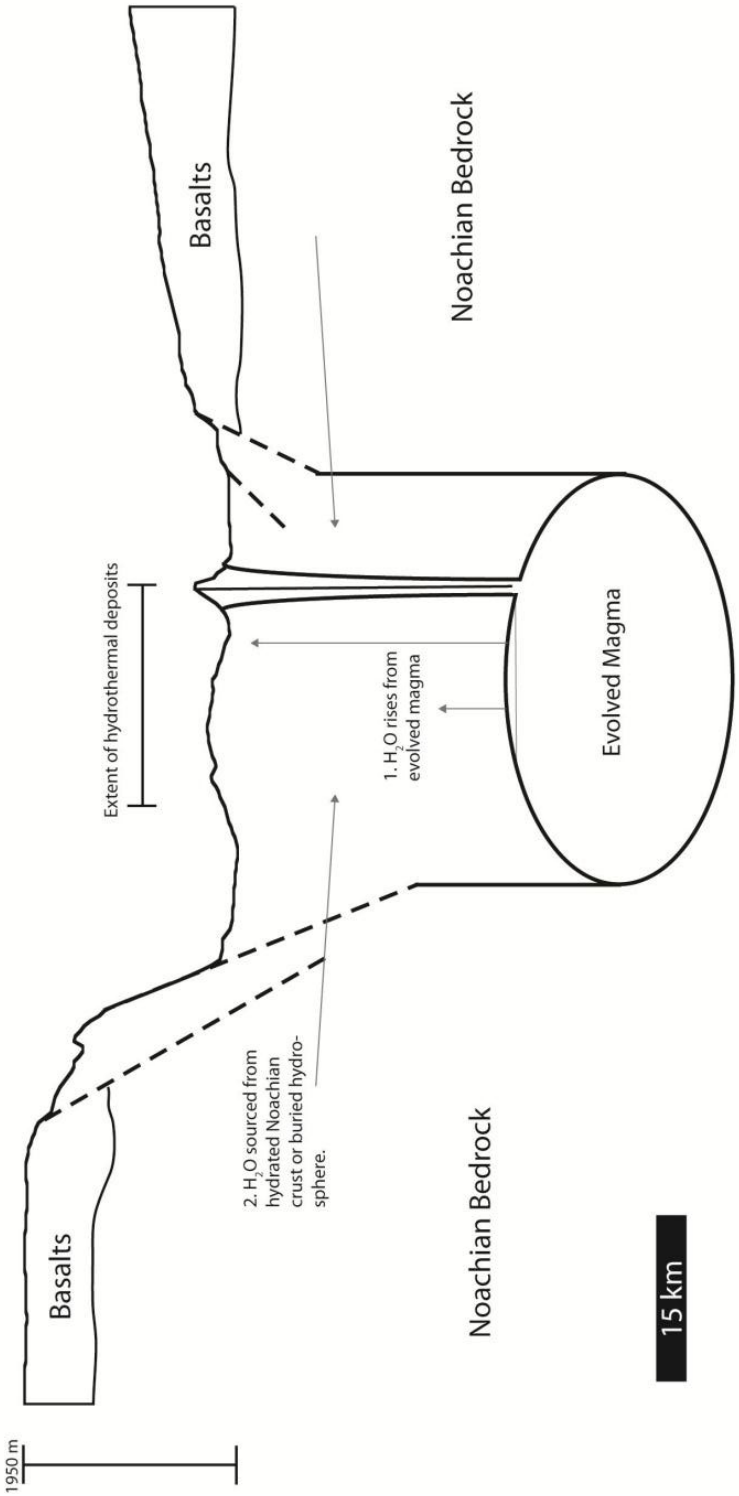

Chapter 4, Figure 9

Chapter 5:

A Synthesis of Martian Volcanic Evolution: Problems and Possibilities.

J.R. Skok

Department of Geological Sciences, Brown University

Introduction

Mars is a volcanic planet. Mars' volcanoes are the largest in the solar system and volcanic flows have covered most of the surface. Understanding the igneous history of Mars provides a deep understanding into the formation, evolution and inner workings of the planet. This thesis, combined with my Masters paper [Skok et al., 2010], explore three important parts of the evolution of the volcanic history of Mars. First we considered the formation of the ancient igneous crust, using excavated mafic lithologies to uncover the early large scale mineral differentiation. We then touch on details of the Hesperian volcanic episode as preserved in the Syrtis Major complex and the transition from the Noachian to Hesperian and how those changes affected the style and composition of the volcanic record and the implications of this change. Finally we explored the end stage of the particular volcanic system with a rare evolved volcanic flow and hydrothermal system in the Nili Patera caldera of the Syrtis Major volcanic complex. Understanding the volcanic history of Mars has important implications for several key aspects of Martian history, including the formation and evolution of the surface environment, the thermal and energy budgets of the crust and the capacity for habitability and its preservation. This work has explored several important questions about the history of Mars but has uncovered many more that will help to refocus future exploration efforts.

Martian Primary Crust: An oxymoron? Chapters one and two began as a project to understand the composition and nature of the primary crust of Mars. 'Primary' is a term used to describe a crust the solidified from a magma ocean, like the lunar highlands, in contrast to secondary crust that forms from melting primary materials and tertiary crust that implies multiple episodes of melting [Taylor, 1992]. As work progressed, I began to move away from the use of the term 'primary' to describe any features on Mars and favored the more generic 'ancient' crust

that I use throughout this thesis. Furthermore, the definition of 'crust' on Mars is difficult to define with current observation as the differences between the deep crust and upper mantle are not well studied. In this work, based on the models presented in chapters 1 and 2, I suggest that the mantle is formed from the primary minerals that formed as cumulates from the magma ocean and the crust as the result of mantle melts. In this paradigm, all of the crust, by definition, is secondary and in some rare locations, tertiary.

Crustal thickness maps have been produced [Neumann et al., 2004] based on topography and gravity data to measure the level of a possible density difference. A density difference could be the result of melting mafic mantle predicted by Elkins-Tanton et al., [2005] to create a basaltic melt that would be rich in incompatibles and Al from the deep garnet layer to produce a substantial plagioclase fraction and creating a measurable density difference. This ambiguity between the difference of the crust and mantle is a key question for future Mars exploration. A much anticipated seismic network would aid understanding of this boundary and constrain the mineral change that marks the boundary between the mantle and crustal interface.

Deep Crust vs. Ancient Crust. A second issue central to the study of the ancient Martian crust is the nature of the excavated material. Chapters 1 and 2 interpret 'excavated' as 'ancient' while these are two could be very distinct terms. On a planet without plate tectonics there are few processes that can recycle or modify the crust that is ancient and deep. However the active volcanic history on Mars would have left a crust riddled with plutons [Wilson and Head, 1994] and volcanic feeder dikes [Pedersen et al., 2009]. Excavation of the central peak could have easily exposed a relatively young pluton instead of the ancient crust. This is one of the central uncertainties to this work and short of isotopic age dating of the material, I do not know of a way to determine the precise geologic history of the lithologies in a single central peak. I believe a

solution to this problem is outlined in the methodology of chapter 2. While an unknown and potentially large number of relatively young plutons may exist in the Martian crust, it is unlikely that they dominate the subsurface volume. Looking at a large number of central peaks should minimize the effects of measuring the composition of an exposed pluton in some of the examined peaks. If some of the central peaks do expose pluton material it should show up as variations in the compositional data. Young Martian volcanics have been fairly well studied with spectroscopic analysis of Hesperian volcanoes [Rogers and Christensen, 2007; Poulet et al., 2009] and laboratory analysis of Martian meteorites [Mittlefehldt, D. W., 1994; Nyquist, L.E., et al., 2001; McSween et al., 2002]. These young volcanics are characterized by enrichments in high-calcium pyroxenes (HCP) and often a basaltic composition. None of the crustal exposures that we examine in Chapters 1 and 2 have spectral signatures consistent with these younger volcanics. They are consistent with Noachian-aged materials [Mustard et al., 2005; 2007], making it difficult to discriminate between a crust formed in the aftermath of the mantle overturn in the first 100 Ma of Mars history and Noachian plutons formed during the next ~600 Ma of the Noachian. A final solution to this problem may well have to wait until we have radiometric dating of the samples in question.

What About the Rest. One final issue regarding the formation of Mars is what happens to all the incompatible elements that do not fit into the mafic mineral crystal structures. The geophysical models [Borg and Draper, 2003; Elkins-Tanton et al., 2005] focus on the olivine and pyroxene and often make allowances for garnet layers in the mantle, but rarely mention other minerals. Drawing attention to this problem on the Moon, is the concept of the KREEP terrain [Shearer et al., 2006]. KREEP (Potassium, Rare Earth Elements, Phosphorous) is a geochemical signature found in Procellarum region thought to be the result of the last remnants of the magma

ocean crystallization stage. A similar process may have occurred on Mars. The cumulate crystallization of Mars would have progressed unit a small regions of melt near the surface were left that were highly enriched in incompatible elements. Even after mantle overturn, these material would likely remain at the top of the mafic mantle cumulates but below eruptions that would form the ancient crust. The presence and implications of this material is not well documented or well discussed in the scientific literature but has important implications for Martian volcanism as I explore in the following section.

Transition to Hesperian Volcanism. The early crustal volcanism would be driven by the initial heat of the planet, generated by accretion and differentiation. We have suggested that the bulk of the ancient crust of Mars was the result of the mantle overturn and related processes. Residual heat would continue to drive the volcanic activity for some time but would eventually tapper off as the planet cooled. However, the geologic record on Mars does not support this simple cooling history of Mars. Instead, about ~500 Ma after the planet formed, a pulse of volcanism began in the Early Hesperian, covering much of the planet [Head and Basilevsky, 2001], with a distinct composition of volcanics [Rogers and Christensen, 2007; Poulet et al., 2009; Skok et al., 2010]. Whereas the crustal formation and Noachian volcanism has likely driven by initial planetary heating from accretion and differentiation, the Hesperian volcanism would have likely had a different driving force, given its timing. This stage of volcanism would be driven by the decay of radioactive elements, notably; ^{40}K (λ=1.248x10^9 years), and ^{238}U (λ=4.468x10^9 years) [Kiefer, 2003]. One key feature of the Hesperian volcanism in comparison to the Noachian mafics is that the pyroxene component of the Hesperian volcanics is highly enriched in Ca [Rogers and Christensen, 2007; Poulet et al., 2009; Skok et al., 2010]. Conventional wisdom is that the Ca content is a proxy for melt temperature [Lindsley, 1983]

with cooler early melts initially melting the weaker bonds of high-calcium pyroxenes (HCP), with the cooler temperatures solely due the steadily decreasing heat budget of Mars. This would lead to melts that result in basalts enriched in HCP. While not contradicting that hypothesis, here we speculate on an alternative cause of the composition change in the Hesperian. The KREEP-like layer we hypothesized would contain the bulk of the mantle's incompatible elements. In this scenario the Hesperian basalts would be sourced from a small region of the mantle that is highly enriched in Ca rather than just being a function of melt temperature. If so, the Hesperian volcanics would provide a view into this analog KREEP units rather than the mantle as a whole, which would have sourced the ancient crust and Noachian volcanism.

The Death of a Volcano. The final step in the life of a volcano are the last sputtering eruptions issuing out small volumes of evolved lavas and using its latent heat to drive a hydrothermal system. The final snapshot of this process is preserved in the Nili Patera caldera on the Syrtis Major volcanic complex. Chapter 4 reports the identification of this system and explores the extent and possible formation scenarios for development. Extensive searching has not found any comparable features so well preserved on other Martian volcanoes. This means that this site offers a rare opportunity to understand the results of the end stage of the volcanic process on Mars.

The first major question regarding this site is just why are there dacite lava flows coming out of this basaltic volcano. Nowhere else on Mars does evidence support an evolved lava flow (though an evolved pluton may have been excavated in a crater to the northwest [Bandfield, 2006]). On Earth, evolved magmas are very common, with dacites forming commonly in subduction zone volcanism [Eichelberger, 1975]. Dacites have even been recorded in rare basaltic terrains on Earth such as the Puna exposure in Hawaii [Teplow et al., 2009], a fairly

good first order analog to Syrtis Major. Why then are they not seen more on Mars? The in-depth analysis of the Hawaiian Puna analog are still in its initial stages and are hampered by the dacites location at a depth of 2415 m [Teplow et al., 2009]. Understanding the details of this analog may help understand the unique property of the Nili Patera dacite. Until then, we can consider a few options. One is that, like Hawaii, may of the volcanoes on Mars produced evolved magmas, but maybe they are also like Hawaii in that the evolved magma may stay deeply buried in the volcanic structure and not visible. Why then would it erupt in Syrtis Major but not on other Martian volcanoes? One potential reason could be the particular morphology of Syrtis Major and Nili Patera Caldera. As seen in Chapter 4. Figure 9, the Nili Patera has a vertical relief of approximately 2 km below the surrounding plains while the Syrtis Major flows have a thickness estimated at ~500 m [Hiesinger and Head, 2004]. This means that the caldera floor is significantly below the volcanic edifice and is embedded in the basement crust. Most other Martian volcanos have some topographic expression that raise the level of their caldera. The low level of the Nili Patera Caldera may mean that the surface is closer to the magma source and make it easier to erupt the evolved lavas. Better understanding of dacite formation on terrestrial basaltic volcanoes may help to understand this rarity on Mars.

The next big question is the nature of the relationship between the dacite flows and the hydrothermal silica deposits. Every silica deposit is seen either on the volcanic cone or on the dacite flow. The simplest solution is that the dacite is directly responsible for the hydrothermal activity. The heat and trapped fluids within the flows could have driven an alteration process occurring solely on the caldera surface with no need of a deep hydrothermal system. While this process could be responsible for the distal and Southwest deposits, the mound building and fan morphology of the proximal units indicate a longer lived, more robust system.

A second scenario is that the dacite marks the remains of the Nili Patera surface at the time of hydrothermal activity. Just south of the dacite flow is a large active dune field [Silvestro et al. 2010] and highly etched and presumed eroded basaltic caldera floor. It could be that the dacite and hydrothermal system was initially more prevalent, but extensive erosional processes active just to the south, etched away at those deposits leaving only the current observed ones left. Deciding between these scenarios will likely require an in-depth surface search for signs of the extent of hydrothermal activity and beyond what can be done with current remote observations.

Life in a Dying Volcano. The Viking lander's non-detection of life lead to the Mars exploration mantra of 'Follow the Water' as a useful sidestep. This search has been an unqualified success, again and again. With that success but still wary of moving to 'Looking for Life', the next step toward that objective is the search for habitability. This goal has proven to be more contentious. 'Habitability' as a concept almost has the implicit requirement of having been inhabited. Do we look for environments that would be habitable had it been on Earth? Or try to focus on environments that would have the right conditions, resources and timing that life (or more likely the molecular precursors to life) could have formed on Mars and then had the good fortune of being preserved? The debate over these questions still rages and will guide most future robotic missions to Mars. This debate sets the stage for the importance of the Nili Patera hydrothermal deposits. All realistic formation mechanisms for these deposits involve water and significant heat and volcanic energy. Similar hydrothermal sites on Earth were always inhabited [Segerer et al., 1993] and are occasionally thought to be the likely point of origin of life on Earth [Nisbet et al., 2001] and the silica deposits are the most robust way of preserving those signs of habitability [Farmer et al., 1999]. Given that this feature was almost certainly habitable (having water and energy sources), the big question remains, was it inhabited? This, of course, is

impossible to tell with remote data (otherwise you would be reading this in Science and/or a Noble broadcast), but the opportunity that life could have started locally given the resources, or that this site could have tapped a potential deep biosphere, as explored in Chapter 4, make this one of the most compelling places to sample on Mars.

Conclusion

This thesis details my best efforts over the past five years to advance the understanding of the volcanic history of Mars. We have learned that the first Martian crust cooled slowly and differentiated into mafic cumulates. We have explored the diverse history of the Northeast Syrtis region, the HCP enrichment of Syrtis Major and the hydrothermal history in Nili Patera. At every step of this process it has become abundantly clear how much more we need to know. More images, more samples, mores measurements and most of all, more understanding. The problems described throughout the thesis and detailed in this chapter will lay the groundwork going forward and lead to even more questions. Rather than this being the end of my conclusions, THIS is just the beginning of the work to come!

References:

Bandfield et al., (2006) Extended surface exposures of granitoid compositions in Syrtis Major, Mars. *Geophys. Res. Lett.*, 33, L06203, doi:10.1029/2005GL025559.

Borg, L.E and D.S. Draper (2003), A petrogenetic model for the origin and compositional variation of the martian basaltic meteorites. *Met. & Planet. Sci*. 38, 1713-1731.

Eichelberger, J.C., (1975), Origin of andesite and dacite: Evidence of mixing at Glass Mountain in California and at other circum-Pacific volcanoes. *GSA Bull.* 86, 1381-1391.

Elkins-Tanton, L. T., Hess, P.C., and E. M Parmentier (2005), Possible formation of ancient crust on Mars through magma ocean processes. *J. Geophys. Res*., 110, E12S01, doi:10.1029/2005JE002480.

Farmer, J.D and Des Marais, D.J. (1999), Exploring for a record of ancient Martian life. *J. Geophys. Res.*, **104**, E11 26977-26995.

Head III, J.W. and A.T. Basilevsky (2001) The Hesperian Period of Martian History: Key Trends in Volcanic and Tectonic Activity. LPSC 32.

Hiesinger, H., and J. W. Head III (2004,) The Syrtis Major volcanic province, Mars: Synthesis from Mars Global Surveyor data. *J. Geophys. Res.*, **109**. E01004,

Kiefer, W.S. (2003), Melting in the martian mantle: Shergottite formation and implications for present-day mantle convection on Mars. *Met & Planet. Sci.*, 39, 12, 1815-1832.

Lindsley, D.H. (1983) Pyroxene thermometry. *Am. Min*., 68, 477-493.

McSween, H. Y. (2002), The rocks of Mars, from far and near. *Met. Planet. Sci*., 37, 7-25.

Mittlefehldt, D. W., (1994), ALH84001, a cumulate orthopyroxenite member of the martian meteorite clan. *Meteoritics*. 29, 214-221.

Mustard et al. (2005), Olivine and Pyroxene Diversity in the Crust of Mars. *Science*, 307, 1594 doi: 10.1126/science.1109098.

Mustard et al. (2007), Mineralogy of the Nili Fossae region with OMEGA/Mars Express data: 1. Ancient impact melt in the Isidis Basin and implications for the transition from the Noachian to Hesperian. *J. Geophys. Res.*, 112, E08S03, doi:10.1029/2006JE002834.

Nisbet, E.G. and N.H. Sleep (2001) The habitat and nature of early life. *Nature*. 409, 1083- 1091.

Neumann, G. A., M. T. Zuber, M. A. Wieczorek, P. J. McGovern, F. G. Lemoine, and D. E. Smith (2004), Crustal structure of Mars from gravity and topography, *J. Geophys. Res*., 109, E08002, doi:10.1029/2004JE002262.

Nyquist, L.E., Bogard D. D., Shih C-Y., Greshake A., Stoffler, D., and O. Eugster (2001), Ages and geologic histories of martian meteorites. *Space Sci. Rev.*, 96, 105-164.

Pedersen, G.B.M, Head III, J.W. and L. Wilson (2009) Formation, erosion and exposure of Early Amazonian dikes, dike swarms and possible subglacial eruptions in the Elysium Rise/Utopia Basin Region, Mars. *Earth & Planet. Sci Lett.*, 294, 424-439.

Poulet, F., Mangold, N., Platevoet, B., Bardintzeff, J.-M., Sautter, V., Mustard, J. F., Bibring, J.-P., Pinet, P., Langevin, Y., Gondet, B., and A. Aléon-Toppani (2009), Quantitative compositional analysis of Martian mafic regions using the MEx/OMEGA reflectance data: 2. Petrological implications. *Icarus*, 201, 1, 69-83.

Rogers, A. D., and P. R. Christensen (2007), Surface mineralogy of Martian low-albedo regions from MGS-TES data:Implications for upper crustal evolution and surface alteration, *J. Geophys. Res.*, 112, E01003, doi:10.1029/2006JE002727.

Segerer et al., (1993), Life in hot springs and hydrothermal vents. Origins of Life and Evolution of Biospheres, Springer Netherlands, 23.

Shearer et al., (2006), Thermal and Magmatic Evolution of the Moon. *Rev. Min. Geochem*., 60.

Silvestro et al., (2010), Ripple migration and dune activity on Mars: Evidence for dynamic wind process. *Geophys. Res. Lett*., 37, L20203, di:10.1029/2010GL044743.

Skok, J. R., J. F. Mustard, S. L. Murchie, M. B. Wyatt, and B. L. Ehlmann (2010), Spectrally distinct ejecta in Syrtis Major, Mars: Evidence for environmental change at the Hesperian-Amazonian boundary, *J. Geophys. Res.*, 115, E00D14, doi:10.1029/2009JE003338.

Taylor, S. R. (1992), Solar System Evolution: A New perspective, 307 pp., Cambridge Univ. Press, New York.

Teplow et al., (2009) Dacite Melt at the Puna Geothermal Venture Wellfield, Big Island of Hawaii. *GRC Trans.,* 33, 989-994.

Wilson, L. and J.W. Head III (1994), Mars: Review and analysis of volcanic eruption theory and relationships to observed landforms. *Rev. Geophys*. 32, 3, 221-263.